Ollscoil na hÉireann

NATIONAL UNIVERSITY OF IRELAND

Formation and Electrical Interfacing of Nanocrystal-Molecule Nanostructures

A Thesis Presented to

The National University of Ireland, Cork

for the degree of

Doctor of Philosophy

By

Nicolas Sassiat

Supervised by Dr. Aidan Quinn

Head of Department: Prof. John McInerney

Tyndall National Institute

University College Cork

Physics Department

June 2011

Table of Contents

Declaration

The work presented in this thesis was supervised by Dr. Aidan Quinn and is Nicolas Sassiat's own work unless otherwise stated.

Experimental data on the formation of hybrid nanostructures in solution were taken from Dr. Claire Barrett, Raquel Palacios and Ethel Noonan (Chapter 2). The synthesis of organic molecules was done by Emma Harvey in Dr. Mary Pryce's laboratory in Dublin College University, Dublin (Chapters 3 and 4). Numerical simulations on the Generalised Multi-particle Mie theory were performed by Dr. Gaëtan Lévêque from the Photonics Theory Group at Tyndall, Cork (Chapter 2), while molecular dynamics simulations investigating binding of molecules on surfaces and miscibility interfaces were conducted by Victor Akujobi, Dr. Michael Nolan and Dr. Damien Thompson from the Electronic Theory Group at Tyndall, Cork (Chapters 2, 3 and 4).

The present thesis is submitted for the degree of Doctor in Philosophy at University College Cork.

Head of UCC Physics Department	Prof. John McInerney
External examiner	PD Dr. Michel Calame
Internal examiner	Prof. Paul Townsend
Supervisor	Dr. Aidan Quinn

Abstract

The objective of this thesis work is to develop methods for forming and interfacing nanocrystal-molecule nanostructures in order to explore their electrical transport properties in various controlled environments. This work demonstrates the potential of nanocrystal assemblies for laterally contacting molecules for electronic transport measurements. We first propose a phenomenological model based on rate equations for the formation of hybrid nanocrystal-molecule (respectively: 20 nm – 1.2 nm) nanostructures in solution. We then concentrate on nanocrystals (~ 60 nm) assembled between nano-gaps (~ 40 nm) as a contacting strategy for the measurement of electronic transport properties of thiophene-terminated conjugated molecules (1.5 nm long) in a two-terminal configuration, under vacuum conditions. Similar devices were also probed with a three-terminal configuration using thiophene-terminated oxidation-reduction active molecules (1.8 nm long) in liquid medium for the demonstration of the electrolytic gating technique. The experimental and modelling work presented in this thesis project brings into light physical and chemical processes taking place at the extremely narrow (~1 nm separation) and curved interface between two nanocrystals or one nanocrystal and a grain of a metallic electrode. The formation of molecular bridges at this kind of interface necessitates molecules to diffuse from a large liquid reservoir into the region in the first place. Molecular bonding must occur to the surface for both molecular ends: this is a low yield statistical process in itself as it depends on orientation of surfaces, on steric hindrance at the surface and on binding energies. On the other hand, the experimental work also touched the importance of the competition between potentially immiscible liquids in systems such that (organo-)metallic molecules solvated by organic solvent in water and organic solvent in contact with hydrated citrate stabilised nanocrystals dispersed in solutions or assembled between electrodes from both experimental and simulations point of view.

Acknowledgments

I would like to thank Dr. Aidan Quinn for giving me the opportunity to read my Ph.D. in the Nanotechnology Group at the Tyndall National Institute. His direction, advice, insights have been inspiring all through my work. The confidence he put in me and the liberty given for trying research work have been invaluable.

The members of my Ph.D. committee, Prof. Stephen Fahy, Prof. Jean-Pierre Colinge and Dr. Alan O'Riordan have also contributed to the direction of this work by giving insightful advice during the progress reviews of my Ph.D. programme. I also wish to thank Dr. Simon Elliott, Dr. Hugh Doyle and Dr. Daniela Iacopino for their suggestions at different stages of my work.

The experimental work would not have been possible without the help of the CFF personnel, and I would like to thank Richard Murphy for his help making sure new design layouts were consistent, Brendan McCarthy, Dan O'Connell for all the cutting-edge lithography work and material deposition, Vladimir Djara for the reliable etching process developed and Mary White and Alan Blake as good coordinators. Along the same lines, John Rea in his time and Donal O'Sullivan machined beautiful essential custom pieces in the mechanical workshop for my work. I also would like to underline the essential help Krimo Khalfi has been providing for maintenance and repair of instruments in the laboratory (SEM, vacuum systems).

Having an educational background in Physics and Engineering but initially little knowledge of Chemistry, I have to thank all the people who helped me on the long way of understanding Chemistry. In that sense, I would like to thank Dr. Grégoire Herzog in the first place and Emma Harvey, Ph.D. student in Chemistry from Mary Pryce's laboratory in Dublin College University, Dublin for the synthesis and the information provided on organic linker molecules I used for my experiments.

I wish to thank both Dr. Claire Barrett and particularly John MacHale for their help in the lab especially when I started my Ph.D. programme. I am grateful to them for exchanging their experimental expertise in using instruments such as the Scanning Electron Microscope and the Atomic Force Microscope or the Cryogenic Probe Stations. I also have to thank Dr. Brenda Long and Dr. Mary Manning for their help in the chemistry lab and for characterisation of sample surfaces.

This work also depends on inputs from simulations performed by Dr. Gaëtan Lévêque and more recently Victor Akujobi, Dr. Micheal Nolan and Dr. Damien Thompson. I wish to underline the very interesting discussions we had with Damien on solvation shells and immiscibility interfaces.

Research is probably all about getting, sharing and transforming knowledge and in that sense I would like to mention the insightful and open-minded discussions related to my work or not I had the privilege to have with my fellow Ph.D. students: Dr. Pierre Lovera, Karen Dawson, Micheal Burke and Andrea Pescaglini.

A peaceful and casual atmosphere is certainly invaluable for completing a Ph.D. work and I would like to underline the support and friendship of many. I would like to pay tribute to former or current Tyndall colleagues, notably Padraig Curran, Brian McCarthy, Yoan Civet and Waleed Moujahid who showed incredible skills playing tag-rugby with me, to Shane McDermott, Dr. Santosh Kulkarni, Nick Holubowitch, Ethel Noonan and Micki Mitchell for their own individual sense of humour, to Pio Jesudoss for his cheerful character, to Dr. Jean-Michel Lamy, Dr. Vanessa Smet and Jennifer Mischieri for relaxing tea-breaks, notably. It was also great to have the company of Tim Januschowski for Deutsch-am-Donnerstag or Français-le-jeudi weekly lunches, to share friendship with some UCC students in the name of Lara Alegre and Cynthia Rodriguez. Thanks again to Tim Januschowski, Pierre Lovera, Karen Dawson and Micheal Burke who also were of great support during difficult times. I would also like to mention my past or current house-mates Martina Molinari, Dr. Lavinia Bhatt, Elena Rossi and Chloé de Buyl Pisco whom I had great discussions with.

Last but not least, thanks to my parents, my sister and my family in general for their encouragement during these past four years away from home.

Nicolas Sassiat

To my Family

Maryann's Law: “You can always find what you're not looking for.”

Chapter 1 – Introduction

1.1 Setting the scene of nanotechnology

1.1.1 Vocabulary

1.1.1.1 Nano-objects

The study of quantum mechanics and phenomena arising at the nanometre scale is a good example of flexible vocabulary. From a strict metering point of view, the nanometre world starts below $0.1\ \mu m$ which is less than a thousandth of the diameter of a human hair. The shape of structures can be compact with similar length in the three directions: a sphere being the limit case. On the other hand, a structure can have a large aspect ratio in which case one dimension is tens to thousands times bigger than one or the two others: the limit case is a wire, and to a lesser degree a rod. A structure can be termed "nano" if at least one of its dimensions is less than $0.1\ \mu m$ (in practice, it can be as high as $0.5\ \mu m$).

For different reasons including scientific and/or media hype, the prefix "nano" is stuck in front of words to insist on the very small nature of objects. In the present work, we will deal with crystals of a nominal diameter ranging from 20 nm to 80 nm: so-called nanocrystals. Organic or organo-metallic linker molecules, which can bind to nanocrystals or electrodes, used in experiments are even smaller: shorter than 2 nm.

1.1.1.2 Continuum to discrete description

Classical Physics and Chemistry usually studies large ensemble of particles acting collectively: planets and stars orbiting, fluxes of particles, energy exchange, etc. Whereas the number of particles may be hidden in certain systems, the concept of mole and conversely the Avogadro number directly touches the notions of the gigantic number of particles involved in macroscopic systems: $N_A = 6.02214078(18) \times 10^{23}\ \mathrm{mol}^{-1}$ (as many entities as in 12 g of isotope carbon $^{12}\mathrm{C}$). The difficulty arises when the interest is based on what happens to entities individually, for a sub-group of them. In order to understand the multi-scale character of the system, we calculate number densities from simple considerations on volume and concentrations of solutions of three pure solvents: water, acetone and dichloromethane along with a candidate solute dissolved into any of them, see Table 1.1.

Material	Molecular weight	Density (kg/L)	Concentration	Inter molecule distance	Number of entities in 10 mL	Number of entities in 100 µL
Water	18.02	1.000	55.5 M	0.3 nm	3.34×10^{23}	3.34×10^{21}
Acetone	58.08	0.791	13.6 M	0.5 nm	8.20×10^{22}	8.20×10^{20}
Dichloromethane	84.93	1.325	15.6 M	0.5 nm	9.39×10^{22}	9.39×10^{20}
Solute			10 mM	5.5 nm	6.02×10^{19}	6.02×10^{17}
			1 µM	118.4 nm	6.02×10^{15}	6.02×10^{13}
			1 nM	1.1 µm	6.02×10^{12}	6.02×10^{10}
			1 pM	11.8 µm	6.02×10^{9}	6.02×10^{7}

Table 1.1. Multi-scale aspect of volume and concentration in Physics and Chemistry.

Whereas molecules of a pure solvent are very close from each other, the distance between solute molecules at concentrations such as 10 mM is significantly larger: more than ten times further (even though the number of entities looks gigantic). As studied for the value of the detection threshold of sensors at the nanoscale,[1] the limiting factor in reactions may well be the diffusion-limited transport time of the analyte to the target area of the sensor (assays).

Very dilute systems and systems studied in nanotechnology in general face a common pitfall. The concept of concentration used in conventional macroscopic studies may break down as the length-scales between entities is no longer negligible compared to the critical dimension of the system. A continuum description will sooner or later show its shortcomings and instead one must use the concept of distributions to account for the discrete nature of the dispersion of solute(s) of interest.

Along the same lines, the continuum description of collective effects created by particles such as permittivity (related to the molecules electrical dipole moment and their polarisability) can become inappropriate. At the particle level, the idea of screening of electrostatic forces does not hold as the discreteness of particles must be taken into account. Similarly, other effects appearing at surfaces immersed liquids such as double-layer or solvation, etc. will be discussed later on in the text.

1.1.2 Dielectrophoresis for directed assembly of nanocrystal(s)

There exist many techniques for the directed assembly of nanoparticles in big numbers,[2] but fewer techniques have been developed to position ideally one particle precisely. An Atomic Force Microscope can be used to displace material on a surface with nanometre precision using the tip of the microscope. Contact-less directed assembly of material is also possible at the nanometre-

scale, in three dimension, thanks to techniques such as optical tweezers[3] or employing the dielectrophoretic force. Dielectrophoresis (DEP) is defined as the translational motion of neutral matter caused by polarisation effects in a non-uniform electric field.[4]

Although uniform electric fields will exert force upon a charged particle and a neutral particle will be polarised but will not move relative to the electrodes, non-uniform electric fields also exert force on neutral particles. Because of the non-uniformity, a neutral particle will be polarised (with both charges being equal), so that the field acting on these separated charges is not equal and results in a net translational motion. The dielectrophoretic force is primarily dependent on the gradient of square of the electric field, see Equation 1.1.

$$\overrightarrow{F_{DEP}} = 2\pi r^3 \varepsilon_m Re[K(\omega)]\vec{\nabla}E^2$$

Equation 1.1 The dielectrophoretic force experienced by a particle or radius, r, in a surrounding medium of permittivity, ε_m, in an electric field, E.

Particles can either move to or away from the region of highest field depending on the value of the real part of the Clausius-Mossotti factor, $Re[K(\omega)]$ where ω is the angular frequency of the AC electrical field ($\omega = 2\pi f$), see Equation 1.2.

$$K(\omega) = \frac{\varepsilon_p^* - \varepsilon_m^*}{\varepsilon_p^* + 2\varepsilon_m^*}$$

Equation 1.2. Clausius-Mosotti factor: ε_p^* and ε_m^* are permittivities of the particle and the surrounding medium respectively, these are imaginary numbers as denoted by *.

The complex permittivity is given by $\varepsilon^* = \varepsilon - i\,\gamma/\omega$, where γ is the conductance. A particle is repelled from the region of highest field if the real part of the Clausius-Mosotti factor is negative, this is termed “negative dielectrophoresis”. In practice, we will aim at having a “positive dielectrophoresis” to direct nanocrystals in nano-gaps, i.e.: the region of highest field.

In the case of gold nanocrystals suspended in water the real part of the Clausius-Mossotti factor is always positive for frequencies below 10^{18} Hz.[5]

Nevertheless, suspended nanocrystals are also subject to a number of other forces. Apart from gravity that is negligible, fixed surface charges (in the silicon oxide beneath the electrode on a silicon chip)[6] and thermal Brownian motion are competing with the dielectrophoretic force. This is presented schematically in Figure 1.1 from ref. [7]: the AC voltage applied between the electrodes to generate the electric field must be sufficiently high to overcome the electrostatic potential at the electrode-solution interface and assemble between the electrodes.

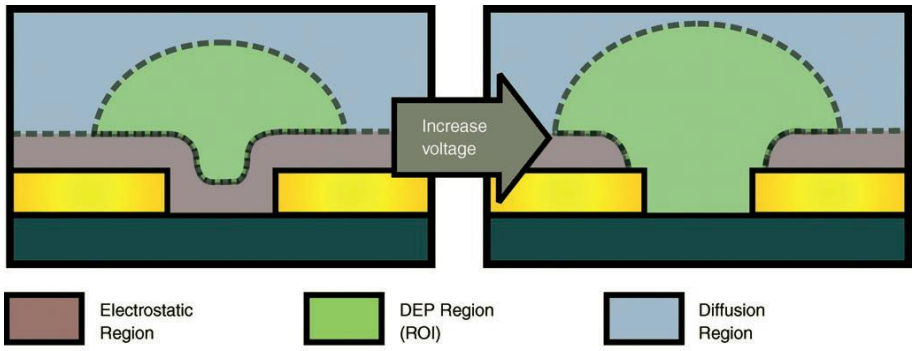

Figure 1.1 (reproduced from ref. [7])"Schematic image showing regions where different forces dominate during DEP assembly of nanoparticles into nanogaps at voltages, lower (left) and higher (right) than the threshold voltage."

1.2 Molecular electronics

The first seeds for the idea of molecular electronics can be found in early studies of charge transport between donor/acceptor molecules carried in the 1950s by R. S. Mulliken then later by A. Szent-Györgyi.[8] More than one generation latter theoretical approaches were initiated by Mark Ratner and Ari Aviram to study molecular rectifiers[9] then molecular logic.[10] After the concept of molecular electronics was established, first implementations for single molecule conductance measurements were conducted by Mark Reed in the late 1990s.[11]

Interest in molecular electronics is widespread. Unlike solid-state electronics, the active material is not made of a doped crystal or doped alloy material but a molecule. This means it is virtually possible to chemically engineer a molecule for a specific intrinsic functionality on a given device. Besides, simple candidate molecules are in the range of a few angstroms while more complex supramolecular assemblies can be as large as a few nanometres; this is indeed another key point in the device geometry shrinking race.

1.2.1 Transport of charge carriers

1.2.1.1 Electrical conductance, G

In the classical view of transport of charge carriers, electrons, negatively charged particles are moving through a conducting medium. The naïve picture is electrons travel straight trajectories over a typical mean distance, named the mean free path, between "collisions" with atom(s) of the conducting medium. The electrons can thus dissipate their energy in the form of phonons eventually dissipated as heat. This classical description is captured by Ohm's law linking voltage, V, across the device to the current, I, flowing through it: $V = R \cdot I$, where the resistance, R, is a measure of how electrically conductive the medium is. Conversely, one can define $G = 1/R$ as the conductance of the piece of material. Macroscopically, the conductance goes as $G \propto S/L$, where S in the cross-section of the supporting medium and L is its length.

Landauer and Buttiker studied charged particle transport by deriving a formalism[12] analogous to light interacting with matter. This description brings ideas of transmission, T, and conversely reflection, R, into place. It introduces the concept of conduction channels: the supporting material is now seen as a medium comprising a number of channels or modes, M, for the particles to be transmitted. On the other hand, the concept of scattering of charged particles with atoms of the medium or between electrons of the electronic gas implies charged particles can move in different directions and not strictly along the direction of the electric field originating from the potential bias. In the original version of the model, reflection is assumed to be an elastic

process: there is no energy exchange involved. Overall, along a given channel, there is a certain probability for charged particles to be transmitted $0 \leq T = 1 - R \leq 1$.

Source and drain contacts are described as reservoirs of electrons connected to the supporting medium.[12] These are brought out of equilibrium when a bias potential is applied. Based on quantum Physics, the derivation of non-equilibrium calculations of current flowing from the source, from the drain, and actually within the channel of the conductance leads to the expression of G as follow:

$$G = \frac{2e^2}{h} \times M \times T$$

Equation 1.3. Expression of the conductance as derived from the Landauer-Buttiker theory (at zero magnetic field).

with e, the charge of an electron and h is the Planck constant. It can readily be seen that for a single channel ($M = 1$) in the best case scenario where $T = 1$, the conductance reaches a maximum finite limit value of $G_0 = 2e^2/h \sim 77.5\ \mu\text{S}$ (or $R \sim 12.9\ \text{k}\Omega$), termed the quantum of conductance.

However, one should note that charge carriers can lose energy during scattering.[13] Inelastic scattering of charged particles will introduce phase-breaking in the wavepacket of carriers. Overall, the three processes of particle transmission, T, reflection, R, and absorption, A, can take place and thus the conservation principle becomes: $T + R + A = 1$.

Interestingly, the quantum description of conductance does relate to the macroscopically Ohm-law description since the it can be proven[12] that the number of modes M and the cross-section S are proportional and so are the transmission T and the inverse of the wire length $1/L$.

1.2.1.2 Quantum transport regimes

There exist a variety of transport mechanisms governing the flow of electrical current. They are nearly all driven by the out of equilibrium chemical potentials between the source and drain reservoirs. Classically, the Ohmic behaviour is the main situation to exist for charge carriers to move. In the case of a heterogeneous device such as a diode, for instance at the contact of two complementary doping areas within a semiconductor (p-n junction) or a metal-semiconductor interface (Schottky diode), carriers have to face a space charge region that may impede their flow. Since the physical extent of the space charge region is modulated by the voltage bias, the current-voltage characteristic is not linear and consequently the conductance of the device depends on the voltage.

However, quantum theory highlights a broader variety of mechanisms in the very low conductance range as well as at the perfect conductance limit, see Table 1.2.

	Trans-mission	**Mechanism**	**Length scale**	**Regime**	**Absorption, A**	**Temperature dependence**
Quantum	$T \ll 1$	Tunnelling	<~2 nm	Direct (low bias) Fowler-Nordheim ($V>V_T$)	$A = 0$ (contact resistance)	None
				Inelastic	A>0 (loss within channel)	None
		Hopping	<~10 nm	Direct	$A = 0$	Thermally activated
	$T = 1$	Ballistic	Nano to Micro-scale	Direct	$A = 0$	None
			Nano to Macro-scale	Superconductance	$A = 0$ (also back at equilibrium)	Only for $T<T_C$
Classical (diffusive)	$T < 1$	Ohmic	Micro to Macro-scale	Ohm-law	$A > 0$	Joule heating

Table 1.2. A summary of transport characteristics and properties.

From the Landauer formalism, one can think of a conductor so short that scattering processes do not take place anymore as the mean free path, λ_m, exceeds the conductor length. In the case a carrier is shot through the medium, it will not suffer any hindrance and as such, the transmission is deterministically $T = 1$. Practically, the regime of direct ballistic conduction only takes place on short wires with locally ideally pure material. Along the same lines, superconductance also falls in the ballistic regime as carriers can fly without friction in wires cooled below their critical temperature. At such low temperature, the (metallic) medium repels any magnetic field so that the Meissner effect appears allowing carriers to flow perfectly. This striking effect even remains after the system is brought back to equilibrium so that carriers can travel indefinitely in rings.

At the opposite of the conductance spectrum, for a very weak transmission $T \ll 1$, tunnelling and hopping currents take place.

The case of tunnelling current has been extensively studied in Physics as it can bring electrical current flowing where in the classical description it should not. While the effect is deleterious in devices like transistors as it introduces current leakage through the gate oxide (or even directly between source and drain), the effect is being investigated for memory devices (charging of a floating gate) or in the case of Single Electron Transistor (SET), to name a few applications. Tunnelling current occurs on very short distances ($\lesssim 2\ \mathrm{nm}$) when an energetic barrier exists between the two out-of-equilibrium reservoirs, see Figure 1.2.

At zero bias, the barrier shape is usually supposed rectangular. For the case of a small barrier (compared to the barrier height) the barrier profile becomes slightly slanted and direct tunnelling takes place. If the bias is increased such that the barrier becomes triangular, the tunnelling current increases in magnitude as studied by Fowler and Nordheim. A transition voltage V_T can be defined as the limit between the two scenarios. The interpretation of the transition voltage is subject to research in the molecular electronics community.[14-16]

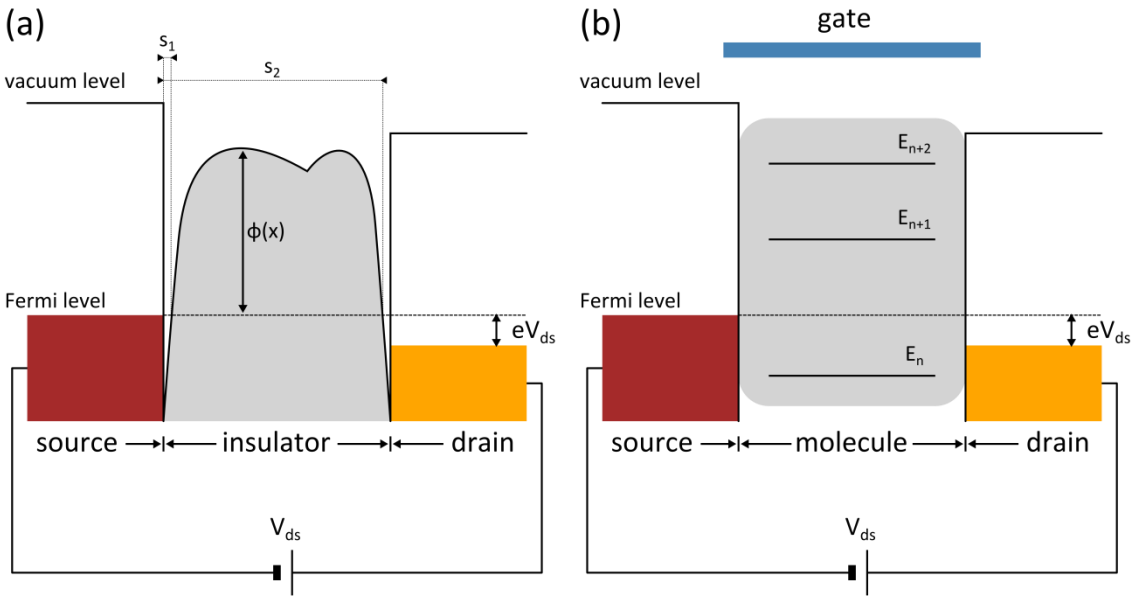

Figure 1.2. Schematics of simplified energy diagrams (for electrons). (a) The texture of the energetic barrier in a metal—insulator—metal junction is shown as the Simmons can account for (s1 and s2 are parameters of the model including the image charge potential). (b) Three energetic levels are represented: none of them are directly accessible within the source-drain bias applied but the gate (electrostatic coupling, photo-activation, electrolytic gating, etc.) provides a way to shift them so as to modulate the conduction.

In 1963, Simmons derived a comprehensive model of tunnelling current encompassing the different scenarios consistently:[17] it has now become the reference model for estimation of tunnelling currents in the approximation of a continuum medium between the electrodes, Equation 1.4.

$$J = J_0 \left(\varphi \cdot exp\left(-A\sqrt{\varphi}\right) - (\varphi + e \cdot V) \times exp\left(-A\sqrt{\varphi + e \cdot V}\right) \right)$$

Equation 1.4. Expression of the tunnelling flux according to the Simmons model. $J_0 = e/2\pi h(\beta \Delta s)^2$ is a characteristic constant of the flux of charge carriers tunnelling through the barrier; φ is an estimate of the possibly textured tunnelling barrier averaged on its thickness including the contribution of the charge image potential; $A = (4\pi\beta\Delta s/h) \cdot \sqrt{2m}$ is a characteristic constant of the barrier related to the tunnel probability; β is a correction factor, Δs is the effective

barrier thickness when charge image potential is taken into account, m is the mass of the free electron, e is the charge of an electron, h is Planck constant and V is the voltage applied across the junction.

Whereas temperature strictly has no influence on tunnelling, low magnitude currents can also be temperature dependent. The thermally activated regime is termed hopping and happens up to slightly longer length-scales ($\lesssim 10\ \mathrm{nm}$). Hot carriers can indeed travel longer distance in this mechanism that cannot be explained using classical Physics (unlike thermionic emission). The most practical method for distinguishing the two contributions is to study transport at different temperatures. In molecular systems, it is usually found that within a certain class of molecules, tunnelling governs transport through the shortest molecules but hopping dominates for longer molecules.[18-20]

Because transport of carriers is by essence an out-of-equilibrium process, relaxation of carriers can happen in the supporting channel. Although very unlikely (the probability of occurrence is usually estimated to be $\sim 10^{-4}$ in molecular systems), carriers tunnelling through a barrier can exchange energy with the medium on the form of absorption and more likely of the release of a phonon. This slight inelastic process is most often studied at low temperature ($4.2\ \mathrm{K}$) due to thermal smearing effect[21-24] and allows the identification of molecular moieties in the medium.

1.2.1.3 Gating of the device

The Integrated Circuit (IC) industry has been growing so dramatically because of the invention of the transistor. Nowadays, the most well known type of transistor is certainly the Field Effect Transistor (FET). The idea of the device functioning is based on a controlled flow of charge carriers (electrons for a n-FET, holes for a p-FET) within the channel between the source and drain terminals thanks to the electrostatic coupling of the channel to a third terminal: the gate.

Architectures for transistors are plenty and the gating effect on charge carriers can be driven by electrostatic coupling, chemical response, photo-response, etc. In all cases, the gate is used to pull or push energy levels of the active material (doped silicon in conventional FET, molecular orbitals in molecules) so that they fall between the chemical potentials of the source and drain reservoirs and therefore modulating the conductance of the device, see Figure 1.2b.

1.2.2 Stakes and challenges of molecular electronics

Quantum Physics has shown transport conditions at the nanometre-scale can be very different from bulk materials. Molecular systems employing few to hundreds of molecules can be first seen as a down-sized version of a thin-film of semiconductor, for which charge transport

theory is well understood. However, one has to be careful as to bear in mind weak processes at macroscopic scale may become dominant at the nanometre-scale.

1.2.2.1 Downsizing to commensurable number of particles

First of all, just as for anything occurring at the nanometre scale, down-sizing gives surfaces a larger role than the volume (scattering of carriers in our case, better response in potential sensors, etc.).

Moreover, a bulk material is, in essence, a many-particle system. Even a nanometre-scale transistor (e.g. at the postulated 22 nm node) involves millions of atoms in the active area. In molecular electronics, the number of atoms is dramatically reduced to thousands or even tens of them. Such a reduction in the number of particles implies a defect can have a potentially large effect that will not be down played as it would be the case in a bulk device. Along the same lines, electron-electron interactions in the gas of electrons or a discrete electron temporarily occupying an energy level in the medium (Coulomb Blockade) can turn out to be a key aspect of the transport process.

1.2.2.2 Molecular Coupling

The field of research in molecular electronics studies molecules connected between two leads. Molecules investigated in the field generally are very short structures of length of only 1 or a few nanometres. To probe the molecules electrically, they must be connected to the outside world. To this regard, at both ends, metallic leads need to join the nanometre scale world of the molecule to the macroscopic world of the scientist. Anchoring of molecules is a particularly challenging technological question as detailed later in the text. But more than this, anchoring a molecule on a surface (or on two or more surfaces) can have an effect on the molecule itself such that one will not study merely the molecule of interest but the system of the molecule bound to the leads.[25] Molecules can be studied in gas phase to identify their composition, the energy landscape along their structure, etc. However, once they anchor on a surface, the molecular bridge will usually have its energy bands shifted and broadened depending on the coupling with the electrodes.[26] The extent of this broadening will thus alter the properties of the “molecule” studied.

A low coupling of the molecule to the electrode is usually achieved by placing alkane chains between the anchor groups and its core so that the wave functions vanish locally along this chain preventing a strong overlap and thus strong changes in the properties of the molecule. On the other hand, conjugated chains or benzene rings are considered as favouring coupling of the molecule to the electrodes.

1.2.2.3 Electrode material, bonding sites and anchor groups

The development of efficient strategies to contact molecules is still the subject of intense experimental and theoretical research. One must admit there are still a lot of unverified assumption associated to this topic and the choice of a given couple of electrode material and molecule anchor group may still mainly be based on practical reasons.

To date, material employed to contact molecules are in vast majority noble metals (minimising the oxidation processes on their surface) such as gold (Au), platinum (Pt), palladium (Pd), silver (Ag), in certain cases even mercury (Hg). In a minority of device designs, semiconductor materials may also be employed as electrodes: for instance, silicon (Si) or gallium-arsenide (GaAs). Most molecular electronics studies rely on Au surfaces for the anchoring of molecules.

Without being exhaustive, anchor groups of organic or organometallic molecules can be based on sulphur, phosphor or nitrogen atoms, see Figure 1.3. There exist a large variety of groups: thiols $-\mathrm{SH}$, isothiocyanate $-\mathrm{NCS}$, methyl sulphide $-\mathrm{SMe}$ or thiophene $-\mathrm{C_4H_3S}$; dimethyl phosphine $-\mathrm{PMe_2}$; amine $-\mathrm{NH_2}$, pyridine $-\mathrm{C_5H_4N}$, etc. New strategies [27] explore the possibility to anchor several groups at the same time or several atoms of the same group [28] as in the case of perforated fullerenes.

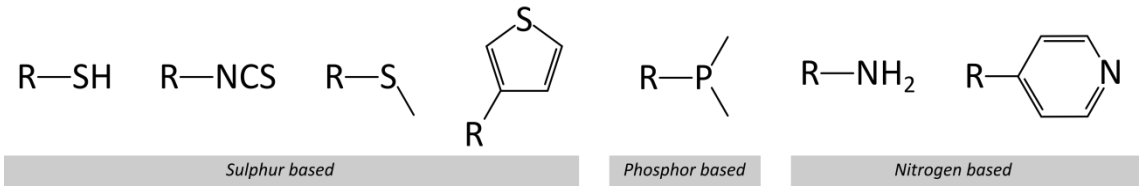

Figure 1.3. Variety of chemical anchor groups used in the field of research on molecular electronics (R, stands for the main structure of the molecule), respectively: thiol, isothiocyanate, methyl sulphide, thiophene, dimethyl phosphine, amine and pyridine.

The exact location of the atomic bonding of a molecule on the electrode surface is still an open question. There are typically three possible case scenarios: hollow-sites (in between three atoms), bridge (between two atoms), on-top (above only one atom), see Figure 1.4.

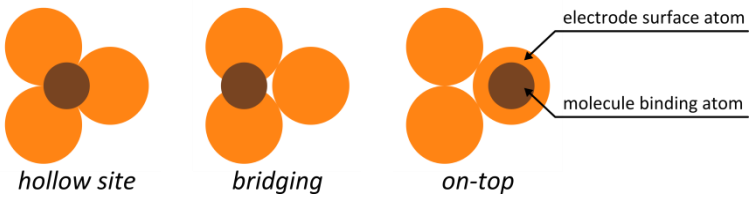

Figure 1.4. Three configurations for anchoring molecules on metal surfaces can exist: hollow-site, bridging, and on-top.

Different studies have shown the remarkable affinity of thiols for Au surfaces, because of the strong s-orbital. It is even shown in experimental works employing the Scanning Tunnelling Microscope Break Junction (STM-BJ) technique that the $\mathrm{S}-\mathrm{Au}$ bond is stronger than a lone $\mathrm{Au}-\mathrm{Au}$ bond itself.[29] The mechanical strength of the $\mathrm{S}-\mathrm{Au}$ bond is also superior to any other anchor groups tested.[30]

However, the electrical conductance is a different property of the molecule-metal bond. It is found that Pt electrodes could well be the material of choice for establishing high single molecular conductance. Interestingly, the metal work function (between Au, Pt and Pd) has little influence: it is the binding (and the resulting coupling) of the molecule that is ascribed to play the biggest role.[31] A recent STM-BJ study also underlines the possibility of direct modulation of coupling to the molecule on the conjugated backbone.[32]

1.2.2.4 Density of states (DOS) and numerical simulations

Many theoretical frameworks have been introduced to model molecular systems anchored to the leads. Early semi-empirical models or simplistic models have been replaced by Density Functional Theory (DFT). DFT is widely used for the calculation of density of states of free-standing or anchored molecules. By solving the Schrödinger equation, this framework gives insights in the filling of molecular orbitals: the Local Density of States (LDOS), and conversely the Projected Density of States (PDOS also called DOS for the sake of simplicity) for different energies about the Fermi level of the electrodes.[33] This visually shows what volume charge carriers are most likely to occupy and thus gives an idea of the way a contacted molecule should conduct by estimating where the Highest Occupied Molecular Orbital (HOMO) and Lowest Unoccupied Molecular Orbital (LUMO) are. The HOMO and LUMO can be approximated to the Valence Band (VB) and Conduction Band (CB) of a bulk semiconductor, respectively.

The landscape drawn from the DFT calculations shows the LDOS is not a pure uniform function of space between the two electrodes. The tunnelling barrier has some texture as opposed to the simplistic approach of a rectangular barrier. According to S. G. Louie *et al.*, in first approximation, if the electron wavelength is far bigger than the thickness of the barrier, one could still consider the barrier as a rectangle. The electron wavelength is $\lambda = h/p$ with h, the Planck constant and p, the particle momentum: $p = mv$, with m its mass and v its speed. Assuming the energy associated to the particle purely originates from kinetic energy ($E = mv^2/2$), one can derive a new expression for the electron wavelength: $\lambda = h/\sqrt{2mE}$. It thus comes that $\lambda_{100\,\mathrm{meV}} = 3.88\,\mathrm{nm}$ and $\lambda_{500\,\mathrm{meV}} = 1.73\,\mathrm{nm}$ which is not significantly larger than the length of molecules we use in this work. From an experimental point of view, this brief calculation of electron

wavelength suggests that the rectangular barrier approximation does not hold for typical experimental bias voltage ~ 0.5 V applied on devices in this work.

To effectively compute the current-voltage response of a molecular system, one needs to rely on Green's functions to integrate the contribution of the different LDOS to the tunnelling or hopping conduction regimes. However currently experimental measurements of molecular junctions probed with the current-voltage technique are not matched by theoretical results of charge transport through such systems. Numerical simulations can only be used for qualitative purposes as the positioning of features in $I(V)$ curves may be slightly different, plus factors of up to two orders of magnitude arise in certain configurations.[34] Improvement in the theoretical description of the molecular junction is thus subject of intense research.[35-36] Nevertheless, for spectroscopy methods such as the Inelastic Electron Tunnelling Spectoscopy (IETS), the agreement is far better. It is often reported that a matching factor of ~0.95 is used to fit the experimental spectra to the predicted response.[21]

1.2.2.5 Measurement techniques

The conventional technique to measure the electrical properties of metal—molecule—metal junctions is a simple current-voltage characteristics, I(V). In certain contacting strategies such as Scanning Tunnelling Mechanical Break Junction or Mechanically Controlled Break Junction, it is preferred to work with current-pulling characteristics, I(s), to circumvent possible instabilities in the system.[37]

Another DC technique consists in measuring devices at the same bias potential for a certain period of time so as to reveal possible fluctuations and patterns in the conductance.[38-39] It is likely that further stress techniques may soon be implemented to evaluate the reliability of metal—molecule—metal junctions.

Finally, the IETS method, which is an AC technique borrowed from surface science, makes possible to investigate structural properties of the bonds within the molecule.[40]

1.2.3 Contacting techniques for molecular electronics applications

Since the first theoretical proposal of molecular electronic devices,[9] it has become more and more clear the first pitfall to overcome is the formation of electrical contacts to molecules. Molecular electronics may represent the near ultimate miniaturisation of devices to the scale of ~1 nm, and provided it exists in the classical form developed by the integrated circuit industry, to date no current technological method is able to offer all the requirements of a compact and reliable contact strategy. In all scenarios, the issues of contact variability and reliability are entangled.[41]

Many contacting strategies have been developed experimentally so as to contact allegedly either single or few or hundred(s) of molecules at a time. There are different ways for classifying the molecular contacting techniques. However such categorisation can sometimes sound artificial as two very different techniques on one aspect have very similar characteristics from other points of view.

Although all techniques developed are still research-focused, some contacting strategies are closer to integration than others. There are four main lab techniques such as Scanning Tunnelling Microscope Break Junction (STM-BJ), Mechanically Controlled Break Junction (MCBJ), Conductive-Probe Atomic Force Microscopy (CP-AFM) and Liquid metal (alloy) drops. On the other hand, four to five on-chip (potentially scalable) techniques exist, namely: electromigration, nano-pores, cross-bars and nanocrystal arrays, see Table 1.3.

Technique	Device integration potential	Operation temperature	Surrounding medium	Junction Area	Research Group
STM-BJ	N/A	4 – 400 K	Vacuum, solvent	<10 nm^2	N. Tao; L. Venkataraman ; C. Nuckolls; M. Mayor; T. Wandlowski
MCBJ	N/A	4 – 400 K	Vacuum, solvent	<10 nm^2	J. M. van Ruitenbeek; M. Calame & C. Schönenberger
CP-AFM	N/A	77 – 400 K	Vacuum, solvent	~100 nm^2	S. M. Lindsay; C. D. Frisbie
Liquid metal drop	N/A	~300 K	Air, solvent	~ 500 μm^2	M. A. Rampi; C. A. Nijhuis & G. Whitesides
Electro-migration	Good	4 – 400 K	Vacuum	<10 nm^2	P. L. McEuen; A. T. C. Johnson; H. van der Zant; M. A. Reed; M. Calame
Nano-pores, Cross-bars	Excellent	4 – 400 K	N/A.	~100 nm^2 (~ 10 μm^2)	J. R. Heath; John H. K. Yip; T. Lee
Nanocrystal arrays	Excellent	4 – 400 K	Vacuum	~ 100 μm^2	M. Calame & C. Schönenberger

Table 1.3. Summary table on techniques employed for contacting molecules. See text below for details.

The work presented in this thesis is a down-sized version of the nanocrystal array technique employing few-nanocrystal assemblies bridging electrodes spaced by a nanometre-scale gap. We now review the contacting strategies via the estimated number of molecules involved in each device method.

1.2.3.1 Contacting single to few molecules

There are three major laboratory techniques to contact few to single molecules.

1.2.3.1.1 Scanning Tunnelling Microscope Break Junction

Numerous research groups, including N. Tao *et al.*,[42] L. Venkataraman and C. Nuckolls *et al.*,[32, 37, 43] M. Mayor and T. Wandlowski *et al.*,[34] and others[44] have demonstrated the use of Scanning Tunnelling Microscope (STM) as a laboratory approach for contacting few- and, in some cases, single molecules. The laboratory device consists of a bottom ultra-flat substrate electrode (usually Au (111) on mica) prepared with a Self-Assembled Monolayer (SAM). The tip of the STM is then brought to the surface and is made collide with it. Then as the tip is pulled away from the substrate surface, the amplitude of the current flowing through from tip to substrate is monitored. As the metallic contact constriction becomes narrowed, the measured conductance

decreases following a three domain sequence. At first, the conductance decreases slowly and "continuously"; then quantised steps (integer values of the quantum conductance G_0) can be noticed: signature of the atomic nature of the metallic constriction; finally, when the conductance drops below sharply again below $1\ G_0$ (the metallic contact is broken), the current flowing from tip to substrate is from tunnelling nature. In this regime and in presence of a SAM on the substrate, contacting a few molecules or even a single becomes possible.

For molecular conductance studies, there are two possible case scenarios. Either current-distance $I(s)$ measurements (at constant bias) can be studied especially in the $I(s)/V \ll 1\ G_0$ domain, or the tip position is frozen (the STM feedback-loop is stopped) when reaching a stable plateau in the former characteristics $I(s)/V \ll 1\ G_0$ and one can then sweep the tip-substrate bias to acquire current-voltage $I(V)$ data. As control experiments, the technique can be applied under vacuum conditions or in the solvent medium.

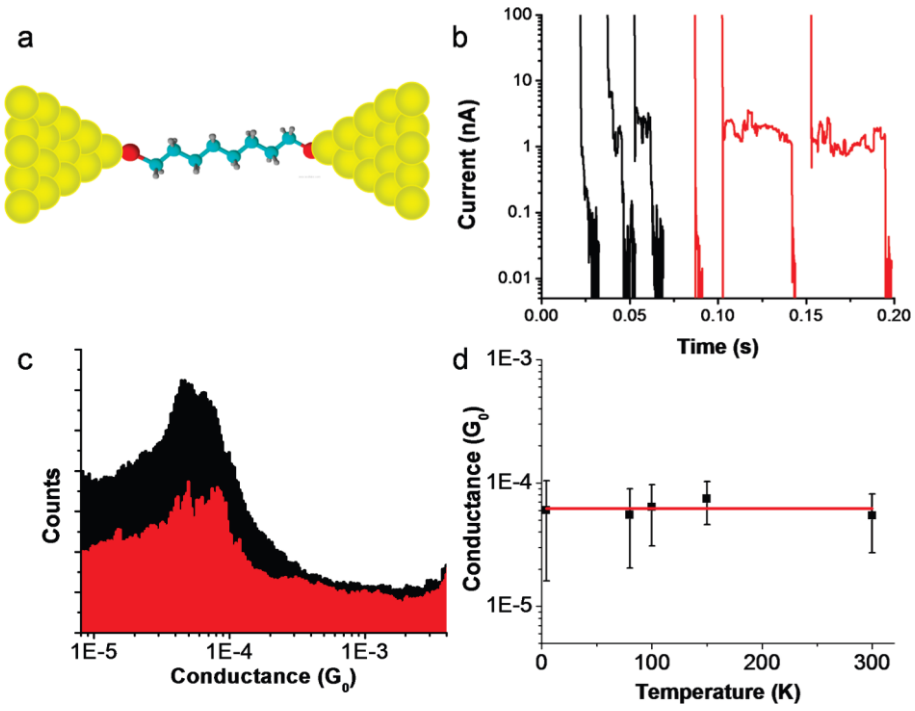

Figure 1.5. (reproduced from ref. [21] "(a) A molecular junction consisting of a single octanedithiol molecule bound to two electrodes. (b) STM breakjunction measurements taken at 300 K (black curves) and 4.2 K (red curves), both show clear steps, but at low temperature the features are much more distinct. (c) Two conductance histograms constructed from thousands of curves similar to those shown in panel b. The black histogram is for 300K and the red histogram is for 4.2K. (d) Peak values of conductance histograms taken at several temperatures between 4.2 and 300 K with a bias of 300 mV. The conductance is independent of temperature indicating tunneling behavior for the octanedithiol molecule."

These routines can be repeated hundreds to thousands of times during an experiment allowing the collection of large amounts of data at cryogenic temperatures just as well as at room temperature. This technique provides indeed large statistics on molecular conductance characteristics. One has to point out that each time the tip is crashed and pulled away from the substrate the atomically sized contact area is changed. When a new molecule is picked, the anchor geometry is likely different each time an attempt is done. Despite these uncertainties on the contact geometry, histograms can be constructed from the experimental curves. In some cases, only part of (60% [21]) of all of the data[32] is considered during the statistics analysis. Conductance histogram plots all show log-normal distribution results as a signature of the contribution of molecules in the system with Full Width at Half Maximum (FWHM) estimated (by this author) at ~ 0.4 decade.

1.2.3.1.2 Mechanically Controlled Break Junction

Changing paradigm, techniques involving horizontal probing of molecules have been developed.[11] The (lateral) Mechanically Controlled Break Junction (MCBJ) technique was pioneered by J. M. van Ruitenbeek *et al.*,[45] and then implemented by M. Calame and C. Schönenberger[46] and S. J. van der Molen[47] for molecular electronics research. In the setup, the substrate is mounted on a stage where it will act as a beam held on its extremities and gently pushed in the middle by a rod. In reaction of this controlled strain, inducing shear mechanical deformations, the substrate surface will bow. The stress caused is exploited by the fact it can open a notch and eventually a break on a metal wire patterned using conventional lithography on a flexible substrate. As with the STM technique, the MCBJ technique also involves a hybrid feedback loop between the mechanical interaction (pushing) and electrical conductance measurement through the wire. When the measured conductance drops sharply below $1\ G_0$ (a sub-nanometre sized cut is open), molecular contribution in the conductance can be measured. A few techniques exist for functionalising the electrodes with molecules: either a SAM was prepared on the wire prior to the MCBJ or molecules dissolved in a solvent in a liquid cell in contact with the broken wire acts as a reservoir for molecules to bind right in the nanometre-sized gap or molecules are deposited by chemical evaporation.

Just like the STM technique, traces of current during mechanical pulling can be studied or any mechanical interaction is stopped (for $I(s)/V \ll 1\ G_0$) and current-voltage $I(V)$ measurements between the two ends of the wire can start. This routine is also repeated hundreds to thousands of times during an experiment providing large data sets and robust statistical analysis. Control experiments in vacuum or passive solvent can also be conducted.

Similarly to the STM technique, the reversibility of the making of the metal—molecule—metal junction implies the contact geometry at the molecule ends is not well controlled and compounds are changing each time, but because hundreds to thousands of measurements are done, substantial statistics can be generated from all data acquired: no data selection is done. In agreement with the STM technique, conductance histogram plots all show log-normal distribution results when molecules are present in the junction. Estimates of the FWHM of the log-normal distributions are also found to be ~ 0.8 decade (value estimated by the author), see Figure 1.6.

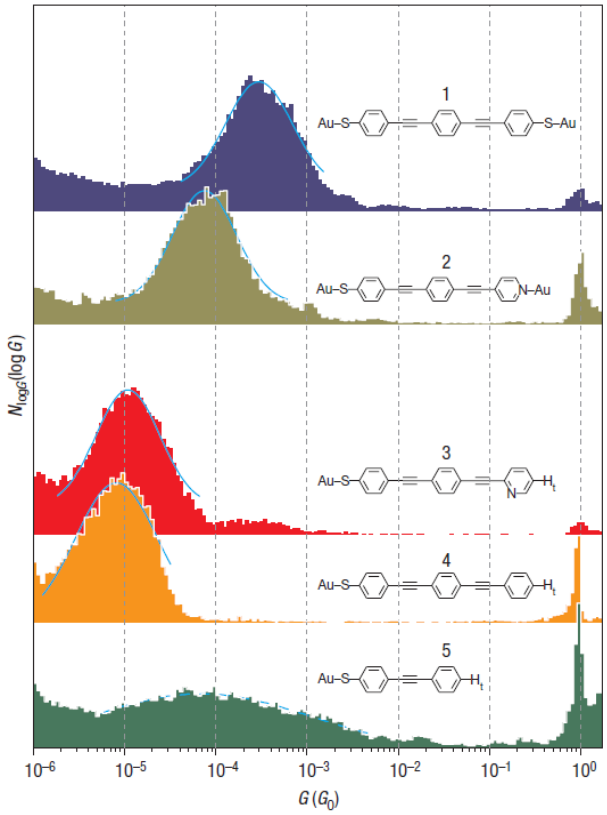

Figure 1.6. "Conductance histograms for the different molecules [studied in [46]]. Comparison of $\log(G)$ histograms for OPE molecules with two linking terminals (molecules 1 and 2), and with only one thiol linker (molecules 3 to 5). Each histogram was built from 100 conductance traces obtained during successive opening cycles […]. The pronounced Gaussian-like peaks (solid lines) in the $\log(G)$ histograms represent the signatures of the specific molecule investigated. The molecular junction conductance is deduced from the peak conductance G_{peak}.". (These measurements were performed in tetrahydrofuran/mesitylene, with 1:4 v/v ratio.)

1.2.3.1.3 Electromigration

Moving away from controlled mechanical stress, the Electromigration technique using pre-patterned wires was developed by groups such as P. L. McEuen *et al.*,[48] A. T. C. Johnson *et al.*,[49] H. van der Zant *et al.*,[50-51] M. A. Reed *et al.*[52] In this case, the wire is being worn down by carefully

passing an electrical current through it. Unlike the Integrated Circuit (IC) industry that strives for avoiding electromigration in interconnection wires, the physical phenomenon of electrons giving away part of their momentum to the metal atoms of the wire is used for creating nanometre-sized gaps in the wire. Although the formation of a gap is reversible in principle: the two electrodes can be fused again into a wire when applying a large bias, experimentally this electromigration process is usually performed only once to create a gap. As per described for the STM and MCBJ techniques, monitoring the conductance makes possible to detect when to stop the electromigration process. Typically, stable 3 nm gaps can be made on gold wires whereas sub 1 nm gap can be fabricated using platinum wires at temperature ~ 400-450 K.[50] Exposure of the electrode to molecules by wetting the substrate with a chemical solution or chemical deposition of molecules in vacuum conditions is achievable to functionalise the nanometre-sized gap.

Then current-voltage $I(V)$ measurements are conducted on molecules bound between the two created electrodes. With this technique, measurements can be performed at cryogenic temperature or room temperature. Limitations come from the fact metallic atoms can diffuse on the electrode surfaces. Depending on the temperature (material dependent) and the pace at which the electromigration process is done a reorganisation occur afterwards reshaping profoundly the gap changing its electronic transmission properties. This phenomenon is termed "self-breaking".[50]

Practically because of the lack of reversibility in the making of the gaps and eventually the metal—molecule—metal junctions, acquiring data is directly limited to the number of devices that can be processed on samples. Intrinsically the statistics accessible is restrained. Conversely, this technique is a potential prototype candidate for integration of molecular devices on chip. In terms of data selection, it appears that in some reports hundreds of devices (418) measured, but only a few tens of them (35) are usually discussed leaving most measured data unexplored.[52]

1.2.3.2 Large molecular arrays

Other techniques have also been investigated so as to contact few to hundreds of molecules at a time.

1.2.3.2.1 Conductive-Probe Atomic Force Microscope

Although the Conductive-Probe Atomic Force Microscopy (CP-AFM) technique developed by S. M. Lindsay *et al.*[53] and C. D. Frisbie *et al.*[18-19, 54] seems quite similar to the STM approach at first glance, it differs on different points. Like the STM technique, a SAM is prepared on an ultra-flat conductive substrate. Moreover the conductive tip of the Atomic Force Microscope (AFM) is also brought into contact with the SAM allowing molecules to bridge the two metal electrodes mentioned. However, unlike the STM technique, the normal operation does not require the tip to

come into contact with the substrate first but directly with the SAM instead. As a matter of fact, because of fabrication limitation the tip radius is on the order of a few tens of nanometres ($20\ \mathrm{nm} \lesssim R \lesssim 50\ \mathrm{nm}$). The contact area, and thus the number of molecules contacted, is therefore much larger than in the STM technique: typically, one estimates ~ 100 molecules are bridging the gap in parallel.

Once in contact with the SAM, the tip position is frozen: the scanning in any direction is stopped. Current-voltage $I(V)$ measurements are finally performed to characterise the assembly of contacted molecules. Intrinsically, this technique has no control on the number of contacted molecules: the packing of molecules in the SAM and the sharpness of the tip are the main factors. Because many molecules in the SAM are contacted in parallel, one cannot rule out the contribution of inter-molecule conduction mechanism.

Like the STM and the MCBJ techniques, this method presents the ability to perform manifold measurements on the same sample. There is no explicit mention in the literature that all data are presented or data selection is applied. However data shown are the result of averaging over 10 to 20 measurements. Although no histograms are presented, errors bars in the resistance of the device are on the order of ~ 0.3 decade (value estimated by the author), see Figure 1.7 and Figure 1.8.

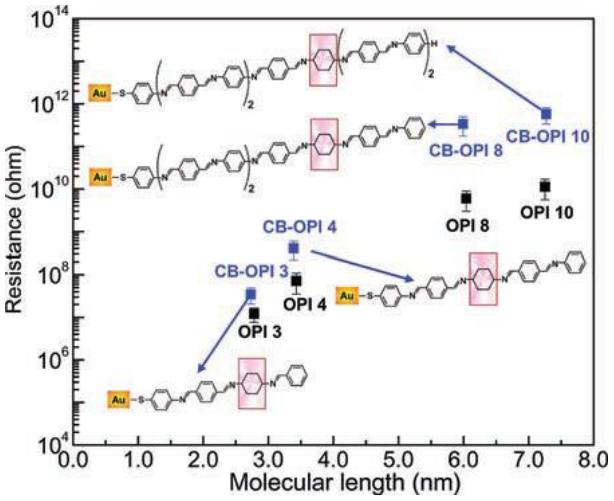

Figure 1.7. (reproduced from ref. [19]) "A semilog plot of R versus L for Au/ONI/Au junctions andconjugation broken Au/CB ONI/Au junctions. Each data point is the average differential resistance from 20 I-V traces in the interval -0.1 to +0.1 V. Error bars represent one standard deviation. The blue circles are the resistances of conjugation-broken ONI (CB ONI) wires. Pink boxes indicate the position where conjugation is broken."

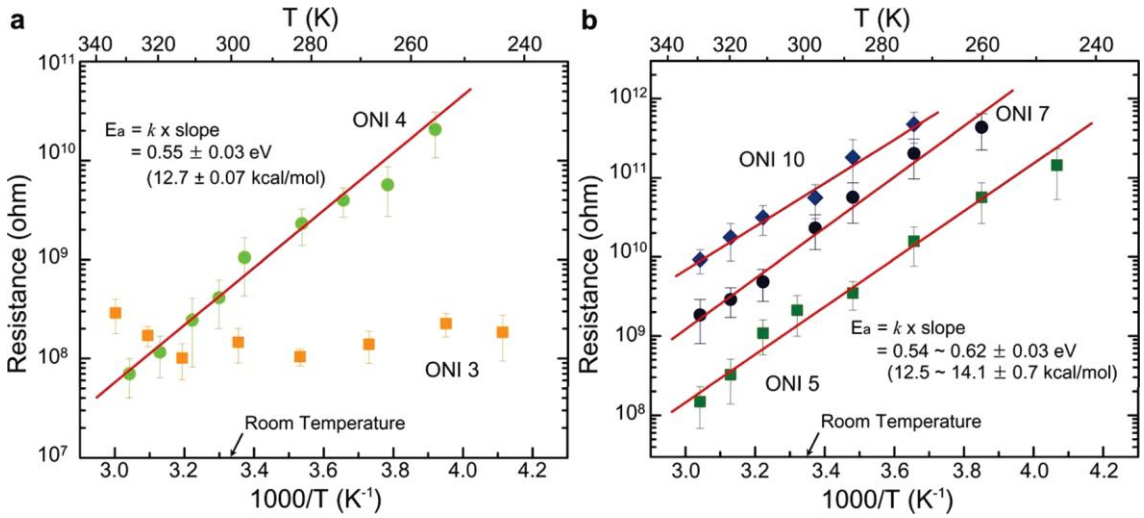

Figure 1.8. (reproduced from ref. [19]) "Arrhenius plot for (a) ONI 3 and ONI 4 and (b) ONI 5, ONI 7, and ONI 10. Each data point is the average differential resistance obtained at six different locations of samples in the range -0.1 to +0.1 V. Error bars represent one standard deviation. Straight lines are linear fits to the data."

1.2.3.2.2 Liquid metal (alloy)

Another option for probing SAM of molecules consists in using a top electrode made of liquid metal (or metal alloy). M. A. Rampi *et al.* have been working on mercury (Hg) drops[55] whereas C. A. Nijhuis with G. Whitesides and co-workers are focusing on gallium-indium in its eutectic form (EGaIn) for the top electrode.[56-60] There exist a few strategies for the bottom contact electrode: another drop can be employed but more generally, an ultra-flat bottom substrate surface is used for hosting the SAM.

Like the CP-AFM technique, there is no control over the exact number of molecules being contacted in parallel and any defects on the surface of the bottom electrode or the local curvature in the prepared liquid-drop tip (particularly true for the EGaIn method) influence the repeatability of conductance measurements.

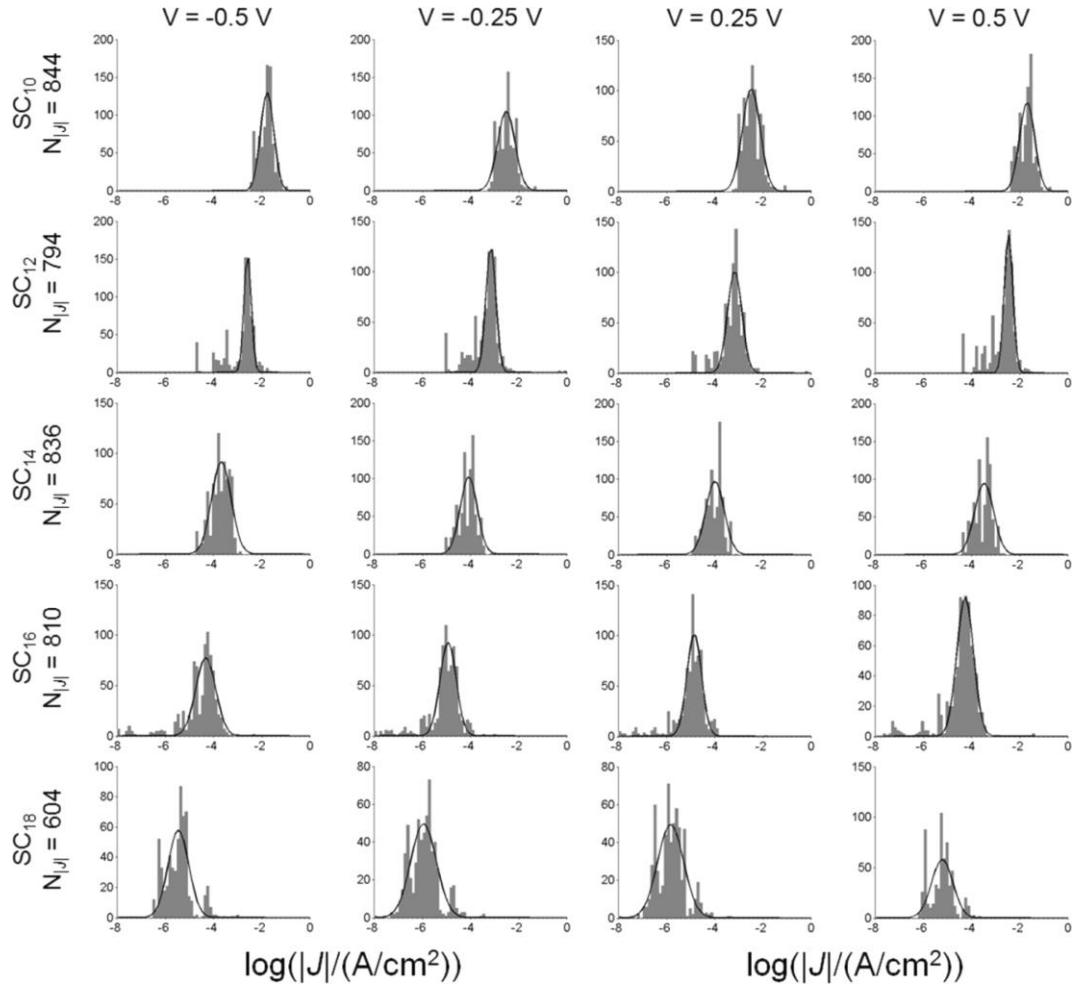

Figure 1.9. (reproduced from ref. [57]) "Summary of data derived from the even-numbered n-alkanethiols at different voltages (from a single user) to illustrate the consistency of the distribution of the data. We show two sets from positive bias and two from negative bias to illustrate that, irrespective of the bias or the voltage (|V| = 0.5 or 0.25 V), the histograms look very similar. Similar observations were made with the odd series."

Initially, results shown in the literature for this technique were selected upon certain rules, but with the advance of the EGaIn method and the possibility of growing number of measurements across different users and molecule candidates, the focus is now to present all data measured. Interestingly it has been demonstrated that for a same metal—molecule—liquid drop junction, variations are noticeable in the conductance measurement distributions showing the need for an even more standard approach in the demanding preparation of samples. Log-normal distributions of current density across data-sets comprising ~ 800 different measurements show variable FWHM values ranging from ~ 0.2 to ~ 1 decade.

1.2.3.2.3 Nanopores, Cross-bar, multilayer graphene

It may appear as the simplest technique in principle, one can devise a device comprising a SAM of molecules sandwiched between two horizontal electrodes as proposed by J. R. Heath *et al.*[61-62] and others.[63-65] The bottom electrode is covered by a thin layer of solid-state insulating layer with the exception of predefined areas where the molecules will be deposited and hopefully packing approximately perpendicular (a tilt angle is usually to be expected on (111) and conversely on polycrystalline surfaces of gold or silver) to the bottom electrode surface. To contact molecules on their other hand, a conductive electrode has to be deposited on top of the SAM. Inherently, the assembly of molecules has defects and direct deposition of metal on the SAM results in the formation of filaments shorting the bottom and top electrodes.

To avoid this major difficulty, some research groups like John H. K. Yip *et al.* employ an intermediate polymer layer PEDOT:PSS (a material widely used in organic solar-cells)[66-67] on ~ 10 to ~ 100 µm diameter circular areas,[68] but this method introduces another series of parameters and variability in the molecular characterisation scheme. A new proposal, demonstrated by the group of T. Lee *et al.* consists in using few graphene sheets at the interface molecule—top electrode in place of the polymer material.[69] Thanks to the electronic properties of graphene this method alleviates the extra conduction barrier otherwise added. Moreover, device fabricated are shown to be robust over time as they are protected from the outside by construction.

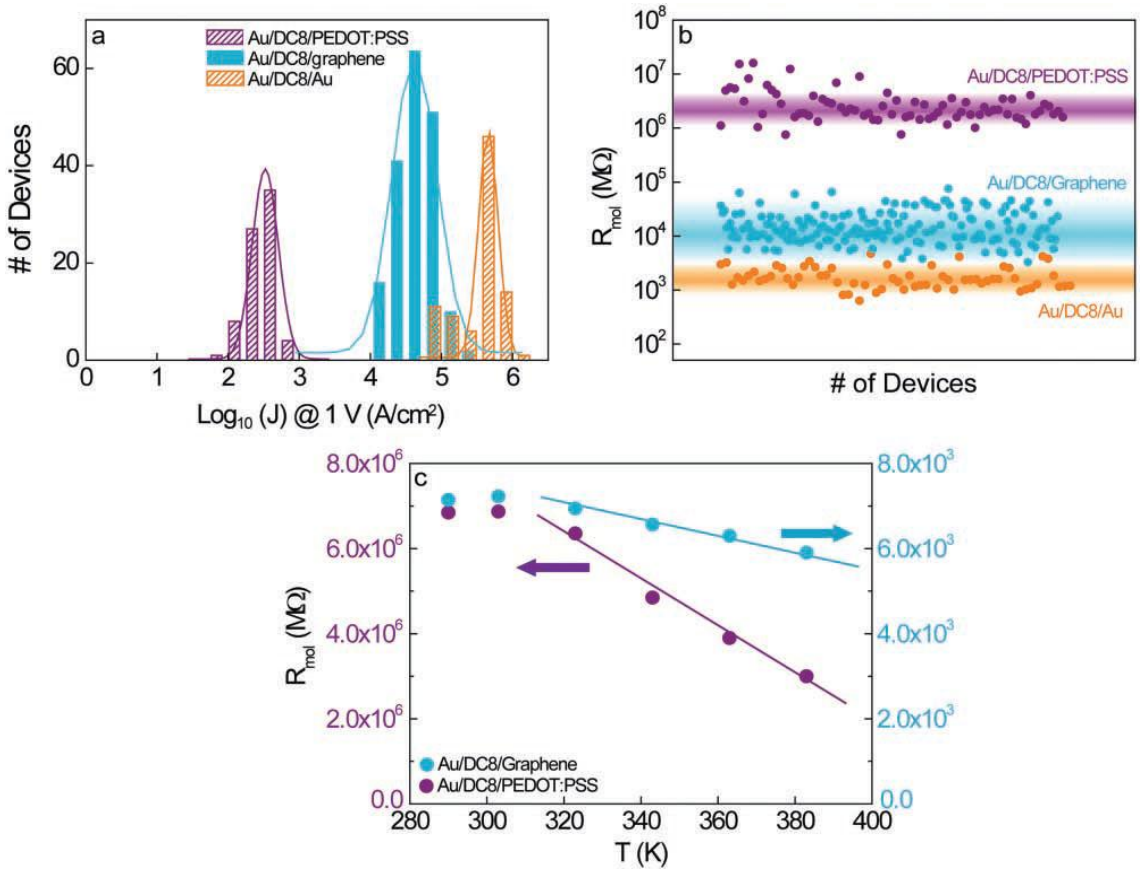

Figure 1.10. (reproduced from ref. [69]) "a) Histogram of logarithmic current densities at 1 V for working molecular devices according to the kind of top electrode (PEDOT:PSS, graphene, or Au). b) The resistance per molecule R_{mol} values for these molecular junctions. c) The R mol values for Au/DC8/PEDOT:PSS and Au/DC8/graphene devices as a function of increasing temperature." The junction area is $12.6\ \mu m^2$.

According to the literature, yields of a minimum $\sim 60\%$ and more generally $\sim 90\%$ can be achieved in the fabrication of such metal—molecule—metal devices. All "working devices" results are then reported showing log-normal distribution of resistance. Although testing the same molecules, results strongly depends on the contact strategy in terms of the system resistance. The FWHM can vary between ~ 0.2 decade to ~ 1 decade.

1.2.3.2.4 Micrometre-scale arrays of nanocrystals

So far the methods presented to characterise molecular junctions rely on single or parallel molecular bridges. The research group of M. Calame and C. Schoenenberger *et al.* proposes to change the paradigm again. The method based on large arrays of nanocrystals consists of two-dimensional array of nanocrystals forming millions of molecular junctions interconnected both in series and parallel.[70-73] The fabrication of the devices starts with the preparation of arrays of thiol-stabilised particles. The arrays are then stamped on an insulating substrate on which electrodes are deposited to form contacts. Whereas particle size is typically ~ 10 nm, the

contacted width on the electrodes is several micrometres large ($\sim 30\ \mu m$) and the gap between electrodes is several micrometres wide ($\sim 10\ \mu m$). Reversible molecular functionalisation of the arrays is achieved by immersion of the device in different chemical solution. Electrical characterisation of the devices is performed via usual current-voltage $I(V)$ measurements between contact pads.

Intrinsically, one does not control the number of bond molecules or the number of junctions involved in measurements but on the other hand, these devices are a good example of largely defect-tolerant architecture. Particularly in case of limited molecular decoration or highly electrically resistive molecular bonds, percolation routes are followed by charge carriers. Individual $I(V)$ characteristics are therefore the result of an averaging of molecular properties and molecular contacts with nanocrystals, providing repeatable measurement results.

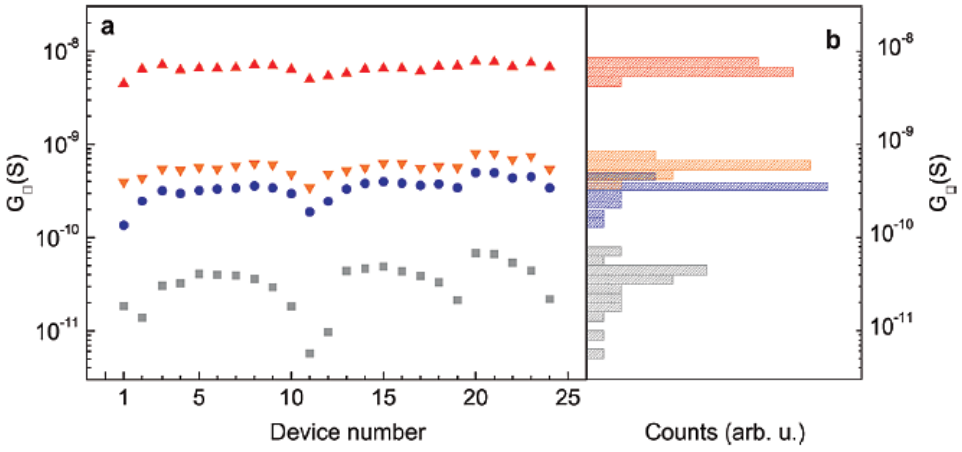

Figure 1.11. (reproduced from ref. [73]) "(a) Sheet conductance of 24 devices from one sample measured at various stages: as-prepared (square), after TTFdT exchange (disc), after oxidation with excess iron chloride (up-triangle), and after reduction with excess ferrocene (down-triangle). (b) Histogram of the sheet conductance values shown in (a)."

The literature does not mention explicitly if all data are presented or data selection is applied.[73] Presented data for different devices on the same sample shows rather narrow distributions. As opposed to previous results in different techniques, a Gaussian distribution tends to match the scattering of the data better than a log-normal distribution (but this may be due to the limited number of devices).

1.2.4 The case of measured data management

Reviewing the methods employed to electrically contact molecules, we have underlined the way experimental results are reported. During the infancy of the field of research on molecular electronics, the temptation of separating the wheat from the chaff was widespread. In other words, data selection of the experimental results has been extensively used to shed light on remarkable behaviour such as Coulomb Blockade, back-gating effect, etc.[52, 74] on one or a few devices amongst hundreds of them tested.

Scientific dishonesty apart, one can interpret this initial trend in only showing the "good results" as a proof of concept molecular electronics devices can exist (and not the contrary).[75] However, a few research groups that once did only show a specific subset of the results[21, 57] now show the entire data. Furthermore with improvements of the different contacting techniques, engineering questions like device reliability and fabrication process yield emerge.

Currently, the number of samples, devices and measurements are reported in most publications ("without any data selection to reveal statistically significant conductance values").[37] Possible discarding of data is clearly stated. Conversely, the method to report data has evolved.[76] Histograms of conductance (mono-dimensional[42] or on the form of mappings[37]) are commonly employed to transform large datasets. More classically overlaps of current (density) characteristics are also used[58] reflecting the log normal distribution of results. In all cases, the statistical nature of the process of formation of and response of electrode-molecule-electrode assembly is not hidden anymore.

1.3 Interfaces in liquids

Nanotechnology is promising to bring in front of the scene "bottom-up" methods for the making of devices. This represents a major change compared to Complementary Metal Oxide Silicon (CMOS) fabrication processes developed by the microelectronics industry. Instead of only dealing with solid-state sources and patterning structures using the so-called "top-down" approach, nanotechnology will open up the door to bottom-up fabrication routes originating from both existing Chemistry methods and inspired by Biology.

The bottom-up approach completely changes the way a desired function can be engineered into a device. Within this context, the fabrication now relies on two different pillars.[77] First, components to be synthesised originate from elementary blocks that will associate automatically when brought together. Within this framework, reactant blocks generate product components, in a similar fashion to Chemistry: this is called "self-assembly". Then, these elements need to be connected together to bring function to a higher level and create actual devices. This step is coined "self-ordering" and would also rely on Chemistry but more likely on recognition mechanisms or automata as found in Biology. Today, self-ordering is still an elusive technique that remains to be truly demonstrated.[25]

To date successful demonstrations of self-assemblies are molecular monolayers adsorbed on surfaces originating from either a gas phase as employed in the case of the Atomic Layer Deposition (ALD) technique or, for instance, from a liquid phase as developed by the Langmuir-Blodgett method. Direct adsorption of molecules from a solution to form a Self Assembled Monolayer (SAM) has also been demonstrated, the SAMs serve as functionalised surfaces in electrochemistry or for biological test assays.

There are a lot of fine physical phenomena occurring at the surface in liquid medium. As opposed to solid-state and vacuum conditions, matter relaxes and rearranges dynamically and constantly. This reorganisation can be forced from an electrical point of view as in electrochemistry on length scales that can typically extend to few micrometres. Rearrangements to shorter length scales down to few ångströms also take place constantly under the pressure of thermal fluctuations: solvent molecules, salt species and any other components perpetually move and relax. The Physics behind these dynamical processes is manifold in terms of length scales, forces and relaxation times. We will detail key influences on interface properties.

1.3.1 Forces at stake between atoms and molecules

Describing the interactions between atoms and molecules as a whole is a very complicated task (from ref. [78], chapters 2-7) . Along the centuries, the approach has evolved from a

mechanistic view (inspired by gravitational effects) to considerations based on thermodynamics and probabilistic views (including the concepts of free energy and entropy). In fact, quantum electrodynamics is the only framework offering an accurate and consistent understanding of the interplay between forces at stake. Nevertheless, the Hellman-Feynman theorem shows intermolecular forces are encapsulated by electrostatics.

Interactions span short to long distance range, typically from below 0.2 nm (equivalent to 1 or 2 atomic distances) to ~100 nm. The magnitude of the interactions can be strong or weak. In this regard, only chemical bonds (like covalent bonds) should be considered as bonds as opposed to physical bonds that are merely interactions. The description covers systems of simple atoms or molecules, atoms or molecules organised in solids, surfaces or colloids in liquids (long range interaction in this case) and also self-assembly. Whereas systems in free-space limited 1 or 2 particle can be analytical characterised, many-body problems must rely to computer simulations such as Monte Carlo, molecular dynamics, etc. Bearing this in mind, key concepts can still be presented.

1.3.1.1 Library of forces

The division of forces based on semi-empirical and semi-classical approach outside the framework of quantum electrodynamics is convenient for simplicity but can be misleading in certain cases. Between charges and permanent dipoles, the description of electrostatics prevails. For induced dipoles, polarisation forces must be employed. Finally, (attractive) covalent or chemical bonding and (repulsive) steric or exchange interactions for very short distances must be described by quantum mechanics. Magnetic contributions are left aside for simplicity.

1.3.1.1.1 Charges, permanent dipoles, induced dipoles

Considerations based on the theory of electrostatics well describe long-range (>1 nm) interactions between particles carrying a charge (ions); neutral particles presenting a permanent dipole, initially studied by Willem Hendrik Keesom (for instance a water molecule); and even induced dipoles, studied by Peter J.W. Debye (like molecules under the influence of an electrical field).

A more in-depth study of matter has shown cohesion in certain materials, or difference in the type of equilibrium phase within a certain class of molecules (alkanes) could not only be explained by classical electrostatics. Quantum mechanics shows that even for neutral molecules and in the absence of external excitation, a vanishing dipole can emerge within covalent bonds. Dispersion forces account for this effect as studied by Fritz London.

Van der Waals forces are often cited to cover the interactions on such systems. Capturing the Pauli exclusion principle (from Quantum Mechanics) van der Waals interactions encapsulate the diverse contributions of orientation (Keesom), induction (Debye) and dispersion (London). MacLachlan introduced a unified equation for the description of these long-range ($\sim 1/r^6$) effect and anisotropic forces that can be attractive and repulsive as Keesom demonstrated.

In principle, the framework jointly offered by electrostatics along with van der Waals considerations allows deriving equations to characterise interactions and interplay between all classes of particles: magnitude of force, particle preferred orientation, etc. Dipolar effects implying retardation effects (change in the orientation of the dipole or its magnitude) must also be taken into account and they introduce more complexity in the equations. In real many-body systems, retardation effects make the forces non-additive and require a self-consistent resolution as dipoles (with a fluctuating magnitude or not) influence each other (orientation-wise).

1.3.1.1.2 Repulsive force

Apart from weak and strong forces acting within nuclei and atoms, the argument explaining cohesion of matter in the physical world as opposed to matter collapsing relies on the electron clouds of atoms/molecules repelling each other at short distance (<0.2 nm).

There is no simple expression describing the anisotropic repulsion. Models such as the hard-sphere model or power-law potential are conceptually practical but without a physical basis, the model of exponential potential has little more physically basis, from a qualitative standpoint only.

1.3.1.2 Lennard-Jones

Particles are subject to pair potentials, w, from which the forces $F(r)$ derivate: $F(r) = -dw/dr$, with r is a distance. A short-coming of simplistic analytical description is to implicitly consider particles as points.

The widely used phenomenological model encompassing attractive and repulsive pair potentials is the Lennard-Jones potential (A, B, ϵ, σ are constants):

$$w(r) = \frac{A}{r^{12}} - \frac{B}{r^6} = 4\epsilon \cdot \left[\left(\frac{\sigma}{r}\right)^{12} - \left(\frac{\sigma}{r}\right)^{6}\right]$$

Equation 1.5. General expression of the Lennard-Jones potential.

Typically, the potential $w(r)$ presents a minimum at $r = 2^{1/6}\sigma$ for which $w_{min} = -\epsilon$. The formulation does not have a solid physical basis since other exponents could be chosen or exponential decays could as well be used to fit experimental data. Nevertheless, the Lennard-

Jones still has the merit to provide a good indication of the energy landscape of atomic/molecular systems, see Figure 1.12a.

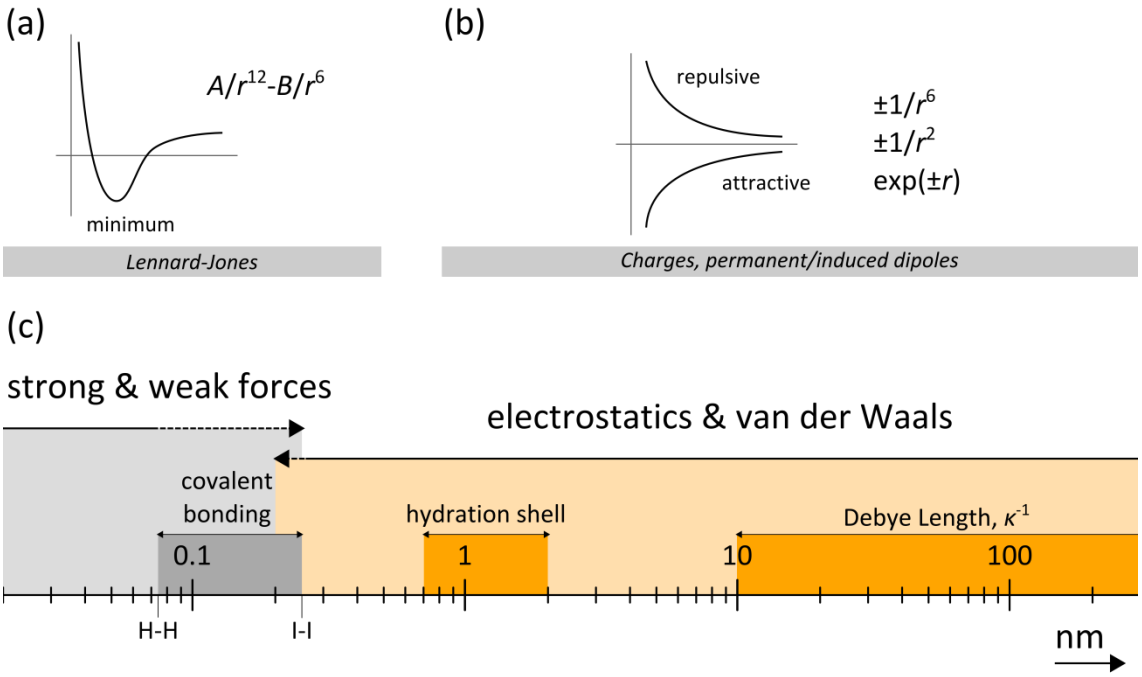

Figure 1.12. Schematic of pair potential and length scale: a, The shape of a typical Lennard-Jones is shown; b, interactions between charges, permanent/induced dipoles can give rise to repulsive or attractive potentials; c, domain of forces against the length-scale.

From Figure 1.12c, it can be seen the forces at stake span a very large range of length-scales.

1.3.1.3 Resolution

The resolution of any system relies on thermodynamic considerations. The chemical potential, μ, sums all the pair potentials of a particular species. At equilibrium, the different chemical potentials of the system must be equal to each other. The Nernst equation (electrostatics $e\Delta\psi$) or solubility (concentrations X_2, X_1) can be derived. All together, one can derive the formula describing a system where $\Delta\mu^i$ represents the difference of energy between the two species (respective to their solid-state for instance), see Equation 1.6.

$$X_2 = X_1 \cdot \exp\left(-\left(\Delta\mu^i + e\Delta\psi\right)/k_B T\right)$$

Equation 1.6. Hypothetical equation of states.

One can readily see the thermal energy, $k_B T$, is a good gauge of the strength of interactions, even though analytical results will mostly provide qualitative estimates only because of the reasons mentioned on the actual complexity of systems studied.

1.3.2 Studied interface systems

Experimental systems use many particles. The work presented in this thesis will touch two main concepts in the field of immersed surfaces. First of all, hydration of molecules will play a key role all along the work: sub nanometre-scale interactions will thus be involved.[79] On the other hand, the effect of the double layer at metal-liquid interfaces (in the case of dispersal of nanocrystals, trapped nanocrystals between electrodes, immersed electrodes) extending to few nanometres will also be investigated.

1.3.2.1 Hydration effect

In a situation of a solute in a solvent, one must decompose the system by focusing on solute-solute, solvent-solvent, solute-solvent interactions plus cavity effects when particles are moved from one place to another.

Water is found to be a very intriguing medium that differs from other solvents (from ref. [78], chapters 8 and 13). Effects like the liquid phase being denser (maximum reached at $4℃$) than the solid phase can be interpreted by examining the very peculiar hydrogen bond: $O\cdots H$ (Although the covalent bond H-O is 0.26 nm in length, $O\cdots H$ is found to be 0.176 nm.). To minimise energy in systems, it appears water molecules prefer organising in a tetrahedral structure both in pure bulk water and in the presence of foreign molecules potentially forming a cage around them.

Both the hydrophobic and hydrophilic effects arise from this phenomenon. It is energetically unfavourable for a water molecule to be isolated in a foreign solvent of molecules presenting no hydrogen bond. Solute of the same molecules surrounded by water molecules is less energetically demanding. These two different cases are both hydrophobic situations. Conversely, the hydrophilic effect comes into play for ions and neutral molecules with well arranged electronegative atoms. It can even happen that the former molecules (when in contact with water) are better in water than with each other and thus dissolve entirely. One must underline the hydrophilic/hydrophobic character is not equivalent to the polar/non-polar nature of molecules.

More specifically in the case of ions in dipolar solvent, the bonding of solvent will occur with privileged directions forming a shell around the ions leading to the concept of hydrated radius. The shell of solvation is a dynamic sub-system . In the case of water molecules in bulk water the "rotational correlation time" is 10^{-11} s however within the primary solvation shell: the water molecules are found to move more slowly like 10^{-9} s or 10^{-6} s to hours. The extent of the solvation zone is found to decay exponentially whereas the relative permittivity is lower at the

centre and increases to the bulk value. In all cases, one must bear in mind the solvation shell is intrinsically a dynamic structure that can accommodate deformations.

1.3.2.2 Double layer

When an object is placed into a liquid, the dissolved salt in the solvent will readily cover the surface of the object forming a film called the double layer (from ref. [78], chapter 12). Helmholtz then Gouy and Chapman and finally Stern studied the structure of the double layer. Calculating the charge distributions within the layer relies on considerations on the chemical potential expression and the Poisson equation, see Equation 1.7.

$$ze\rho = -\varepsilon_0 \varepsilon_r \nabla^2 \psi$$

Equation 1.7. Poisson Equation governing the spatial distribution of charges, $\varepsilon_0 \varepsilon_r$ is the permittivity of the medium, ψ is the potential, ρ is the charge distribution, and the ze the charge carried by the particles considered.

We present the usual phenomenological approach of the double layer configuration.

Depending on the surface potential of the object, the affinity of ions with the surface material, etc. cations or anions will bond or adsorb on the object surface creating an outer surface charge called the Stern layer. The Stern layer is delimited by a virtual plane (Stern plane) touching the ions aggregated on the surface. Ions in the Stern layer interact with counter ions of the solvent (by the means of the electrostatic force) by attracting them to accommodate the local surface charge thus creating a second layer. However in this case, the distribution of counter ions through space is diffuse and increases gradually to reach the bulk concentration. Conversely, ions presenting the same charge as the ones in the Stern layer also occupy loosely the second layer so that their local concentration decays to reach the bulk value. The term of ionic atmosphere is often used to describe the distribution of ions in the double layer, see Figure 1.13.

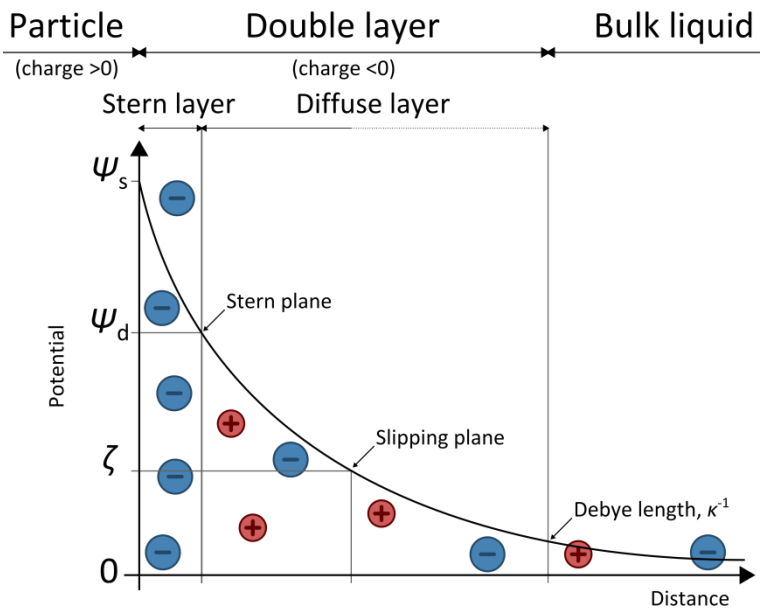

Figure 1.13. Schematic detailing the structure of the double-layer at an electrode surface, surface potential, ψ_s; potential at the Stern layer, ψ_d; potential at the slipping plane, ζ.

The Gouy-Chapman-Stern description presented above does not cover many important details such as the discreteness of charges at the object surface, the finite size of ions themselves, any image forces or van der Waals dispersion contributions, it does not account for solvation effects either. These further effects cannot be ranked *a priori* as their respective magnitude depends on the system studied.

Despite all these approximations, this model helps understanding the organisation of the double-layer. Typically, the Stern layer is an ion thick. For low bias potential of the object (<25 mV) the inverse of the Debye length, κ, can be estimated using the Graham equation. It goes as the square root of bulk salt concentrations (with $\rho_{i,\infty}$ the bulk concentration of a particular ion and z_i its valence), see Equation 1.8.

$$\kappa = \left(\frac{e^2}{\varepsilon_0 \varepsilon_r k_B T} \sum_i \rho_{i,\infty} z_i^2 \right)^{1/2}$$

Equation 1.8. Inverse of the Debye Length: decaying constant in unit of inverse length.

For instance, an electrolyte composed of monovalent ions such as NaCl dissolved in water with a concentration of 1 mM, the Debye length is ~10 nm (and becomes ~300 nm for a lower concentration 1 µM).

Dejarguin and Landau then Verwey and Overbeek derived a theory (DLVO) studying the influence of van der Waals interactions within the double layer. The theory has been successful in explaining phenomena found in colloidal science. It shows that two surfaces (typically nanocrystal ones) can come into strong adhesive contact when the potential or charge they carry is lowered by a more effective ion binding (in the Stern layer) or by improving the double-layer screening by the means of an increase of the electrolyte salt concentration. However, if the surface potential or charge is not substantially decreased, the two surfaces may still adhere in a less stable and reversible configuration if a secondary minimum exist in the energy vs. distance diagram.

A measure in the stability of colloids is the ζ-potential. As detailed, the double-layer is a structure comprising ions organised in a diffuse fashion from the object surface towards the bulk solution. This many-body system is dynamical in nature: ions are relatively mobile so that their positions fluctuate. Nevertheless on can define a slipping plane as a virtual boundary in the double-layer before which ions are stable and after which ions are more labile: on the form of a dispersed medium. The ζ-potential is the potential at the slipping plane (in principle different from the Stern plane), see Figure 1.13. A value above $|\zeta| \gtrsim 25\,\mathrm{mV}$ can be taken as a cut-off criterion of colloidal stability.

1.4 Scope of the thesis

1.4.1.1 Modelling of hybrid nanocrystal-molecule assemblies in solution

Based on the first experimental results of Dr. Claire Barrett and subsequent experimental developments conducted by Ethel Noonan, it was shown hybrid structures comprising nanocrystals ranging between 20 nm to 80 nm in diameter linked by organometallic and biological based molecules of ~ 1 nm or longer can be formed in solution by careful control of the self-assembly process.

Chapter 2 of this work presents a framework for modelling the making of *n*-mers where n denotes the number of nanocrystals in a nanostructure. Experimental UV-visible absorption spectra are processed using the Beer-Lambert law so as to extract the concentration of *n*-mers (1-mers and 2-mers only), where n represents the number of nanocrystals in the structure, in the early stage of the preparation of *n*-mers.

In parallel silicon samples are continuously prepared from aliquots taken from the main solution. Their surface is imaged by Scanning Electron Microscope (SEM) to reveal the statistical distribution of *n*-mers by randomly spotting nanostructures immobilised.

The formation of *n*-mers first seen as a promising candidate for the contacting strategy of single molecules[80] turned out to be a model system providing insightful information on the binding process of molecules on highly curved gold surfaces, e.g. nanocrystals and metal electrode grains. A model based on a system of rate-equations was developed by the author to model the evolution of the population distribution of *n*-mers. It first gives insights in the main factors driving the formation of such nanostructures by consistently fitting statistical data extracted from the Beer-Lambert law and/or the SEM image analysis. We also believe the prediction of the evolution of *n*-mers population is possible for carefully controlled experiments.

1.4.1.2 Functionalisation of directed assemblies of few nanocrystals

We present a versatile method for interfacing small assemblies of molecules between laterally patterned metal nanoelectrodes ($\sim 40\,\mathrm{nm}$ electrode gap) using citrate-stabilised metal nanocrystals ($\sim 60\,\mathrm{nm}$ core diameter) trapped in/over the gap using dielectrophoresis.

Initial electrical characterisations were carried on trapped nanocrystals on functionalised electrodes. However, in order to decorrelate the contributions of the different components of the electrode—[molecule(s)]—nanocrystal—[molecule(s)]—electrode double junction, electrical characterisation of the device was performed after each significant process step: starting with as-

received electrodes, after trapping of particle, after blank immersion in solvent dissolving molecules, after molecular functionalisation.

We first demonstrate the functioning of the hybrid architecture of functionalised nanocrystals by organic molecules as well as effects of simple non-aqueous solvents on the conductance of trapped nanocrystal devices.

1.4.1.3 Electrolytic gating of functionalised few-nanocrystal assemblies

Because gating ~ 1 nm long molecules is extremely challenging by means of electrostatic coupling (as found in a normal transistor), the idea of electrolytic gating of molecules emerged. As we saw, ions dissolved in a liquid medium the solvent itself have a strong influence in the very close vicinity of surfaces: in the form of solvation shells developing around molecules and the ionic atmosphere present in the double-layer.

Electrolytic gating has been studied by other groups in systems such as STM-BJ, Hg liquid-drop, and to a lesser extent in large nanocrystal arrays.

An entirely new platform for electrical characterisation was developed by the author. A system of easily removable on chip cell was designed. A Faraday cage system paired with low noise and anti electrostatic-defect protection interface connections were specially made. A custom interfacing programme of the parameter analyser was also developed.

We demonstrate the functioning of the platform for electrochemistry applications (as bi-potentiostat mode). We also investigate the stability of nanocrystal assemblies in solvents and the possibility of electrolytic gating of functionalised nanocrystal assemblies in gaps.

1.5 References

1. Sheehan, P. E.; Whitman, L. J., Detection Limits for Nanoscale Biosensors. *Nano Letters* **2005,** *5* (4), 803-807.
2. Grzelczak, M.; Vermant, J.; Furst, E. M.; Liz-Marzán, L. M., Directed Self-Assembly of Nanoparticles. *ACS Nano* **2010,** *4* (7), 3591-3605.
3. Ashkin, A.; Dziedzic, J. M.; Bjorkholm, J. E.; Chu, S., Observation of a single-beam gradient force optical trap for dielectric particles. *Opt. Lett.* **1986,** *11* (5), 288-290.
4. Pohl, H. A., *Dielectrophoresis: the behavior of neutral matter in nonuniform electric fields*. Cambridge University Press: New York, 1978; Vol. 1, p 590.
5. Gierhart, B. C.; Howitt, D. G.; Chen, S. J.; Smith, R. L.; Collins, S. D., Frequency Dependence of Gold Nanoparticle Superassembly by Dielectrophoresis. *Langmuir* **2007,** *23* (24), 12450-12456.
6. Valtiner, M.; Kristiansen, K.; Greene, G. W.; Israelachvili, J. N., Effect of Surface Roughness and Electrostatic Surface Potentials on Forces Between Dissimilar Surfaces in Aqueous Solution. *Advanced Materials* **2011,** *23* (20), 2294-2299.
7. Barsotti, R. J.; Vahey, M. D.; Wartena, R.; Chiang, Y. M.; Voldman, J.; Stellacci, F., Assembly of metal nanoparticles into nanogaps. *Small* **2007,** *3* (3), 488-499.
8. Szent-Györgyi, A., Bioelectronics. *Science* **1968,** *161* (3845), 988-990.
9. Aviram, A.; Ratner, M. A., Molecular rectifiers. *Chemical Physics Letters* **1974,** *29* (2), 277-283.
10. Aviram, A., Molecules for memory, logic, and amplification. *J. Am. Chem. Soc* **1988,** *110* (17), 5687 - 5692.
11. Reed, M. A.; Zhou, C.; Muller, C. J.; Burgin, T. P.; Tour, J. M., Conductance of a Molecular Junction. *Science* **1997,** *278* (5336), 252-254.
12. Datta, S., *Quantum Transport: Atom to Transistor*. 2nd ed.; Cambridge University Press: 2005; Vol. 1, p 418.
13. Emberly, E. G.; Kirczenow, G., Landauer theory, inelastic scattering, and electron transport in molecular wires. *Physical Review B* **2000,** *61* (8), 5740.
14. Huisman, E. H.; Guédon, C. M.; van Wees, B. J.; van der Molen, S. J., Interpretation of Transition Voltage Spectroscopy. *Nano Letters* **2009,** *9* (11), 3909-3913.
15. Song, H.; Reed, M. A.; Lee, T., Single Molecule Electronic Devices. *Advanced Materials* **2011,** *23* (14), 1583-1608.
16. Trouwborst, M. L.; Martin, C. A.; Smit, R. H. M.; Guédon, C. M.; Baart, T. A.; van der Molen, S. J.; van Ruitenbeek, J. M., Transition Voltage Spectroscopy and the Nature of Vacuum Tunneling. *Nano Letters* **2011,** *11* (2), 614-617.
17. Simmons, J. G., Generalized Formula for the Electric Tunnel Effect between Similar Electrodes Separated by a Thin Insulating Film. *Journal of Applied Physics* **1963,** *34* (6), 1793-1803.
18. Ho Choi, S.; Kim, B.; Frisbie, C. D., Electrical Resistance of Long Conjugated Molecular Wires. *Science* **2008,** *320* (5882), 1482-1486.
19. Choi, S. H.; Risko, C.; Delgado, M. C. R.; Kim, B.; Brédas, J.-L.; Frisbie, C. D., Transition from Tunneling to Hopping Transport in Long, Conjugated Oligo-imine Wires Connected to Metals. *Journal of the American Chemical Society* **2010,** *132* (12), 4358-4368.
20. Lu, Q.; Liu, K.; Zhang, H.; Du, Z.; Wang, X.; Wang, F., From Tunneling to Hopping: A Comprehensive Investigation of Charge Transport Mechanism in Molecular Junctions Based on Oligo(p-phenylene ethynylene)s. *ACS Nano* **2009,** *3* (12), 3861-3868.
21. Hihath, J.; Bruot, C.; Tao, N., Electron-Phonon Interactions in Single Octanedithiol Molecular Junctions. *ACS Nano* **2010,** *4* (7), 3823-3830
22. Long, D. P.; Troisi, A., Inelastic Electron Tunneling Spectroscopy of Alkane Monolayers with Dissimilar Attachment Chemistry to Gold. *Journal of the American Chemical Society* **2007,** *129* (49), 15303-15310.

23. Wang, W.; Scott, A.; Gergel-Hackett, N.; Hacker, C. A.; Janes, D. B.; Richter, C. A., Probing Molecules in Integrated Silicon-Molecule-Metal Junctions by Inelastic Tunneling Spectroscopy. *Nano Letters* **2008,** *8* (2), 478-484.
24. Rahimi, M.; Hegg, M., Probing charge transport in single-molecule break junctions using inelastic tunneling. *Physical Review B (Condensed Matter and Materials Physics)* **2009,** *79* (8), 081404-4.
25. Joachim, C.; Gimzewski, J. K.; Aviram, A., Electronics using hybrid-molecular and mono-molecular devices. *Nature* **2000,** *408* (6812), 541-548.
26. Moth-Poulsen, K.; Bjornholm, T., Molecular electronics with single molecules in solid-state devices. *Nat Nano* **2009,** *4* (9), 551-556.
27. Cheng, Z. L.; Skouta, R.; Vazquez, H.; Widawsky, J. R.; Schneebeli, S.; Chen, W.; Hybertsen, M. S.; Breslow, R.; Venkataraman, L., In situ formation of highly conducting covalent Au-C contacts for single-molecule junctions. *Nat Nano* **2011,** *6* (6), 353-357.
28. Schneebeli, S. T.; Kamenetska, M.; Cheng, Z.; Skouta, R.; Friesner, R. A.; Venkataraman, L.; Breslow, R., Single-Molecule Conductance through Multiple π−π-Stacked Benzene Rings Determined with Direct Electrode-to-Benzene Ring Connections. *Journal of the American Chemical Society* **2011,** *133* (7), 2136-2139.
29. Xu, B.; Xiao, X.; Tao, N. J., Measurements of Single-Molecule Electromechanical Properties. *Journal of the American Chemical Society* **2003,** *125* (52), 16164-16165.
30. Frei, M.; Aradhya, S. V.; Koentopp, M.; Hybertsen, M. S.; Venkataraman, L., Mechanics and Chemistry: Single Molecule Bond Rupture Forces Correlate with Molecular Backbone Structure. *Nano Letters* **2011,** *11* (4), 1518-1523.
31. Ko, C.-H.; Huang, M.-J.; Fu, M.-D.; Chen, C.-h., Superior Contact for Single-Molecule Conductance: Electronic Coupling of Thiolate and Isothiocyanate on Pt, Pd, and Au. *Journal of the American Chemical Society* **2009,** *132* (2), 756-764.
32. Meisner, J. S.; Kamenetska, M.; Krikorian, M.; Steigerwald, M. L.; Venkataraman, L.; Nuckolls, C., A Single-Molecule Potentiometer. *Nano Letters* **2011,** *11* (4), 1575-1579.
33. Heimel, G.; Zojer, E.; Romaner, L.; Brédas, J.-L.; Stellacci, F., Doping Molecular Wires. *Nano Letters* **2009,** *9* (7), 2559-2564.
34. Mishchenko, A.; Vonlanthen, D.; Meded, V.; Buerkle, M.; Li, C.; Pobelov, I. V.; Bagrets, A.; Viljas, J. K.; Pauly, F.; Evers, F.; Mayor, M.; Wandlowski, T., Influence of Conformation on Conductance of Biphenyl-Dithiol Single-Molecule Contacts. *Nano Letters* **2009,** *10* (1), 156-163.
35. Solomon, G. C.; Herrmann, C.; Hansen, T.; Mujica, V.; Ratner, M. A., Exploring local currents in molecular junctions. *Nat Chem* **2010,** *2* (3), 223-228.
36. Bergfield, J. P.; Solomon, G. C.; Stafford, C. A.; Ratner, M. A., Novel Quantum Interference Effects in Transport through Molecular Radicals. *Nano Letters* **2011,** *11* (7), 2759-2764.
37. Quek, S. Y.; Kamenetska, M.; Steigerwald, M. L.; Choi, H. J.; Louie, S. G.; Hybertsen, M. S.; Neaton, J. B.; Venkataraman Latha, Mechanically controlled binary conductance switching of a single-molecule junction. *Nat Nano* **2009,** *4* (4), 230-234.
38. Ohmann, R.; Vitali, L.; Kern, K., Actuated Transitory Metal−Ligand Bond As Tunable Electromechanical Switch. *Nano Letters* **2010,** *10* (8), 2995-3000.
39. Kim, Y.; Song, H.; Kim, D.; Lee, T.; Jeong, H., Noise Characteristics of Charge Tunneling via Localized States in Metal−Molecule−Metal Junctions. *ACS Nano* **2010,** *4* (8), 4426-4430.
40. Kim, Y.; Hellmuth, T. J.; Bürkle, M.; Pauly, F.; Scheer, E., Characteristics of Amine-Ended and Thiol-Ended Alkane Single-Molecule Junctions Revealed by Inelastic Electron Tunneling Spectroscopy. *ACS Nano* **2011,** *5* (5), 4104-4111.
41. Mayor, M.; Weber, H. B., Statistical Analysis of Single-Molecule Junctions. *Angew. Chem. Int. Ed.* **2004,** *43* (22), 2882-2884.
42. Huang, Z.; Chen, F.; D'Agosta, R.; Bennett, P. A.; Di Ventra, M.; Tao, N., Local ionic and electron heating in single-molecule junctions. *Nat Nano* **2007,** *2* (11), 698-703.
43. Quinn, J. R.; Foss, F. W.; Venkataraman, L.; Breslow, R., Oxidation Potentials Correlate with Conductivities of Aromatic Molecular Wires. *Journal of the American Chemical Society* **2007,** *129* (41), 12376-12377.

44. Malen, J. A.; Doak, P.; Baheti, K.; Tilley, T. D.; Majumdar, A.; Segalman, R. A., The Nature of Transport Variations in Molecular Heterojunction Electronics. *Nano Letters* **2009,** *9* (10), 3406-3412.
45. Muller, C. J.; van Ruitenbeek, J. M.; de Jongh, L. J., Experimental observation of the transition from weak link to tunnel junction. *Physica C: Superconductivity* **1992,** *191* (3-4), 485-504.
46. Wu, S.; Gonzalez, M. T.; Huber, R.; Grunder, S.; Mayor, M.; Schonenberger, C.; Calame, M., Molecular junctions based on aromatic coupling. *Nat Nano* **2008,** *3* (9), 569-574.
47. Huisman, E. H.; Trouwborst, M. L.; Bakker, F. L.; de Boer, B.; van Wees, B. J.; van der Molen, S. J., Stabilizing Single Atom Contacts by Molecular Bridge Formation. *Nano Letters* **2008,** *8* (10), 3381-3385.
48. Park, J.; Pasupathy, A. N.; Goldsmith, J. I.; Soldatov, A. V.; Chang, C.; Yaish, Y.; Sethna, J. P.; Abruña, H. D.; Ralph, D. C.; McEuen, P. L., Wiring up single molecules. *Thin Solid Films* **2003,** *438-439*, 457-461.
49. Johnston, D. E.; Strachan, D. R.; Johnson, A. T. C., Parallel Fabrication of Nanogap Electrodes. *Nano Letters* **2007,** *7* (9), 2774-2777.
50. Prins, F.; Hayashi, T.; Steenwijk, B. J. A. d. V. v.; Gao, B.; Osorio, E. A.; Muraki, K.; Zant, H. S. J. v. d., Room-temperature stability of Pt nanogaps formed by self-breaking. *Applied Physics Letters* **2009,** *94* (12), 123108.
51. Osorio, E. A.; Ruben, M.; Seldenthuis, J. S.; Lehn, J. M.; van der Zant, H. S. J., Conductance Switching and Vibrational Fine Structure of a [2 × 2] CoII4 Gridlike Single Molecule Measured in a Three-Terminal Device. *Small* **2010,** *6* (2), 174-178.
52. Song, H.; Kim, Y.; Jang, Y. H.; Jeong, H.; Reed, M. A.; Lee, T., Observation of molecular orbital gating. *Nature* **2009,** *462* (7276), 1039-1043.
53. Cui, X. D.; Primak, A.; Zarate, X.; Tomfohr, J.; Sankey, O. F.; Moore, A. L.; Moore, T. A.; Gust, D.; Harris, G.; Lindsay, S. M., Reproducible Measurement of Single-Molecule Conductivity. *Science* **2001,** *294* (5542), 571-574.
54. Wold, D. J.; Frisbie, C. D., Fabrication and Characterization of Metal−Molecule−Metal Junctions by Conducting Probe Atomic Force Microscopy. *Journal of the American Chemical Society* **2001,** *123* (23), 5549-5556.
55. Tran, E.; Duati, M.; Whitesides, G. M.; Rampi, M. A., Gating current flowing through molecules in metal–molecules–metal junctions. *Faraday Discuss.* **2006,** *131*, 197-203.
56. Nijhuis, C. A.; Reus, W. F.; Barber, J. R.; Dickey, M. D.; Whitesides, G. M., Charge Transport and Rectification in Arrays of SAM-Based Tunneling Junctions. *Nano Letters* **2010,** *10* (9), 3611-3619.
57. Thuo, M. M.; Reus, W. F.; Nijhuis, C. A.; Barber, J. R.; Kim, C.; Schulz, M. D.; Whitesides, G. M., Odd−Even Effects in Charge Transport across Self-Assembled Monolayers. *Journal of the American Chemical Society* **2011,** *133* (9), 2962-2975.
58. Nijhuis, C. A.; Reus, W. F.; Whitesides, G. M., Mechanism of Rectification in Tunneling Junctions Based on Molecules with Asymmetric Potential Drops. *Journal of the American Chemical Society* **2010,** *132* (51), 18386-18401.
59. Tran, E.; Duati, M.; Ferri, V.; Müllen, K.; Zharnikov, M.; Whitesides, G. M.; Rampi, M. A., Experimental Approaches for Controlling Current Flowing through Metal-Molecule-Metal Junctions. *Advanced Materials* **2006,** *18* (10), 1323-1328.
60. Yaffe, O.; Scheres, L.; Puniredd, S. R.; Stein, N.; Biller, A.; Lavan, R. H.; Shpaisman, H.; Zuilhof, H.; Haick, H.; Cahen, D.; Vilan, A., Molecular Electronics at Metal/Semiconductor Junctions. Si Inversion by Sub-Nanometer Molecular Films. *Nano Letters* **2009,** *9* (6), 2390-2394.
61. Collier, C. P.; Mattersteig, G.; Wong, E. W.; Luo, Y.; Beverly, K.; Sampaio, J.; Raymo, F. M.; Stoddart, J. F.; Heath, J. R., A [2]Catenane-Based Solid State Electronically Reconfigurable Switch. *Science* **2000,** *289* (5482), 1172-1175.
62. Collier, C. P.; Wong, E. W.; Belohradský, M.; Raymo, F. M.; Stoddart, J. F.; Kuekes, P. J.; Williams, R. S.; Heath, J. R., Electronically Configurable Molecular-Based Logic Gates. *Science* **1999,** *285* (5426), 391-394.

63. Green, J. E.; Wook Choi, J.; Boukai, A.; Bunimovich, Y.; Johnston-Halperin, E.; DeIonno, E.; Luo, Y.; Sheriff, B. A.; Xu, K.; Shik Shin, Y.; Tseng, H.-R.; Stoddart, J. F.; Heath, J. R., A 160-kilobit molecular electronic memory patterned at 10^{11} bits per square centimetre. *Nature* **2007,** *445* (7126), 414-417.
64. Wu, W.; Jung, G. Y.; Olynick, D. L.; Straznicky, J.; Li, Z.; Li, X.; Ohlberg, D. A. A.; Chen, Y.; Wang, S. Y.; Liddle, J. A.; Tong, W. M.; Williams, R. S., One-kilobit cross-bar molecular memory circuits at 30-nm half-pitch fabricated by nanoimprint lithography. *Applied Physics A: Materials Science & Processing* **2005,** *80* (6), 1173-1178.
65. Shimizu, K. T.; Fabbri, J. D.; Jelincic, J. J.; Melosh, N. A., Soft Deposition of Large-Area Metal Contacts for Molecular Electronics. *Advanced Materials* **2006,** *18* (12), 1499-1504.
66. Ng, Z.; Loh, K. P.; Li, L.; Ho, P.; Bai, P.; Yip, J. H. K., Synthesis and Electrical Characterization of Oligo(phenylene ethynylene) Molecular Wires Coordinated to Transition Metal Complexes. *ACS Nano* **2009,** *3* (8), 2103-2114.
67. Akkerman, H. B.; Kronemeijer, A. J.; van Hal, P. A.; de Leeuw, D. M.; Blom, P. W. M.; de Boer, B., Self-Assembled-Monolayer Formation of Long Alkanedithiols in Molecular Junctions. *Small* **2008,** *4* (1), 100-104.
68. Kronemeijer, A. J.; Akkerman, H. B.; Kudernac, T.; van Wees, B. J.; Feringa, B. L.; Blom, P. W. M.; de Boer, B., Reversible Conductance Switching in Molecular Devices. *Advanced Materials* **2008,** *20* (8), 1467-1473.
69. Wang, G.; Kim, Y.; Choe, M.; Kim, T.-W.; Lee, T., A New Approach for Molecular Electronic Junctions with a Multilayer Graphene Electrode. *Advanced Materials* **2011,** *23* (6), 755-760.
70. Liao, J.; Bernard, L.; Langer, M.; Schönenberger, C.; Calame, M., Reversible Formation of Molecular Junctions in 2D Nanoparticle Arrays. *Advanced Materials* **2006,** *18* (18), 2444-2447.
71. Bernard, L.; Kamdzhilov, Y.; Calame, M.; van der Molen, S. J.; Liao, J.; Schönenberger, C., Spectroscopy of Molecular Junction Networks Obtained by Place Exchange in 2D Nanoparticle Arrays. *The Journal of Physical Chemistry C* **2007,** *111* (50), 18445-18450.
72. Cheng, W.; Park, N.; Walter, M. T.; Hartman, M. R.; Luo, D., Nanopatterning self-assembled nanoparticle superlattices by moulding microdroplets. *Nat Nano* **2008,** *3* (11), 682-690.
73. Liao, J.; Agustsson, J. S.; Wu, S.; Schönenberger, C.; Calame, M.; Leroux, Y.; Mayor, M.; Jeannin, O.; Ran, Y.-F.; Liu, S.-X.; Decurtins, S., Cyclic Conductance Switching in Networks of Redox-Active Molecular Junctions. *Nano Letters* **2010,** *10* (3), 759-764.
74. Kubatkin, S.; Danilov, A.; Hjort, M.; Cornil, J.; Bredas, J.-L.; Stuhr-Hansen, N.; Hedegard, P.; Bjornholm, T., Single-electron transistor of a single organic molecule with access to several redox states. *Nature* **2003,** *425* (6959), 698-701.
75. Ioannidis, J. P. A., Why Most Published Research Findings Are False. *PLoS Med* **2005,** *2* (8), e124.
76. González, M. T.; Wu, S.; Huber, R.; van der Molen, S. J.; Schönenberger, C.; Calame, M., Electrical Conductance of Molecular Junctions by a Robust Statistical Analysis. *Nano Letters* **2006,** *6* (10), 2238-2242.
77. Heath, J. R.; Kuekes, P. J.; Snider, G. S.; Williams, R. S., A Defect-Tolerant Computer Architecture: Opportunities for Nanotechnology. *Science* **1998,** *280* (5370), 1716-1721.
78. Israelachvili, J. N., *Intermolecular And Surface Forces (Second Edition)*. 2nd ed.; Elsevier Science: 1991; Vol. 1.
79. Liu, Y.; Lu, H.; Wu, Y.; Hu, T.; Li, Q., Hydration and coordination of K^+ solvation in water from ab initio molecular-dynamics simulation. *The Journal of Chemical Physics* **2010,** *132* (12), 124503-4.
80. Dadosh, T.; Gordin, Y.; Krahne, R.; Khivrich, I.; Mahalu, D.; Frydman, V.; Sperling, J.; Yacoby, A.; Bar-Joseph, I., Measurement of the conductance of single conjugated molecules. *Nature* **2005,** *436* (7051), 677-680.

Chapter 2 – Numerical modelling of the formation of nanocrystal-molecule-nanostructures

2.1 Introduction

The field of molecular electronics aims at understanding electronic properties of molecules attached between electrodes. To conduct experimental studies on (opto-)electronic properties of molecules, it is necessary to connect these molecules. One of the building blocks widely used in nanotechnology is ligand-stabilised nanocrystals. Inorganic nanocrystals with a core diameter ranging from ~ 2 to ~ 100 nm are attractive candidates as node connectors for molecules (~ 1 nm) and electrodes fabricated by using top-down e-beam lithography (~ 30-50 nm electrode gaps). Due to the size of the nanocrystal, these hybrid nanocrystal-molecule nanostructures also present the advantage of locally amplifying the electromagnetic field. This effect can be used to excite molecules using for instance the Surface Enhanced Raman Scattering.[1]

A key challenge in this regard lies in development of methods to form nanocrystal-molecule nanostructures with control over their (possibly interdependent) geometric and electronic properties. The formation of nanostructures through molecular recognition (e.g., binding of a sulphur end group on a molecule to a gold nanocrystal) is a kinetic process, which can be considered as an analogue to the nucleation and formation of islands on surfaces, i.e., cluster growth.[2] In this work, the nanocrystal-molecule structures formed in solution through mixing of nanocrystals and bi-functional linkers are generally referred to as "*n*-mers", where n represents the number of nanocrystals in the structure.

The chemical structure of the linker molecule is given in Figure 2.1a. The isothiocyanate (NCS) groups on these linkers can form stable bonds with gold, thus enabling the formation of dimers and higher-order *n*-mers. The separation between the sulphur end groups on each linker has been calculated from X-ray crystallography data to be 1.2 nm.[3] Figure 2.1b shows a schematically overview of the formation process leading to structures containing one nanocrystal ("1-mers", *n* = 1), two nanocrystals ("2-mers", *n* = 2) and higher order *n*-mers. The process was initially developed by Dr. Claire Barrett and has been improved by Raquel Palacios and now Ethel Noonan (respectively former intern student and currently Ph.D. student in the Nanotechnology Group) who have been working on this technique to make *n*-mers in different conditions, notably using longer and more complex site binding molecules. Unless otherwise stated, the experimental datasets originate from Dr. Claire Barrett's work. The formation of nanocrystal-molecule nanostructures is monitored on-line using UV-visible absorption spectra and off-line using Scanning Electron Microscope (SEM) micrographs. Figure 2.1c shows a typical UV-visible absorption spectrum. Figure 2.1d shows an annotated high-resolution SEM images of *n*-mers drop-deposited onto silicon substrates following formation in solution through mixing of citrate-stabilised Au nanocrystals (with core diameters, $d = 20 \pm 2$ nm) and $Re_2(DMAA)_4(NCS)_2$ linkers. It

is important to note that the description of the *n*-mer does not specify the number of molecules attached to each nanocrystal.

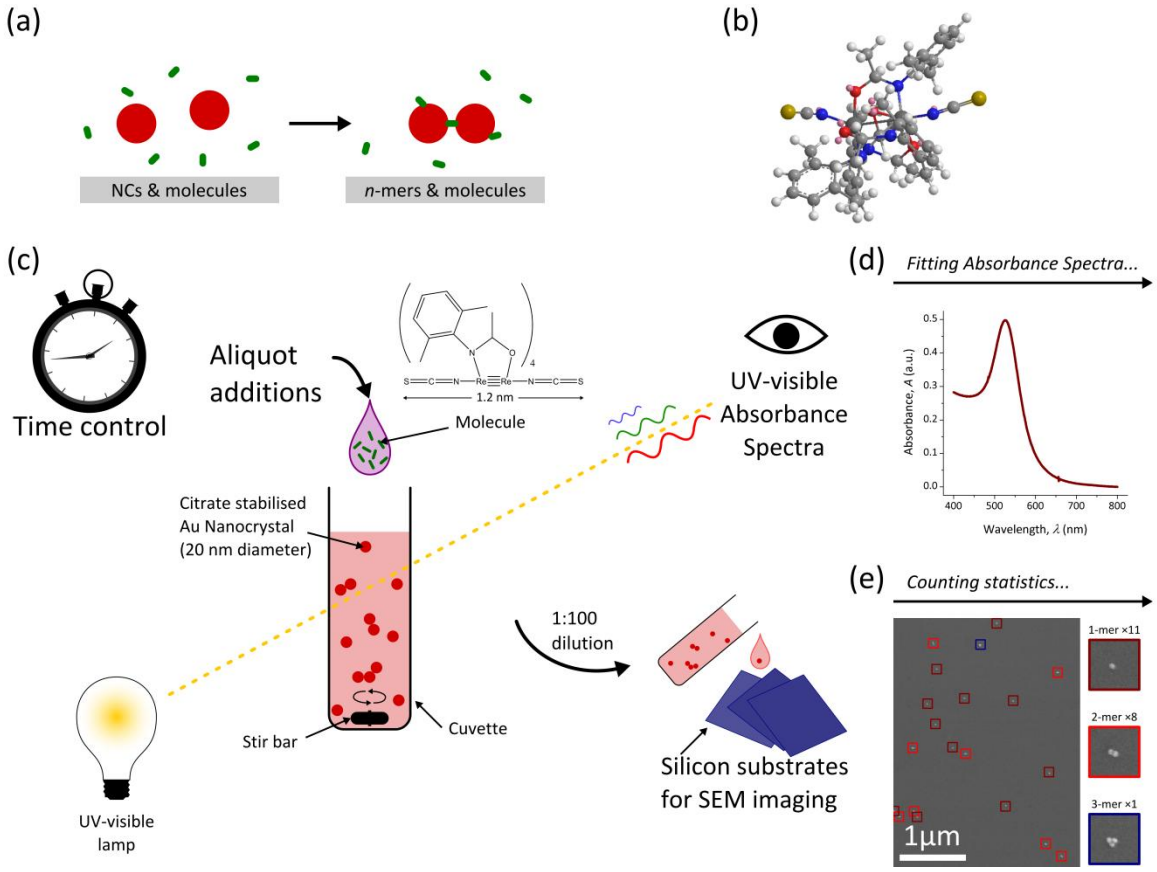

Figure 2.1 (a) Principle of conversion of citrate stabilised gold nanocrystals into more complex hybrid nanocrystal-molecules *n*-mers, where n represents the number of nanocrystals. (b) 3D chemical structure of the dirhenium-tetra(2,6-dimethylacetanilido)-di-isothiocyanate bi-functional linker molecule, $Re_2(DMAA)_4(NCS)_2$. (c) Experimental protocol for the formation of the *n*-mers. (d) Typical UV-visible absorption spectra acquired. (e) Typical Scanning Electron Microscope image obtained (11 1-mers, 8 2-mers and 1 3-mers can be counted on the image).

The controlled formation of *n*-mers is experimentally challenging on its own due to the large numbers of parameters involved in the mechanism. The idea here is to model the interactions – in bulk solution – between nanocrystals and molecules in order to understand the growth of nanocrystal/molecule clusters. We rely on a phenomenological model based on a system of rate-equations (superseding the initial full random-walk approach, Appendix 6.4). The high flexibility of the model allows accounting for molecular decoration of nanocrystals surface quantitatively, whereas effects like perturbation of the double-layer around nanocrystal surfaces or solvation issue are qualitatively considered.[4]

It is shown that the model can accommodate inputs from other experimental techniques and theoretical considerations so as to deliver even better results on the population evolution of the *n*-mers (for *n*=1, 2, 3, ...) from both descriptive and predictive point of views.

2.2 Methods

2.2.1 Experimental protocol

We briefly reproduce the key aspect of the experimental protocol from ref. [5].

Ultrapure deionised water with resistivity 18.2 MΩ cm (ELGA PURELAB Ultra) was used in all experiments. To improve the stability of the nanocrystals, 3 mM aqueous tri-sodium citrate was added to the nanocrystals prior to use. The bi-functional linker molecule (dirhenium-tetra(2,6-dimethylacetanilido)-di-isothiocyanate, later named $Re_2(DMAA)_4(NCS)_2$), see Figure 2.1a, was synthesised as previously described [3] and dissolved in acetone prior to use.

Any contamination of the glassware can interfere with the stability of the nanocrystals and cause spurious aggregation, therefore all glassware was initially cleaned using a 3-step solvent clean (tricholorethylene, warm acetone, isopropanol), before final cleaning steps using aqua-regia (3:1 $HCl:HNO_3$) to remove any gold residue, and piranha solution (3:1 $H_2SO_4:H_2O_2$) to remove organic residue. **Warning**: Aqua-regia and piranha are very corrosive and must be treated with extreme care; they react violently with organic material.

To form *n*-mers, a 3 mL aliquot of diluted d = 20 nm Au nanocrystal solution (3.5×10^{11} nanocrystals/mL) was decanted into a clean cuvette with a single magnetic stir-bar and the UV-Visible absorption spectrum was recorded using an Agilent 8453 spectrophotometer. Re linker molecules were added to the nanocrystals using a carefully controlled process. The cuvette was removed from the spectrometer and placed on stirrer plate, set to stir at a moderate rate to ensure even dispersion of the linker molecules. Aliquots (5 – 10 µL each) of 10 µM $Re_2(DMAA)_4(NCS)_2$ in acetone (ACS grade) were added to the nanocrystal solution at 1 – 3 minute time intervals. It was important to add the molecules by inserting the tip of the pipette below the solution surface because otherwise a layer with high linker concentration formed at the top of the solution. After each cycle of linker addition and mixing, the cuvette was re-inserted into the spectrometer and the UV-Visible absorbance was recorded at a range of wavelengths (λ, $200\,\mathrm{nm} < \lambda < 1100\,\mathrm{nm}$) at regular intervals (1-10 minutes). Addition of a large excess of linker to the nanocrystals caused rapid aggregation and precipitation of the nanocrystals.

In order to quantify the distribution of nanocrystal-molecule nanostructures, SEM-based nanovisualisation (JSM-6700F, JEOL UK Ltd.) was developed to record and statistically analyse the populations of 1-mers, 2-mers, 3-mers and higher order *n*-mers formed. Samples for SEM were prepared by dilution (100x) of the nanocrystal-molecule solution, followed by deposition of single 40 µL drops onto individual silicon chips (substrate resistivity ~5 mΩcm). Following deposition, the solution was wicked away using filter paper and allowed to dry in air. Control samples were

also prepared using unmodified Au nanocrystals from the same batch used to prepare the *n*-mers. For each substrate, approximately 100 nanostructures were counted at 10 - 20 random locations. For large *n*-mers ($n > 25$) the approximate number of nanocrystals was estimated based on the area of the nanostructure.

2.2.2 Continuity conditions

From the description of the experimental protocol, one can exhibit the conditions of continuity. Strictly speaking, over the course of the experiment, the cell in which the *n*-mers are being made is an open system since aliquots of molecular solution are added and on the other hand, small volumes from the mixture prepared can also be removed. Nevertheless during the time span between these additions and/or samplings the system (mixture in the cell) is closed. Moreover, one keeps record of any volume added/sampled which allows keeping track of the overall material quantity involved.

It is helpful to work on with the nanocrystal number continuity argument. We declare N_{nc} is the total number of nanocrystals in the system at any time, t, it accounts for all the nanocrystals in the cell regardless of the nanostructure they are comprised in. $N_{nc}(0)$ is indeed the number of nanocrystals at the beginning of the experiment. There will only be a difference $N_{nc}(0) - N_{nc}(t) \geq 0$ if one removes a certain amount of liquid from the cell, for instance for SEM samples preparation. This is described by the change: $N_{nc}(t+\delta t) = N_{nc}(t) \times \left(\frac{V(t+\delta t)}{V(t)}\right)$, with $V(t)$ the volume at a given time. It is therefore possible to describe the number of different *n*-mers, N_n, at any time within the cell, see Equation 2.1.

$$N_{nc}(0) \geq N_{nc}(t) = \sum_{n=1}^{n_{\max}} n \cdot N_n(t)$$

Equation 2.1. Conservation of the nanocrystal number within the cell: nanocrystals may be organised in various nanostructures.

In place of nanocrystal numbers, it can be more practical to work with concentrations. A concentration C_n is defined the number N_n normalised by the known remainder volume: $C_n(t) = N_n(t)/V(t)$. In this case, we also need to account for the volume added in the form of molecular solution aliquots, see Equation 2.2.

$$C_{\mathrm{nc}}(0) \geq C_{\mathrm{nc}}(t) = \sum_{n=1}^{n_{\max}} n \cdot C_n(t)$$

Equation 2.2. The concentrations of nanostructures is related to the overall concentration of nanocrystal in the cell.

Indeed $C_0(t)$ is a controlled experimental function as dilution due to molecular aliquot addition occurs regardless of the *n*-mers complexity. Sampling of the mixture is not *n*-mers complexity selective either.

Conversely, the number of molecules present in the cell is described by carefully accounting for any addition/removal of aliquots to/from the system.

$$N_{mol}(t+\delta t) = \left(N_{mol}(t) + N_A \cdot c_{mol} \cdot \delta V_{added}(t+\delta t)\right) \times \left(1 - \frac{\delta V_{removed}(t+\delta t)}{V(t)}\right)$$

Equation 2.3. Monitoring of the number of molecules in the system.

One needs to bear in mind these descriptions hold true on the basis that the distributions of the different species are uniform across the cell. In other words, it does not cover the case where there some sort of a precipitation mechanism occurs: if it ever happens, these considerations are biased.

Formation of *n*-mers is experimentally driven by the addition of molecules in the cell. Nonetheless, we need to bear in mind that during the process of adding molecules, one also dilutes the overall solution in the cell. Each time the molecule:nanocrystal ratio, $R_{mol:nc} = N_{mol}(t)/N_{nc}(t)$, is changed, there is conversely a change in the value of the concentration of nanocrystals within the cell (across all possible *n*-mers species formed), $C_{nc}(t)$, and for the concentration of molecules in the cell as well, $C_{mol}(t)$.

2.2.3 Extracting population data

We explore two ways of extracting the population of *n*-mers using the two experimental sources of data following the work-flow presented in Figure 2.2.

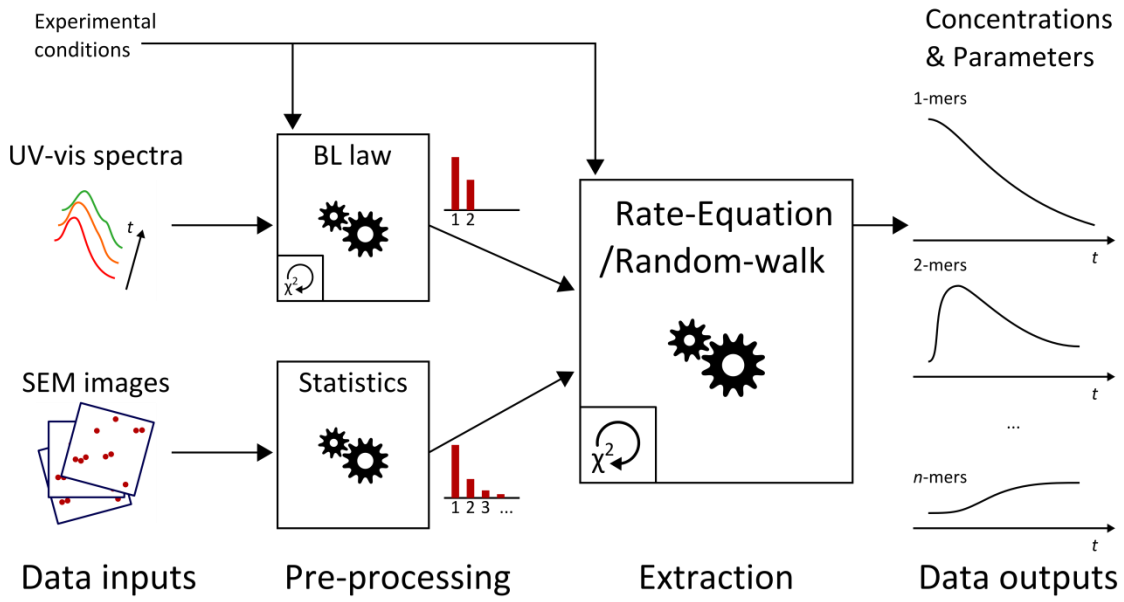

Figure 2.2 Simulation work-flow: UV-visible absorption spectra are processed using the Beer-Lambert law to obtain 1-mers and 2-mers concentrations, SEM images are analysed manually for counting the numbers of different *n*-mers present on the sample surface. The rate-equation model processes these data further to determine the evolution of the population of *n*-mers over time.

2.2.3.1 UV-visible absorption spectra analysed with the Beer-Lambert law

The analysis we present below is based on the Beer-Lambert law which relies on the superposition principle. This assumes that overall the processes conducting to the absorption spectra are a result of a linear optical response when light passes through the cell. Each species present in the pot contributes to the absorption spectrum $A(\lambda)$ (λ is the light wavelength), via its own extinction coefficient $\mathcal{E}_n(\lambda)$ and its concentration C_n in the cuvette. The absorbance is also dependent on the light path length ℓ which is a constant in the experimental setup, see Equation 2.4.

$$A(\lambda) = \sum_{n=1}^{n_{\max}} A_n(\lambda) = \ell \times \left(\sum_{n=1}^{n_{\max}} \mathcal{E}_n(\lambda) \cdot C_n \right)$$

Equation 2.4 The Beer-Lambert law.

Assessing the list of species in the cuvette is the first step for working out the absorption spectrum. During the course of the experiment, aliquots containing molecules solvated in acetone are added in the solution of nanocrystals. This will eventually lead to the formation of *n*-mers nanostructures. The characteristic wavelength range for monitoring the plasmon-resonance of the *n*-mers nanostructures is $[400; 800]$ nm, however the absorbance of the linker molecules (as well as the solvent they are dissolved in) vanishes for wavelength greater than $\lambda > 350$nm. Therefore we will ignore the molecule contribution to the spectra.

On the other hand, to build the spectrum, extinction coefficients of pure *n*-mer species need to be known. The extinction coefficient of 1-mers is determined by measuring the UV-vis absorption spectrum of a solution of citrate-stabilised gold nanocrystals. For higher order *n*-mers it is unfortunately not possible to get an experimental spectrum, since there is no reliable technique to achieve mono-dispersed samples of such species. Another option is to rely on simulations based on the Mie theory (Appendix – 6.1, p. 188), but the disadvantage of this technique is the computation of spectra becomes ever more complicated with high order *n*-mers. The optical response of asymmetric *n*-mers structures is dependent on the cross section being seen as by the light shined through the cuvette. All in all, only the extinction coefficients of 2-mers can be reliably described using simulations.

Even though, it is a limitation of the method, we are mostly interested in the formation of 2-mers and as a first approximation we will postulate that only 1-mer and 2-mer nanostructures are present in the pot. The implementation of Beer-Lambert law for the absorption spectrum becomes Equation 2.5. $\epsilon(\lambda, t)$ represents the residual error on the suggested absorption spectra and is expected to increase over the course of the experiment.

$$A(\lambda, t) = \ell \times [\mathcal{E}_1(\lambda) \cdot C_1(t) + \mathcal{E}_2(\lambda) \cdot C_2(t) + \epsilon(\lambda, t)]$$

Equation 2.5. Expression of a predicted absorption spectrum (based on the Beer-Lambert law).

For consistency, all measured spectra are background subtracted against the blank cuvette. All the more, all spectra are zeroed at $\lambda = 800\text{nm}$ to get rid of any residual scattering that would offset the spectrum by a constant value on the wavelength range investigated.

With the further constraint of a two-species system (1-mers and 2-mers), the continuity relation is reduced to one degree of freedom: since 1-mers can only join to form 2-mers or vice-versa. Rewriting the relationship normalised by $C_{nc}(t)$, at any t we obtain $1 = N_1 + 2 \cdot N_2$ where N_1 and N_2 are fraction of 1-mers and 2-mers respectively.

Finally, the absorption spectrum is fully described by the relationship presented in Equation 2.6 ($\mathcal{E}_1(\lambda)$, $\mathcal{E}_2(\lambda)$ are the extinction coefficients of 1-mers and 2-mers, respectively). To this extent, constructing a spectrum is equivalent to defining the normalised number of 1-mers, N_1.

$$A(\lambda, t) = [\ell \cdot C_{nc}(t)] \times \left[N_1(t) \cdot \left(\mathcal{E}_1(\lambda) - \frac{\mathcal{E}_2(\lambda)}{2}\right) + \frac{\mathcal{E}_2(\lambda)}{2}\right]$$

Equation 2.6. Simplified expression of a predicted absorption spectrum (based on the Beer-Lambert law).

This method is implemented using the Matlab™ language. One has to acknowledge the fact a red-shift of the region of the Plasmon-resonance peak (if not the spectrum as a whole) is observed soon after the first molecular solution aliquots. It is believed to be the consequence of a change of the permittivity of the liquid medium around the gold particles resulting from molecular adsorption on these surfaces. At this stage, the fast red-shift change is taken into account by readily translating the initial pristine $\mathcal{E}_1(\lambda)$ spectrum of the relevant wavelength red-shift, $\Delta\lambda\sim 3$ nm.

A one free parameter curve fitting routine is performed consistently across a UV-vis absorption spectra data set so as to determine the values of $N_1(t)$ and conversely $N_2(t)$. For each measured spectrum, $A_{meas}(\lambda_p, t)$, a simulated spectrum, $A_{simu}(\lambda_p, t)$, is computed. The typical wavelength range for λ_p is $[400; 800]$ nm with steps of $\delta\lambda = 1$ nm (experimental resolution) meaning $m = 400$ points per fit. Suggested spectra are tested against the measured spectra. The least mean square estimator χ^2 is used to evaluate the accuracy of the fitting procedure, see Equation 2.7.

$$\chi^2(t) = \frac{1}{m-1} \times \sum_{p=1}^{m} \left(A_{meas}(\lambda_p, t) - A_{simu}(\lambda_p, t) \right)^2$$

Equation 2.7. Definition of the optimisation estimator for the Beer-Lambert fitting routine.

Also, to account for the fact that the simulated spectra for the 2-mers might potentially have incorrect amplitude, a constant factor κ can be implemented: $\mathcal{E}_2(\lambda) \longrightarrow \kappa \cdot \mathcal{E}_2(\lambda)$. This factor is kept constant over the course of an experiment. Note that for the sake of simplicity, the proportion of 2-mers in Transverse Electric (TE) and Transverse Magnetic TM) configurations are taken identical: $\mathcal{E}_2(\lambda) = \left(\mathcal{E}_{2,TE}(\lambda) + \mathcal{E}_{2,TM}(\lambda) \right) \times \kappa/2$.

A cut-off value for $\epsilon(t)$ can be proposed to stop the Beer-Lambert fit routine when the suggested spectra are too divergent from experimental results but presently, the quality of the fit is decided upon manual considerations.

2.2.3.2 SEM image analysis

A lengthy counting routine is performed manually on the SEM images taken. The number of *n*-mers for each class is recorded for each image. Using the table of records of each sample, the mean value (M_n) of each class of *n*-mers observed is calculated. The calculation of the normalised number of *n*-mers concentration (N_n) is described in Equation 2.8.

$$N_n(t) = {C_n(t)}\Big/{C_{nc}(t)} = M_n(t)\Big/\sum_{n=1}^{n_{\max}} n \cdot M_n(\mathrm{t})$$

Equation 2.8. Expression of concentration of *n*-mers as a function of counted particles on SEM images taken on random spots on samples surface.

One must underline the fact the accuracy of calculated concentration is subject to the maximum number, n, of *n*-mers taken into account. Choosing an unrealistic small value for n would introduce a bias in the statistics but a sufficiently large value ensures relevance of the concentration estimation. In practice, $n = 20$ is a typical value. It therefore sets the size of the family of concentrations.

Multiple samples may have been prepared for a certain time. In these cases, mean and standard deviation values can be estimated and for the sake of simplicity, we will also refer to them as (N_n) and (σ_n), respectively.

2.2.4 The rate-equation model

We propose a phenomenological model to simulate the formation of *n*-mers.[6]

2.2.4.1 System of rate-equations

We introduce the terminology of "cluster" or "species" or "entity" to name a certain type *n*-mers. We focus for instance on *n*-mers, their number within the cell is the figure N_n. Some *n*-mers can be formed as a result of the aggregation of lower order clusters, hence the term of generation, $G(N_n)$. Some can be consumed resulting of their own dissociation into sub-clusters, this is captured by the recombination term, $R(N_n)$.

Because the solution in the cell is stirred after aliquots of molecules, the concentration of *n*-mers can indeed be considered uniform across the cell. Hence, there is no diffusion originating from a gradient of concentration as described by Fick's law, however locally self diffusion (with D_n, the diffusivity constant) still exists due to the thermal energy carried by particles as described by the concept of random walk (as we shall discuss later in the text, see paragraph 2.4.3.1.1, p. 73).

The evolution of species population can thus be described by a general differential "budget" equation, see Equation 2.9.

$$\frac{\partial N_n}{\partial t} = \underbrace{G(N_n)}_{\text{generation}} - \underbrace{R(N_n)}_{\text{recombination}}$$

Equation 2.9. General rate equation describing the evolution of *n*-mers.

The solution of the above equation must be calculated for each time span for which the concentration of molecules is constant within the cell. In practice, the concentration of *n*-mers is given by $C_n(t) = C_{nc}(t) \times N_n(t)$ and it will exhibit discontinuities each time aliquots containing molecules are added.

Following the principle "nothing is lost, nothing is created, everything is transformed" stated by Lavoisier, the description of i-mers evolution shows the formation of a certain type of entity always is done at the expense of others or at least another entity type. The formation of *n*-mers or growth of clusters is the result of the aggregation of simpler form of *n*-mers. For instance, if we consider a pool where only monomers, 2-mers and 3-mers can exist, starting with a population of an ideal mono-dispersed solution of monomers, 2-mers can be readily formed with monomers while 3-mers may be formed by the association of three monomers or more likely using one monomer and one 2-mer, see Figure 2.3.

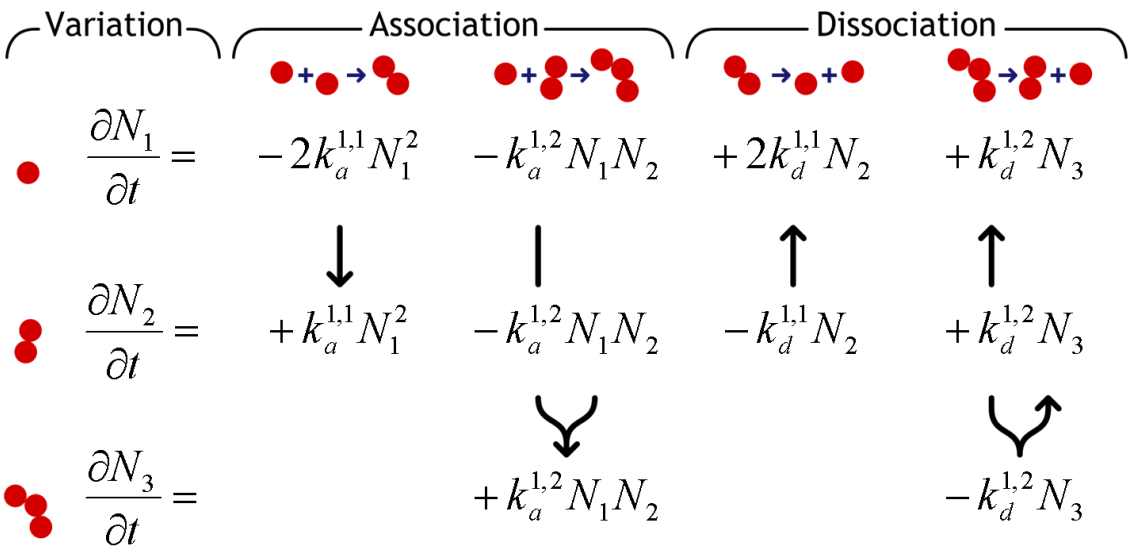

Figure 2.3. System of equations for a three species system: the conversion of 1-mers, 2-mers and 3-mers is put into equation.

In our case N_n are the numbers of *n*-mers, $k_a^{i,j}$ are the association rate constants involving *i*-mers and *j*-mers (about to form (*i*+*j*)-mers=*n*-mers). Likewise $k_d^{i,j}$ are the dissociation rate constants breaking a (*n*=*i*+*j*)-mers into *i*-mers and *j*-mers.

Accordingly variations of any *n*-mers are influenced by the balance between

i. gains by the aggregation of lower order *j*-mers or the dissociation of higher order *k*-mers and
ii. losses by aggregation of *i*-mer with other *n*-mers to form higher order structures, or the dissociation of *k*-mers.

We must point out that the writing of these coupled equations assumes from the start the maximum degree of complexity of possible *n*-mers in the pool. This can be seen as a shortcoming, but fortunately simulations show that working with ten different *n*-mers species is sufficient to match experimental data.

Also, although increasing the possible highest order *n*-mers should *prima facie* lead to an ever expanding possibility of interactions between different *n*-mers and so increasingly complex equations in a tree-like fashion, we can make the assumption that encounters involving more than two particles are relatively improbable. This removes all the $k_a^{i,j,\cdots}$ coefficients. Conversely $k_d^{i,j,\cdots}$ coefficients will be ignored as the process can be tailored in simpler dissociations involving merely two new clusters at a time. These assumptions were tested by performing simulations with three-species interactions and very little difference was observed.

Moreover, we consider that the capacity of association of any two clusters is not driven by their respective complexity, neither is the dissociation of a cluster toward specific sub-clusters. Accounting for all the effects and assumption discussed above, the developed equation of *n*-mers evolution can be derived, see Equation 2.10.

$$\frac{\partial N_n}{\partial t} = \sum_{\substack{i+j=n \\ 0<i\leq j}} \underbrace{k_a^{i,j} \cdot N_i N_j}_{(N_i,N_j)\rightarrow N_n} + \sum_{j>n}^{n_{\max}} \underbrace{\left(1+\delta_{j,2n}\right) k_d^{n,j-n} \cdot N_j}_{N_j \rightarrow (N_n, N_{j-n})} - \sum_{i=1}^{n_{\max}-n} \underbrace{\left(1+\delta_{n,i}\right) k_a^{n,i} \cdot N_n N_i}_{(N_n,N_i)\rightarrow N_{n+i}} - \sum_{\substack{i+j=n \\ 0<i\leq j}}^{n_{\max}} \underbrace{k_d^{i,j} \cdot N_n}_{N_n \rightarrow (N_i,N_j)}$$

Equation 2.10. Developed equation of formation/consumption of i-mers entities (where $\delta_{i,j}$ is the Kronecker symbol).

Along with the relation of continuity of number of nanocrystals in the pool $N_{total} = \sum_{n=1}^{\infty} n \cdot N_n$.

2.2.4.2 The role of rate coefficients

Within the framework of the phenomenological model proposed, both sets of coefficients $k_a^{i,j}$ and $k_d^{i,j}$ play the key role of governing the growth of clusters. As an analogy to Chemistry these coefficients will be called rate coefficients from now on. Let us consider the case of a certain *n*-mer (with $n = 12$, for instance), see Figure 2.4. It is the result of the association of two entities and conversely it can also dissociate back into two other entities. Figure 2.4a presents a naïve view of a *n*-mer represented as a linear chain with a possible decomposition into a *i*-mer and *j*-mer. The two types of rate constants can be gathered into two matrices that are by

construction symmetrical and contain undefined values since the pool of different species is limited to a finite value, $n_{\max}$, see Figure 2.4b-c.

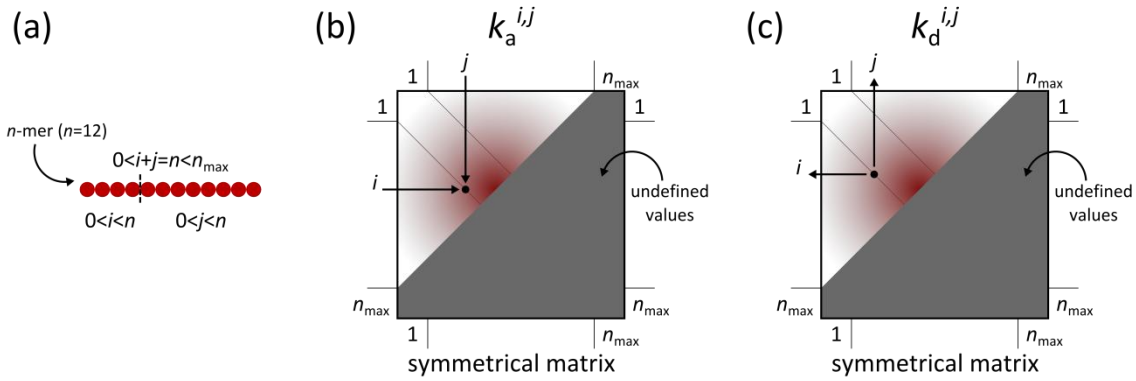

Figure 2.4. Association and dissociation rate coefficient matrices: (a) For instance, a 12-mers can be the result of the association of a 4-mers with a 8-mers or conversely a 12-mers can dissociate into a 4-mer and 8-mers. (b) and (c) respectively present the association and dissociation matrix of *i*-mers and *j*-mers converted into *(i+j)*-mers and reciprocally.

For simplicity, the superscripts i, j of the forward and reverse reactions may be dropped later in the text.

2.2.4.3 Four elementary steps

Although the description has been focusing on nanocrystals, a dispersal of nanocrystals is stable for months. Nevertheless, the controlled addition of linker molecules governs the progressive aggregation between nanocrystals. Hence, the model must include a description of the influence of molecules added in the system. We propose that linker molecules can bind to and ultimately cover the surface of nanocrystals.

In order to model the cluster growth shown experimentally, we postulate that the formation of clusters is driven by two basic mechanisms:

i. molecule adsorption/desorption onto/from a nanocrystal surface,
ii. the association/dissociation of molecule-bearing clusters.

This can be represented schematically using the chemical equation formalism, see Figure 2.5.

.

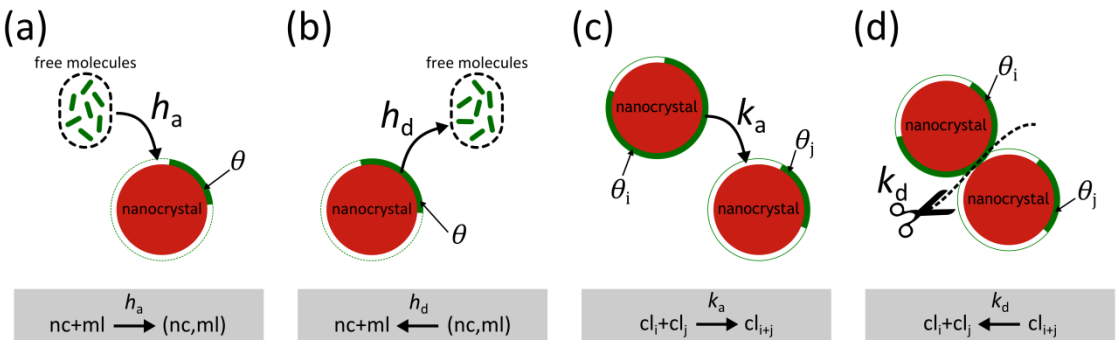

Figure 2.5. Schematic (not to scale) of the four elementary steps involved in the cluster growth: nanocrystals are represented by red discs and molecules by green dots, the thick green contour around nanocrystals highlights the fact some molecules are bond on the surface. This is quantified by the relative coverage, θ. (a) Adsorption of molecules on a nanocrystal surface, driven by the constant, h_a. (b) Desorption of molecules back to solution, driven by the constant, h_d. (c) Association of two clusters via linker molecules, driven by the coefficient k_a. (d) Dissociation of a cluster, driven by the coefficient k_d. In the chemical equations, nc, ml and cl stands for nanocrystal, molecule and cluster, respectively.

Whereas the system of coupled equations model the phenomenon depicted by Figure 2.5c-d, we will introduce the Langmuir isotherm equation describing the coverage of a surface by molecules as presented in Figure 2.5a-b.

2.2.4.4 Molecular decoration of the nanocrystal surface

We adopt the description of the Langmuir isotherm to model molecules binding on one nanocrystal surface. In itself, this formalism also is a rate-equation.

We assess the propensity of a molecule to adsorb is proportional to

i. the number, M, of available molecules at a given time,
ii. the free space on the nanocrystal surface defined as the difference between the maximum number, $m_{\max}$, of molecules and the number of molecules, m, already sitting on the surface normalised by $m_{\max}$,
iii. and finally the adsorption rate constant, h_a.

On the other hand the mechanism of molecule desorption is referred as the product of

i. the quotient of molecules sitting over $m_{\max}$
ii. and the desorption rate constant, h_d.

The expression of desorption is simpler because since molecular concentration is relatively low we consider the reservoir is prone to accept any molecule that would desorb from a nanocrystal surface.

The Langmuir isotherm equation is written to highlight the relative molecular coverage, $\theta = m/m_{\max}$, i.e.: the normalised number of molecules sitting on the surface.

$$\frac{\partial \theta}{\partial t} = (1 - \theta) \cdot M \cdot h_a - \theta \cdot h_d$$

Equation 2.11. Langmuir isotherm equation.

Whereas the number of free molecules, M, is implicitly assumed constant in the simplest form of the Langmuir isotherm, we implement a slightly more elaborate expression for M to account for the fact the reservoir of free molecules is not constant as molecules are adsorbing on nanocrystal surfaces: $M \longrightarrow R_{mol:nc} - \theta \cdot m_{\max}$. In this way, the number of free molecules available per nanocrystal may drop to 0 if $R_{mol:nc} < m_{\max}$.

A key parameter of the model for which we need to propose a reasonable value is the maximum number of linker-molecules that can bind a nanocrystal surface, $m_{\max}$. Two points of view were used for its estimation (using experimental data and geometrical reasoning).

One can first employ available data for typical molecular coverage on planar surfaces. For instance, it has been demonstrated that the limiting coverage of citrate molecules on planar gold substrate,[7] is $\sim 3 \times 10^{-10}$ mol.cm^{-2} which is equivalent to a molecular footprint of $1.8\ \mathrm{nm}^2$. However, the curvature of a plane is null by definition. One can reasonably expect a higher coverage of molecules on real nanocrystal surfaces based on a geometrical reasoning.[8]

We must also be careful to remember that the gold nanocrystals are stabilised by adsorbed citrate ions and the binding of linker-molecules will result in a sort of mixed self-assembled layer by either replacement of citrate ions or merely addition of the linker molecules. While thiol-based molecules have the possibility to displace contaminants,[9] there is currently no quantitative experimental argument in favour of any of these two case scenarios for the thiocyanate linker molecules in use for the formation of *n*-mers. Atomic-scale simulations by Dr. Micheal Nolan and Dr. Damien Thompson *et al.* (unpublished slab calculations data) seem to indicate citrate ions are likely to remain bound to the nanocrystal surfaces in presence of linker molecules: the hypothesis of displacement is therefore discarded. Moreover, the binding of –NCS groups on gold surfaces seems to be enhanced on non-(111) surfaces.

Using experimental values from X-ray crystallographic studies on similar linker molecules,[3] we estimate the maximum number of molecules to be approximately $m_{\max} \sim 250$ molecules attached on a single $20\ \mathrm{nm}$ diameter gold nanocrystal, see Table 2.1.

Nanocrystal diameter (nm)	**Surface area, πd^2 (nm^2)**	**Number of molecules (1.8 nm^2 footprint)**	**Number of molecules (5 nm^2 footprint)**	**Curvature (nm^{-1})**
10	314	175	63	0.200
20	1257	698	251	0.100
30	2827	1571	565	0.067

Table 2.1. Molecular footprint calculations on a planar surface.

2.2.4.5 Influence of the molecular decoration

Modelling of the formation of cluster growth implies four elementary rate coefficients: the duo (h_a, h_d) describing the molecular linker coverage of a nanocrystal surface and (k_a, k_d) the parameters related to cluster association/dissociation. Unlike (h_a, h_d) which are assumed to be simple constants (for a given molecular concentration within the cell) in the sense they do not depend on cluster formation, (k_a, k_d) are seen to be dependent on the molecular coverage, for instance nanocrystals need at least one molecule to allow association. As there is no direct experimental information of the cluster decoration we propose simple mechanism for the driving of cluster association and dissociation.

Although one molecule is sufficient for association, a few molecules are likely to be involved in the association. Assuming the coverage is homogeneous on the nanocrystal surfaces (no molecular layer island), we can imagine two situations accommodating the efficiency of sticking when two surfaces come in proximity: either (i) the more surfaces are decorated the better it is, or (ii) molecular layer interpenetration of molecular stacking impedes the sticking based on steric hindrance argument or because di-sulphide bonds are weak compared to sulphur-gold bonds. The two scenarios will be investigated, see Figure 2.6.

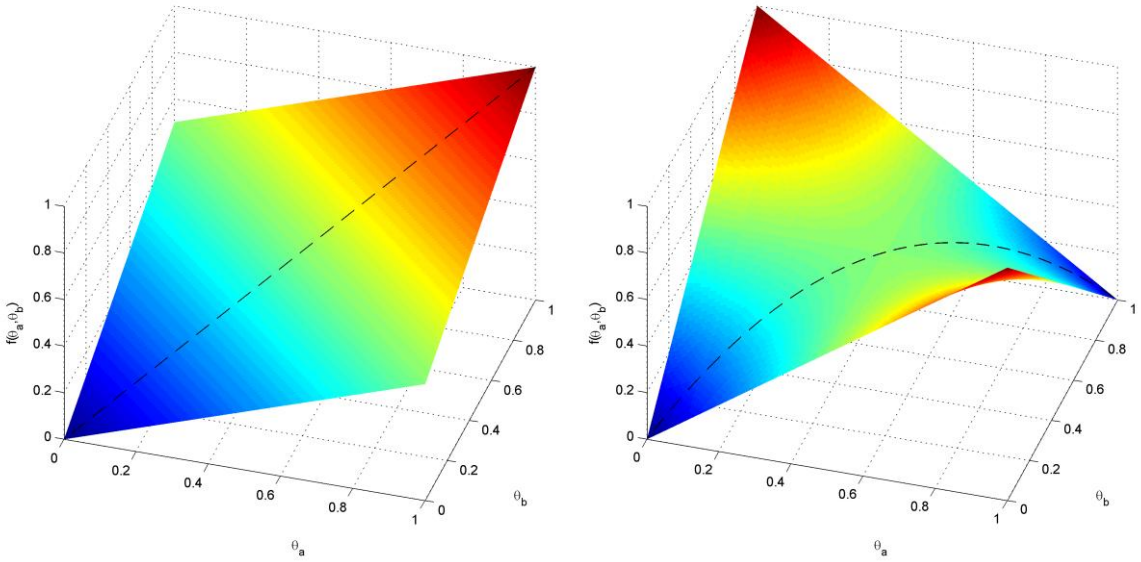

(a) $S = f(\theta_a, \theta_b) = (\theta_a + \theta_b)/2$ (b) $S = f(\theta_a, \theta_b) = \theta_a(1 - \theta_b) + \theta_b(1 - \theta_a)$

Figure 2.6. When two crystals are brought in contact, the propensity for them to adhere is dependent on their respective relative surface coverage as these surface plots indicate. (a) In this case scenario, the sticking propensity is simply proportional to each nanocrystal coverage, unlike in (b) where maximum adhesion probability occurs when one crystal is totally decorated while the other is bare, on the other hand intermediate situation is found when any of the two surfaces is half decorated. For both plots, the dashed line indicates the particular case of two identical surface coverage as is used in the rate equation model.

As we consider that the more molecules involved in the junction between two nanocrystals the stronger the structure is, we suggest the dissociation is related to the lack of molecular coverage via the steric factor $S = (1 - \theta)$. This latter expression is arguably simple. The dissociation of two nanocrystals implies merely that the contact area has to be totally free of molecules.

In summary, in place of simple rate constants, we must redefine these coefficients to include the contribution of molecular coverage. Indeed the association constants become $k_a \longrightarrow k_a \times f(\theta)$, and conversely, the dissociation constants: $k_d \longrightarrow k_d \times (1 - \theta)$.

2.3 Results

We first present the design of experiments to recapitulate the key characteristics of the joint process and characterisation flow, see Figure 2.7.

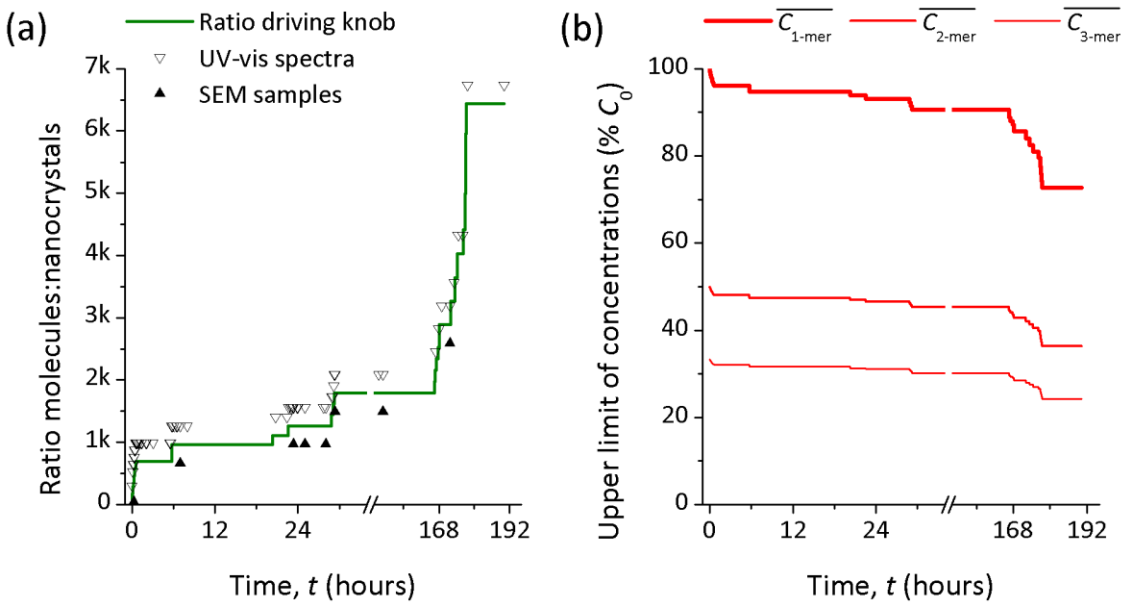

Figure 2.7. Design of experiment: a, the driving knob of the experiments: the molecule:nanocrystal ratio is plotted, open triangles show the times at which UV-vis absorption spectra were taken, filled triangles are for SEM samples; b, due to the addition of aliquots of linker molecules, nanostructures are diluted, the upper limit of concentrations are presented for 1-mers, 2-mers and 3-mers entities.

A significant number of UV-vis absorption spectra were taken, in real time, at key time points for monitoring changes in the optical response of the cell during the process. In parallel, fewer drop-cast samples were also prepared and subsequently imaged by SEM, see Figure 2.7a (a UV-vis spectrum was taken for each SEM sample). These two separate samplings are the experimental datasets on which the rate-equation model is applied to after data pre-processing: Beer-Lambert law curve fitting for spectra, counting statistics for SEM images.

As aliquots of solution containing linker molecules added in the cell, the nanostructures are being diluted. Figure 2.7b shows the upper bound limit of concentrations (in percentage of $C_0 = C_{nc}(0)$) for 1-mers, 2-mers and 3-mers. It can readily be seen dilution is not a negligible aspect of the process: after 30 hours, the concentrations of nanocrystals (regardless of the nanostructures they may be in) has decreased to 90%, while at the end of the experiment it is just above 72%. Upper bound concentrations of 2-mers and 3-mers are merely calculated based on the assumption of a perfect conversion of all nanocrystals into 2-mer or 3-mer nanostructures respectively: $\overline{C_{n-mers}} = C_{nc}/n$.

2.3.1 Pre-processing of input data

2.3.1.1 Beer-Lambert law

All acquired spectra are processed using the Beer-Lambert's law. We present in particular the results of the series of curve fitting for the first three time points for which SEM samples were prepared, see Figure 2.8.

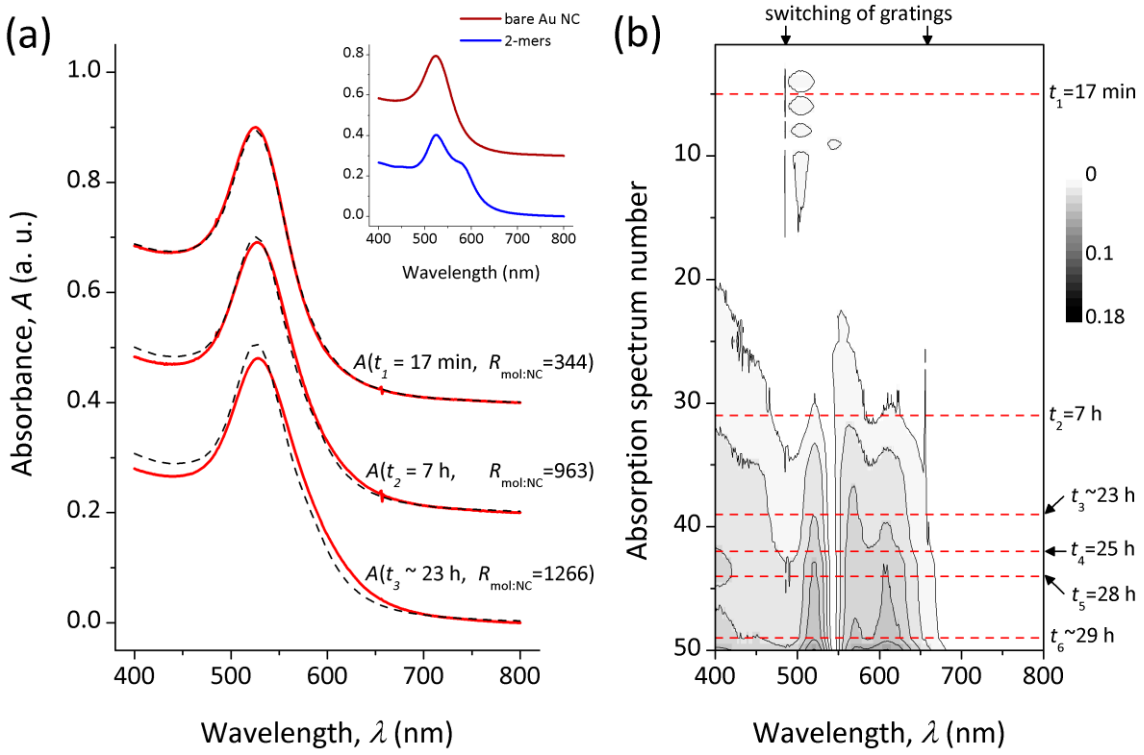

Figure 2.8. UV-visible absorption spectra curve fitting based on Beer-Lambert law. (a) three experimental spectra are presented along with the best fitting curve based on the absorbance of bare Au nanocrystal and simulated 2-mers optical response. (b) Map of the difference between experimental and simulated spectra for all spectra acquired: the shade of grey darkens with the discrepancy in the fitting results (the vertical trails mark the switching of gratings).

The first spectrum presented, $A(t_1)$, was taken 17 min after the process of *n*-mers formation was initiated. The reconstructed curve overlaps the experimental spectrum well. The fit for the second spectrum presented, $A(t_2)$ (after 7 h), also agrees well with the experimental data. However, for the next time for which a SEM sample was prepared (after 23 h 20 min), a discrepancy between experiments and simulations is noticeable, see Figure 2.8a. We attribute the increasing difference between experimental data and best fit curve as a signature that higher order nanostructures (more complex than just 1-mers and 2-mers) are present in the solution and therefore contribute to the optical response via their own absorbance and concentration.

To investigate the fitting accuracy, we plot the map of difference between experimental and simulated absorption spectra for the entire series of acquired spectra. The vertical trails seen for $\lambda = 486\,\mathrm{nm}$ and $\lambda = 658\,\mathrm{nm}$ are measurement artefacts due glitches in the switching of diffraction gratings in the measurement setup, see Figure 2.8b.

The number of the absorption spectrum acquired is related to the advance of the *n*-mer formation. As time goes by, the discrepancy between experimental and simulated spectra increases in a certain spectral range. From this map, the results of the spectrum curve fitting can be deemed valid up until ~8 h (spectrum number 32). Afterwards, the error is too large and the extraction of 1-mer and 2-mer concentration values cannot be trusted.

The processing of the optical dataset is thus a short time scale method to extract the populations of 1-mers and 2-mers, in the approximation they are the two species mainly contributing to the absorption properties of the solution.

2.3.1.2 SEM counting statistics

Images taken at random locations on the different SEM samples are analysed manually in order to count the number of different nanostructures on the surface of the sample. This method is supposed to give insights in the population of *n*-mers in solution, without bias as prior to drop casting of the solution on conductive samples, the solution is further diluted x10-100 times in order to prevent aggregation of nanostructures on the surface during drying and thus false counting.

We present the results of counting statistics for 1-mers to 6-mers from t_1 to t_6. The figures are normalised concentrations (or numbers), C_n, in percentage of the overall nanocrystal concentration within the cell at the time of sample preparation, C_{nc}(t), see Figure 2.9.

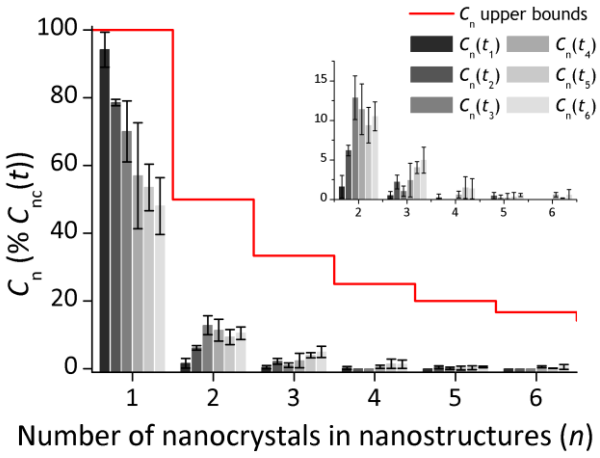

Figure 2.9. Extraction of population data from SEM samples for times up to ~30 hours.

As a guide to the eye, the upper bound limit for each species type is indicated in red. It can readily be seen there is no type of nanostructures that tops the theoretical limit. 1-mers to 6-mers and beyond occupy a certain fraction of the overall nanocrystal concentration.

Compared to the Beer-Lambert law fit, the analysis of SEM samples images offer the possibility of estimation of a broader range of entities that may be formed. Nanostructures comprising up to ~20 nanocrystals can be counted for high accuracy (when more numerous, some nanocrystals may be hidden by others as organised in three dimensional structures). Both datasets will be analysed using the rate-equation model.

2.3.2 Modelling of *n*-mers formation

The system of rate-equations presented is of first order but non linear. When limited to merely two entities: 1-mers and 2-mers and excluding a dependency of the forward and reverse rate coefficients of cluster formation on the nanocrystals surface coverage by molecules, an analytical solution can be found (Appendix 6.3).

In practice however, more nanostructures types are likely to interact. Also, the addition of molecules by careful inclusion of aliquots within the cell is seen to play a significant role in the formation of *n*-mers nanostructures. As a matter of fact the dependency on coverage must be taken into account and so must be the dilution of the overall solution. We propose to account for this by consistently including the factor of overall change in concentration, $\Delta^* C(t) = C_{nc}(t)/C_0$, in the rate coefficients definition: $k_a^{p,q} \longrightarrow k_a^{p,q} \times (\Delta^* C)^2$ and $k_d^{p,q} \longrightarrow k_d^{p,q} \times (\Delta^* C)$.

2.3.2.1 Case scenarios

As a typical value for the maximum number of molecules that can bind on a nanocrystal surface was chosen, $m_{max} = 250$, a total of four different parameters governing the evolution of *n*-mers population remains: (h_a, h_d, k_a, k_d). This handful of parameters results in a high flexibility of the model for outputting different populations evolution situations. Three case scenarios of interest are presented in Figure 2.10.

In scenario A, the evolution of each entity type is subtle. After 24 h, the conversion of 1-mers into more complex species is still carrying on but represents only 7% of all nanocrystals. Moreover, looking at the 2-mers and 3-mers species, one can notice a cross-over in the population fraction already occurred. In this situation, over the course of 24 h, more 3-mers than 2-mers are formed.

In scenario B, the evolution of *n*-mers populations is more abrupt. The formation of *n*-mers clearly follows the law of molecule:nanocrystal ratio resulting from addition of aliquots of linker

molecules in the cell. Populations of *n*-mers rapidly reach a steady-state until the ratio is changed again. It seems this is favouring the conversion of 1-mers into more complex entities as the concentration of 1-mers keeps dropping, however, the concentration of 2-mers is about to saturate whereas more 3-mers are being slowly formed.

In scenario C, the conversion of 1-mers can be deemed complete after 6 hours in favour of more complex *n*-mers species. The concentration of 1-mers drops sharply within the first ~1 h, while the population of 2-mers reaches a maximum after ~50 min before slowly decaying. In a similar fashion, the population of 3-mers saturates after ~85 min and vanishes. More complex species such as 5-mers and beyond take over later on at ~11 h (not shown for clarity in Figure 2.10). In this type of case scenario, a larger than simply 10-species-limited pool may be needed for accuracy in the *n*-mers population description as the conversion to high order *n*-mers may artificially be stopped to the most complex species allowed in the system of rate equations (presently 10-mers).

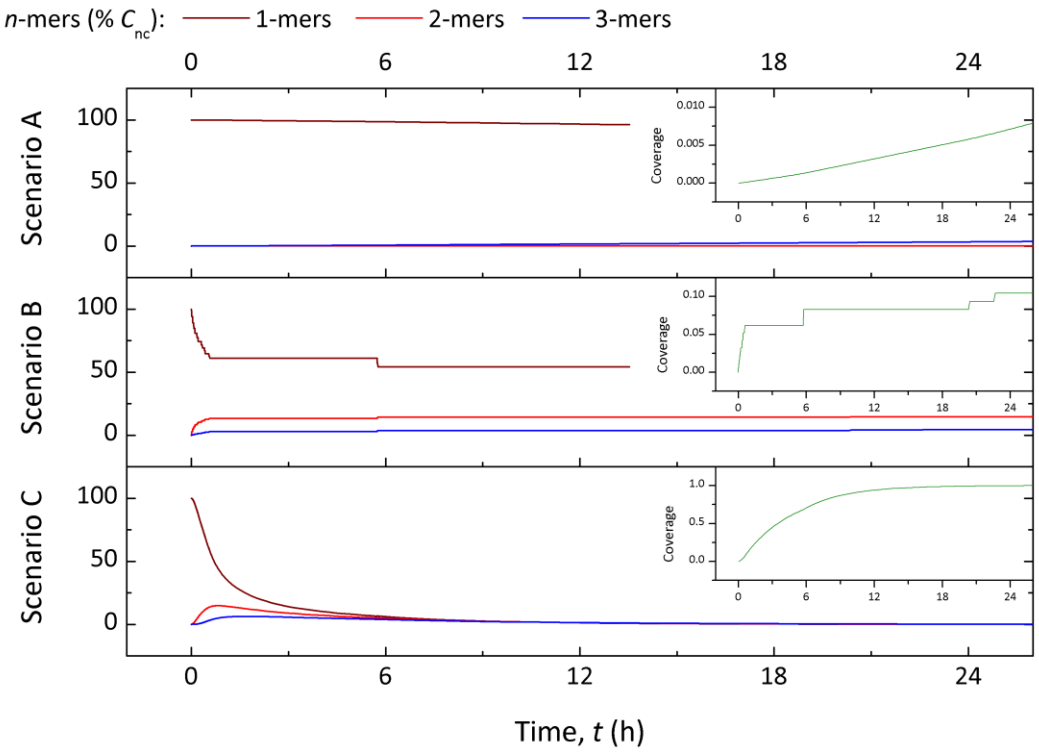

Figure 2.10. Cases scenarios of the evolution of *n*-mers population: 1-mers, 2-mers and 3-mers concentrations are presented along with the molecular coverage in each case (using the experimental law of molecule:nanocrystal ratio and overall solution dilution, a limited pool of 10 different *n*-mers species is implemented).

In Figure 2.10, the inset included for each scenario shows the molecular coverage of nanocrystals surface. While in scenario A, the coverage is very limited: $\theta < 0.01$, it is ten times higher in scenario B and follows the evolution of the molecules:nanocrystal ratio. For scenario C,

nanocrystals are supposedly entirely decorated with molecules: any further molecular addition in the cell will only dilute the overall solution containing the poly-dispersal of *n*-mers.

2.3.2.2 Coupled effects

The consistency of the model is further tested in limit situations. As expected, if the rate of molecular adsorption is set to $h_a = 0$ (regardless of all other parameter values), the process of *n*-mers formation does not trigger. Conversely if one sets the rate of cluster association to $k_a = 0$, although the nanocrystal surfaces may become decorated (depending on the values of the couple (h_a, h_d)), there is no formation of clusters of any kind. In the former two limit situations, the conversion of 1-mers into *n*-mers is purely switched off.

By construction of the rate-equation model, the formation is *n*-mers is coupled to both molecular decoration and cluster association. We investigate the influence of the four parameters (h_a, h_d, k_a, k_d) using the experimental conditions of molecules:nanocrystal changing ratio, see Figure 2.11.

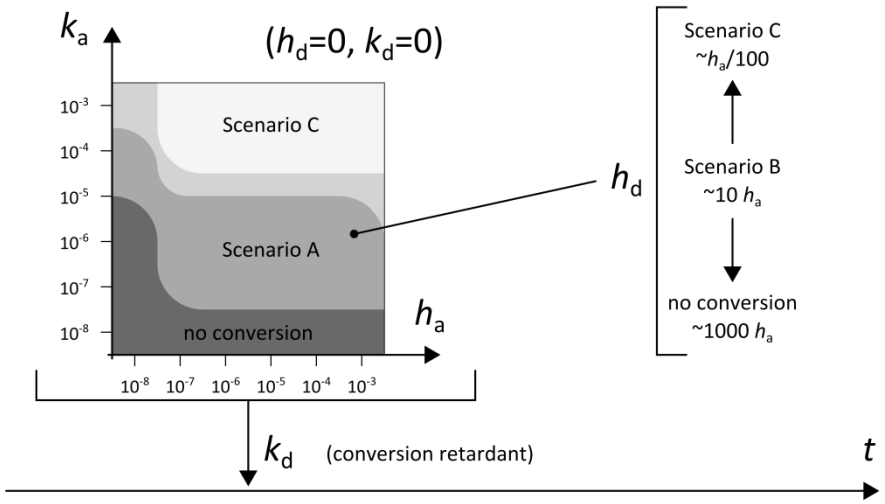

Figure 2.11. Schematic of the parameter influence on the *n*-mer population evolution (the experimental conditions of molecule:nanocrystal changing ratio are used). Parameters k_a and h_a appear to have the strongest influence on the type of conversion scenario as shown in the two dimensional map estimated for $h_d = 0 = k_d$. Modifying the value of $h_d$compared to $h_a$also alter the type of *n*-mer conversion scenario. Finally, the higher the value of k_d, the the later the onset of the conversion will take place.

We first set both reverse rate coefficients to zero ($h_d = 0 = k_d$) to investigate the influence of forward rate coefficients. The two dimensional matrix of values explored show three regimes are accessible. For very low values of both coefficients virtually no conversion occurs as the decoration of the nanocrystals surface is too low and because the association of clusters is too

unlikely. For higher values of h_a and k_a, scenarios A and C can happen. It also appears k_a has the strongest influence on the efficiency of 1-mers conversion into *n*-mers.

Regardless of the couple (h_a, k_a) considered, the value of the rate coefficient for cluster dissociation is found to be a conversion retardant in the sense it only delays the time at which higher order *n*-mers are being formed but does not change the conversion regime.

However, the rate coefficient governing molecular desorption from nanocrystals surfaces is found to have a strong influence on the regime otherwise observed. Using h_a as a reference, if the value of h_d is too high, the conversion of 1-mers into *n*-mers is cancelled. Interestingly for $h_d \sim 10h_a$, the scenario B emerges. Finally, when this reverse constant is brought further down below the value of the forward reaction of molecular adsorption, scenario C takes place. Depending on the value of (h_a, k_a), the scenario A may also finally occur.

2.3.2.3 Experimental data fitting

Datasets of both origins are analysed using the rate equation model. We must underline, estimations of *n*-mer populations are different: the transform of the UV-visible dataset tend to overestimate the population of 1-mers (and conversely underestimate 2-mers) compared to the SEM counting statistics.

The estimation of *n*-mers populations from UV-visible absorption spectra data is limited to 1-mers and 2-mers. For this dataset, we implement a version of the system of rate-equations comprising only two possible entity types. Nanostructure counting statistics from SEM images shows higher order *n*-mers exist. Based on the complexity of *n*-mers observed, we choose to expand the system of rate-equations to a pool of 10 types of *n*-mers (1-mers, 2-mers, …, 10-mers). In this particular case, instead of calculating the fitting optimisation estimator on the entire range of *n*-mers in the pool, it will be merely based on *n*-mers made of 4 nanocrystals at the highest as the counts of higher order *n*-mers are too small and would therefore introduce a bias.

The fit on *n*-mers populations estimated from UV-visible spectra is conducted for a time span of $t \leq 8\ \mathrm{h}$ (as afore discussed), the data fitting of SEM statistics data presented is performed for a longer time window: $t \leq 30\ \mathrm{h}$ (subset of the entire experiment duration), see Figure 2.12.

In Figure 2.12a, we focus on a time span of 8 h to essentially show points related to the UV-visible dataset. Two separate fittings are conducted: for time $t \leq 8\ \mathrm{h}$ where the *n*-mers populations estimation is appropriate (further absorption spectra built upon the mere contributions of 1-mers and 2-mers deviate too much from experimental spectra). For this time

span, the population data points seem consistent and are relatively well matched by the rate-equation model.

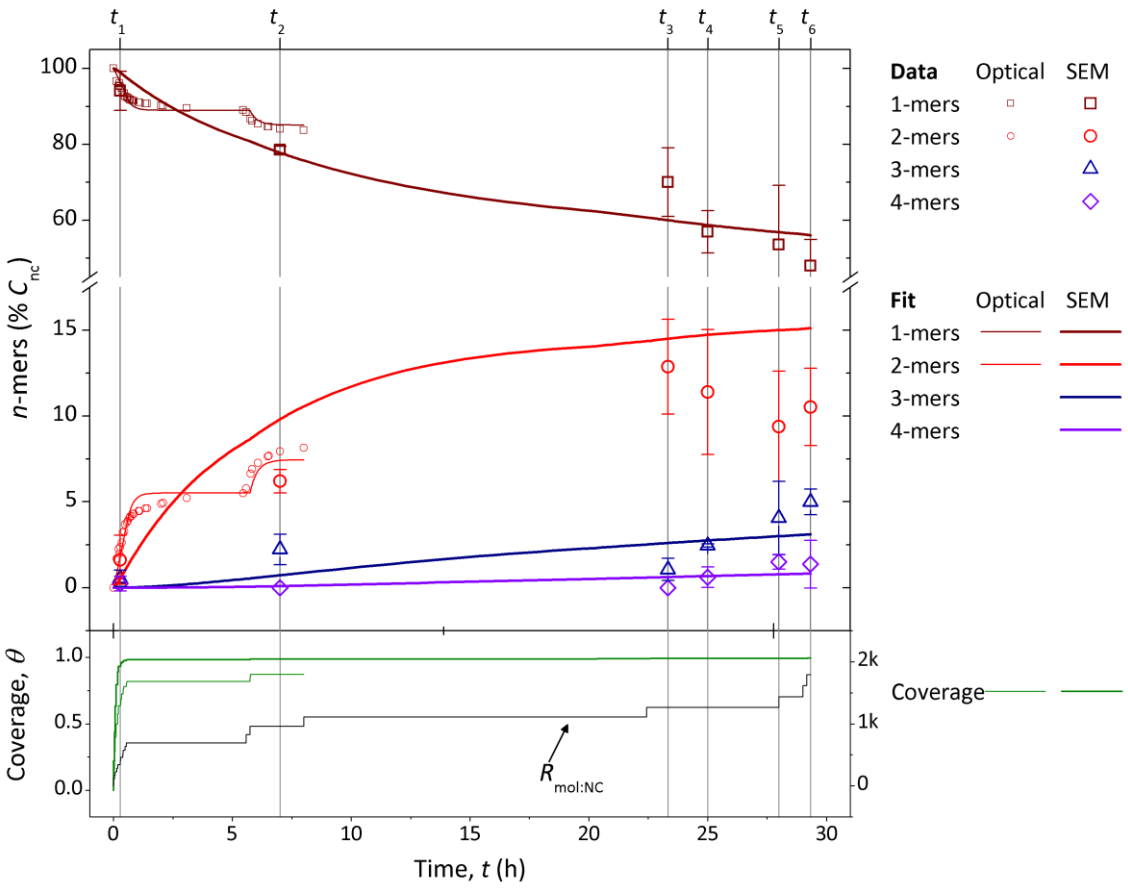

Figure 2.12. Experimental data fitting employing the rate-equation model (smallest symbols are taken from the transform of the UV-visible dataset, largest symbols originate from the SEM counting statistics) the maximum number of bound linker molecules is set to 250. (a) For the first few hours, a scenario of type B seems to be the best match for points from the UV-visible dataset. (b) For longer time scales, the SEM statistics data set has fewer points so that convergence of the fit is more difficult to achieve, a scenario of type A is found best for matching experimental data.

For longer times, the dataset from SEM statistics is used, see Figure 2.12b. For clarity, only nanostructures comprising 4 nanocrystals at maximum are presented. As opposed to the UV-visible dataset, the curves representing the evolution of *n*-mers population seem to indicate a scenario of type A is more suitable for characterising the evolution of *n*-mers population over time. However, one must acknowledge formation of *n*-mers following a scenario of type B cannot entirely be ruled out. More experimental data points are needed.

Regardless of the datasets, the pace of decoration of the nanocrystal surface with linker molecules is rapid. Within the first few minutes, more than 50% of the surface is covered.

The system of rate-equations offers great flexibility for dataset fitting. In order to obtain better curve fitting, we explore the possibility of relaxing the constraint on the maximum number of linker molecules that can bind on the nanocrystals ($m_{\max}$), see Table 2.2.

Dataset	h_a $(\mu m^3 s^{-1})$	h_d (s^{-1})	k_a $(\mu m^3 s^{-1})$	k_d (s^{-1})		$m_{\max}$	χ^2	R^2	Scenario
Optical (8 h)	4.2×10^{-4}	4.3×10^{-2}	8.8×10^{-5}	5.5×10^{-3}	*	250	0.006	0.901	B
Optical (8 h)	5.1×10^{-2}	4.3×10^{-2}	1.1×10^{-3}	1.2×10^{-2}		1,680	0.003	0.942	B
SEM (30 h)	6.7×10^{-3}	5.2×10^{-2}	8.1×10^{-6}	1.4×10^{-3}	*	250	0.029	0.847	A
SEM (30 h)	2.3×10^{-3}	3.1×10^{-4}	6.2×10^{-5}	8.7×10^{-4}		1,436	0.013	0.926	B

Table 2.2. Summary of the rate-equation parameters, the * denotes the constraint on the maximum number of molecules that can bind onto the surface of a nanocrystal.

When constraints on fitting parameters are all relaxed, the number $m_{\max}$ is largely increased to values greater than physically realistic (even if the surface of nanocrystals was bare). On the other hand, a scenario of type B is found optimal for both datasets.

2.4 Discussion

We attempt to interpret the output values of the rate-equation model by extraction of parameter properties.

2.4.1 Beer-Lambert curve fitting

Extraction of *n*-mers populations from UV-visible absorption spectra reveals to be challenging for two reasons.

First of all, the lack of ability to reliably model the optical response of pure high order *n*-mers species ($n > 2$) in solution is the main drawback. If the extinction coefficients of these *n*-mers could be simulated including contribution of different three dimensional conformations and accordingly interactions with light-polarisation, more realistic spectra could be built even at longer time scales offering the possibility to monitor and model in real time the evolution of *n*-mer populations.

Secondly, the peak shift readily observed after the few first molecular linker aliquots added in the cell cannot be attributed to the presence of acetone in solution (demonstrated experimentally in control experiments). It seems to be an indication that in place of a change in the permittivity of the overall solution medium, the peak shift must be due to a change occurring at the nanocrystals surface (thus modifying their plasmon resonance frequency). This local medium surface change must be the signature of a very fast influence of molecules in the nanocrystal surface vicinity. One can suppose molecules could indeed be binding quickly on these surfaces. In this case, the change in peak position (at the start of *n*-mer formation) should be related to the nanocrystal surface coverage and thus could be modelled via the Langmuir isotherm equation. Finer observations of this effect could also be consistently correlated with the rate coefficients of molecular decoration in the rate-equation model.

2.4.2 Rate-equation model

In Chemistry, the equilibrium reaction between two reactants forming one product is fully characterised with two rate constants. On one hand, the rate of the forward reaction, $\overline{\overline{k_a}}$, is in units of $\mu m^3 s^{-1}$, it describes the association/aggregation reaction in our case. On the other hand, the rate of the reverse reaction, $\overline{\overline{k_d}}$, is in units of s^{-1}, it accounts for the desorption/dissociation reaction.

In order to form a product, the reactants need to come into contact. This is formalised by the collision theory. The reverse reaction does not rely on a collision event, hence the difference of units between the two constants.

2.4.2.1 Limit case at equilibrium

Before going further into the effective values of $(\overline{\overline{k_a}}, \overline{\overline{k_d}})$ we must point out the fact their ratio has an interesting physical meaning. Looking at the equations for monomers, 2-mers and 3-mers, one can see that $\overline{\overline{k_a}}/\overline{\overline{k_d}}$ will tend to drive the overall populations towards more or less complexity. Provided that $\overline{\overline{k_a}}/\overline{\overline{k_d}} > 1/c_0$, formation of higher order *n*-mers would be favorable and the pool would eventually contain "infinitely" complex clusters. On the other hand if $\overline{\overline{k_a}}/\overline{\overline{k_d}} \leq 1/c_0$, complex *n*-mers formation would not be favoured unless, there is a large imbalance of monomers as it is typically the case experimentally since we initially work with a solution of citrate-stabilised nanocrystals.

2.4.2.2 Structure of rate coefficients

According to Chemistry, rate constants can be split into three main components: the attempt frequency, Z, the likelihood of the reaction due to potential steric hindrance, S, and the exponential factor due to the energy barrier to be overcome, W, see Equation 2.12.

$$k = \underbrace{Z}_{\substack{attempt \\ frequency}} \times \underbrace{S}_{\substack{steric \\ hindrance}} \times \underbrace{W}_{\substack{energy \\ barrier}}$$

Equation 2.12. Rate constant structural decomposition.

It is of interest to determine what the limiting process in a reaction is. Two situations can arise: reactant transport is limiting and/or the energy barrier the reactants must overcome is limiting. Both rate constants capture indeed much information such as the decoration of the particles surface, possible competitive surface effect on the area of contact between nanocrystals and also physical transport properties for the lone association rate constants, $\overline{\overline{k_a}}$.

Originally, the concept of attempt frequency is related to a molecular vibration. Nevertheless, for the forward reaction, it will rather capture the transport properties resulting in particle collision. Hence the problem engages multi-scale physics considerations.

Moreover looking at the collection of SEM images, it appears clusters are not necessarily linear-chain structures but usually adopt more compact configurations. This should be captured by rate coefficients with indices (i, j), see Figure 2.4.

For instance assuming a compact configuration, qualitative considerations of steric hindrance will indicate the likelihood of association should decrease as both p and q gets bigger. Conversely, the possibility of dissociation of a cluster into similar cluster sizes should be the least probable as opposed to only one nanocrystal desorbing. However, since there is no direct experimental

information on this particular aspect and for the sake of the model simplicity, we do not alter separately the value of rate coefficients on this basis.

2.4.3 Driver of *n*-mers formation

As we have already seen cluster formation is the result of two coupled phenomena: adsorption of molecular linkers on nanocrystals surfaces and then aggregation of decorated nanocrystals. On the other hand, the possible dissociation of nanocrystal(s) from clusters is assumed to result from a collective desorption of molecules potentially driven by their internal reorganisation.

In the following, we explore particle transport and the activation energy associated with each elementary step.

2.4.3.1 Particle transport and encounters

Within the cell, the situation we are dealing with involves at the beginning merely two types of entities: single nanocrystals and free molecules. During the process of *n*-mers formation, potentially many kinds of particle species appear: 1-mers, 2-mers, …, *n*-mers. Diffusion compared to convection is slow and so the stirring of the solution totally changes the mass transport properties. For simplicity, we propose the stirring is so efficient it makes the distribution of the different entities uniform – on average – at all time. Despite the stirring, molecules and *n*-mers are still moving around randomly. We suggest the motion can still be described by the Brownian approach.

To get insight in the properties of diffusive encounters, we propose to consider only two particles A and B spaced by a certain distance, r. They have a radius R_A and R_B and diffuse into space with a diffusion coefficient D_A and D_B, respectively. After a certain time, because of their Brownian motion, they can be, on average, anywhere on a perimeters of radius r_A and r_B, see Figure 2.13, such that $r = r_A + r_B$.

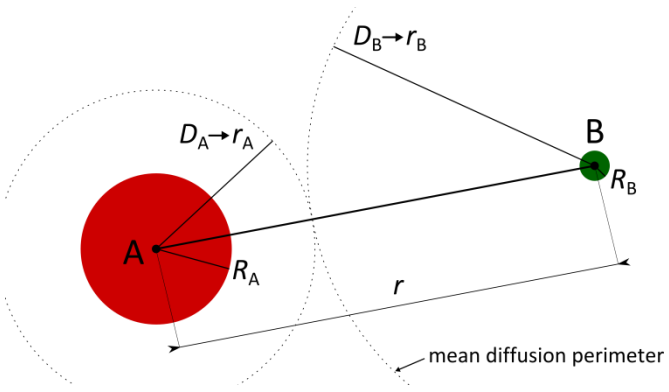

Figure 2.13. Brownian motion between two particles.

According to the description of random walk,[10] the minimum mean time for collision would be given by $r = \sqrt{6t} \times \left(\sqrt{D_A} + \sqrt{D_B}\right)$ or equivalently Equation 2.13.

$$t_{encounter} = \frac{r^2}{6\left(\sqrt{D_A} + \sqrt{D_B}\right)^2} = \kappa_t \times r^2$$

Equation 2.13. Average time for the encounter between two diffusive particles.

But because of the diffusive transport, the particles may well meet somewhere else: not along the axis but on coronae around the axis with a gradual decreasing probability. With such expression, we would still have to integrate over the distribution of distances between particles to get estimates of time, probability and efficiency of encounter.[11]

In place of an analytical solution, we rely on random-walk simulations to estimate the rate of encounter.

2.4.3.1.1 Random-walk model

The concept of random-walk is widely used to model Brownian motion.[10] Random-walk simulations are commonly used for mimicking Fick's diffusion phenomenon, by confining then releasing particles. More generally, it encompasses diffusive physical transport of particles. The stochastic trajectories of three different particles are plotted at different times, see Figure 2.14.

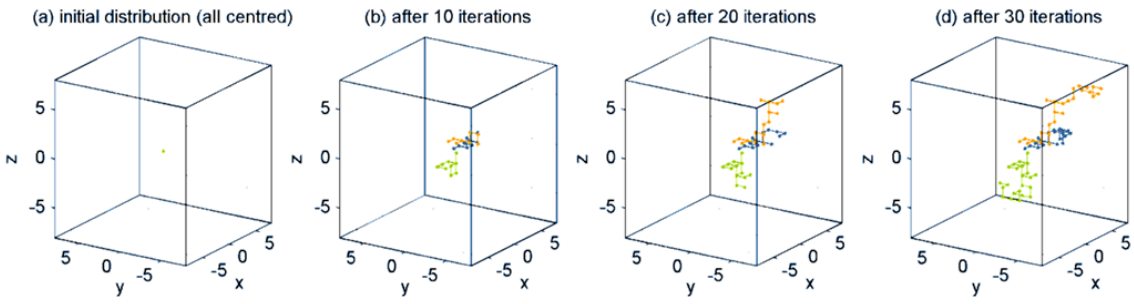

Figure 2.14. Random walk is a practical tool to model diffusion phenomenon.

To model particle displacements, we implement a random walk approach [10] allowing particles to move in three dimensions hopping on nodes of a discrete mesh. Strictly speaking stochastic displacement can occur to any point around the original one. We merely restrain the available positions to a discrete mesh for more simplicity so that at any time a particle can hop on a node close-by as follow: either $\pm x$ or $\pm y$ or $\pm z$. There are thus six different possibilities.

Theoretically, a three dimensional random walk implementation is characterized by the equation $\langle r^2 \rangle = 6D \times t$ showing that the average square of the displacement, $\langle r^2 \rangle$, is a linear function of time, t. In other words, the root mean square particle displacement, $\sqrt{\langle r^2 \rangle}$, evolves

with the square root of time unlike motion with a constant speed, for instance. The proportionality factor is the product of the diffusivity, D, with 6: the number of new positions available at any time, see Figure 2.15.

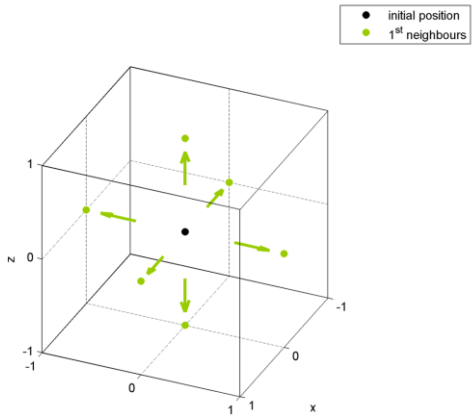

Figure 2.15. Schematic of the different positions available in the case of a three dimensional discrete random-walk.

Typically, one defines the mesh constant, $\ell = \sqrt{\langle r^2 \rangle}$, as so that at each hop, a particle moves from a node to another with a time scale of $\tau \sim \ell^2/6D$. Moreover as we model particles diffusing in a pot and their distribution is overall uniform, we consider a mesh with a certain extension. Cyclic boundary conditions are then implemented so that when a particle is about to reach the limit of the mesh, it comes back at the opposite edge. All in all, the number of particles studied is kept constant: the net flux at the boundaries is null.

2.4.3.1.2 Diffusion coefficients

We consider the classic Stokes-Einstein relation to get an initial value for the translational diffusivity of $20\ \mathrm{nm}$ diameter gold nanocrystals immersed in an aqueous solution, D_{nc}, see Equation 2.14. It is proportional to the thermal energy ($k_B T$), inversely proportional to both the dynamic viscosity of the medium (η), in our case water, and the hydrodynamic diameter of the diffusing nanocrystal (δ_{nc}), taken as the nanocrystal diameter of 20 nm. Two extreme situations can be described to model the interaction between a particle and the medium in which it is flowing:[12] either (i) the particle is ideally slipping, $\gamma = 2$, or (ii) it is sticking to the medium, $\gamma = 3$.

$$D_{nc} = \frac{k_B T}{\gamma \pi \eta \delta_{nc}}$$

Equation 2.14. Stokes-Einstein diffusion coefficient.

We will consider sticking conditions ($\gamma = 3$) for the calculation of diffusivity of 20 nm nanocrystals in water, giving $D_{nc} \sim 25\ \mu\mathrm{m}^2\mathrm{s}^{-1}$ at room temperature. On the other hand several

techniques have been investigated to determine experimentally the value of diffusivity for different particle sizes in different media. Results indicate that measured diffusivities for nanoparticles in the range of 80 to 250 nm in diameter (Xu *et al.*[13]) as well as down to 2 nm crystals (Wuelfing *et al.*[14]) are nicely fitted by the Stokes-Einstein equation, see Figure 2.16. Thus the computed value seems physically realistic.

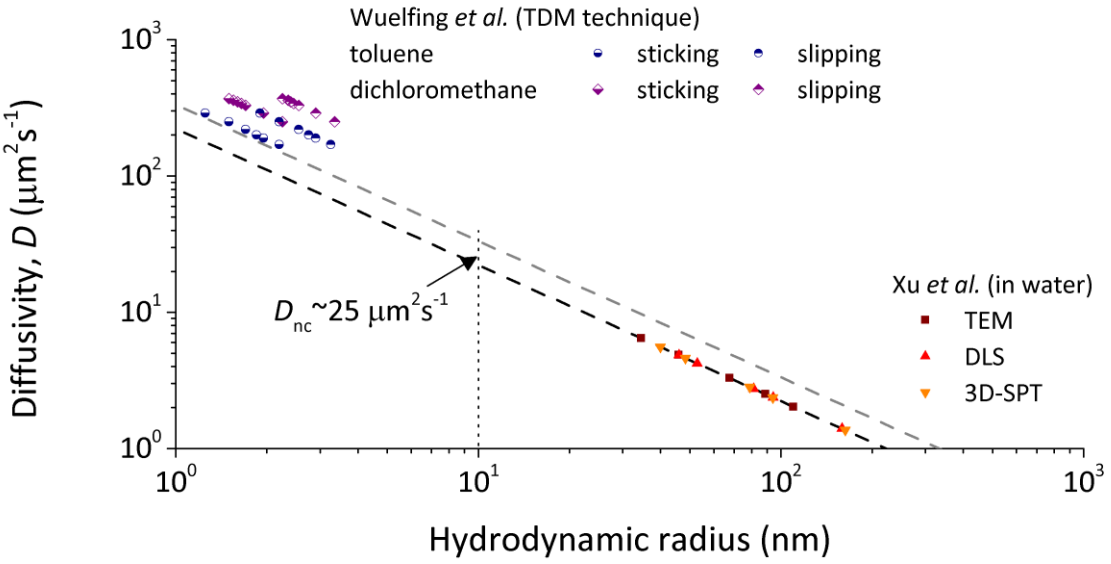

Figure 2.16. Overview of diffusivity measurements against nanocrystal hydrodynamic radius. The experimental value of Wuelfing *et al.* are slightly offset because the solvent in use is different from water whereas theoretical calculations were conducted using values for the water solvent.

Although at start clusters are simple single nanocrystals, ideally we need to know what the diffusivity is for any of the *n*-mers involved. Likewise it is relevant to look for estimates of cross-sections for new cluster species appearing in the pool.

Reusing High-Resolution Scanning Electron Microscope images initially obtained for cluster population counting statistics, cluster spatial configurations are investigated. We can first approximate a dimer as a rugby-ball-like ellipsoid and work out the effective diffusivity coefficient provided that (a, b) are the long and short axis lengths, respectively,[15-16] Equation 2.15.

$$D_{ellipsoid} = \frac{k_B T}{\gamma \pi \eta} \times \frac{\ln(2a/b)}{a}$$

Equation 2.15. Diffusion coefficient of an ellipsoid.

On the other hand, Hoffmann *et al.*[17] presented a study of cluster diffusivities using both depolarised dynamic light scattering and hydrodymanic models to calculate both rotational and translational diffusivities for clusters made of up four particles.

Nevertheless, it is however interesting to propose a simpler trend law employing geometric arguments based on *n*-mer shapes observed. We now consider *n*-mers as having a ball-shape whose radius is a function of the number of nanocrystals, see Figure 2.17a. Luckily diffusion coefficients of the form $D_n = D_1/\sqrt{n}$ (with D_n the diffusivity of an *n*-mer) are very close to those given by the ellipsoid approach, see Figure 2.17b. Even though these approximations may look a bit crude, it provides estimates that are still better than the zero-order approximation of a cluster as a single nanocrystal.

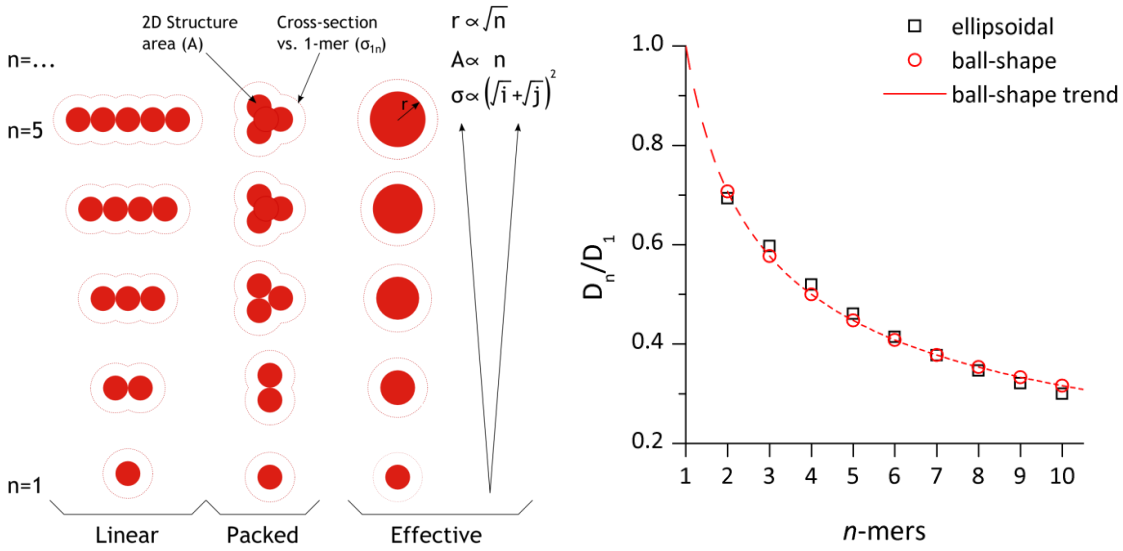

Figure 2.17. (a) Schematic of the two extreme cluster shape classes: linear versus close packed. Using geometrical argument, an effective ball-shaped cluster is derived to provide a trend for cross-sections and diffusivity coefficients. (b) Plot of the expected diffusivities of *n*-mers using both the ellipsoidal and the effective 2D surface area (ball-shape) approaches: changes are small and the more practical expression for ball-shape diffusivity will be used.

Diffusivity of molecules is also a relevant parameter in the problem. Although we do not have a calculated value for the linker-molecule ($Re_2(DMAA)_4(NCS)_2$) diffusivity,[18] we can get a fair estimate from values reported for other molecules provided that the molecular mass is the leading term, see Table 2.3. For calculation, we will consider the value $D_{ml} = 10D_{nc} = 250\ \mu m^2 s^{-1}$.

Molecule	**Molecular mass, g.mol^{-1}**	**Diffusivity, μm^{2}s^{-1}**
Sucrose	342	523
Ribonuclease	13683	119
$Re_2(DMAA)_4(NCS)_2$	1141	$5D_{nc} \leq D_{ml} \leq 20D_{nc}$

Table 2.3. Diffusion coefficients for various molecules in water at 20°C or 25°C (Numerical values are reproduced from ref. [15]).

2.4.3.1.3 Encounters

Particles are allowed to hop (on discrete positions) in a random walk fashion that is totally independent of any other particles. Although this method ignores both long and short range forces such as electrostatic repulsion, van der Waals attraction and solvation processes, we can get estimates of the time necessary for two particles to meet. We are concentrating on the possibility of collisions between building blocks of a cluster: encounters between a nanocrystal and a molecule, and encounters between like particles (nanocrystals).

The idea is to study a large group of particles that can move following the random-walk law. The discrete mesh we use is isotropic: for all directions (either $\pm x$ or $\pm y$ or $\pm z$), the mesh pitch is the same, ℓ. Entities can be all the same or they can be of two kinds. In the case of two types of entities A and B, $\ell = 2(R_A + R_B)$, for investigations on encounters between like-particles A, $\ell = 4R_A$. In this way, when two particles A and B or A and A occupy the same node, we can record that they have "collided".

This fixes the minimum time between two jumps for the particles with the highest diffusivity. To account for the possible difference in diffusivity between particles A and B, $D_A < D_B$ (for instance $D_{nc} < D_{mol}$), particles A only retain their position for a few iterations (depending on the value of D_A/D_B).

The size of the mesh depends on the number of particles studied. To mimic an infinite space, the boundary conditions are made cyclic (conservation of the number of entities). At start, particles are scattered on the mesh with a critical spacing related to their concentration. For instance, single nanocrystals will be spaced with a length of $L \sim C_{nc}^{-1/3} \sim 1.4\ \mu\text{m}$, whereas the mesh is much more refined ($\ell \ll L$). Moreover, the number of entities involved in the simulations can be chosen independently. The simulations test encounters between 1-mers and either molecules, other 1-mers or 2-mers, see Figure 2.18.

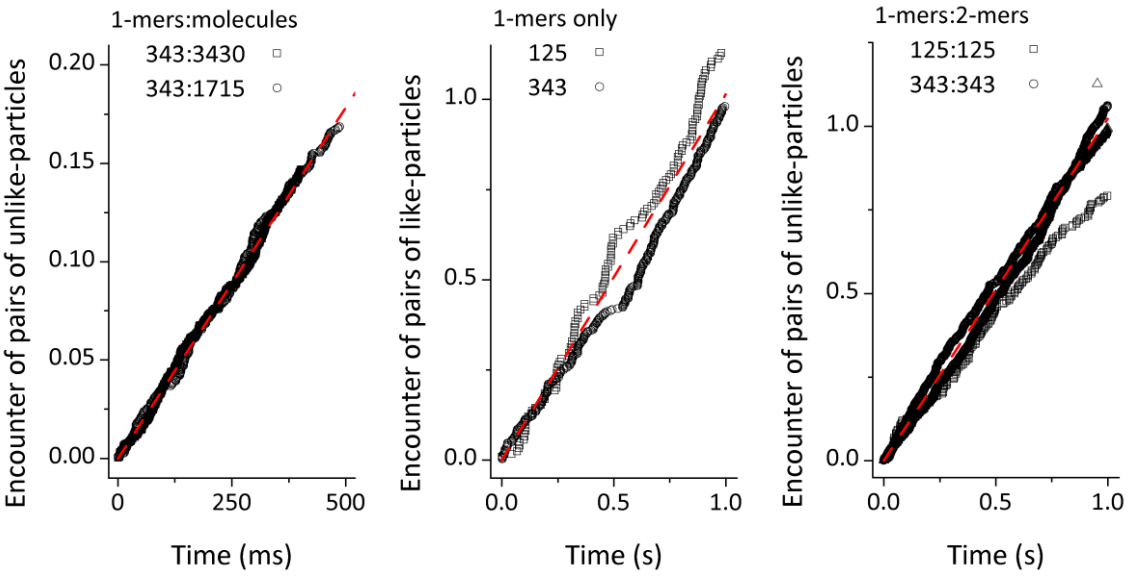

Figure 2.18. Random-walk simulations of encounters of pairs of particles for unlike-particles and like-particles. For all simulations the concentration of 1-mers is set to the experimental concentrations of nanocrystals before any linker molecule is added: $C_{nc}(0)\sim 0.35\ \mu m^{-3}$. (a) Between 1-mers and molecules, the rate of encounter is $\upsilon\sim 3.58\ s^{-1}$. (b) Inter 1-mers, the rate of encounter is $\upsilon\sim 1.01\ s^{-1}$. (c) Between 1-mers and 2-mers, the rate of encounter is $\upsilon\sim 1.02\ s^{-1}$.

The random-walk simulations show encounters between pairs of 1-mers and molecules are more frequent than between like or unlike *n*-mers. Moreover, based on Figure 2.18b-c the rate of encounters seems to be roughly constant. Within the cell and during the course of the experiment, more complex and less mobile nanostructures, *n*-mers, are formed with substantially smaller concentrations. Random-walk simulations testing encounters between the different species could be conducted to fine tune the value of coefficients $k_a^{i,j} \propto \upsilon_{encounter}$.

For simplicity however, we merely assign a constant value for the rate of encounters between *n*-mers: $\upsilon_{encounter}\sim 1\ s^{-1}$. As for encounters between molecules and *n*-mers, the value of $\upsilon\sim 3.6\ s^{-1}$ is used.

2.4.3.2 Molecular coverage

From surface science, we know a Self Assembled Monolayer (SAM) does not cover a surface in its entirety, only up to a certain fraction which can be close to 100%, though.[19] As a matter of fact θ is termed as relative surface coverage to reflect the fact that it is ratio of molecules currently adsorbed to the total number of molecules that can be, $m_{\max}$.

Studies of alkanethiol molecules on gold (111) surfaces reveal that at relatively dilute concentrations on the order of $\sim 1\ mM$, two regimes are observed for the formation of a SAM.[9] Within minutes, the surface is nearly completely decorated but it will still take a few hours for the

monolayer to reorganise itself and reach its equilibrium conformation. While the first step (anchoring) is governed by surface/anchor group of the molecule, the second step of molecular rearrangement is driven by inter-molecule interactions. The kinetics is well described by the Langmuir isotherm equation, and thus the expression of the coverage (or fraction of monolayer), see Equation 2.16.

$$\theta = \frac{M}{M + (h_a/h_d)} \times [1 - \exp(-(M \cdot h_a + h_d)t)] = K \times [1 - \exp(-h_{observed}t)]$$

Equation 2.16. Analytical solution of the simplest form of the Langmuir isotherm equation (M is assumed constant) governing the coverage of a surface by molecules.

The anchoring step is over after less than ~1 min ($h_{observed} \times 5$) for ~ 1 mM solution but it can take ~100 min for ~ 1 µM molecular solution.[9, 20-21]

With these figures in mind and treating bound citrate ions as contaminants, since 10 µM aliquots are dispensed in the cell for the formation of *n*-mers, one expects the completion of the anchoring step to take ~100 min. However, the formation of *n*-mer nanostructures does not necessitate the formation of a complete (mixed) monolayer and thus aggregation of nanocrystals can take place much sooner.

Qualitatively, the results from the rate-equation model for the coverage of nanocrystal surfaces are consistent with these experimental observations, see Figure 2.12 (for the simplest form of the steric hindrance factor $S \sim \theta$, see Figure 2.6).

2.4.3.3 Activation energy

The backbone structure of rate coefficients was detailed in Equation 2.12. We investigate the properties of the term describing the energy barrier to be overcome, W. We propose it originates from the concept developed in Arrhenius' law in place of the exponential factor. Besides, the attempt frequency of dissociation of a molecule from a nanocrystal surface is related to a molecular vibration, on the order of $\nu_{dissociation} \sim k_B T/h \sim 6.25 \times 10^{12}$ s^{-1}. Using this formalism, the forward and reverse rate coefficients expression can be fully expanded ($\left(E_a^{mol:nc}, E_d^{mol:nc}, E_a^{cl:cl}, E_d^{cl:cl}\right)$ respectively are the forward and reverse activation energies for molecular adsorption and clusters formation), see Equation 2.17.

$$\begin{cases} h_a \simeq \nu_{encounter} \times \exp\left(-E_a^{mol:nc}/k_B T\right) \\ \\ h_d \simeq \nu_{dissociation} \times \exp\left(-E_d^{mol:nc}/k_B T\right) \end{cases}$$

$$\begin{cases} k_a \simeq \nu_{encounter} \times \theta \times \exp\left(-E_a^{cl:cl}/k_B T\right) \\ \\ k_d \simeq \nu_{dissociation} \times (1-\theta) \times \exp\left(-E_d^{cl:cl}/k_B T\right) \end{cases}$$

Equation 2.17. Expanded expressions of rate coefficients for molecular decoration of nanocrystals surface and clusters formation.

At this stage it is practical to introduce the enthalpy of reaction, $\Delta H = E_a - E_d$. Although it can be argued the expressions in Equation 2.17 down play the role of steric hindrance, the estimations of enthalpy or reaction are believed not to be changed dramatically, as the activation energies are encapsulated in exponential functions. For the different fits presented in Figure 2.12, we calculate the corresponding activation energies so as to provide a value for the enthalpy of molecular binding and cluster formation, see Table 2.4.

Dataset	$E_a^{mol:nc}$ **(meV)**	$E_d^{mol:nc}$ **(meV)**	$\Delta H^{mol:nc}$ **(meV)**	$E_a^{cl:cl}$ **(meV)**	$E_d^{cl:cl}$ **(meV)**	$\Delta H^{cl:cl}$ **(meV)**
Optical (8 h)	102	366	-264	105	389	-284
SEM (30 h)	70	364	-293	132	404	-272

Table 2.4. Estimation of enthalpy of reactions for different datasets ($m_{\max} = 250$). The values are derived from optimised values of the rate coefficients: h_a, h_d, k_a and k_d. Because of the sensitivity of the model to the rate coefficient values, the estimate of activation energies are defined at ±5 meV or better.

These estimates tend to indicate that the enthalpy of both processes are negative $\Delta H < 0$: the reactions are exothermic. This indicates that a system comprising a linker-molecule and a bare nanocrystal has its energy lowered when the molecule is bound on the nanocrystal surface instead of remaining apart. From there we can conclude the dissociation energy is at least equal to the enthalpy energy: once attached, a linker molecule is unlikely to desorb and consequently any nanocrystal anchored on a cluster is very likely to remain part of it since presumably a few molecules are involved in the junction between two nanocrystals.

This method seems to lead the conclusion products are more thermodynamically stable than the reactants, see Figure 2.19.

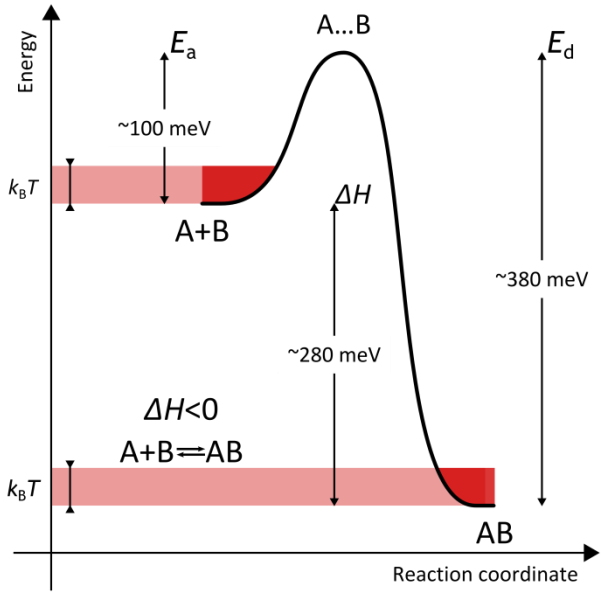

Figure 2.19. Energy diagram of the molecular decoration of nanocrystals surface and clusters formation along the reaction coordinate.

2.4.3.4 Other experimental factors

Despite the fact data fitting is improved for values of $m_{\max}\sim 10^3$, such estimate for the upper bound values of adsorbed on nanocrystal surfaces is unrealistic. We estimate ~250 molecules have room to bind on a single nanocrystal surface at maximum.

The quick peak shift in the UV-visible response of the nanocrystal dispersal and the fitting of the experimental datasets shows nanocrystals should be fully decorated very quickly, i.e.: in a matter of minutes. Nevertheless, the *n*-mer populations appear to remain correlated to the addition of subsequent aliquots, for time points t_2, t_3, t_6 and more clearly for $t_8\sim 7$ days, see Figure 2.9.

Although at start, it could be argued this fact results of a slow conversion response into higher order *n*-mers, this cannot explain the statistics observed at $t_8\sim 7$ days.

The linker molecules employed are hydrophobic. It is assumed they are solvated by a shell of acetone molecules[4] as a mixing buffer with water molecules (This acetone shell is understood to act as a leaky physical barrier for the binding of molecules on nanocrystals surfaces.). A possibility is that escalating addition of aliquots could result in the precipitation/centrifugation of the acetone solvated molecules at the bottom of the cell thus dramatically decreasing the effective number of available molecules per nanocrystal over the entire course of the experiment.

Figure 2.7b shows the effective dilution resulting from addition of aliquots. It could be proposed the acetone added disrupt the charge balance within the double-layer around the

nanocrystals resulting in a crashing of the dispersal. This scenario is allegedly happening between time points t_7 and t_8.

Changing the perspective of the discussion, studies of surface functionalisation show temperature is a key factor in facilitating or impeding the binding of molecules on surfaces. Temperature conditions were not controlled during this exploratory experimental work. This factor may explain disparities in the numbers of 2-mers and the sudden drop of 1-mers observed at t_8.

2.5 Conclusion

Based on experimental results from Dr. Claire Barrett's work on the formation hybrid nanostructures, called *n*-mers, comprising nanocrystals linked by molecules, we present a framework for the modelling of *n*-mers populations evolution. Using datasets from different sources: UV-visible absorption spectra of the dispersal of nanostructures in the cell and SEM images of drop-casted samples prepared at different times, a system of rate-equations is derived to characterise the various populations of this many-body system.

We show the model can accommodate different case scenarios for cluster growth and essentially fit the distributions of populations found experimentally. After reviewing the transport properties of the entities in the cell based on random-walk simulations, we present estimates of the enthalpies of reaction for molecular decoration of nanocrystal surfaces and cluster association on the basis of the values of the optimised fit parameters.

Thanks to the model flexibility, data from other experimental techniques such as dynamic light scattering spectroscopy could be fed into the model so as to provide faster feedback on kinetics information characterising the *n*-mer formation process. Theoretical considerations on the free energy of *n*-mer nanostructures[22-24] could also be included in the definition of rate coefficients for finer results.

We believe the framework offers the ability to both describe and predicts the formation of *n*-mers assuming that experimental conditions are well controlled, in particular temperature. However it appears the modelled experimental technique cannot selectively produce a mono-dispersed solution of a given *n*-mers population. Complementary techniques such as fine-tuned centrifugation[25] or more probably size-selective nanopore filtration[26] could lead to enhancement of the relative abundance of a particular *n*-mer type.

2.6 References

1. Nie, S.; Emory, S. R., Probing Single Molecules and Single Nanoparticles by Surface-Enhanced Raman Scattering. *Science* **1997,** *275* (5303), 1102-1106.
2. Venables, J. A.; Spiller, G. D. T.; Hanbucken, M., Nucleation and Growth of Thin-Films. *Rep. Prog. Phys.* **1984,** *47* (4), 399-459.
3. Lydon, D. P.; Spalding, T. R.; Gallagher, J. F., Substitution reactions of rhenium-chloride bonds in [Re2(DMAA)4Cl2], (DMAA=2',6'-dimethylacetanilido); synthesis and characterisation of [Re2(DMAA)4X2] (X=NCO, NCS, N3) and [Re2(DMAA)4Ln][SbF6]2 (n=2, L=pyridine; n=1, L=4,4'-bipyridine). *Polyhedron* **2003,** *22* (9), 1281-1287.
4. Bishop, K. J. M.; Wilmer, C. E.; Soh, S.; Grzybowski, B. A., Nanoscale Forces and Their Uses in Self-Assembly. *Small* **2009,** *5* (14), 1600-1630.
5. Barrett, C. Charge Transport in Nanoscale Structures and Devices. University College Cork, Cork, 2009.
6. Hosokawa, K.; Shimoyama, I.; Miura, H., Dynamics of self-assembling systems—Analogy with chemical kinetics—. *Artif. Life* **1995,** (15).
7. Nichols, R. J.; Burgess, I.; Young, K. L.; Zamlynny, V.; Lipkowski, J., A quantitative evaluation of the adsorption of citrate on Au(1 1 1) using SNIFTIRS. *Journal of Electroanalytical Chemistry* **2004,** *563* (1), 33-39.
8. Hill, H. D.; Millstone, J. E.; Banholzer, M. J.; Mirkin, C. A., The Role Radius of Curvature Plays in Thiolated Oligonucleotide Loading on Gold Nanoparticles. *ACS Nano* **2009,** *3* (2), 418-424.
9. Bain, C. D.; Troughton, E. B.; Tao, Y. T.; Evall, J.; Whitesides, G. M.; Nuzzo, R. G., Formation of monolayer films by the spontaneous assembly of organic thiols from solution onto gold. *Journal of the American Chemical Society* **1989,** *111* (1), 321-335.
10. Giordano, N. J.; Nakanishi, H., *Computational Physics (Second Edition)*. 2nd ed.; Pearson Education Ltd.: London, 2006; p 560.
11. Ziff, R. M.; Majumdar, S. N.; Comtet, A., Capture of particles undergoing discrete random walks. *The Journal of Chemical Physics* **2009,** *130* (20), 204104-5.
12. Li, J. C. M.; Chang, P., Self-Diffusion Coefficient and Viscosity in Liquids. AIP: 1955; Vol. 23, pp 518-520.
13. Xu, C. S.; Cang, H.; Montiel, D.; Yang, H., Rapid and quantitative sizing of nanoparticles using three-dimensional single-particle tracking. *Journal of Physical Chemistry C* **2007,** *111* (1), 32-35.
14. Wuelfing, W. P.; Templeton, A. C.; Hicks, J. F.; Murray, R. W., Taylor Dispersion Measurements of Monolayer Protected Clusters: A Physicochemical Determination of Nanoparticle Size. *Anal. Chem.* **1999,** *71* (18), 4069-4074.
15. Dill, K. A.; Bromberg, S., *Molecular Driving Forces: Statistical Thermodynamics in Chemistry & Biology*. Garland Science: 2003; Vol. 1, p 686.
16. Han, Y.; Alsayed, A. M.; Nobili, M.; Zhang, J.; Lubensky, T. C.; Yodh, A. G., Brownian Motion of an Ellipsoid. *Science* **2006,** *314* (5799), 626-630.
17. Hoffmann, M.; Wagner, C. S.; Harnau, L.; Wittemann, A., 3D Brownian Diffusion of Submicron-Sized Particle Clusters. *ACS Nano* **2009**.
18. Gannon, G.; Larsson, J. A.; Greer, J. C.; Thompson, D., Guanidinium Chloride Molecular Diffusion in Aqueous and Mixed Water−Ethanol Solutions. *The Journal of Physical Chemistry B* **2008,** *112* (30), 8906-8911.
19. Ulman, A., Formation and Structure of Self-Assembled Monolayers. *Chemical Reviews* **1996,** *96* (4), 1533-1554.
20. Karpovich, D. S.; Blanchard, G. J., Direct Measurement of the Adsorption Kinetics of Alkanethiolate Self-Assembled Monolayers on a Microcrystalline Gold Surface. *Langmuir* **1994,** *10* (9), 3315-3322.
21. Sang-Woo, J., Characterization of self-assembled phenyl and benzyl isothiocyanate thin films on Au surfaces. *Surface and Interface Analysis* **2006,** *38* (3), 173-177.

22. Saunders, S. R.; Eden, M. R.; Roberts, C. B., Modeling the Precipitation of Polydisperse Nanoparticles Using a Total Interaction Energy Model. *The Journal of Physical Chemistry C* **2011,** *115* (11), 4603-4610.
23. Ivanov, M. R.; Bednar, H. R.; Haes, A. J., Investigations of the Mechanism of Gold Nanoparticle Stability and Surface Functionalization in Capillary Electrophoresis. *ACS Nano* **2009,** *3* (2), 386-394.
24. Gemici, Z.; Schwachulla, P. I.; Williamson, E. H.; Rubner, M. F.; Cohen, R. E., Targeted Functionalization of Nanoparticle Thin Films via Capillary Condensation. *Nano Letters* **2009,** *9* (3), 1064-1070.
25. Chen, G.; Wang, Y.; Tan, L. H.; Yang, M.; Tan, L. S.; Chen, Y.; Chen, H., High-Purity Separation of Gold Nanoparticle Dimers and Trimers. *Journal of the American Chemical Society* **2009,** *131* (12), 4218-4219.
26. Krieg, E.; Weissman, H.; Shirman, E.; Shimoni, E.; Rybtchinski, B., A recyclable supramolecular membrane for size-selective separation of nanoparticles. *Nat Nano* **2011,** *6* (3), 141-146.

Chapter 3 – Formation and electrical characterisation of electrode – molecule(s) – nanocrystal – molecule(s) – electrode junctions

3.1 Introduction

Since the first theoretical proposal of molecular electronic devices,[1] it has become more and more clear the first pitfall to overcome is contacting molecules. Molecular electronics may represent the near ultimate miniaturisation of devices to the scale of ~ 1 nm, and provided it exists in the classical form developed by the integrated circuit industry, to date no current technological method is able to offer all the requirements of a compact and reliable contact strategy. In all scenarios, the issues of contact variability and reliability are entangled.

Many contacting strategies have been developed experimentally so as to contact allegedly either single or few or hundred(s) of molecules at a time. Although all techniques developed are still research focused, some contacting strategies are closer to integration than others. There are four main intimate laboratory techniques such as Scanning Tunnelling Microscope Break Junction (STM-BJ),[2-4] Conductive-Probe Atomic Force Microscopy (CP-AFM),[5] Liquid metal (alloy) drops[6-7] and Mechanically Controlled Break Junction (MCBJ).[8-9] On the other hand, four to five on chip and self-contained techniques exist, namely: electromigration,[10-12] nano-pores,[13] cross-bars[14] and nanocrystal arrays.[15-17] The work presented here is a down sized version of the former technique employing few-nanocrystal assemblies bridging electrodes spaced by a nanometre-scale gap.

We present a versatile method for interfacing small assemblies of molecules between laterally patterned metal nanoelectrodes ($\sim 30\,\mathrm{nm}$ electrode gap) and citrate-stabilised metal nanocrystals ($\sim 60\,\mathrm{nm}$ core diameter) trapped in/over the gap using dielectrophoresis. The devices are studied via both electrical current-voltage characterisation in vacuum before and after molecular functionalisation, and scanning electron microscopy (SEM) imaging. The candidate molecule investigated is a thiophene-terminated "rigid-rod" linker — 1,4 di(3-thiophene)ethynylbenzene (DTEB). The molecule is of interest due to the novel thiophene anchor groups (for binding to gold surfaces) and a conjugated backbone that should facilitate the transport of charge carriers.

We first detail the fabrication/characterisation process starting with wafer fabrication of nanoelectrodes, dielectrophoretic trapping of gold nanocrystals and finally the molecular functionalisation conditions. We also report on the current-voltage $I(V)$ measurement protocol as well as on the Scanning Electron Microscopy imaging. The method of compiling large datasets from different sources is also detailed.

In a second part, we show results of $I(V)$ measurements on these "few-nanocrystal" assemblies at different stages of the fabrication process. The Influence of the immersion step in non-aqueous solvent is shown to be of more importance than initially anticipated. We also report

on the measurement on a comprehensive fabrication process flow by measuring devices after each critical step revealing effectively induced changes in the conductance as opposed to experimental uncertainty.

Finally, we discuss the results with the help of different models. We introduce a reworked version of the Simmons model to get insights in the background conductance, a geometrical model is derived to quantify the potential molecular decoration in the junctions. A resistor network model is implemented and we show the three models work consistently together as a tool for the estimation of single molecule conductance.

3.2 Method

We propose a method for contacting molecules laterally using nanocrystals allowing sequential measurements. This down-sized version of the nanocrystal array, concept developed by M. Calame and C. Schönenberger *et al.*, presents common challenges with all other methods in the field but has the potential to provide key step by step information on the formation of laterally contacted single- or few-molecule devices. In the following, we will assess the scalability of this contacting strategy. Thanks to this methodology, devices are characterised by current-voltage measurements at room temperature in vacuum conditions after each process step to investigate the variation of the electrical response.

3.2.1 Device fabrication and characterisation overview

Devices are characterised using current-voltage measurements at room temperature in vacuum conditions. The source-drain bias voltage is swept in that sequence 0 V → 0.5 V → -0.5 V → 0 V. We obtain two different traces for a given bias polarity. We term the dynamic conductance measured after the trapping of nanocrystal in the gap: G_{nc}, while the dynamic conductance measured after functionalisation in molecular solution is termed: G_{nc-mol}. Unless otherwise stated, the values of dynamic conductance are averaged across the different measurements performed on a same device at the same process conditions, hence the error bars shown in Figure 3.1a for instance (the standard deviation is calculated based upon the different conductance measurements).

In Figure 3.1a, we present two current-voltage characteristics, $I(V)$, for the same device after two different steps of the fabrication process. When nanocrystals have just been trapped (gray curve in the plot), the current-voltage response is linear and the magnitude of the current is less than $I_d \sim 0.87$ nA at $V_{ds} = 0.5$ V. We estimate the low bias conductance being $\sim 2 \times 10^{-5}\ G_0$. On the other hand, the current-voltage response is greatly enhanced after immersion of the device for 24 hours in a 5 mM solution of the organic linker molecule: 1,4 di(3-thiophene)ethynylbenzene (DTEB). The characteristic (green curve in the plot) shows a net and steady increase in the current, for instance the current is now $I_d \sim 13.5$ nA at $V_{ds} = 0.5$ V. The 0 V bias conductance is estimated to be $G \sim 3 \times 10^{-4}\ G_0$, this represents a ~17 fold increase in conductance at low bias which is consistent with the ~15 fold increase at $V_{ds} = 0.5$ V since the characteristics can be deemed linear.

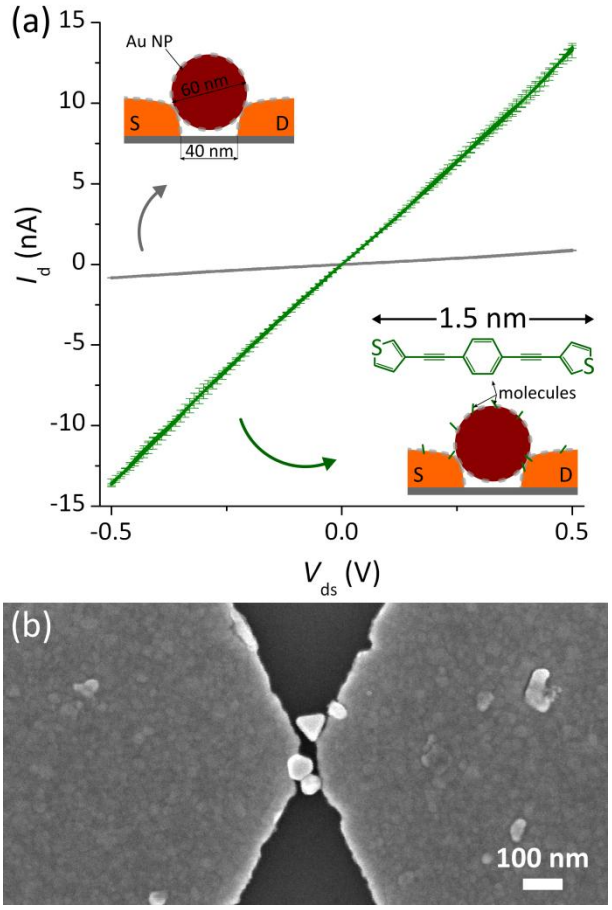

Figure 3.1. Current-voltage measurements. (a) Current-voltage measurements at different stages of the fabrication of the same device. The source-drain bias was swept from 0 V → 0.5 V → -0.5 V → 0 V. The gray curve shows the I(V) characteristic after the nanocrystals were trapped, device conductance being $G_{nc} \sim 2 \times 10^{-5}\ G_0$, the green curve shows a net increase in the current for the same device after immersion in molecular solution $G_{nc-mol} \sim 3 \times 10^{-4}\ G_0$. (b) Scanning Electron Micrograph of the same device: the gold electrodes on a thin multi-layer of platinum on titanium are defined by e-beam: SiO_2/Ti (3 nm)/Pt (3 nm)/Au (20 nm), 3 nanocrystals were trapped.

The candidate molecule investigated is a thiophene-terminated "rigid-rod" linker — 1,4 di(3-thiophene)ethynylbenzene (DTEB). The molecule presents the interest of having two thiophene rings as anchor groups on gold surfaces (nanocrystal, patterned electrodes) and a conjugated backbone from one end to another allowing the transport of charge carriers. One can note the molecule is symmetrical. A UV-visible spectrum of a solution of this molecule shows it absorbs in the near UV band with a maximum peak at ~320 nm. This indicates the HOMO—LUMO gap of the DTEB molecule is expected to be rather large ~3.87 eV. The electrical charge transport is thus expected to be non resonant tunnelling and hole-mediated as the Fermi level of the metallic nodes should not be matching any of the molecular orbitals at low bias $|V_{ds}| \leq 0.5$ V, even in the fully bound configuration of the molecule between metallic terminals. The magnitude of the

current at the maximum bias applied tends to corroborate the idea the mechanism of charge transport is tunnelling. Moreover, unless otherwise stated, we exclude resonant tunnelling from one electrode to another via the nanocrystal, as this conduction regime would enhance the current value by interplay in the transmission probabilities through the two junctions in series.

Imaging the device by Scanning Electron Microscopy (SEM) reveals the composition of the assembly of nanocrystals bridging the electrodes. In Figure 3.1b, the source electrode is on the left hand side, the drain on the right hand side. Three 60 nm diameter gold nanocrystals can be seen in the centre of the image. They appear bright not because they are charging but because their geometry (high surface/volume ratio) facilitates the generation of secondary electrons, and also because of their proximity to the gold electrodes. A tetrahedron is attached to the drain electrode, two more complex and smoother polyhedrons (rhombic triacontahedron?) are bridging the gap. We argue that because the electrodes are ~26 nm thick (3 layers of 3 nm titanium, 3 nm platinum, 20 nm gold), only one nanocrystal is fully bridging the gap, the other is simply touching the source electrode and the bridging particle. Another argument in favor of particles being in close vicinity of gold surfaces is the fact nanocrystals look dull when immobilised on non conductive surfaces such as the thermally grown silicon oxide present underneath the gold electrodes (~80 nm thick on a highly n-doped silicon substrate).

In house lithography of e-beam electrodes produces 40 nm gap electrodes reliably. Gold nanocrystals with a diameter of 60 nm were chosen to comply with the lithography performance.

3.2.2 CMOS compatible fabrication

A wafer-level nanoelectrode fabrication process was developed for two-terminal electrical interfacing of nanostructures, see Figure 3.2. A range of electrode geometries and gap sizes with critical dimensions down to 40 nm were fabricated using electron-beam lithography (JBX-6000FS, JEOL UK Ltd.), metal evaporation (3 nm Ti, 3 nm Pt, 20 nm Au) and lift-off. Micron scale tracks and larger contact pads were fabricated using optical lithography, metal evaporation (10 nm Ti, 10 nm Pt, 200 nm Au) and lift-off. Following fabrication, the dice were solvent cleaned in a commercial resist remover solution (RM1165), and finally stored under isopropyl alcohol until used.

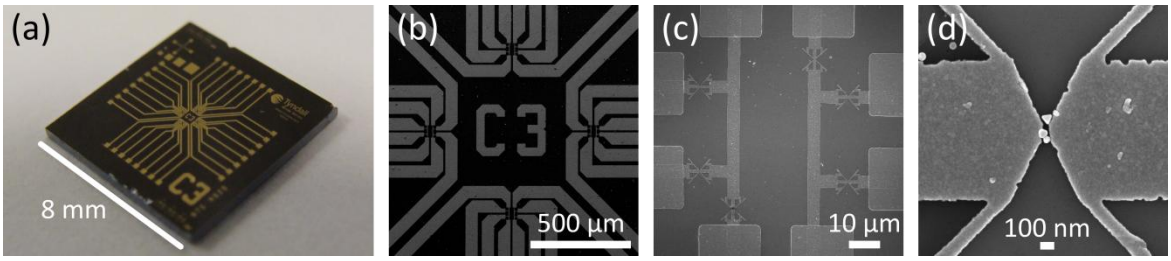

Figure 3.2. Zoom in on a device from chip-scale to nanometre scale. (a) A photograph of the chip shows the overall layout design. (b) Scanning Electron Micrograph at low magnification of the centre of the chip showing four distinct e-beam fields, (c) focuses on the "eastern" e-beam field containing 6 different devices contacted via 2 common source electrodes, (d) is a close-up on the device presented in Figure 3.1, showing a broader view of the nanocrystal assembly bridging the gap.

The device fabrication relies on three main milestones each done in different laboratories.

We start with a classical 100 mm wafer of silicon. The substrate is usually highly doped level (As), n-type (~1-5 mΩ.cm). The first steps are performed in the CMOS compatible clean-room, in the Central Fabrication Facilities in the Tyndall National Institute. Wafers are oxidised in a furnace with a dry process to provide a smooth natural silicon oxide (thickness ≥ 50 nm). The back oxide layer may be stripped away for the deposition of aluminium to serve as a back contact. This step was finally skipped towards the end of the Ph.D. work. Alignment marks (crosses located 40 mm from the centre of the wafer) are also etched on the substrates for further e-beam lithography steps.

Wafers are then handed for the metal lithography steps in the Compounds Semiconductor Laboratory. We rely on a hybrid lithography process. Firstly, nano-scale electrode gaps are made by e-beam lithography (A ~ 100 nm thin ZEP 520A resist layer is exposed at 50 kV for the highest pattern resolution possible on adjacent fields of 80×80 µm^2 with a current of ~ 100 pA for a typical dose of 110 µC.cm^{-2}), metal evaporation (e.g.: 3 nm Ti, 20 nm Au) and lift-off of the first thin metal layer. The thickness is typically 20 nm. Then, larger contact pads are defined using an optical lithography step is done followed by lift-off of the second metal layer which is thicker, typically 200 nm. An overlap of at least 5 µm ensures a proper contact of the electrodes between the two lithography steps, see Figure 3.3. The electrodes are made of gold on a thin adhesion layer of titanium or platinum on titanium (chromium was eventually discarded as it may be incompatible with other potential further processing steps). E-beam evaporation is the technique for these metal depositions.

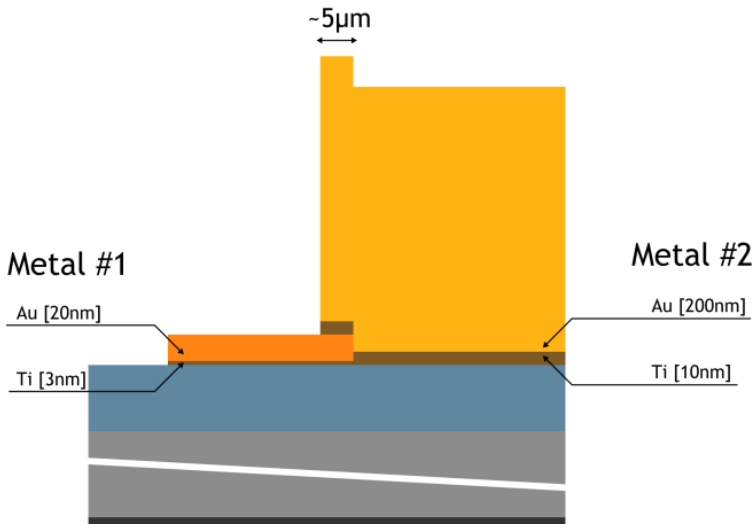

Figure 3.3. Hybrid lithography cross-section schematic, the overlap between the e-beam pattern and the optical lithography defined tracks is about 5 µm in length. Electric tests performed on shorted gap electrodes indicated the contact between the two metals is typically less than a few ohms (2 point measurements).

An aspect of the Ph.D. work has been to improve the fabrication process.

A new optical mask ensuring the contact between the e-beam defined electrodes and the bond pads for the measuring probes has been designed. The new optical mask brought more samples for the same wafer size, as well as more devices per samples, see Figure 3.4.

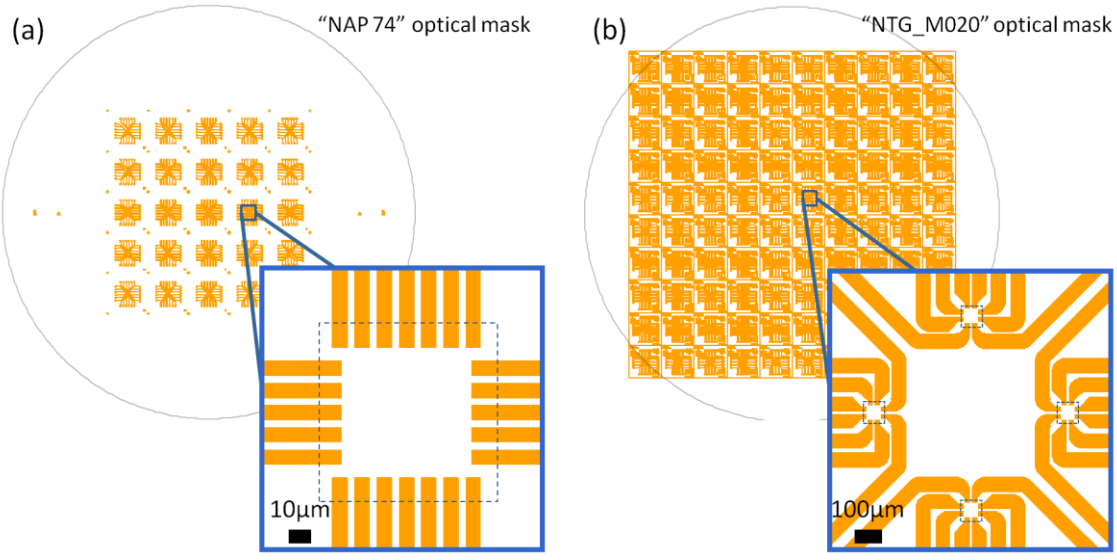

Figure 3.4. Improvement in the optical mask design for contacting electrodes. (a) The initial "NAP 74" optical mask for the second metallisation delivered 25 electrodes chips 10×10 mm^2 each having 24 bond pads routing to 1 single e-beam field. (b) The improved optical mask delivers more dies out of the same silicon wafer substrate size: the "NTG_M020" optical mask provides 76 chips with a reduced size of 8×8 mm^2 having 4 sets of 8 bond pads routing to 4 separate e-beam fields (32 bond pads in total).

Along the same lines, as it appeared the method of back-contacting the samples was not particularly relevant due to the length scale of the devices (gate oxide thickness being far greater than the junction length scale), the step was skipped in later fabrication runs. As a result, it was believed the silicon oxide surface was less subject to contamination during the process. Finally, we moved the oxide thickness from 50 nm to 90 nm (matching the needs of the Graphene project within the Nanotechnology Group at Tyndall) so as to facilitate the continuous process development and control. Conversely, although highly doped and degenerated silicon substrates increase the risk of leakage through the insulating silicon oxide layer and increase parasitic capacitance between metal tracks and electrodes with the silicon underneath, advance in the process development during the Ph.D. programme resulted in the adoption of this substrate for all the devices fabricated.

3.2.3 Nanometre scale device fabrication process/characterisation flow

Finally, the last steps of the device fabrication are performed in our laboratories in conjunction with characterisation. Commercially available citrate-stabilised gold nanocrystals in water (British Biocell International) are trapped in the electrode gaps using an AC electrical field. The dielectrophoresis force drives the particle(s) into the gap. The electrode chips are then immersed in non-aqueous solvent to mediate the functionalisation of the exposed gold surfaces by candidate molecules and/or investigate the influence of the sole solvent on the assemblies of nanocrystals.

A significant number of devices were fabricated employing the first generation of device characterisation employing tetrahydrofuran ($7 \times 20 + 2 \times 24 = 188$ devices involved at start) or dichloromethane ($3 \times 24 = 72$ devices in the design) as a solvent for mediating molecular functionalisation, representing a total of 211 devices (across 12 samples) studied before and after molecular immersion, see Figure 3.5a. Nevertheless these preliminary results did not provide any information on the role played by the sole solvent immersion step on the junctions. A new series of measurements was designed to study the influence of the sole solvent-immersion step: 228 devices (across 10 samples) were processed for a total of 169 working devices before/after solvent exposure, see Figure 3.5b. Amongst these, a subset of 96 devices (across 4 different samples) was studied and 60 devices were fully characterised in the form of measurements of conductance after each process step: after trapping, after solvent immersion, after molecular functionalisation, see Figure 3.5c.

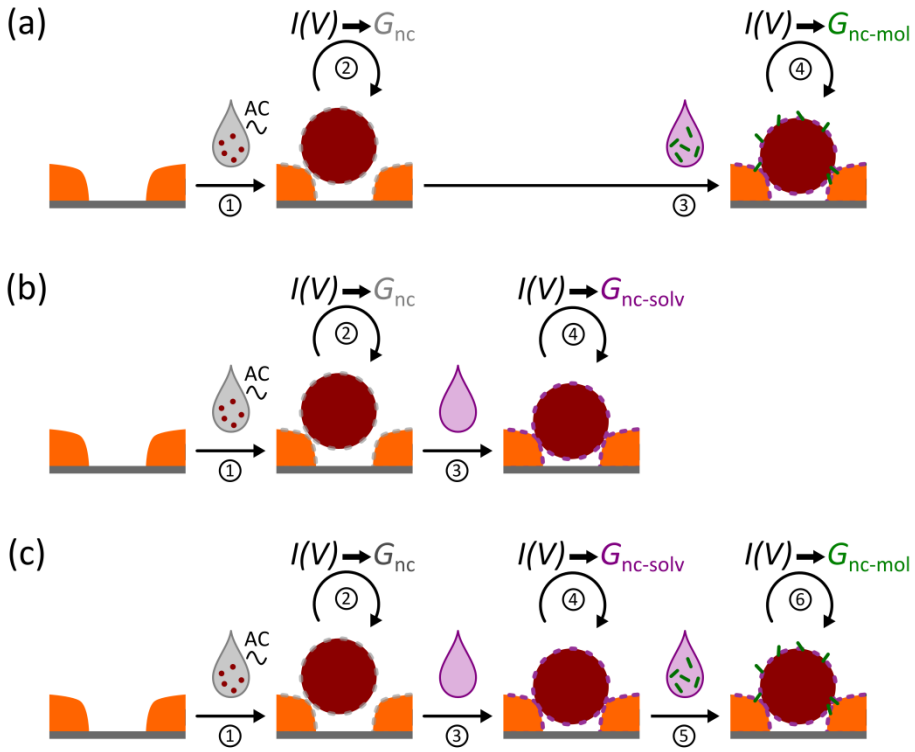

Figure 3.5. The process-characterisation flow is portrayed showing the different stages of the device making and electrical characterisation: e-beam electrodes are defined first, then one or a few nanocrystals are trapped by dielectrophoretic force in the gap. (a) After this preliminary step: the initial naive method consists functionalising the devices with molecules (for 24 hours). (b) To investigate the influence of non-aqueous solvent(s) on the nanocrystal assemblies an intermediate process step was included in the process flow. (c) Finally the main body of the results presented in this work follows the comprehensive joint fabrication/characterisation process flow. After each process step, current-voltage measurements are performed in a vacuum chamber to provide insights in the device conductance.

After each fabrication process step, electrical measurements of the devices are performed in a high vacuum chamber (base pressure: $P_{\text{vacuum}} \lesssim 2.5 \times 10^{-4}$ Pa). From the I(V) characteristics, the conductance at low bias is estimated: as trapped nanocrystals, G_{nc}, after solvent immersion, $G_{nc-solv}$, after molecular functionalisation, G_{nc-mol}.

Only after the electrical characterisation is complete can the samples be imaged using a Scanning Electron Microscope.

3.2.3.1 Dielectrophoretic trapping of nanocrystals in nano-gaps

Once the patterning of nanometre scale electrodes is finished, the fabrication process steps are done in non clean-room environments for practical reasons. In order to minimise possible contamination of the devices, samples are stored in isopropyl alcohol up until the dielectrophoretic trapping routine starts.

In order to position a gold nanocrystal in the gap, we can use the dielectrophoretic force. Based on earlier works from Dr. Claire Barrett,[18] we investigated the dielectrophoretic trapping of 60 nm gold particles between "facing-finger" electrodes with inter-electrode gaps ~ 40 nm.

For all trapping experiments, a waveform generator was used (Agilent AG33220A). The samples were mounted in a manual probe station (Wentworth PML8000). A drop (4 µL) of commercially available citrate stabilised Au nanocrystals in water (diluted 1:10 in de-ionised water) was placed on the central region of the sample. An AC voltage with frequency ($f = 1\ \mathrm{MHz}$) and peak-to-peak amplitude (V_{p-p}) in the range of 1.4 V ≤ $V_{p\text{-}p}$ ≤ 1.7 V for electrode chip based on the design shown in Figure 3.4a (~ 50 nm SiO_2) and 2.0 ≤ $V_{p\text{-}p}$ ≤ 2.3 V for those based on Figure 3.4b (~ 90 nm SiO_2) was applied for 60 seconds to trap the nanocrystals. These conditions normally ensured particles were trapped in more than 50% of the gaps. For each set of values for the trapping parameters (f, $V_{p\text{-}p}$), the process was repeated across up to 4 sets of 6 nanogaps on each chip. When the process was completed for all electrodes, the sample was briefly rinsed in isopropyl alcohol (<5 min) and blown dry in a gentle stream of nitrogen.

The nanocrystals are trapped in the gap by the dielectrophoresis force and held in place by van der Waals forces. The mechanical stability of these assemblies has been tested by different methods. The trapped nanocrystals resist day-long exposure to a variety of solvents, air exposure for months, sonication in water for minutes, and silicon nitride/oxide etching process steps.

The simplest method for trapping nanocrystals consists of applying the AC voltage bias onto a circuit where the load is just the device itself. The lack of feedback information on how successful the process is presents an obvious drawback as we need to wait until the electrical device characterisation is complete to check the particle assembly under a Scanning Electron Microscope, plus the inherent variability in the device making cannot be addressed by fine tuning the trapping parameters.

To overcome these shortcomings, we have been designing and investigating setups to get insights in the dielectrophoresis trapping process. We present three different setups on the dielectrophoretic trapping process designed to provide real-time feedback mechanism, see Figure 3.6.

The setup A employs an oscilloscope (Tektronix TDS3032B) for the feedback loop, in a similar setup to that proposed by the M. Calame and C. Schönenberger group.[19] Assuming a particle is bridging the gap, the impedance Z_{DUT} is expected to change and as a result, the drop of voltage across a dummy resistor R should vary (increase). Unfortunately this setup seems to suffer from a very low Signal/Noise ratio. For frequencies $\leq 100\,\mathrm{kHz}$ the trace of voltage against time is stable as expected as these conditions are not optimal for dielectrophoretic trapping of particles. However for frequencies closer to the trapping frequency, the voltage across the dummy resistor is unstable and presents slight dips and bumps that cannot be used to assign nanocrystals bridging the gap.

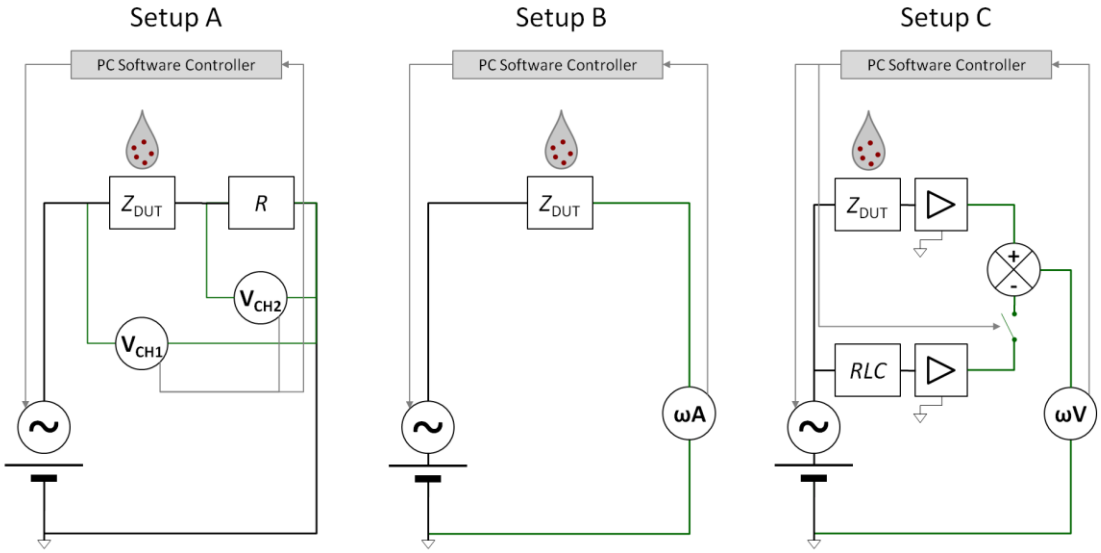

Figure 3.6. Investigation on setups for providing feedback when trapping particles: Setup A comprehends an oscilloscope (TDS3032B) monitoring the voltage drop notably monitoring the voltage change across a dummy resistor; Setup B relies on a lock-in amplifier (SR850) in a current reading mode monitoring the change in current passing through the device under test; Setup C is based on a differential voltage measurement across a calibrated RLC bridge using a lock-in amplifier (SR850) operating in voltage mode.

The Setup B uses a lock-in amplifier in current reading mode. The instrument is configured so as to measure the magnitude of the current flowing at the excitation frequency. The impedance Z_{DUT} can then be calculated. The setup C, which may be termed "bridge-enhanced" spectroscopy,[20] uses a lock-in amplifier as a voltage comparator of the converted currents/voltages between Z_{DUT} and a matching RLC circuit. Because the lock-in amplifiers available in the laboratory (Stanford Research System SR830 or SR850) do not operate at frequencies above $100\,\mathrm{kHz}$, we also proposed the concept of alternating dielectrophoretic trapping and spectroscopy probing until a noticeable current or voltage change is measured.

Just like for setup A, we faced the issue of a very unfavourable background impedance signal in setup B, masking the small impedance change due to particle trapping. It also remains unclear what the contribution of coupled capacitance of the silicon substrate with the metal tracks and electrodes is on the overall measurement ($C_{\mathrm{substrate}} \sim 500\ \mathrm{pF}$ estimated from thermal oxide thickness and metal track length, assuming the silicon material is highly conductive). Attempts of measuring the impedance of a bare nanometre-scale gap showed values suggesting a strong coupling with the silicon substrate underneath or parasitic contributions of BNC cables. Setup C however is believed to master these problems by implementing a differential measurement along with a lock-in amplified signal measurement mechanism. Further work will focus on this aspect.

Nevertheless even without a real-time feedback system, typically one to very few (~5) particles are trapped. Bridging systems of two-particle in series are rare and parallel assemblies of bridging particles are limited to 3 nanocrystals at most, see Figure 3.7.

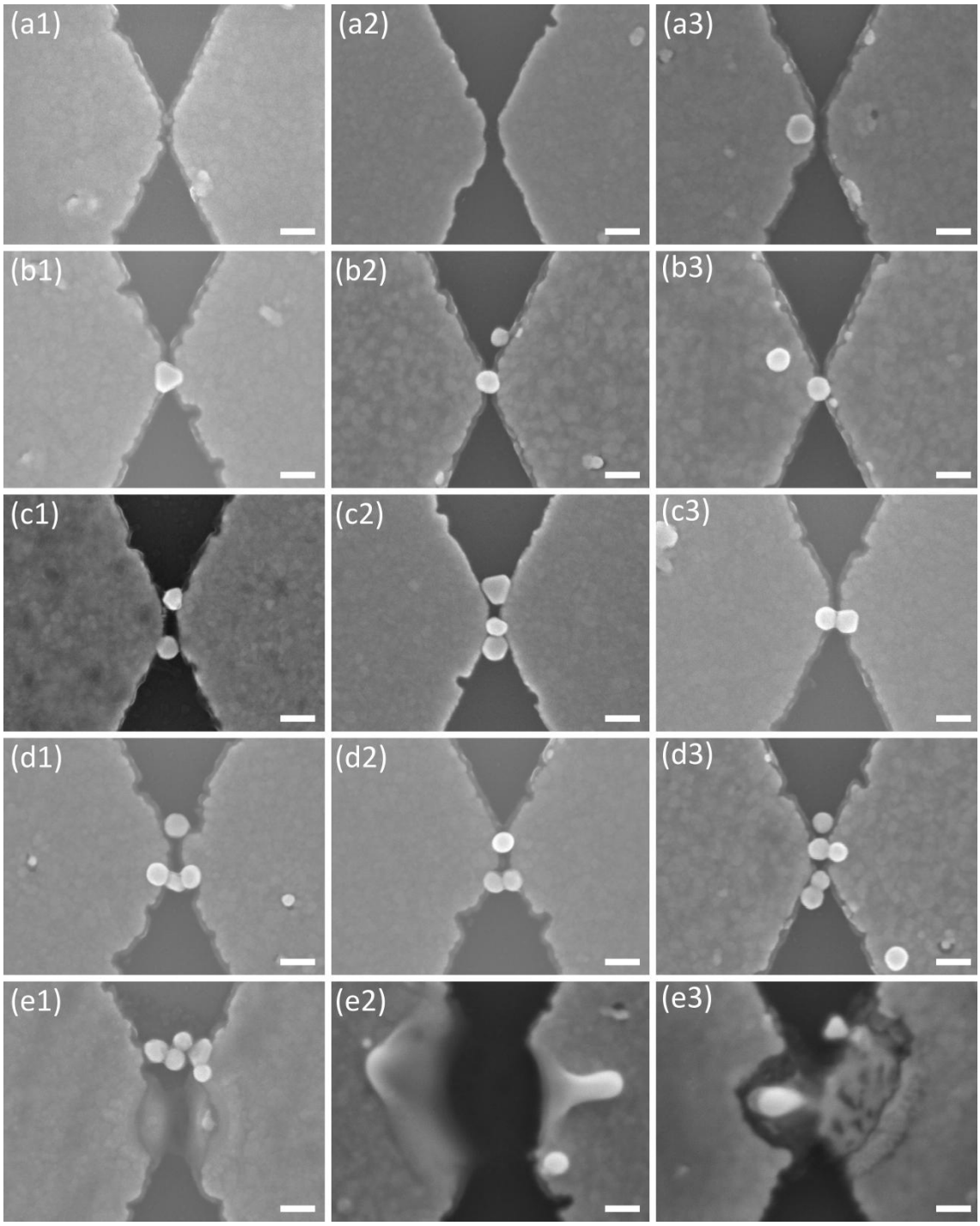

Figure 3.7. Compilation of Scanning Electron Microscopy images of typical nanocrystal assemblies. An overview of typical devices imaged by Scanning Electron Microscopy is presented. The scale bar is 100 nm in all images. Panels (a1-a3) show nano-scale gaps left empty after trapping (~25% of the cases). Panels (b1-b3) show the case of single particles trapped. Panels (c1-c3) show parallel or series assemblies. Toogether, panels (b) and (c) account for most trapping cases. Panels (d1-d3) present more complex nanocrystal assemblies (with both parallel and series nanocrystal bridging). Panels (e1-e3) show damage caused to the nanoscale gap during measurement for which a large bias was applied, $|V_{ds}| > 0.5\ \mathrm{V}$. Other damage patterns (not shown here) may be observed at the scale of a few micrometres as opposed to a few nanometres resulting from an ESD failure.

The SEM images show grain boundaries in the metallic electrodes. Although the electrodes are typically made of three different stacked metallic layers (3 nm Ti, 3 nm Pt, 20 nm Au), we believe the grains noticeable are made of gold. Qualitatively, it looks the grain size distribution is centred at ~40 nm (2/3 of the nanocrystals diameter) in the bulk of the electrode whereas the electrode edges tend to show larger grain sizes in some places (bigger than the nanocrystals, marked by notches on the edges).

3.2.3.2 Molecular functionalisation

The thiophene-terminated "rigid-rod" linker — 1,4 di(3-thiophene)ethynylbenzene (DTEB) molecule was synthesised by Emma Harvey in the laboratory of Dr. Mary Pryce in DCU, Dublin. According to the ChemDraw software, the molecule length is calculated to be 1.5 nm, see Figure 3.8. It can be dissolved in non-aqueous solvents like tetrahydrofuran or dichloromethane.

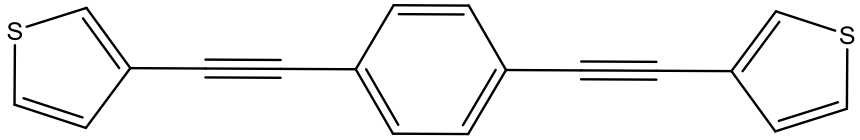

Figure 3.8. Chemical formula of the "rigid-rod" linker molecule –1,4 di(3-thiophene)ethynylbenzene (DTEB) in use for functionalisation the nanocrystal assemblies.

For the comprehensive fabrication/characterisation process, a solution of 2 mM DTEB in dichloromethane was prepared. Electrode chips were immersed in small volumes of the non-degassed solution for ~ 24 hours in the laboratory (in the dark and at room temperature) for the functionalisation step. No temperature control was applied during the immersion. The sample was then rinsed briefly in isopropyl alcohol (<5 min) and blown dry in a gentle stream of nitrogen.

It is believed the immersion of the sample in the molecular candidate solution results in the adsorption of molecules on the exposed gold surfaces area. The molecular functionalisation thus consists in a self-assembled layer being formed on the electrodes and particle(s). More interestingly molecules may adsorb in the junction area between the particle and the electrode.

3.2.3.3 Current-Voltage measurement technique

We use the classical technique of performing current versus voltage measurements I(V) on nanocrystal-molecule devices. They are characterised using semiconductor parameter analysers: Agilent HP4156A, Agilent E5270B interfaced to a PC by a custom programme developed by the author. For all measurements, a voltage bias is forced between the source and drain and/or source and gate and currents flowing through the source, drain and gate ports are recorded, see Figure 3.9a.

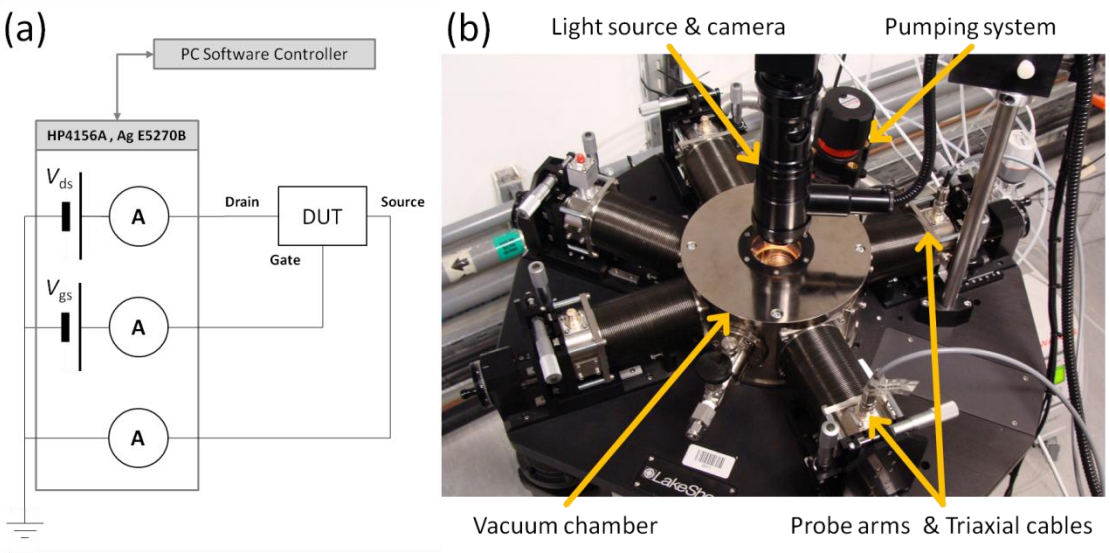

Figure 3.9. Devices are tested using semiconductor parameter analysers. (a) Schematic of the current-voltage measurement setup interfaced to a PC. (b) Photograph of one of the two cryogenic probe stations used for the room temperature measurements under vacuum (Lakeshore TTPX Cryogenic Probe Station). Devices were all tested at $V_{gs} = 0$ V.

Devices are measured in either of the manual cryogenic probe-stations under high vacuum: Lakeshore TTP4-HF-HT Desert System or Lakeshore TTPX Cryogenic Probe Station, see Figure 3.9b. For low-temperature measurements, cryogenic liquids such as liquid nitrogen or liquid helium can be used along with electrical heaters. A custom setup involving three different temperature probes (installed inside the vacuum chamber and along the cryogenic liquid flow system) are coupled to a PID temperature controller so that a chosen temperature, T, for the current-voltage measurements can be set in the range of $4.2\ \mathrm{K} \leq T \leq 400\ \mathrm{K}$ (with a precision better than 1 Kelvin).

Current flowing through the source and drain ports are recorded. By construction of the devices, it is expected source and drain currents are equal in magnitude and opposite in sign. A correlation test is ran for each trace between source and drain currents (I_S and I_D, respectively) to check the relevance of the measurement. In case of a correlation factor below 0.95, the entire measurement is discarded. When the test is passed, we consider $I_d = (-I_S + I_D)/2$ as a measure of the current passing through the device.

For all devices, multiple measurements are done for which different voltage scan rates are chosen so as to test the repeatability of the current-voltage response. In most cases, device characteristics overlap nicely. Typically curves are constructed from series of measurements performed using with at least two different voltage scan rates.

Each measurement data is processed so as to generate an interpolated $I(V)$ curve onto a chosen and constant voltage bias fine grid. The interpolation routine is based on the "Spline" method ensuring the output trace passes exactly through the actual measured data points. This initial layer of data processing will make it easy to compare device responses and characteristics regardless of where the actual measurement points were taken. Once this is done, we use the Savitsky-Golay filter[21] on interpolated data so as to gently smooth the $I(V)$ characteristic. A first order filter on a 5-point window is implemented. Current-voltage characteristics are presented showing the average data (line) and standard deviation (error bars) of the current-voltage values for each voltage bias of the interpolation grid. Consistently with the measurements, the curves obtained present little broadening, see Figure 3.10.

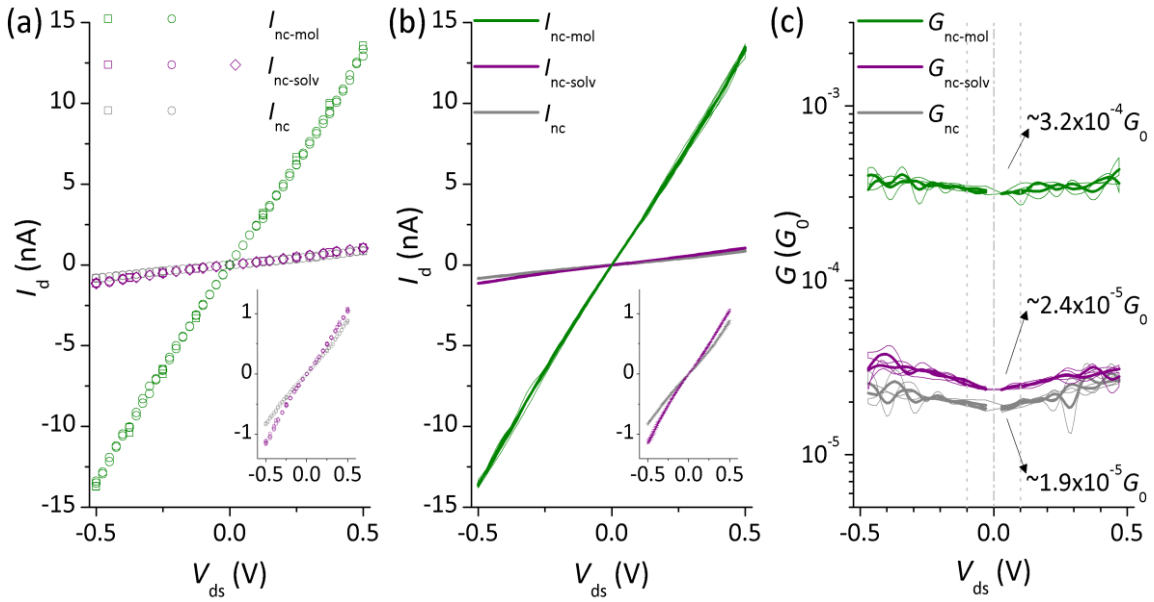

Figure 3.10. We present the example of the device shown in Figure 3.1. (a) Raw current-voltage measurements are presented for the three process steps. The responses after trapping and after solvent immersion are very similar. However the molecular functionalisation brings a stronger current response against the voltage excitation. Two sweeps were completed for I_{nc} (voltage step size: 250 mV, then 25 mV), three sweeps for $I_{\mathrm{nc\text{-}solv}}$ (voltage step size: 125 mV, 50 mV, and finally 50 mV), and two sweeps for $I_{\mathrm{nc\text{-}mol}}$ (voltage step size: 125 mV, then 25 mV). (b) The interpolation of the raw data is shown using a pre-defined grid with a step size of 10 mV. The average and standard deviation values are presented for each process step. (c) Using the interpolated values, the first derivation of the current-voltage is calculated. This shows the value of the conductance versus the voltage, the estimate of low bias conductance is shown for the positive quadrant $|V_{ds}| \leq 100$ mV. The uncertainty on the estimates of conductance can be related to the standard deviation of the different differentiated curves: it is limited to $4 \times 10^{-7}\ G_0$ for G_{nc}, $6 \times 10^{-7}\ G_0$ for $G_{\mathrm{nc\text{-}solv}}$ and $1 \times 10^{-5}\ G_0$ for $G_{\mathrm{nc\text{-}mol}}$ respectively.

The first and second derivatives of the source-drain current are then calculated using a local estimation of the slope on a 5-point window. As for the interpolated $I(V)$ data, each derivative is smoothed using the same Savitsky-Golay filtering. The advantage can be readily seen on the aspect of the curves: smoother curves with damped fluctuations are observed. We use the first derivative of the current to estimate the value of the dynamic electrical conductance $G = (dI/dV)/G_0$ (see Figure 3.10). Generally, the value of G does not vary much over the source-drain bias window. Conversely with the results for direct $I(V)$ measurements, the values of the dynamic conductance for positive and negative excitations are nearly symmetrical. We estimate the near 0 V bias conductance ($|V_{ds}| \leq 100$ mV) by averaging the values of G over this range for each quadrant. One can calculate the second derivative of the current but fluctuations that may arise are actually artefacts of the calculations.

Moreover, the dynamic value of the conductance may be averaged over the positive (negative) range and simply referred as conductance. We may then use the symbols G_{nc}, $G_{nc-solv}$ and G_{nc-mol} in place of $\langle G_{nc} \rangle$, $\langle G_{nc-solv} \rangle$ and $\langle G_{nc-mol} \rangle$ for the sake of simplicity.

For the first few devices measured, rather large voltage bias conditions were explored, exceeding ± 1 V, resulting in irreversible modifications (damage) of the device, see Figure 3.11. It was found that, at room temperature, instabilities (hysteresis: trace and retrace being different, pronounced non-repeatability: 2 consecutive measurements being different) in the current-voltage characteristics appear for biases above ± 0.7 V.

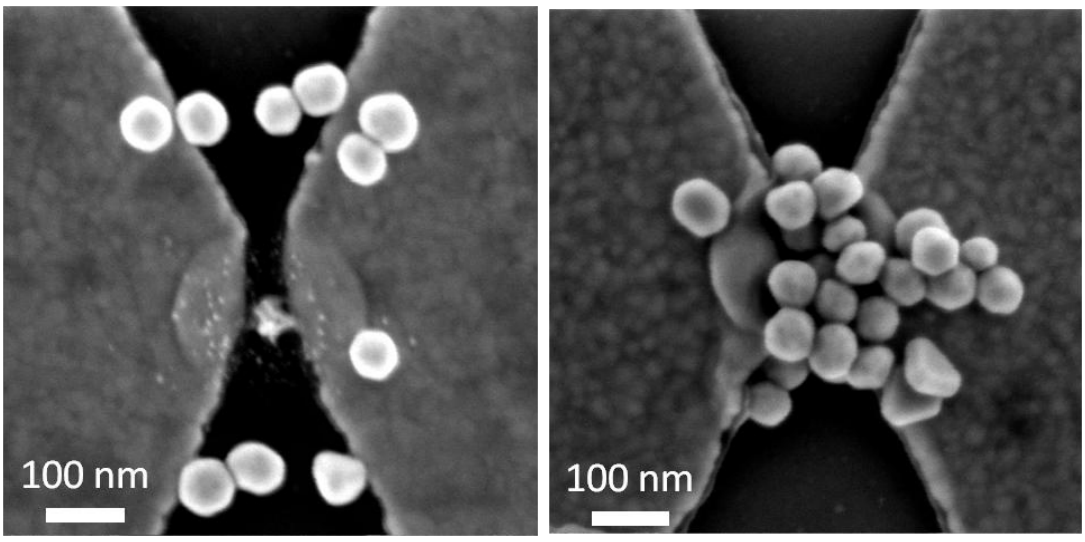

Figure 3.11. Scanning Electron Micrographs of damaged devices because of overload when applying a too large voltage bias V_{ds}. (a) A nanocrystal is believed to have burst in the middle of the nano-gap (device: X-4407_W1_L_0204). (b) This assembly of nanocrystals is also irreversibly damaged due to the electrical stress applied (device: X-4407_W1_J_ 1316). The SEM images were acquired with the JEOL JSM 6700-F instrument.

Eventually, the investigation protocol was typically to bias the device in the range $-0.5\ \mathrm{V} \leq V_{ds} \leq +0.5\ \mathrm{V}$ at maximum. In certain cases however the devices may have been tested further, only after the nominal bias range was tested.

3.2.3.4 Scanning Electron Microscopy of devices

Samples were imaged using a Scanning Electron Microscope to reveal the particle distribution in the electrode gap region (using either a JEOL JSM 6700-F, JSM 7001-F or JSM 7500-F). SEM micrographs were taken for each device in order to analyse the particle distribution in the region of interest about the electrode gap. Among other characteristics, records of the number of particles bridging the gap in the shortest chain were taken into consideration to qualify the effectiveness of the DEP trapping. We distinguished three different populations:

i. no particles bridging the gap,
ii. the shortest chain was composed of only one particle ($N_{DEP,compo} = 1$),
iii. the chain contained two nanocrystals or more.

Some of the gaps may not have fallen into these populations, for instance when the gap was somehow hidden, damaged, etc.

A routine imaging was performed for each device manufactured, at a magnification of at least $\mathrm{X}\ 10{,}000$ for empty gaps or damaged devices, at $\mathrm{X}\ 30{,}000$ or higher for devices presenting a nanocrystal assembly, see both Figure 3.7 and Figure 3.11.

First of all, it consistently appears the absence of particle in the gap is highly correlated to a conductance attributable to an open circuit. Typically about $|I_s| = I_d = 100\ \mathrm{fA}$ at $V_{ds} = 0.5\ \mathrm{V}$ is defined as the limit of accurate conductance detection: $G_{lim} \sim 2.5 \times 10^{-9} G_0$. Nevertheless, there are a few occasions where a conductance can be measured even if no particle is noticeable in the gap. This can be explained by acknowledging the electrode fabrication process is not perfect. Metal (gold) filaments, thin titanium oxide layer (from the adhesion layer), or even some process residues may provide a way for carriers to flow between the electrodes.

Looking at the situation where one or more particles form(s) a chain bridging the gap, one can see there is a very wide distribution of conductivities associated: from below the limit of detection to one tenth of the quantum conductance, $G_0 = 2e^2/h \sim 77.5\ \mu\mathrm{S}$ (a very limited number of devices presented a conductance on the order of or above 100 times the quantum conductance). Overall, it looks like the structure of a particle chain does not dictate a particular conductance.

3.2.4 Compiling data from different sources

The device manufacturing process is of low yield. Moreover a device can only be screened as a "working device" if it is electrically measured. The quantity of raw data $I(V)$ is indeed significant and to avoid being overwhelmed, there is a need to organise these information into a meaningful and relevant fashion for notably allowing comparison between devices.

At room temperature and at low source-drain bias regime $|V_{ds}| \leq 0.5$ V, the technique in itself does not provide directly much information as the response of such devices seems to be following a linear regime. In order to get more insights in the mechanism of transport for charge-carriers, we try to highlight trends in the data set by relying on different data processing methods.

A flexible Matlab™ programme has been written to parse in an automatic manner all information acquired during measurements on the form of raw data text files. An $I(V)$ characteristic consists in applying a voltage bias sweep and recording values of currents, this can be done over different ranges, sweep polarity and trace directions.

The programme uses three batch files providing links to raw data files or manually generated statistical data.

3.2.4.1 Current-Voltage data

Let us concentrate on the $I(V)$ data files. The programme will read all linked data files and extract the information herein. Figure 3.12 summarises the organisation of the structure 'rdev' used to collect the raw data. There is one entry for each device in the structure. For each entry, raw measurement data of each measurement performed on that particular device is also stored. Another structure 'pdev' contains the interpolated and further processed data. Finally a third structure 'edev' is used to store temporary calculated data for each device.

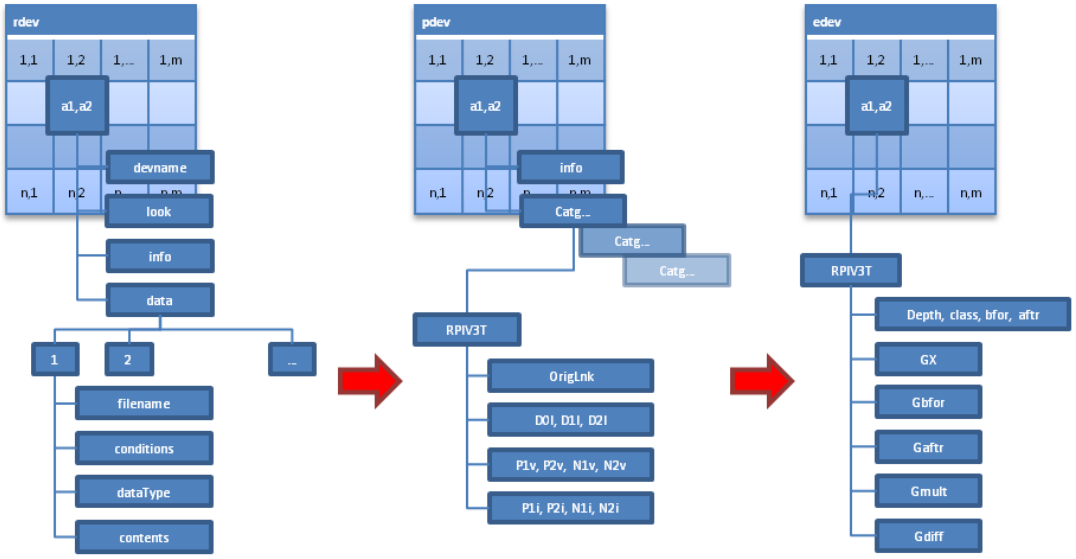

Figure 3.12. Tree-view schematic of the internal structures 'rdev', 'pdev' and 'edev' used in the Matlab programme. They are partially expanded for the first device. The 'rdev' (r for raw) structure contains all the digested raw data, 'pdev' (p for parsed) gathers processed data (using the interpolated data to calculate conductance, etc.), 'edev' (e for explore) has a content that changes depending on the plot requested.

For each measurement, the bias conditions and current measurement conditions are extracted. A copy of the measurement values (voltage bias values and current data points) is done. At no time is the raw data altered. The programme always keeps raw records intact. As a pre-processing step, the recorded voltage sweeps are then all classified into four different divisions: depending on the sweep polarities and the trace directions. Sorting raw data in this context ensures consistent comparisons between data sweeps.

The programme does a second pre-processing to sort this information into categories depending on the process step at which a measurement was performed: after trapping, after immersion in a solvent, after functionalisation with molecules, or virtually any other step or combination of them.

Within each of these categories, the raw data is processed so as to extract the interpolated $I(V)$ curves, the first and second derivatives as well as details on the potential bias conditions, explored range, etc. Indeed the first and critical data processing that the programme performs is analysing these currents: it interpolates the values onto a chosen and constant voltage bias grid. The data interpolation is merely based on a first order polynomial regression ensuring the output trace passes exactly through the actual measured data points. This initial layer of data processing will make it easy to compare device responses and characteristics regardless of where the actual measurement points were taken.

From the interpolated curves, a large variety of plot types is available. For instance $I(V)$ on a log-log plot, so-called Fowler-Nordheim plot $\left[ln\left(\frac{I}{V^2}\right)\right]$ $vs.\left(\frac{1}{V}\right)$ and $Q(t)$ charge-time dependent plots can be investigated to monitor the device behaviour. In practice, the information derived from the first derivative of the current reveals the most detail.

3.2.4.2 DEP trapping data

Manufacturing of the nanocrystal-molecule devices remains a statistical process. As such, it is critical to keep as much detail as possible about the process conditions. For that matter, for each device manufactured, the date; the surface cleaning and treatment; the dielectrophoretic trapping frequency; driving voltage and duration; the back contact and user comments are recorded.

A manual image analysis routine was developed to extract key parameters of the nanocrystal distribution in the assembly trapped in the electrode gaps.

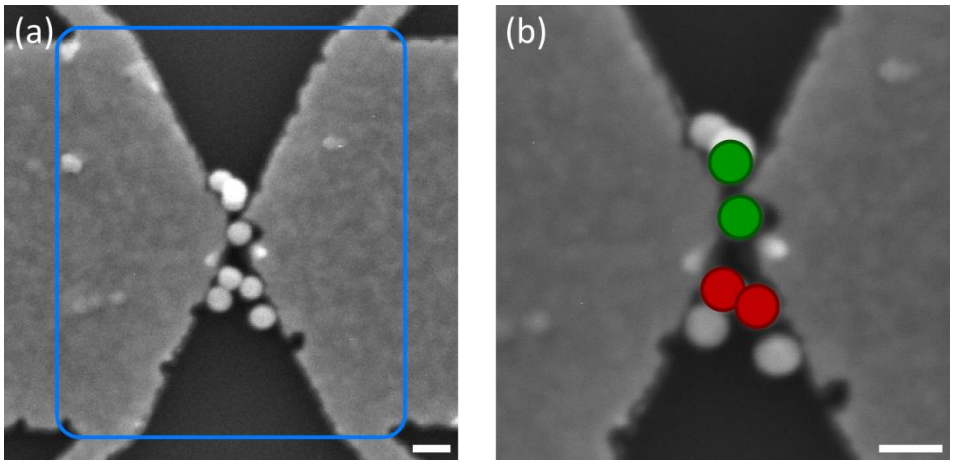

Figure 3.13. Example of analysis of the DEP trapped particles in the electrode gap region. (a) SEM of the area of interest considered for counting nanocrystals is presented. (b) Zoom-in image of the same device: one can identify the presence of 8 gold nanocrystals. Based on the electrode thickness (~ 26 nm), nanocrystal diameter (60 nm, nominal value) and nanocrystal brightness, 3 bridges can be detected. As a guide to the eye, we overlay coloured disc on top of particles forming an identified bridge, in one case: in green colour (single particle bridge) and in the other in red colour (two-particle bridge). The shortest bridge is made of only one particle. Scale bars are $100\ \mathrm{nm}$ on both pictures.

First of all, the number of particles ($N_{DEP,all}$) in the vicinity of the gap is recorded. For practical reason, the region of interest is mainly defined by the electrode design, i.e.: we count particles sitting within a rectangle of $800\ \mathrm{nm} \times 1\ \mu\mathrm{m}$ as can be seen on Figure 3.13. Then, two other numbers are extracted to characterise the composition of structures bridging the gap, if

any. On one hand, the shortest bridge is looked for and the number of particle(s) in it is stored ($N_{DEP,compo}$), on the other hand, we estimate the number of parallel bridges ($N_{DEP,bridges}$).

The number of particles in the region of interest is believed to provide qualitative information about the DEP trapping process: we aim at a rather low number, i.e.: less than 10 particles.

At this stage we need to underline the fact the conductance of a contacted molecule is expected to be far lower than the quantum conductance, (i.e.: resistance $\gtrsim 1\ \mathrm{M\Omega}$). In that sense we aim at having the shortest bridges in our nanocrystal-molecule devices to avoid series of resistance, i.e: $N_{DEP,compo} = 1$ and conversely, we also aim at lowering the number of bridges to avoid parallel conductance paths ($N_{DEP,bridges} = 1$). Ideally, the device would only present one particle bridging the gap between the two electrodes which simplifies the analysis of the electrical device characteristics.

To work in parallel with the $I(V)$ measurement database, two supplementary databases have been created to compile links to SEM micrographs and relevant manual DEP trapping qualification statistics.

3.3 Results

For all the data presented, only measurements performed in the range $-0.5\ \mathrm{V} \leq V_{ds} \leq +0.5\ \mathrm{V}$ (with a tolerance of $\pm 10\%$) are presented. If ever a device was measured at any stage at tougher bias conditions, all further measurements are discarded as it clearly appears that non-linearity effects that may arise in the $I(V)$ curves are merely the result of nanocrystal-metal electrode excitation, instability and eventually leading to morphological changes, as shown in Figure 3.11.

Comparing all device responses (across the entire dataset or part of it), the current-voltage characteristics appear roughly symmetrical about the point of 0 V bias. We calculate the rectification factor $Z(V_{ds}) = |I(-V_{ds})/I(V_{ds})|$ to investigate the propensity to conduct the current better in negative bias conditions than in positive bias conditions. The rectification factor is near unity for all devices over the entire source-drain bias window ($|V_{ds}| \leq 0.5\ \mathrm{V}$). This shows positive and negative bias excitations are extremely similar if not equivalent: there is very little asymmetry in the device response under positive and negative biases.

Along the same lines, linear I(V) responses are observed most frequently, but non-linear characteristics are observed repeatedly for some devices. Linear response in the I(V) curves occur in most cases while sigmoid-like curves are seen in ~ 15% of the cases (for the comprehensive process flow data set). Based on these observations, we will thereafter only present results from measurements performed in positive bias conditions (unless otherwise stated).

3.3.1 As trapped nanocrystal assemblies in nano-gaps

Electrical tunnelling current through assemblies of nanocrystal bridging the nano-scale electrodes is measurable in more than 62% of the devices. The entire data set and to a lesser degree sub data sets shows a log normal distribution of conductance at low bias: $G_{nc} < G_0$, where G_0 is the quantum conductance, see Figure 3.14. The distributions are centred at $\sim 2 \times 10^{-5} G_0$. The large variety of junction configurations (at the angstrom/nanoscale) in terms of interface distance, area and permittivity explains this wide-spread distribution resulting from tunnelling current at low bias $|V_{ds}| \leq 100$ mV (only positive quadrant presented here).

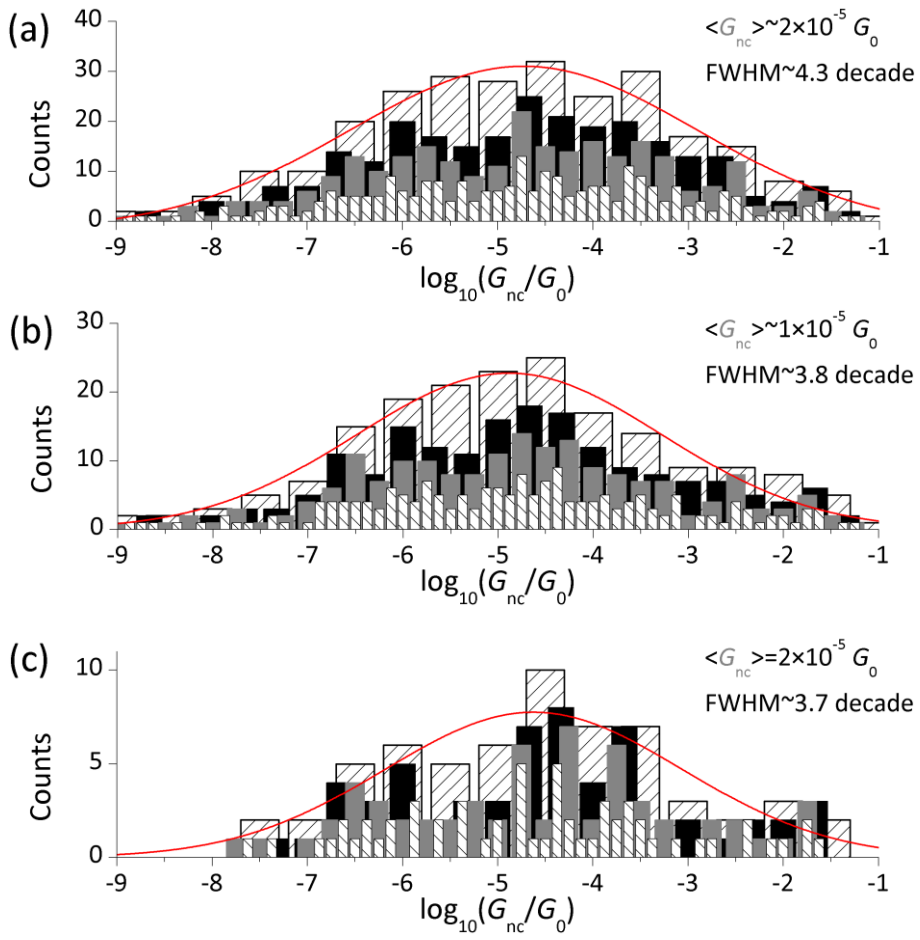

Figure 3.14. Histograms of the after trapping conductance estimates (Gnc). In all sub-figures, different bin sizes (per decade: 1, 2, 3, 4 and 8 bins) are used to build the histograms. The distribution of G_{nc} is distributed on a wide band spanning across 8 decades. (a) Conductance estimates at low bias are shown for all devices characterised at the stage of as trapped nanocrystals: results for 380 devices are compiled in this plot. A decimal log normal distribution is found for largest bin sizes: a signature of the tunnelling nature of the current (log dependence), the distribution seems to peak at $\sim 2 \times 10^{-5} G_0$ with a FWHM of ~4.3 orders of magnitude. (b) Sub-set histogram of (a): Conductance estimates are shown for 185 devices (notably including the ones used for the study of solvent immersion effects). The distribution is centred at $\sim 1 \times 10^{-5} G_0$, with a similar FWHM~3.8 decades. (c) The sub-set of data used in the text for studying fully molecular functionalised devices is also presented. These results originate from four different chips comprising a total of 96 devices. Values are presented for 60 devices for which measurements after all process steps could be performed (more than 62% of the devices prepared). In good agreement with the two other data-sets, the decimal log-normal distribution presents a peak at $\sim 2 \times 10^{-5} G_0$.

Even with an extremely careful control of the surface cleaning and preparation, the variability in distance and shape of the interfaces between metallic nodes cannot be suppressed. Therefore, the large distribution in conductance at low bias is believed a characteristic of assemblies of nanocrystals.

Let us explore the landscape of one nanocrystal—electrode interface. The gold nanocrystals used for the assembly between electrodes are colloids stabilised in a buffer solution of trisodium citrate in water solvent. Quantum chemistry simulations performed by Damien Thompson in the Electronics Theory Group at Tyndall show citrate molecules bind on gold surfaces using only one of the three carboxyl groups, forming a neutral covalent bond COO—Au. The two other deprotonated carboxyl groups are found to be screened by Na^+ counter-ions, see Figure 3.15. When trapping particles using the dielectrophoresis force, the gold electrodes are exposed to the buffer solution for a typical duration of 45 minutes, allowing citrate ions to bind on the electrode surfaces. Afterwards the samples are simply dried in a stream of nitrogen (as opposed to be baked in vacuum at high temperatures). Based on the grounds of molecular dynamics simulations on the hydrophilic nature of the citrate sodium complex, it is believed a nanometre thin film of water remains adsorbed covering gold surfaces, notably in the electrode—nanocrystal interface. From simulations on (111) gold surfaces the coverage by citrate ions screened by sodium cations is dense with an apparent monolayer thickness of ~ 0.7 nm. Moreover the few layers of water molecules expected to remain present should form a film of a thickness on the order of 0.5 nm.

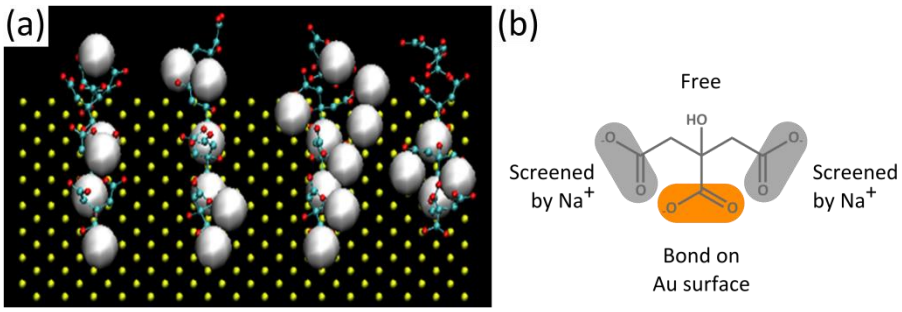

Figure 3.15. Citrate bonding on gold (111) surface in the presence of sodium cations. (a) Molecular dynamics of tri-sodium citrate covered Au nanocrystals in water (performed by Dr. Damien Thompson, Cork), after 20 ns of free dynamics, each citrate has 1-2 remaining sodium counter ions; short inter-citrate distances means cations are continuously shuffled between citrates as well as between carboxylates on each citrate. Persistent ion pairing at the surface reduces the NP-NP repulsion. Water molecules (not shown for clarity) mediate carboxylate-sodium-carboxylate charge networks and assist re-shuffling of cations at the surface. (b) Summary schematic of the chemical structure of the citrate ions bound on a gold surface and screen by Na^+ cations.

3.3.2 Solvent immersion effect

Measurements after trapping of nanocrystals show a background conductance, G_{nc}. As discussed the electrode—nanocrystal interface is not bare implying that charge carriers (likely holes) do not tunnel through vacuum but rather through a mixture of stabilising citrate ions screened by sodium counter-ions with water molecules adsorbed.

To characterise the influence of the exposure of the nanocrystal assemblies to non-aqueous solvents (typical solvents for molecules to be studied), we have conducted experiments involving different samples (for a total of 169 devices) and several non-aqueous solvents (hexane, dichloromethane, tetrahydrofuran, isopropyl alcohol, acetone) with different polarities and dielectric permittivities, see Table 3.1.

Solvent	**Hexane (HXN)**	**Dichloromethane (DCM)**	**Tetrahydrofuran (THF)**	**Isopropyl alcohol (IPA)**	**Acetone (ACN)**
Permittivity	ε_r~1.89	ε_r~8.93	ε_r~7.52	ε_r~20.18	ε_r~21.01

Table 3.1. Solvent and related permittivity (experimental values taken from ref. [22]).

For each solvent, we report the solvent immersion contribution by plotting the low bias conductance measured after solvent immersion ($G_{nc-solv}$) versus its value just after trapping (G_{nc}) in a log-log plot, see Figure 3.16. The bisector line (dashed gray line) indicates the limit case of no change ($G_{nc-solv} = G_{nc}$). As a guide to the eyes, we also show lines marking an increase or a decrease by a x5 fold factor (dashed red lines, above and below the bisector line respectively).

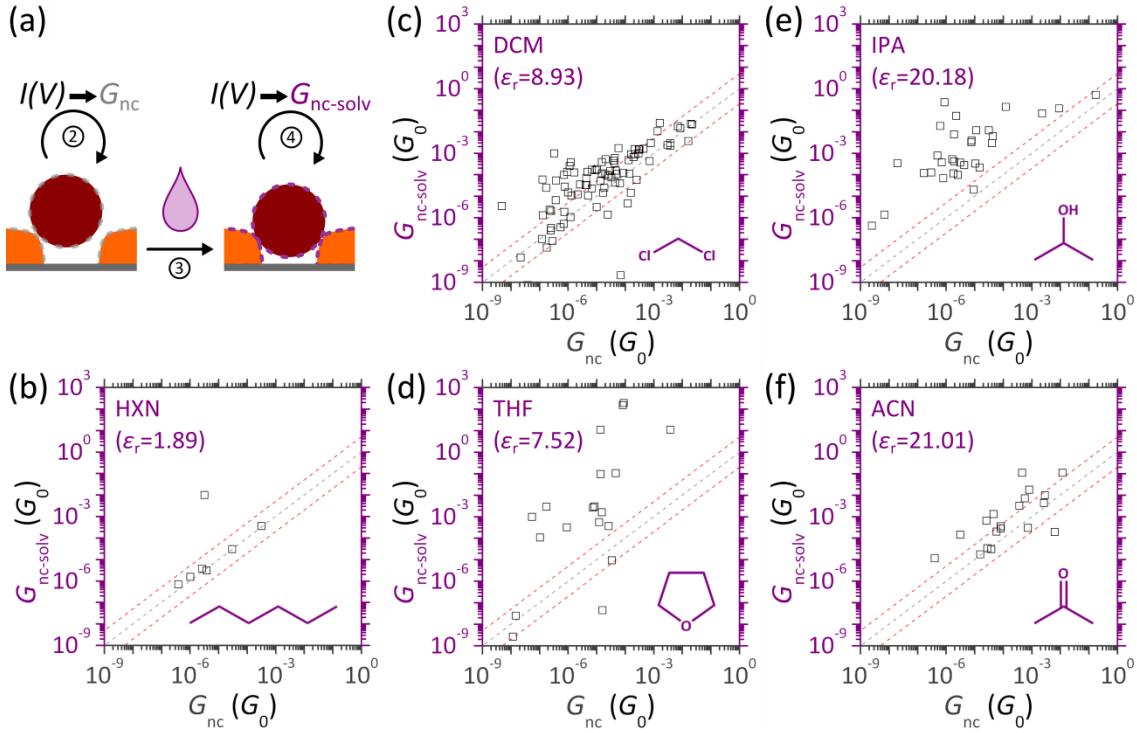

Figure 3.16. Investigations of the solvent immersion step on the conductance of devices. (a) After dielectrophoresis trapping of nanocrystal(s), the assemblies are characterised electrically to estimate their conductance at low bias: G_{nc}. Afterwards, electrode chips comprising up to 24 devices are immersed into a pure solvent for ~24 hours. Following the solvent exposure, devices are re-measured in the same vacuum conditions at room temperature to estimate the conductance $G_{nc-solv}$. Several non-aqueous solvents with different permittivities and polarities were experimentally investigated: (b) hexane (7 devices); (c) dichloromethane (88 devices); (d)

tetrahydrofuran (20 devices); (e) isopropyl alcohol (34 devices); (f) acetone (20 devices). As a guide to the eyes, the gray dashed line marks the bisector line ($G_{nc-solv} = G_{nc}$), whereas the red dashed lines correspond to an increase or decrease by a factor of 5, respectively.

For all solvents, points are scattered about the bisector line. For the few devices presenting large low bias conductance values $G_{nc} > G_0$ (not shown in the plots), the solvent immersion step does not lead to any noticeable change in conductance ($G_{nc-solv} \sim G_{nc}$). While hexane (Figure 3.16b) shows the lowest spread of data points with a near zero variation except for one outlier point, isopropyl alcohol (Figure 3.16e) markedly leads to higher conductance after solvent immersion (mainly by at least 2 orders of magnitude). The solvent tetrahydrofuran (Figure 3.16d) seems to present the largest scattering: rather large $G_{nc-solv}/G_{nc}$ ratios, and large spread of $G_{nc-solv}$ for a given G_{nc} range of values. Overall, we found a certain correlation between the permittivity of solvents and the likelihood of conductance change. The general trend is high permittivity solvents lead to higher $G_{nc-solv}/G_{nc}$ ratios.

3.3.3 Comprehensive process flow

A sub-set of 96 devices is fully characterised. Based on the results presented in Figure 3.16 and on the solubility of DTEB molecules, dichloromethane was chosen as the mediating solvent (the fabrication process flow is summarised in Appendix – 6.6, p. 205).

From all data measured across four different samples comprising $24 \times 4 = 96$ devices, we present a total of 60 fully characterised devices. The remainder, $96 - 60 = 36$ devices did not show measurable electrical response. Low bias conductance data extracted from $I(V)$ data acquired after each process step are presented for each device: after trapping (G_{nc}), after solvent-immersion ($G_{nc-solv}$) and after molecular functionalisation (G_{nc-mol}). On a device basis these values form triplets. The values presented in the discussion are for a positive bias as the rectification factor $Z(V) \sim 1$.

We propose to partition the entire dataset into three classes, regardless of the device origin, see Figure 3.17b. Conductance values are consistently classified using the following scheme: class A corresponds to devices having $G_{nc-mol} < G_{nc}$, class B gathers devices for which $G_{nc} < G_{nc-mol} < G_{nc-solv}$, and finally class C groups devices such that $G_{nc} < G_{nc-solv} < G_{nc-mol}$. For more readability of the plot, triplets of values are sorted by increasing values of $G_{nc-solv}$ within each class.

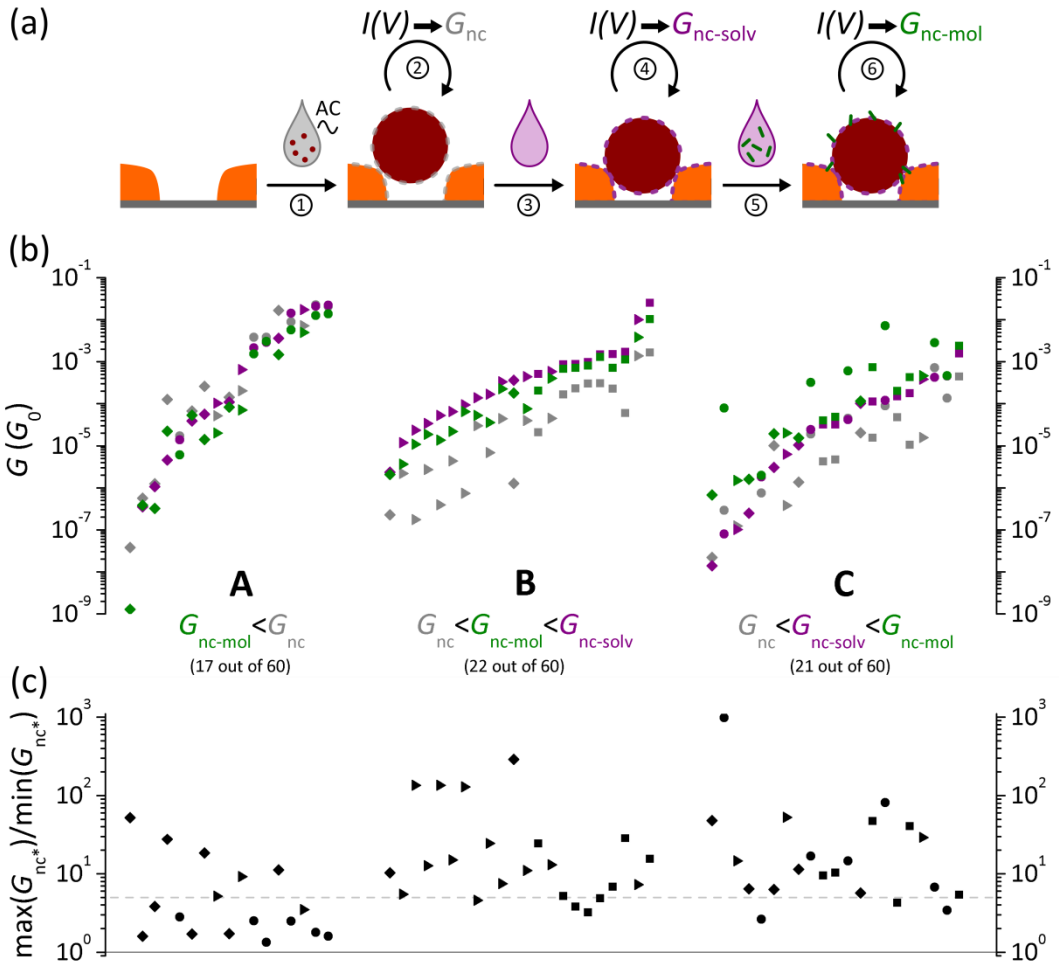

Figure 3.17. (a) Reminder on the fabrication process-steps investigated: triplets of estimated conductances are consistently compared on a device basis. (b) The scatter plot presents conductance values after trapping (G_{nc}, gray points), after solvent-immersion ($G_{nc-solv}$, purple points) and after molecular functionalisation (G_{nc-mol}, green points). More than 60 devices across four different chips are shown (hence the different symbols: circle, diamond, triangle and square). As a guide to the eye, we propose to sort the data into three classes: A (17 devices), B (22 devices) and C (21 devices) depending on the relative value of conductance at low bias measured after each process step. (c) To investigate the relevance of variations within triplets values (G_{nc}, $G_{nc-solv}$ and G_{nc-mol}) across the dataset, we define the contrast factor (ratio of the maximum over the minimum for a given triplet). As a guide for the eyes, the dashed gray line marks x5 value delimiting the threshold for which substantial changes happen.

At first glance, on a device basis, comparing the amplitude of triplets for the three classes, one can readily see class A presents the lowest variation. This is confirmed by plotting per triplets the ratio of the maximum over minimum conductance value, see Figure 3.17c. Most points in class A are centred at x2.5 or at least below the x5 threshold (dashed line), whereas the vast majority of points for both classes B and C are above this threshold.

By definition, class A devices exhibit the cases $G_{nc-mol} < G_{nc}$. Most triplets of points are closely packed. For the few devices with the largest amplitude between points, G_{nc} is greater than both $G_{nc-solv}$ and G_{nc-mol} (4 cases): this fact tends to indicate these devices were decaying. Moreover, two other devices present rather large amplitude between the triplets, such that $G_{nc-mol} < G_{nc} < G_{nc-solv}$. All other 11 devices present a contrast between the maximum and minimum measured values of conductance below the x5 threshold: this illustrates the case of device stability to both the exposure to the solvent and molecules. In essence, class A accounting for 17 out of 60 devices (28%), reveals aspects of the intrinsic variation of the measurement methodology.

Class B, encompasses $22/60 \sim 37\%$ of the cases. A net increase in conductance is measured at $G_{nc-solv}$ as opposed to G_{nc}. The distribution of the ratio between $G_{nc-solv}/G_{nc}$ is mainly scattered above the x5 threshold, see Figure 3.18a. Conversely with the study of class A showing the intrinsic variation of measurements, one can notice the functionalisation of devices does not bring any further improvement in the conductance, see Figure 3.18b. Nevertheless the decrease in conductance is very limited since the distribution of $G_{nc-solv}/G_{nc-mol}$ does cross-over the x5 threshold limit for only 1 device out of 22. We conclude the molecular functionalisation is not successful for any of these devices.

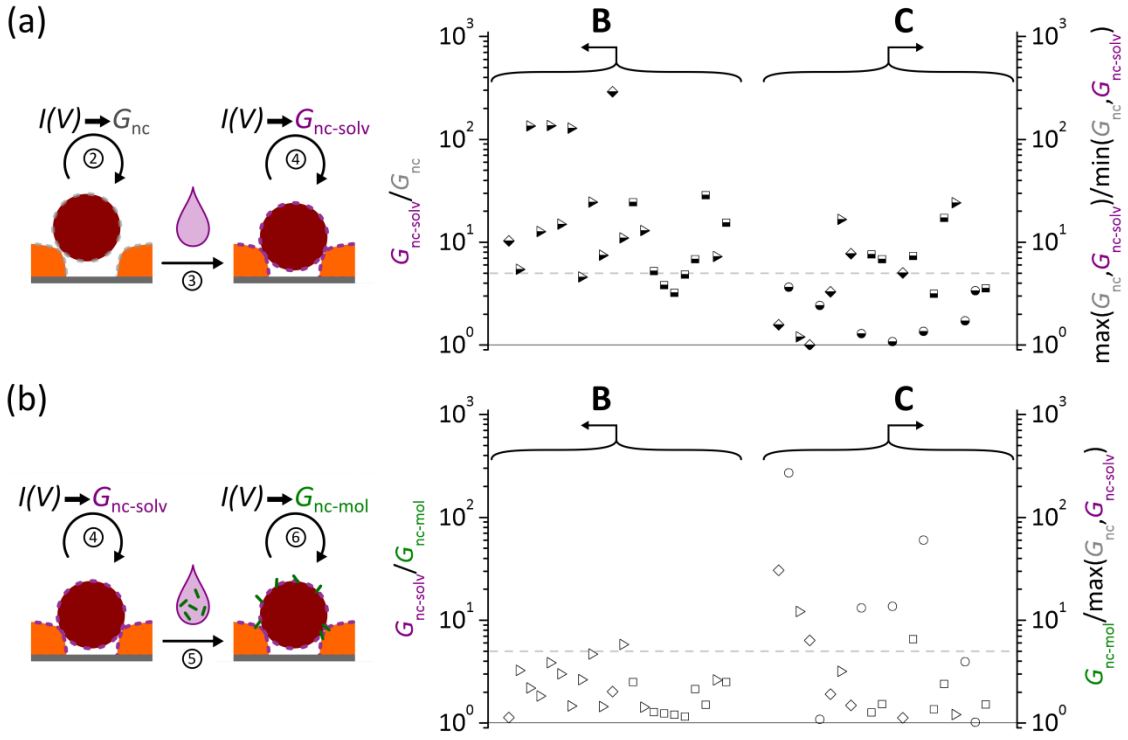

Figure 3.18. Statistical analysis of the data points acquired for 60 different devices across 4 different samples for which a full characterisation was performed (G_{nc}, $G_{nc-solv}$ and G_{nc-mol}). (a) The change from G_{nc} to $G_{nc-solv}$ is investigated for both classes B and C: while the change is significant for all

devices of class B, the scattering for devices of class C is more limited. (b) The change from $G_{nc-solv}$ to G_{nc-mol} is plotted for both classed B and C: the scattering is limited for devices of class B whereas 8 devices show in class C present a noticeable increase.

Finally class C, comprising $21/60 \sim 35\%$ of devices, highlights improvement in conductance after functionalisation: G_{nc-mol} is greater than both G_{nc} and $G_{nc-solv}$. For these devices, the solvent immersion step does not necessarily improve the conductance as shown by the limited scattering of points G_{nc}, $G_{nc-solv}$, see Figure 3.18a. We believe the net increase in conductance after molecular functionalisation is a signature of successful molecular decoration of the device junctions for 8 devices out of 21, see Figure 3.18b. Otherwise, little variations are observed consolidating the idea of intrinsic variation of the measurement methodology: scattering of the distribution below the x5 threshold, see Figure 3.18c.

Overall for the 3 classes from the main dataset presented (including a total of 60 devices) $G_{nc-solv}$ is significantly larger than G_{nc} in 43% of the cases. This corroborates the influence of the sole solvent-immersion step that was studied earlier on.

For sufficiency, we also present the results without partitioning the data into three different classes. We reproduce the conductance results on the dataset of devices from the comprehensive fabrication process. For more readability, the triplets are sorted by increasing values of $G_{nc-solv}$, see Figure 3.19.

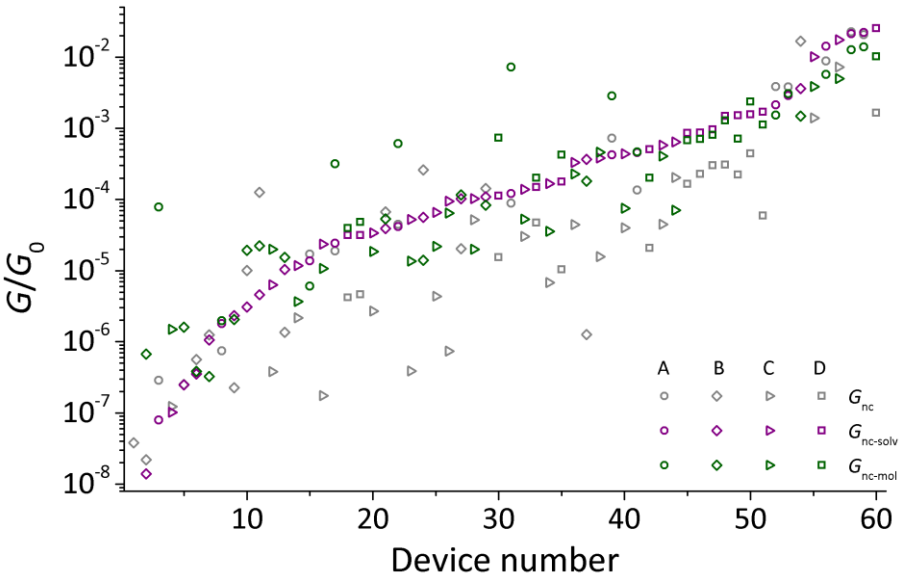

Figure 3.19. Scatter plots showing the entire dataset without partition: triplets of data points of the 60 device dataset (across four different chips: A, circle; B, diamond; C, triangle; D, square) are shown. Conductance values are sorted by increasing values of $G_{nc-solv}$.

Regardless of the electrode chip on which the measurements were performed, values of G_{nc} are mostly scattered below the $G_{nc-solv}$ values, as explained in the previous section 3.3.2 (p. 112).

On the other hand, values of G_{nc-mol} are scattered more uniformly about the $G_{nc-solv}$ values. Nevertheless for a few devices, the values of G_{nc-mol} is markedly larger than $G_{nc-solv}$ (and G_{nc} as well, mostly): we propose the molecular functionalisation process step was effective for these few devices.

Overall, looking at the scattering of triplets, the larger changes between conductance measurements occur for $G/G_0 < 10^{-3}$. This tends to set an upper bound value for the estimation of molecular conductance.

We note that the two descriptions of the data obtained (with or without classification) provide equivalent outcomes that will be discussed thereafter.

3.4 Discussion

We propose different and consistent approaches to model the metal electrode– (molecule-nanocrystal assembly)–metal electrode and thus get insights in the junction properties. Firstly, the Simmons model is introduced to define the extent of the effective background conductance area. Then, we study the junction from a geometrical point of view. Finally the concept of a resistor network is implemented to estimate the single molecular conductance.

3.4.1 The electrode—nanocrystal interface viewed by the Simmons model

Current-voltage $I(V)$ characteristics of similar assemblies of nanocrystals in nano-gaps measured by Dr. Claire Barrett[18] show the conduction of current is not temperature dependent. Furthermore because the conductance is well below the quantum conductance G_0, this is suggesting the main electronic transport mechanism is tunnelling. In a first approximation, the flux of carriers (holes or electrons) can be estimated using the Simmons model.

We propose to use the Simmons model as a tool for investigating the properties at stake in the tunnelling current on assemblies of nanocrystals in nano-gaps. The Simmons model was originally developed to study planar tunnelling junctions.[23] To accommodate the model with our device geometry, differentiating/integrating is introduced in the equation of transport.

As opposed to the initial planar device geometry studied by Simmons, the nanocrystal—electrode interface of our system is curved by construction. One of the characteristics of the tunnelling current is its exponential decay with the electrode separation. Based on this property, we consider in terms of a "classical" description that the charge carrier only "travel" the shortest distance.

We propose a simplistic view of the energy landscape across the metal electrode-molecule-nanocrystal junction, see Figure 3.20a. The shape of the textured barrier is rather crude but is believed to be qualitatively appropriate. From the experimental conditions we can survey the species likely to be present in the junction: the nanocrystal stabilising agents, i.e. sodium and citrate in their ionic form: $\mathrm{HO(C_3H_4)(COO^-)_3}$ anion balanced with 3 $\mathrm{Na^+}$ cations, deionised water, isopropyl alcohol (IPA), plus extra fabrication residues. As a first approximation, we assume we can depict the background medium in the active area of the junction as a continuum whose properties are assumed uniform and isotropic. This will set constant values for the electrical permittivity ε_r, and the effective mass m^*.

In order to describe the junction, we consider both the nanocrystal and the electrode to have a certain curvature at the vicinity of the junction such as they can be merely described as spheres (with possibly different radii: R_1, R_2). This way the problem is axially-symmetric: the landscape is

invariant by rotation around the centre-to-centre axis, see Figure 3.20b. The inter node distance is noted d.

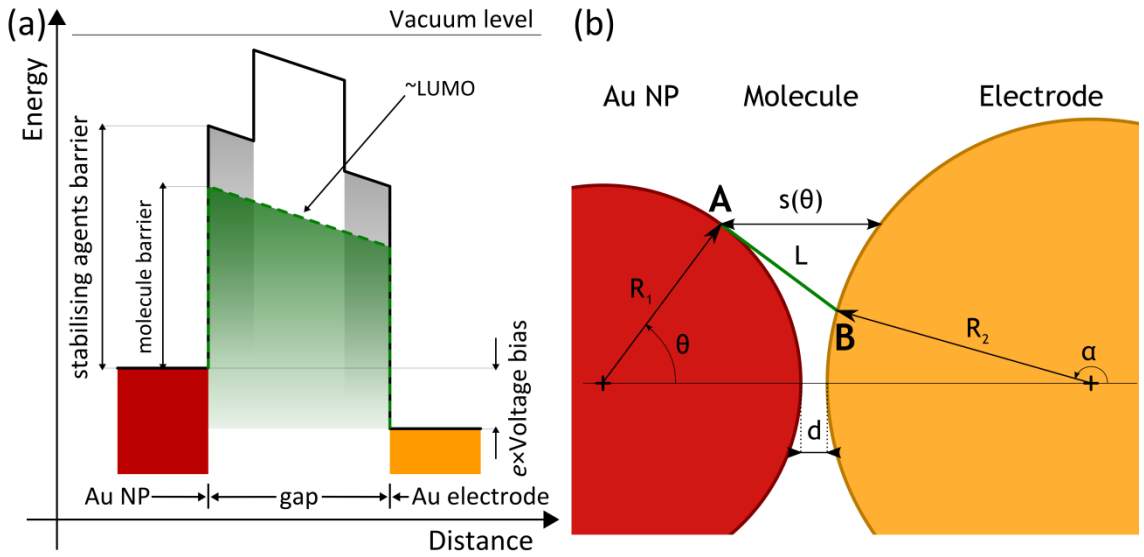

Figure 3.20. Schematic of the nanocrystal-molecule-electrode junction. (a) Energy landscape (in the case of a slight bias). The texture of the barrier is merely anecdotic but shows a molecule is expected to provide a more conductive channel once it is bonded, for instance the Lowest Unoccupied Molecular Orbital (LUMO). (b) Schematic of the binding of a "rigid-rod" molecule in the nanocrystal-electrode interface.

The energy landscape being simplified, we need to focus on the nanocrystal-electrode junction separation $s(\theta)$, as shown earlier on Figure 3.20a. Using simple geometrical arguments, we can derive the expression of the separation as a function of the angle θ, see Equation 3.1. This holds true even for a planar electrode when $R_2 \to +\infty$, narrowing the third term down in the equation.

$$s(\theta) = d + R_1 \cdot \big(1 - cos(\theta)\big) + R_2 \cdot \left(1 - \sqrt{1 - \left(\frac{R_1}{R_2} \cdot sin(\theta)\right)^2}\right)$$

Equation 3.1. Angular separation between surfaces of a nanocrystal and an electrode.

The integral of the flux of tunnelling current is thus done along portions of facing spheres along the centre-to-centre axis, see Equation 3.2.

$$dI/d\theta = J(\theta) \times dS$$

Equation 3.2. Tunnelling current as a function of the deviation angle.

For the integral calculus, we use the definition of solid angle for getting the expression of an infinitesimal corona surface in spherical coordinates. Bearing in mind the flux of tunnelling

current is assumed to be parallel to the axis of the interface, only the projection of the normal vector on the axis of the interface contributes to the current, see Equation 3.3.

$$dS = 2\pi(R_1)^2 \cdot \sin(\theta) \cdot \cos(\theta) \cdot d\theta$$

Equation 3.3. Expression of the infinitesimal corona surface in spherical coordinates, depending on θ, for the calculation of the tunnelling current in the electrode—nanocrystal interface.

The value of the tunnelling current will asymptotically tend to a finite value. This limit value is self-defined by the curvature of the interface nodes. Practically we integrate the tunnelling flux for deviation angle of the centre-to-centre axis up to $20°$ (~10 nm off axis) for which value the current does not increase anymore by any measurable amount. The experimental current resolution is approximated to be I_{res}~100 fA. Implementing the curvature into the Simmons model presents the advantage of removing the unknown of the extent of the tunnelling area, see Figure 3.21.

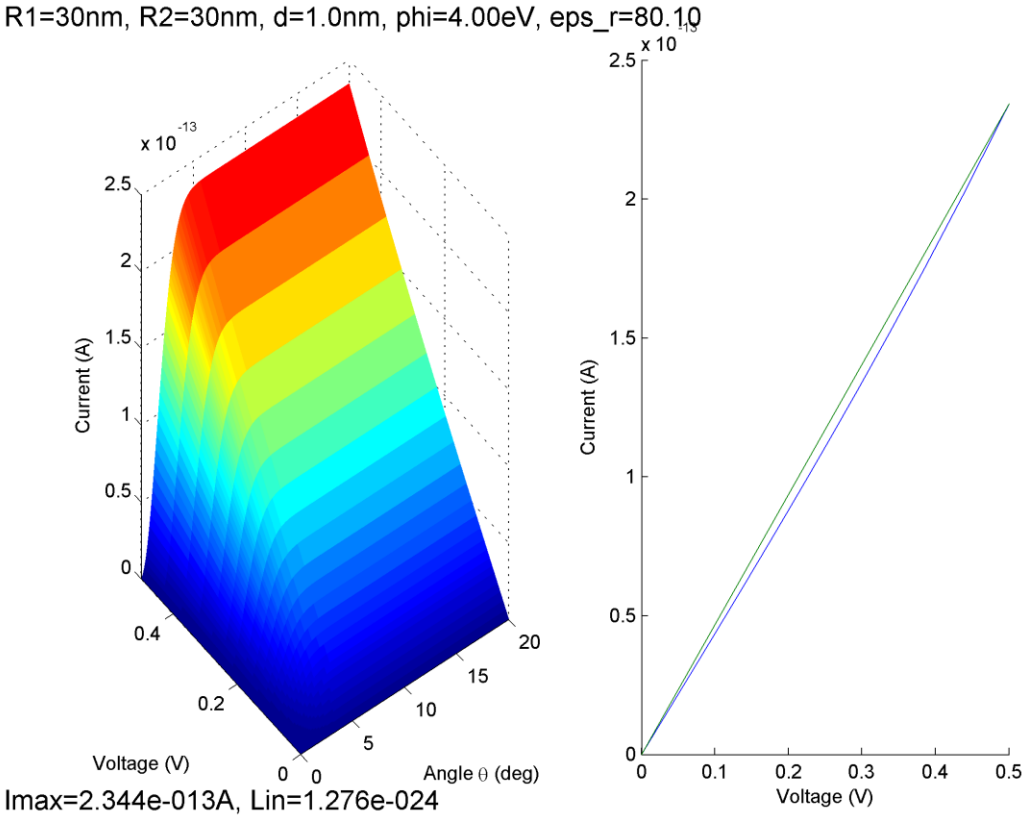

Figure 3.21. Simulation of the tunnelling current between two curved nodes, $R_1 = R_2 = 30$ nm, the shortest distance $d = 1$ nm, the work function is set to $\phi = 4.0$ eV and the medium permittivity in the junction is set to $\varepsilon_r = 80.1$. (a) A 3D map shows the magnitude of the current as a function of the bias voltage, V_{ds} and the deviation angle, θ. For $\theta > 10°$, the current levels off. (b) The corresponding $I(V)$ characteristic is given and shows a near perfect linear regime (blue curve close to the green curve). At maximum the current equals I~0.23 pA in this case.

3.4.2 Solvent stress on the nanocrystal assemblies

3.4.2.1 Hypotheses screened based on the Simmons model

We investigate four different parameters: the inter-node distance, d (ranging from 0.2 nm to 2.0 nm), the energetic barrier height, ϕ (range: 2.0 eV to 4.5 eV), the relative permittivity of the medium at the interface, ε_r (within 8.93 to 80.1), and the radius of the electrode node R_2 (from 20 nm to 3000 nm, i.e.: almost planar). We found nearly linear or weakly sub-linear response for all simulated current-voltage characteristics ($V_{ds} \leq 0.5$ V). The largest non-linear responses occur for the characteristics with the highest current magnitude. Overall, this parameter window covers the spectrum of currents (or conductivities) observed in our measurements.

We found the parameters can be ranked in terms of decreasing importance as follow: $d > \phi > \varepsilon_r > R_2$: the distance having the strongest effect, whereas the influence of the curvature R_2 is extremely subtle. The decimal log of the conductance versus distance regardless of other parameter values gives a decaying slope, β (semi log-y plot) of ~7.264 decades/nm ($\beta \sim 0.7264$ Å^{-1}),[5, 24-25] or conversely 1 decade of change in the current means a displacement of ~ 1.38 Å between the two nodes. Distinguishing values of the set barrier height, the exponential decay values are split such that the decaying constant ranges in 0.62 Å$^{-1} \leq \beta \leq 0.97$ Å^{-1}, see Figure 3.22.

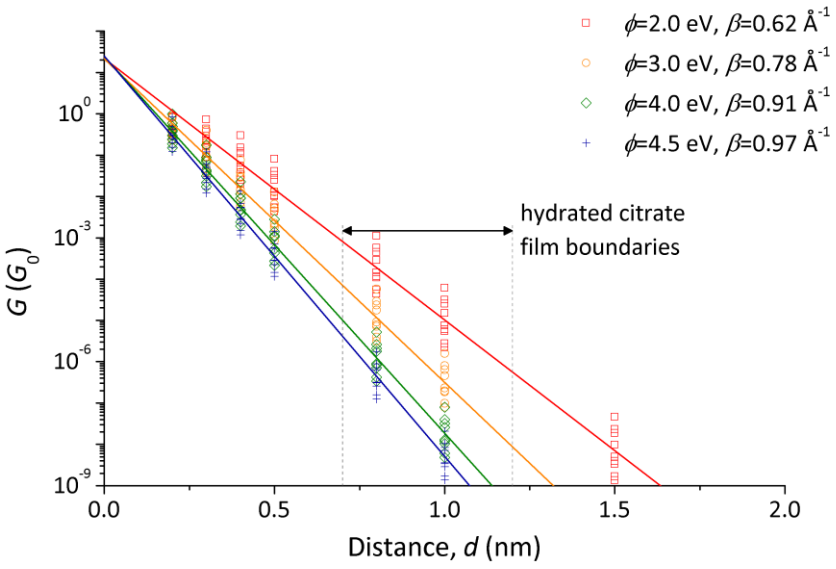

Figure 3.22. Simulations results from the Simmons model for the parameter window investigated. Conductance are plotted against the nanocrystal—electrode distance, values below $G < 1 \times 10^{-9}\, G_0$ are not shown as they are not experimentally measurable. Values of conductance are plotted separately for the different values of the energy barrier, ϕ. Although a scattering is still noticeable, fit lines are calculated for the 4 series of data versus the distance. A linear relationship is visible exhibiting the exponential decay values of $\beta \sim 0.62$ Å^{-1} in the best situation and $\beta \sim 0.97$ Å^{-1}

for the higher value. Interestingly, the boundaries for the nominal thickness of the hydrated citrate-sodium film would tend to indicate conductance G_{nc} should not exceed $\sim 10^{-3}\ G_0$ (if it is present).

For the range of parameters explored, it appears a given response in conductance can lead to a quite broad parameter window. Interestingly, the parameter window extent widens as the conductance drops. Conversely, if a device exhibits an increase in conductance after solvent immersion, the possible values characterising the electrode—nanocrystal interface narrows down. Moreover, both simulated and measured conductance values exist for a distance smaller than the nominal thickness of citrate ions bound on gold surfaces.

Across the entire conductance spectrum, changing the work function phi from 2.0 eV to 4.5 eV leads to a decrease in device conductance. However, one can identify two different regimes: down until $G_{nc} \sim 1 \times 10^{-4}\ G_0$ ($I_{\max} \sim 10$ nA), the conductance increases at most by two decades when ϕ decreases. For lower conductance, until $G_{nc} \sim 1 \times 10^{-9}\ G_0$, the increase in conductance can be driven up by either 3 or 4 decades, depending on the initial distance, d.

A variation of the permittivity leads to more subtle effects. There is a very small effect for conductivities above $G_{nc} > 0.1\ G_0$ (factor ~3). Decreasing the permittivity in the sequence 80.1, 20.18, 8.93 will improve the conductance by 0.8 decade only if $G_{nc} > 1 \times 10^{-4}\ G_0$. Below this value, the conductance will be enhanced by 1.4 decade for a similar change, see Figure 3.23.

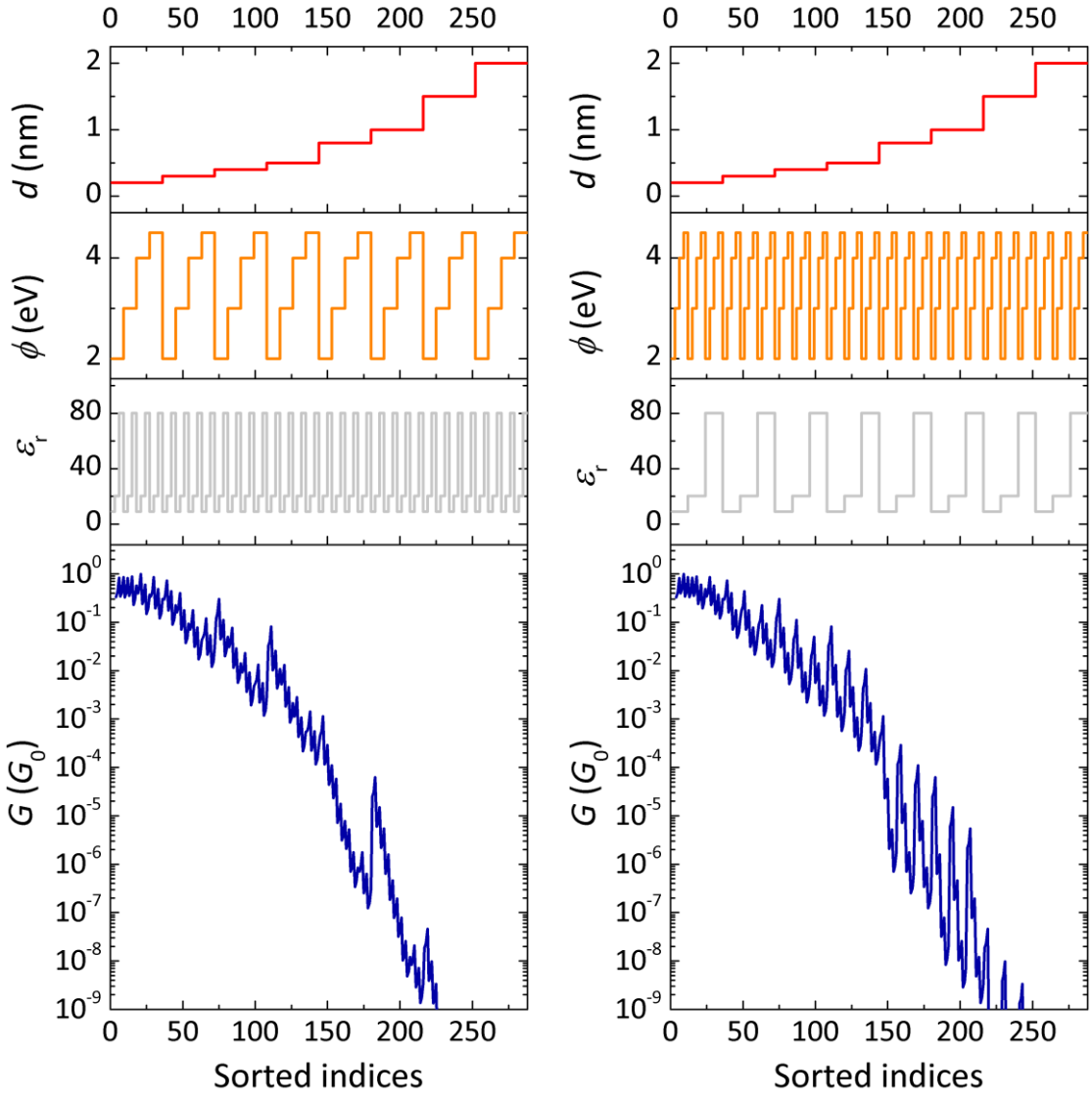

Figure 3.23. Influence of investigated parameters on the simulated conductance values by the Simmons model. To visually exhibit the dependency of the conductance on the investigated parameters, we sort the values by factors. (a) Parameters are sorted by d, then ϕ, then ε_r. The conductance decreases by several orders of magnitude as d is varying, but discontinuities in the decaying pattern can be seen with little fluctuations. (b) Parameters are sorted by d, then ε_r, then ϕ. Even if the conductance still decreases, a saw-teeth pattern is readily seen. This indicates that the dependency of the conductance value on parameters is as follow: $d > \phi > \varepsilon_r (> R_2)$. The value of R_2 varies from 20 nm to 3,000 nm in the present simulations: the curvature of the facing electrode is found to have the least influence amongst the four parameters investigated.

To summarise, minimising the distance or lowering the barrier or reducing the permittivity or a combination of these effects will always increase the conductance of the system. All other parameters being constant, a change in the electrode separation of 1 Å is enough to modify the conductance by ~ 0.7 decade. One can imagine the solvent immersion can create a slight perturbation in the van der Waals interactions holding the nanocrystals in place between the

electrodes leading to a change of its position within the gap and thus changing the magnitude of the tunnelling current flowing through the device.

On the other hand, a change in the relative permittivity across the interface will also alter the conductance of the junction but by a far more reduced magnitude: at most 1 decade in the case of a complete solvent exchange at the interface.

3.4.2.2 Solvent mixing at the electrode—nanocrystal interface

Molecular dynamic simulations (conducted by Victor Akujobi and Dr. Damien Thompson, Cork) show that a reorganisation of the landscape at the interface by displacement of citrate ions on facing gold surfaces seems unlikely. Nevertheless, study of a bulk interface between two semi-infinite reservoirs of water and dichloromethane shows a skin of 0.5 nm in thickness forms readily and acts as an emulsion barrier, see Figure 3.24a. At the nanocrystal—electrode interface one can imagine that the inter penetration of the solvent molecules within the nanometre-thin film of water and citrate ions can take place leading to a change in the effective permittivity between the two metallic nodes.

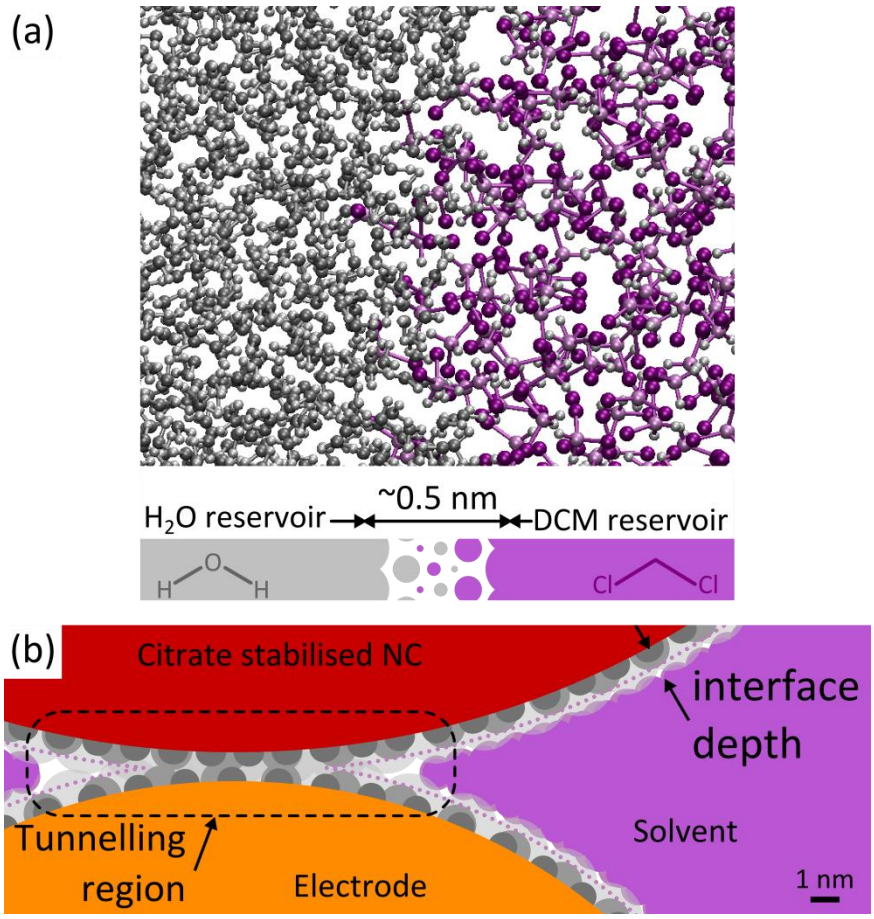

Figure 3.24. Geometrical consideration of the penetration depth of the organic solvent in the hydrated citrate-sodium film. (a) Molecular dynamics simulation of the interface between water and dichloromethane (performed by Victor Akujobi and Dr. Damien Thompson, Tyndall), the structure is

presented 140 ps after the two phases were brought into contact. Dichloromethane molecules start to cross over within a few picoseconds, with a steady ~4% "crossed over" population forming after ~50 ps. The relaxed interface has a few-Angstrom mixing phase, though the water/organic phases do not mix extensively. The thickness of the emulsion is only ~0.5 nm. (b) Simplistic schematic with a continuous view of the interface between a 30 nm radius nanocrystal and an electrode (with a local radius curvature taken to be 20 nm) immersed in a non-aqueous solvent. The competition between the non-aqueous solvent molecules and the citrate-sodium water based film is shown.

Based on geometrical considerations, we picture in more details the landscape of the nanocrystal—electrode interface, see Figure 3.24b. We derive an expression of the off-centre distance, h, to the waist of the nanocrystal—electrode interface covered by a the stabilising layer of citrate molecules along with the counter ions and water molecules, see Equation 3.4.

$$\sqrt{(R_1 + e)^2 - h^2} + \sqrt{(R_2 + e)^2 - h^2} + (R_1 + R_2 + d) = 0$$

Equation 3.4. Expression of the distance to the waist of the interface electrode—nanocrystal covered by a thin hydrated layer of tri-sodium citrate.

Numerically solving of the equation allows estimation of a value for h. A minimum separation of 1 nm between the nanocrystal and the electrode is considered in the schematic. In this context, because the value of the penetration skin is only 0.5 nm, it appears that the non-aqueous solvent molecules are unlikely to reach the centre region of the interface. Nevertheless, this description is based on a continuum approach and does not consider possible discrete solvent molecules diffusion above the emulsion barrier. Only molecular dynamics simulations can determine the effective intrusion of solvent molecules in the stabilising wetting film.

Practically, the interplay between the two scenarios is probable. Nevertheless, based on the magnitude of the two effects we believe the scenario of a repositioning of nanocrystals within the gap is actually dominant.

Further experimental tests could be developed to investigate *in situ* both the kinetics of the penetration of the stabilising film at the interface by non-aqueous solvents by the means of conductance measurements over time, as well as to characterise the degree of reversibility of the phenomenon to determine if engineering of the conductance of the to-be-functionalised nanocrystal assemblies in the gaps is possible.

3.4.3 Molecular junctions

The devices studied are typically a double junction system. The voltage drop is distributed across the two junctions: evenly in the case of a perfectly symmetrical electrode—nanocrystal—electrode situation, but the voltage drop will more likely be concentrated on the most resistive junction that will thus dominate the electrical response of the system. In the following we concentrate the discussion on only one nanocrystal—electrode interface. Any estimates of molecular conductance are at worst underestimated by a factor of 2.

Macroscopically, the molecular functionalisation can only be deemed successful if only the two junctions are sufficiently decorated with molecules creating supplementary conduction channels. In our system, there is no way to specifically target the bonding of molecules at the interface. An efficient bonding of the molecules on gold surfaces in general is indeed needed to maximise the probability of functionalising both interfaces and thus having a detectable molecular contribution. Thankfully sulphur-based anchor groups such as thiols, isothiocyanates or thiophenes are well known to bind to gold surfaces. We follow the standard routine of leaving samples immersed for 24 hours in a ~2 mM DTEB solution in dichloromethane at room temperature in the dark to maximise the probability for the molecular functionalisation.

Chemical and physical studies of Self Assembled Monolayer (SAM) formation on Au (111) surfaces as well as STM break junction and CP-AFM techniques developed to electrically contact one to few molecules adsorbed on ultra-flat mono-crystalline surfaces (usually Au 111) have shown a large variety of molecular adsorption configurations exist depending on molecular packing, anchor groups and the force of contact applied.[3, 26-27]

Because of the nature of sequential measurements on our devices, we propose to model the changes in conductance after molecular functionalisation (from $G_{nc-solv}$ to G_{nc-mol}) by the formation of resistor networks. In this scheme, molecules adsorbed at the interfaces during the molecular functionalisation act as extra channels in parallel: the conductance of these channels is intimately related to the type of molecular contacts. From both experiments and theory reported in the literature, the conductance of fully bound molecules (G_1) is one to two orders larger than configurations for which molecules are only half bounded (conductance G_2), see Figure 3.25. Moreover as the anchoring angle on the metal surfaces plus twisting of the thiophene/benzene rings along the backbone are not controlled, a broadening of the conductance values is expected. As reported experimentally using techniques like STM-BJ or MCBJ, decimal log distributions of conductance generally present peaks centred at G_1 with a FWHM of ~0.8 decade at most.

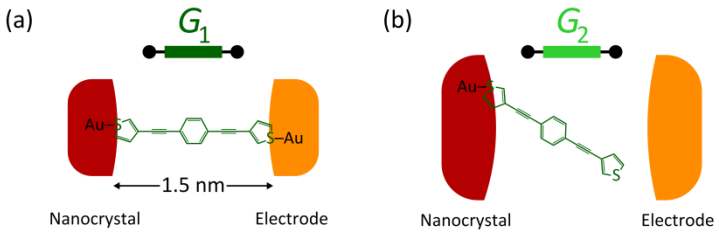

Figure 3.25. Binding configuration of a molecule at the nanocrystal-electrode interface. (a) Fully-bound configuration, the junction presents a conductance G_1. (b) Merely half-bounded configuration, in this case the junction presents a conductance of G_2.

3.4.3.1 Limiting case of molecular decoration

Based on geometrical considerations where nanocrystals and electrode gold grains are modelled with a locally spherical shape, we can estimate upper bounds for the number of fully bonded molecules at one interface. Molecules are pictured as rods bridging two opposing surfaces, see both Figure 3.20b and Figure 3.25.

We denote L as the length of the molecule, and the on-axis distance d between the two nodes can range in $0 \leq d \leq L$: corresponding to two extreme situations respectively where the junction is shorted, and when only one molecule can link the two nodes when laying right on the centre-to-centre axis.

When a molecule is fully bound, each of its extremities is touching a node. We note A the anchor point on the sphere of radius R_1 and B on the second sphere. The situation is parameterised as follow.

$$A: \begin{bmatrix} R_1 \cdot cos(\theta) \\ R_1 \cdot sin(\theta) \end{bmatrix}, B: \begin{bmatrix} R_2 \cdot cos(\alpha) \\ R_2 \cdot sin(\alpha) \end{bmatrix} + \begin{bmatrix} R_1 + d + R_2 \\ 0 \end{bmatrix}$$

Equation 3.5. Parametric equations of the two-dimensional problem of molecular binding.

For a given angle θ, we look for having $\left\|\overrightarrow{AB}\right\|$=L, the molecular length as described on Figure 3.20 (b). This defines two possible angles α on the second sphere: the molecule binding either in a diverging fashion or toward the o*n*-axis line. The junction decoration can be maximised by choosing the molecule orientation. For $R_1 \leq R_2$, the best scenario is to let molecules binding downward as it maximises the number of fully bound molecules. Finally, we need to describe the packing within the molecular array in the junction: p describes the nearest distance between two molecular anchor points.

The situation is axially-symmetric so we assume the molecular decoration to be similar. In order to estimate the upper bound for the number of fully bonded molecules in the junction we use an algorithm that adds up molecules on coronae, see Figure 3.26c. The starting (and most

outer) corona hosts molecules with an orientation parallel to the centre-to-centre line. The subsequent coronae, if they exist, will contain fewer molecules as the anchor points move closer to the on-axis line.

The total number of molecules is given by the sum of molecules attached on all these coronae. We investigate several cases scenario exploring a range of values for R_1 (and R_2) as well as changing the value of the inter node distance d. One of the two nodes can also be constrained to a pure plane configuration, see Figure 3.26a,b. The upper number of molecules is maximised in this situation compared to when two surfaces with finite curvature are considered.

The upper bound value is highly dependent on the inter molecule distance parameter p, as can be seen in Figure 3.26a ($p = 1.5L, p = 2.0L, p = 3.0L$). As discussed earlier, citrate molecules are bound to the surface of nanocrystals. As a matter of fact, these molecules will cause a steric hindrance for the adsorption of further linker molecules in the junction. This is crudely taken into account by adjusting p to a rather large value compared to the lattice parameter of the DTEB linker molecules (when in crystalline form).

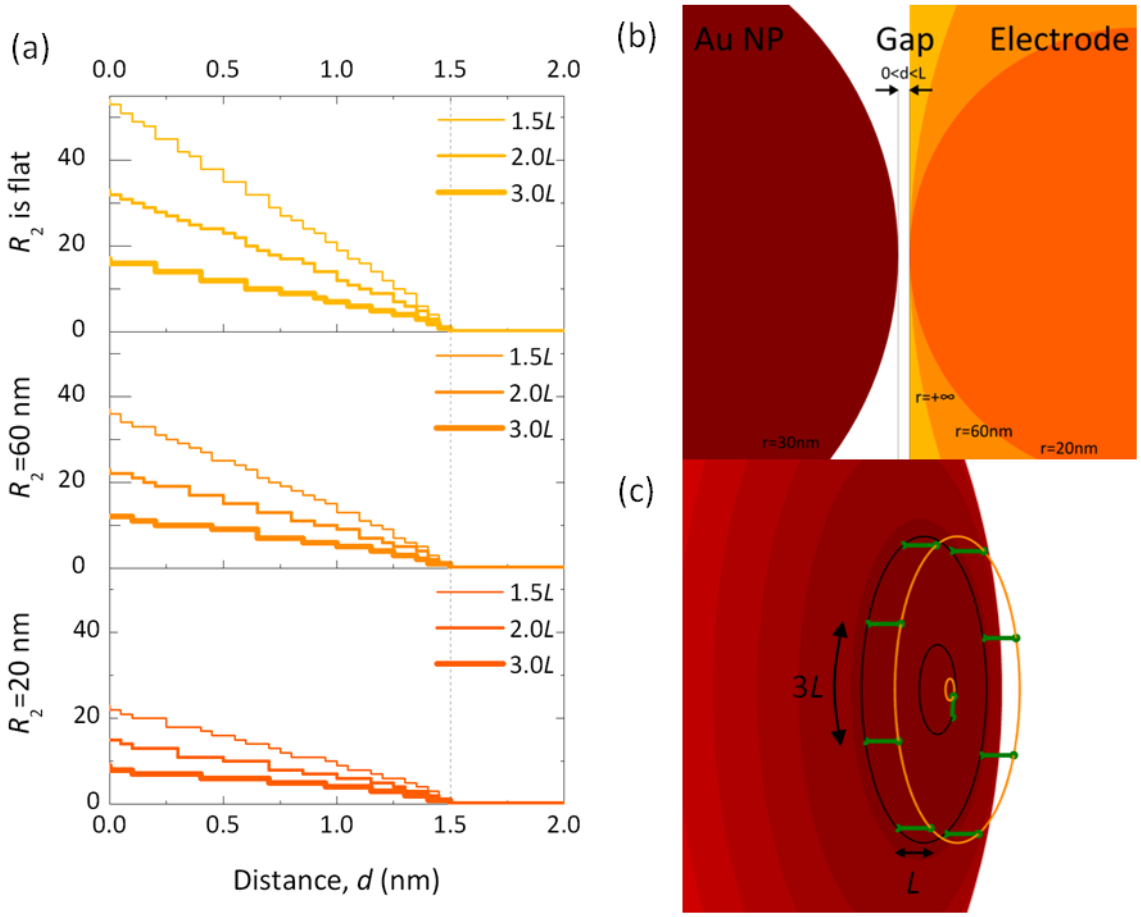

Figure 3.26. Study of the molecular bridging decoration at a nanocrystal—electrode interface. Based on geometrical considerations, we calculate the upper bound values of fully bond molecules at the interface. (a) Three parameters are investigated: the curvature of the facing electrode, R_2,

the shortest distance between the two metallic nodes, d, as shown in (b), and the close-packing parameter, p (shortest distance between two molecules). L is taken as the length of the molecule, as shown in (c). Overall, it appears, that up to ~ 50 molecules can fully bind on flat electrode in the very dense packing scenario while ~ 5 molecules only can bind in the case of a small gold grain on the electrode and a sparse molecular packing.

The contact radius is similar to the CP-AFM method: nanocrystals have a nominal radius of 30 nm (provided it can be modelled as a sphere), moreover visual inspection of gold grains on fabricated electrodes also seems to indicate the local radius of contact is a few tens of nanometres. We show the influence of the interface separation and the minimum molecular spacing on the total number of molecules that can fully bind in that 3D geometry, see Figure 3.26a. In good agreement with CP-AFM studies contacting closely packed molecules (~100 molecules contacted at a time),[25] we estimate that up to ~50 molecules can fully bind at one interface.

3.4.3.2 Molecules forming resistor network

The differential increase in conductance between the solvent-immersion and molecular functionalisation steps is believed to be the signature of bonded molecules at the interfaces. To model the molecular contribution to the conductance, we implement the idea of resistor networks.

The increase in conductance between pre- and post-immersion is believed to be the result of molecular adsorption in the active area of the junction. We postulate molecules may adsorb in different main configurations as depicted in Figure 3.27. Each molecular binding configuration is associated with a conductance channel type through which charge carriers can be transmitted.

We propose to describe the active area of the junction as an assembly of parallel conductance components. The overall measured increase of device conductance, $\Delta_+G = G_{nc-mol} - G_{bg}$ (with $G_{bg} = \max(G_{nc}, G_{nc-solv})$), is indeed described by a linear combination a_i of channels (of intrinsic conductance G_i), plus a final residue ϵ whose origin is mainly due to measurement inaccuracy, see Equation 3.6.

$$\Delta_+G = G_{nc-mol} - G_{bg} = \left(\sum_{i=1}^{n} a_i \cdot G_i\right) + \epsilon$$

Equation 3.6. Differential increase in conductance decomposed as a linear combination of conductance channels.

For the sake of simplicity and due to the finite current measurement resolution capabilities, we limit the analysis to two different conductance channels, see Equation 3.7.

$$\Delta_+ G = G_{nc-mol} - G_{bg} = a_1 \cdot G_1 + a_2 \cdot G_2 + \epsilon$$

Equation 3.7. Simplified decomposition of the linear combination of conductance channels.

Based on theoretical and experimental works,[28] it is expected that the ratio between the postulated conductance channel types is at least one if not two orders of magnitude: $10 \leq G_1/G_2 \leq 100$. This ensures the uniqueness of the linear combination extraction.

In order to find out the respective numbers (a_1, a_2) of the different channel types, we analyse the data using the cascade descent method based on the Euclidian division principle. Any number x can be described by the relationship: $x = b \cdot q + r$, where b the divisor, q the quotient and r the remainder. Let $E[.]$ denote the floor function defined by $E\left[\frac{x}{b}\right] = q$.

We implement this method on the conductance difference to recursively determine the values of (a_1, a_2) using a set of estimated values for (G_1, G_2). The simple cascade analysis algorithm is described in Equation 3.8: a_1 is first determined and from the first remainder a_2 can be found. This routine could be repeated again to get other values such as $a_3, \dots, a_n$.

$$a_1 = E\left[\frac{\Delta_+ G}{G_1}\right];\ a_2 = E\left[\frac{\Delta_+ G - a_1 \cdot G_1}{G_2}\right];\ a_i = E\left[\frac{\Delta_+ G - \left(\sum_{k=1}^{i-1} a_k \cdot G_k\right)}{G_i}\right]$$

Equation 3.8. Definition of the linear combination coefficients.

From the geometrical analysis of the junction profile we can estimate the upper bound value of typically $\overline{a_1} \sim 10$, as seen on Figure 3.26. One can expect values for a_2 and $(a_1 + a_2)$ to sensibly be of the same order of magnitude. Furthermore, by definition the rule $a_2 < G_1/G_2$ also applies and the calculation based on the maximum molecular coverage of projected area present another constraint on the value $\overline{a_2}$.

Finding values for the numbers (a_1, a_2) of the different channel types requires setting values for their intrinsic conductance values (G_1, G_2). In Figure 3.27, values from 8 different devices (across 4 different samples) show two different groups can be identified.

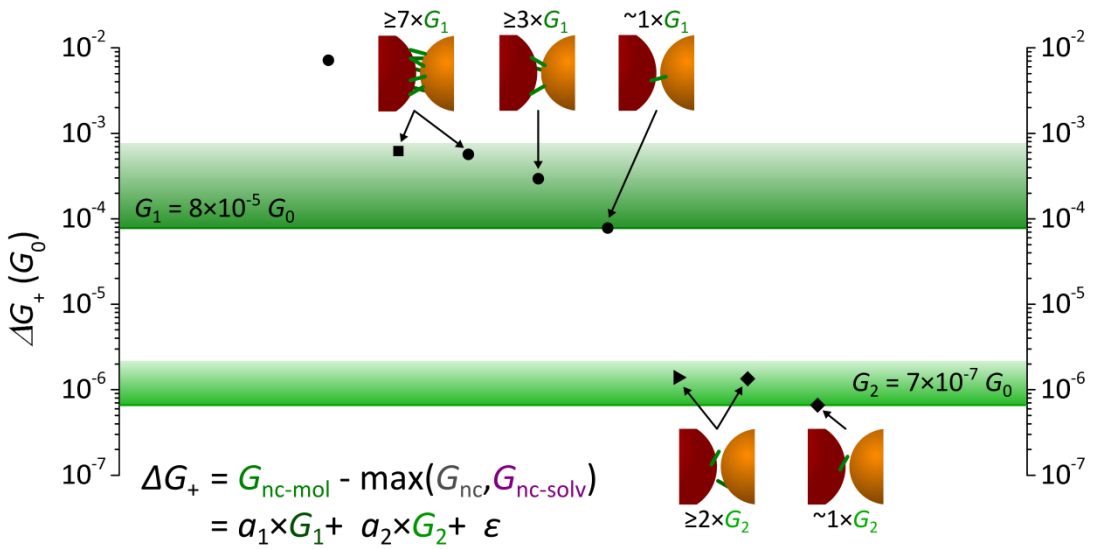

Figure 3.27. Resistor network. Within the entire dataset of fully characterised devices, 8 of them exhibit a net increase in conductance after functionalisation $G_{\text{nc-mol}}$ compared to after solvent-immersion $G_{\text{nc-solv}}$ (4 samples: circle, diamond, triangle and square). Two groups of values can be identified as depicted by the resistance network schematics presented on each side. They show the decomposition in different parallel channels: $a_1 \times G_1$ and $a_2 \times G_2$. A molecule bond on both ends provides a channel of conductance of the order of a single molecule conductance; a molecule only bound at one end only results in a molecule—vacuum kind of contact equivalent to a conductance channel several orders of magnitude smaller, $G_1 \gg G_2$. The two bands with a gradient of green colours indicate the unavoidable fluctuations and therefore broadening of the values of G_1 and G_2.

We propose to define values for G_1 and G_2 on the basis there seems to be two clear different contributions in the distribution of Δ_+G. The value of these two conductance channels G_1 and G_2 are set to the minimum in these two groups. Using the routine implementing the Euclidian division explained in Equation 3.7, the coefficients a_1 then a_2 are found sequentially as $G_1 \gg G_2$ ensuring the oneness of the linear combination. Because of the unavoidable value fluctuation and therefore broadening for G_1 and G_2, we will only discuss about the leading coefficient value for the linear combinations. The values in the distribution of Δ_+G actually are convolutions of the broadening of G_1 and the variable integer number of channels a_1 (G_2 and a_2, respectively).

For devices presenting a modest increase in conductance $\Delta_+G \ll G_1$, we found that 1 to 2 conductance channels exist (value of coefficient a_2). For devices showing a larger increase in conductance $\Delta_+G \geq G_1$, 1 to 7 channels are present except for the last device. These figures are consistent with the geometrical model developed to estimate the molecular decoration at the interface. However, using this initial guess of G_1, the last device appears to have 91 channels created at any one interface which is unlikely. Nevertheless we can argue, that this particular

device could be hosting neatly bound molecules (from an electrical point of view) maximizing the conductance at the molecular level. In this scenario, increasing the guessed value of G_1 by half of the typical FWHM for similar measurements brings the number of fully bound molecules down to 36 which sounds possible according to our geometrical model and the CP-AFM method.

Overall the results of the resistor-network model seem consistent with estimates of molecular coverage and more importantly with literature values for single molecular conductance. In our system $G_1 \sim 8 \times 10^{-5} G_0$; $G_2 \sim 7 \times 10^{-7} G_0$ which is consistent with the literature.[9, 29-32] We must however mention the unavoidable fluctuations in molecular bonding and consequently the broadening of the conductance values for the two configurations considered: G_1 and G_2. Nonetheless the uncertainty on the value of G_1 and G_2 is also conversely described by the integer decomposition (as $\overline{a_1} \sim 10 \sim \overline{a_2}$) of the resistor network model.

The results on molecular functionalisation represent a yield of more than $7/60 \sim 11\%$ for the 60 devices for which conductance could be estimated (7% within the initial overall 96-device pool).

Conversely in order to test the robustness of the method, the same analysis can be run on data points originating from the distribution of pronounced conductance change from G_{nc} to $G_{nc-solv}$, in class B. Although the number of points in class B is greater than in class C: 18 points as opposed to 8 points, the distribution of points $\Delta_+ G = G_{nc-solv} - G_{nc}$ is broad and nearly uniform and thus does not support the idea of any preferred values or ranges.

In spite of the inability to entirely decorrelate the contribution of the solvent itself on the citrate-sodium water film at the nanocrystal—electrode interface during the molecular functionalisation process step, the results of this statistical test consolidates the idea that the resistor networks model reveals only the signature of the presence of DTEB molecules in the junctions and does not reflect the changes originating from pure solvent immersion effect.

3.5 Conclusion

We have developed and demonstrated a versatile method for laterally contacting molecules combining conventional top-down e-beam lithography with bottom-up DEP trapping of small numbers (<5) of citrate-stabilised gold nanocrystals (~60 nm in diameter) for the deployment of metallic nodes as a contacting strategy for molecular electronics.

We show advances and improvements in the manufacturing quality control of samples. The assembly of nanocrystal(s) between electrodes is shown to lead to very large variety of conductance values that can be narrowed using particular DEP trapping conditions. It is believed there remains an opportunity to improve the feedback *in situ*, during the trapping, allowing an even better control of the nanocrystal assembly.

We show evidence of sub-nanometre reorganisation of the nanocrystal—electrode interfaces resulting from exposure to non-aqueous solvents mediating the adsorption of molecules on metallic surfaces stabilised with hydrated citrate-sodium complexes. The platform of nanocrystal assembly bridging nanometre scale gaps (~ 40 nm) is bringing into light the influence of immiscible mediums on (sub-)nanometre curved interfaces opening interesting possibility for the characterisation of emulsions near surfaces in extremely confined/close vicinity.

Studying the variety of current-voltage responses both per device and across the full dataset we show molecular functionalisation is successful in 7 out of 60 devices that showed measureable conductance following nanocrystal trapping. The simplistic resistor network proposed enables to extract typical values of molecular conductance in different bonding configurations, in good agreement with the literature. We show the “rigid-rod” linker 1,4 di(3-thiophene) ethynylbenzene molecules comprising a conjugated backbone and thiophene anchor groups have a single molecule electrical conductance of ~ 8×10^{-5} G_0 while the conductance of partial bonding configurations is ~ 7×10^{-7} G_0.

The demonstrated functional hybrid assemblies of nanocrystals contacting few molecules opens the possibility of further experimental work employing the effect of nanocrystal plasmon resonance to excite molecular states within the junction or the electrolytic gating method to address molecular levels and exhibit increased conductance.

3.6 References

1. Aviram, A.; Ratner, M. A., Molecular rectifiers. *Chemical Physics Letters* **1974,** *29* (2), 277-283.
2. Huang, Z.; Chen, F.; D'Agosta, R.; Bennett, P. A.; Di Ventra, M.; Tao, N., Local ionic and electron heating in single-molecule junctions. *Nat Nano* **2007,** *2* (11), 698-703.
3. Quek, S. Y.; Kamenetska, M.; Steigerwald, M. L.; Choi, H. J.; Louie, S. G.; Hybertsen, M. S.; Neaton, J. B.; Venkataraman Latha, Mechanically controlled binary conductance switching of a single-molecule junction. *Nat Nano* **2009,** *4* (4), 230-234.
4. Mishchenko, A.; Vonlanthen, D.; Meded, V.; Buerkle, M.; Li, C.; Pobelov, I. V.; Bagrets, A.; Viljas, J. K.; Pauly, F.; Evers, F.; Mayor, M.; Wandlowski, T., Influence of Conformation on Conductance of Biphenyl-Dithiol Single-Molecule Contacts. *Nano Letters* **2009,** *10* (1), 156-163.
5. Ho Choi, S.; Kim, B.; Frisbie, C. D., Electrical Resistance of Long Conjugated Molecular Wires. *Science* **2008,** *320* (5882), 1482-1486.
6. Tran, E.; Duati, M.; Whitesides, G. M.; Rampi, M. A., Gating current flowing through molecules in metal–molecules–metal junctions. *Faraday Discuss.* **2006,** *131*, 197-203.
7. Nijhuis, C. A.; Reus, W. F.; Barber, J. R.; Dickey, M. D.; Whitesides, G. M., Charge Transport and Rectification in Arrays of SAM-Based Tunneling Junctions. *Nano Letters* **2010,** *10* (9), 3611-3619.
8. Reed, M. A.; Zhou, C.; Muller, C. J.; Burgin, T. P.; Tour, J. M., Conductance of a Molecular Junction. *Science* **1997,** *278* (5336), 252-254.
9. Wu, S.; Gonzalez, M. T.; Huber, R.; Grunder, S.; Mayor, M.; Schonenberger, C.; Calame, M., Molecular junctions based on aromatic coupling. *Nat Nano* **2008,** *3* (9), 569-574.
10. Park, J.; Pasupathy, A. N.; Goldsmith, J. I.; Soldatov, A. V.; Chang, C.; Yaish, Y.; Sethna, J. P.; Abruña, H. D.; Ralph, D. C.; McEuen, P. L., Wiring up single molecules. *Thin Solid Films* **2003,** *438-439*, 457-461.
11. Prins, F.; Hayashi, T.; Steenwijk, B. J. A. d. V. v.; Gao, B.; Osorio, E. A.; Muraki, K.; Zant, H. S. J. v. d., Room-temperature stability of Pt nanogaps formed by self-breaking. *Applied Physics Letters* **2009,** *94* (12), 123108.
12. Song, H.; Kim, Y.; Jang, Y. H.; Jeong, H.; Reed, M. A.; Lee, T., Observation of molecular orbital gating. *Nature* **2009,** *462* (7276), 1039-1043.
13. Wang, G.; Kim, Y.; Choe, M.; Kim, T.-W.; Lee, T., A New Approach for Molecular Electronic Junctions with a Multilayer Graphene Electrode. *Advanced Materials* **2011,** *23* (6), 755-760.
14. Green, J. E.; Wook Choi, J.; Boukai, A.; Bunimovich, Y.; Johnston-Halperin, E.; Delonno, E.; Luo, Y.; Sheriff, B. A.; Xu, K.; Shik Shin, Y.; Tseng, H.-R.; Stoddart, J. F.; Heath, J. R., A 160-kilobit molecular electronic memory patterned at 10^{11} bits per square centimetre. *Nature* **2007,** *445* (7126), 414-417.
15. Liao, J.; Bernard, L.; Langer, M.; Schönenberger, C.; Calame, M., Reversible Formation of Molecular Junctions in 2D Nanoparticle Arrays. *Advanced Materials* **2006,** *18* (18), 2444-2447.
16. Cheng, W.; Park, N.; Walter, M. T.; Hartman, M. R.; Luo, D., Nanopatterning self-assembled nanoparticle superlattices by moulding microdroplets. *Nat Nano* **2008,** *3* (11), 682-690.
17. Liao, J.; Agustsson, J. S.; Wu, S.; Schönenberger, C.; Calame, M.; Leroux, Y.; Mayor, M.; Jeannin, O.; Ran, Y.-F.; Liu, S.-X.; Decurtins, S., Cyclic Conductance Switching in Networks of Redox-Active Molecular Junctions. *Nano Letters* **2010,** *10* (3), 759-764.
18. Barrett, C. Charge Transport in Nanoscale Structures and Devices. University College Cork, Cork, 2009.
19. Bernard, L. Expanding the Horizon of Molecular Electronics via Nanoparticle Assemblies. University of Basel, Basel, 2006.
20. Pingree, L. S. C.; Hersam, M. C., Bridge-enhanced nanoscale impedance microscopy. *Applied Physics Letters* **2005,** *87* (23), 233117-3.
21. Hihath, J.; Bruot, C.; Tao, N., Electron-Phonon Interactions in Single Octanedithiol Molecular Junctions. *ACS Nano* **2010,** *4* (7), 3823-3830

22. Lide, D. R., *CRC Handbook of Chemistry and Physics (76th Edition)*. 76th ed.; CRC Press: 1995; Vol. 1.
23. Simmons, J. G., Generalized Formula for the Electric Tunnel Effect between Similar Electrodes Separated by a Thin Insulating Film. *Journal of Applied Physics* **1963,** *34* (6), 1793-1803.
24. Wold, D. J.; Haag, R.; Rampi, M. A.; Frisbie, C. D., Distance Dependence of Electron Tunneling through Self-Assembled Monolayers Measured by Conducting Probe Atomic Force Microscopy: Unsaturated versus Saturated Molecular Junctions. *The Journal of Physical Chemistry B* **2002,** *106* (11), 2813-2816.
25. Wold, D. J.; Frisbie, C. D., Fabrication and Characterization of Metal−Molecule−Metal Junctions by Conducting Probe Atomic Force Microscopy. *Journal of the American Chemical Society* **2001,** *123* (23), 5549-5556.
26. Zhou, J.; Chen, G.; Xu, B., Probing the Molecule−Electrode Interface of Single-Molecule Junctions by Controllable Mechanical Modulations. *The Journal of Physical Chemistry C* **2010,** *114* (18), 8587-8592.
27. Franco, I.; George, C. B.; Solomon, G. C.; Schatz, G. C.; Ratner, M. A., Mechanically Activated Molecular Switch through Single-Molecule Pulling. *Journal of the American Chemical Society* **2011,** *133* (7), 2242-2249.
28. Salomon, A.; Cahen, D.; Lindsay, S.; Tomfohr, J.; Engelkes, V. B.; Frisbie, C. D., Comparison of Electronic Transport Measurements on Organic Molecules. *Advanced Materials* **2003,** *15* (22), 1881-1890.
29. Vonlanthen, D.; Mishchenko, A.; Elbing, M.; Neuburger, M.; Wandlowski, T.; Mayor, M., Chemically Controlled Conductivity: Torsion-Angle Dependence in a Single-Molecule Biphenyldithiol Junction. *Angewandte Chemie International Edition* **2009,** *48* (47), 8886-8890.
30. Mishchenko, A.; Zotti, L. A.; Vonlanthen, D.; Bürkle, M.; Pauly, F.; Cuevas, J. C.; Mayor, M.; Wandlowski, T., Single-Molecule Junctions Based on Nitrile-Terminated Biphenyls: A Promising New Anchoring Group. *Journal of the American Chemical Society* **2010,** *133* (2), 184-187.
31. Hihath, J.; Tao, N., Rapid measurement of single-molecule conductance. *Nanotechnology* **2008,** *19* (26), 7.
32. Ko, C.-H.; Huang, M.-J.; Fu, M.-D.; Chen, C.-h., Superior Contact for Single-Molecule Conductance: Electronic Coupling of Thiolate and Isothiocyanate on Pt, Pd, and Au. *Journal of the American Chemical Society* **2009,** *132* (2), 756-764.

Chapter 4 – Development of the electrolytic gating technique for nanocrystal-molecule assemblies

4.1 Introduction

The typical length of a molecular wire is on the order of 1 nm. All methods employed in the literature so far for contacting molecules are bulky in the sense that, at best, the two connected "leads" have a sort of wide funnel shape leading to the macroscopic world of the scientist. Having a third electrode or "gate", in the terminology of semiconductor Field Effect Transistor (FET) devices, is of paramount interest as it can open the possibility to control the conductance of an electrode-molecule-electrode junction. Although challenging, this allows studying the location of the energy levels (so-called Highest Occupied Molecular Orbital, HOMO, and Lowest Unoccupied Molecular Orbital, LUMO) across the junction. Based on the ~ 1 nm length scale, only a few techniques can be employed for gating such a junction reliably and reproducibly.

Studies on solid-state FET-like devices show that the electrostatic gating is effective only if the gate oxide thickness is not more than 30% of the channel length.[1] This cannot be achieved in the case of molecular devices, as the gate oxide must be at least ~ 1 nm thick to avoid tunnelling leakage between source (or drain) and the gate electrodes. Nevertheless a small number of experimental studies have been reported on this device architecture with ~5 nm thick gate oxide.[2-3] These studies show the yield of having a gated junction is very limited, typically $\sim 35/418 = 8\%$.[3]

A second possibility is to rely on light-induced change of charge-separation [4] or conformation [5] or isomerisation of molecules to alter the overall junction conductance. Employing nanocrystals can be helpful as surface plasmon resonance may enhance the electromagnetic field and thus maximise the gating effect.[6-7]

Another possibility is to apply tensile or compressive stress on molecules to control the molecular junction conductance. This was demonstrated on setups employing STM-BJ systems.[8-10]

A fourth and emerging technique for probing the electrical characteristics of a molecular junction is to implement what is termed an electrolytic gating.[11] To date, a few research groups have implemented this method for gating molecular devices using electrolytes: on STM-BJ setups,[12-20] on liquid-drop devices[21-22] and on laterally contacted nano-scale polymers.[23-26] The medium in which the device is placed is a solvent with a high permittivity (typically water: $\varepsilon_r \sim 80$) with a supporting electrolyte which contains ions and counterions.

Electrochemistry studies show that a double-layer of ions forms at the interface between electrodes immersed in a liquid medium as discussed in section 1.3 of chapter 1 (p. 28). Any potential applied at an electrode decays steeply in the solution because of the reorganisation of

mobile ions around it. Electrochemistry also offers the possibility of modifying the oxidation state of molecules dissolved in liquid or attached at an electrode surface, see Figure 4.1.

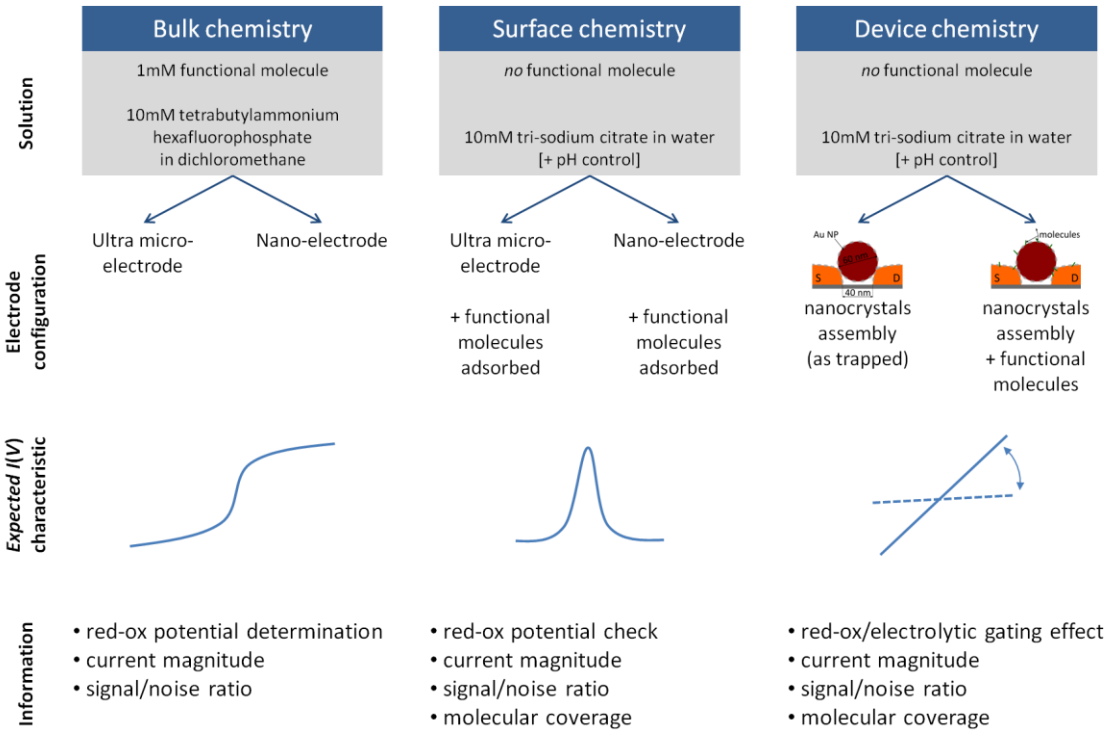

Figure 4.1. The convergence of electrochemistry and FET-like molecular device probing opens up a variety of possible work directions:[27] bulk electrochemistry can study dissolved molecules, surface electrochemistry can study molecules attached to the working electrodes. We propose to study molecules decorating assemblies of nanocrystals trapped in nanometre-scale gaps.

Both double layer modification and oxidation-reduction processes could be exploited to gate few-molecule devices and we propose to investigate the possibility of implementing this technique on nanocrystal assemblies trapped in nano-gaps.

The present work aims at the development of a platform allowing electrical measurements to be performed in wet conditions to study nanocrystal assemblies trapped in nano-gaps and investigate the electrolytic gating technique. Moving to electrical measurements at room temperature, in wet conditions on nanoscale devices with high resistance gives rise to several engineering and fundamental scientific challenges that we propose to tackle in this work.

4.2 Methods

To pursue electrolytic gating on molecular wires, we build on the device platform developed for dry measurements. The device architecture tested is still made of trapped nanocrystals between electrodes "decorated" afterwards with linker molecules. However performing measurements using a liquid medium on top of the device does change some of the sample manufacturing process steps as well as the instrumentation required to probe it.

4.2.1 Experimental setup

Moving from a dry (insulating) to a wet (semi-conducting) medium around the device implies we need to account for an extra conducting path through the solution when performing electrical characterisation measurements. Even though this leakage current cannot be suppressed, it can be decreased by insulating the exposed track leads from the solution. Insulation with a dielectric needs to be made down to within a few micrometres laterally from the nanocrystal-molecule nanostructure in order to minimise Faradic currents.

On the other hand, the wet medium needs to be contained in an electrochemical cell that has a reduced size. This puts constraints on the sample layout design, but also on the electrical probing technique, and finally on the means to control integrity of the chemical content of the solution and how the solution actually wets the sample surface over the course of the measurements.

4.2.1.1 Chip layout design

The new chip layout design has to comply with three major specifications: first of all, the planar dielectric layer must be reliable, so must be the electrical contacting via the bond pads, and finally the sample size must accommodate the maximum number of devices without being impractically large.

The first requirement is fulfilled with the deposition of a silicon nitride (SiN_x) passivation layer on the surface of the electrode chips.[28] A layer of SiN_x with a typical thickness of ~ 500 nm is deposited by Plasma-Enhanced Chemical Vapour Deposition (PECVD). An in-house developed recipe by Vladimir Djara, for Reactive Ion Etching (RIE), was used to subsequently etch the material in an anisotropic manner, yielding sharp etch profiles and thus retaining the integrity of the pattern geometry.

The thickness of ~ 500 nm of SiN_x appears to be a good trade-off between electrical insulation of the tracks from any liquid and the ability to perform lithography with a sufficient resolution for patterning the dielectric layer in order to open micrometre-scale windows in the passivation layer.

Early tests showed the deposition and etch fabrication process of SiN_x works nicely for samples having ~ 20 nm thick gold electrodes. It was also shown that nanocrystals trapped prior to this process remain still in place, see Figure 4.2.

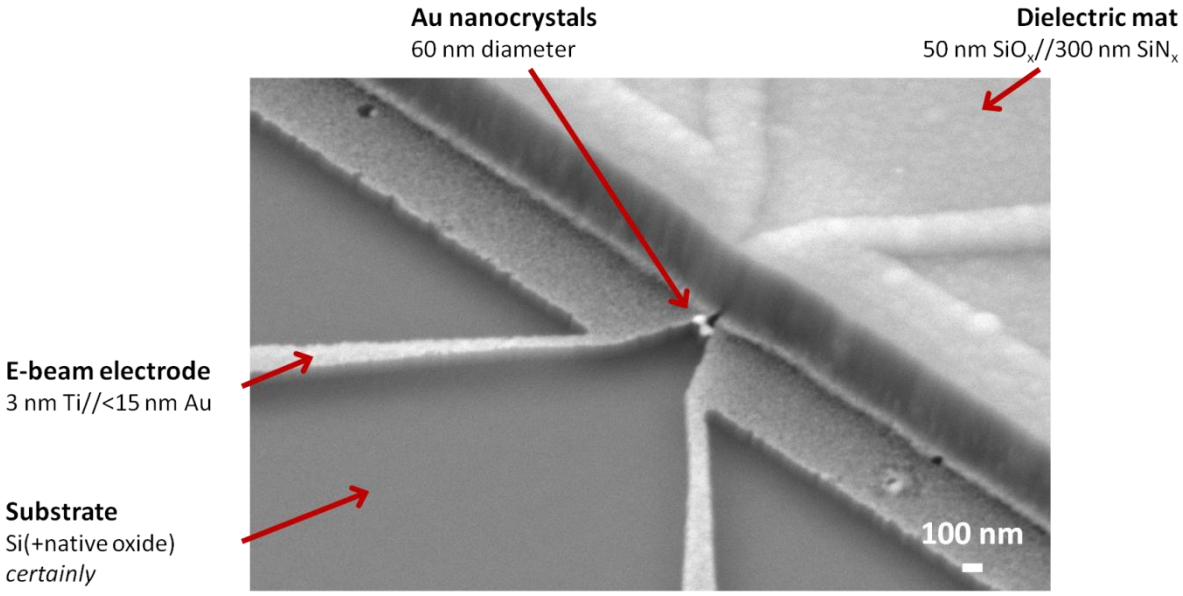

Figure 4.2. Titled Scanning Electron Microscope image of a sacrificed electrode chip for the development of the deposition and etch of SiN_x dielectric insulation mat comprising at that time a bi-layer of silicon nitride and silicon dioxide. The nanocrystals were trapped prior to the deposition of the insulating layer. The alignment of the etch line with the electrodes is fortuitous. (sample: X-4407_W1_A_0304; imaging conditions: 45° tilt, 15 mm working distance, X30,000 magnification; instrument: JEOL JSM 7500-F).

Two layers of metal were used for the definition of electrodes following the same process flow as in chapter 3. First of all, e-beam lithography was used to pattern nanometre-scale electrodes (3 nm Ti, 3 nm Pt, 20 nm Au, chromium is not used to avoid delaminating of the electrodes),[29] then optical lithography was employed to overlay micrometre-scale contact tracks and bond pads.

The windows in the SiN_x layer were patterned (at die level) via an optical mask using a cascade alignment method: the mask was first coarsely aligned to the optical metallisation via standard alignment marks, then high precision alignment was performed using Vernier gratings defined during the e-beam lithography step. Alignment on the Vernier gratings is done in both X and Y directions on two opposing corners of the samples. This technique allows minimising the alignment uncertainty to <500 nm and down to ~ 200 nm in the best conditions, see Figure 4.3.

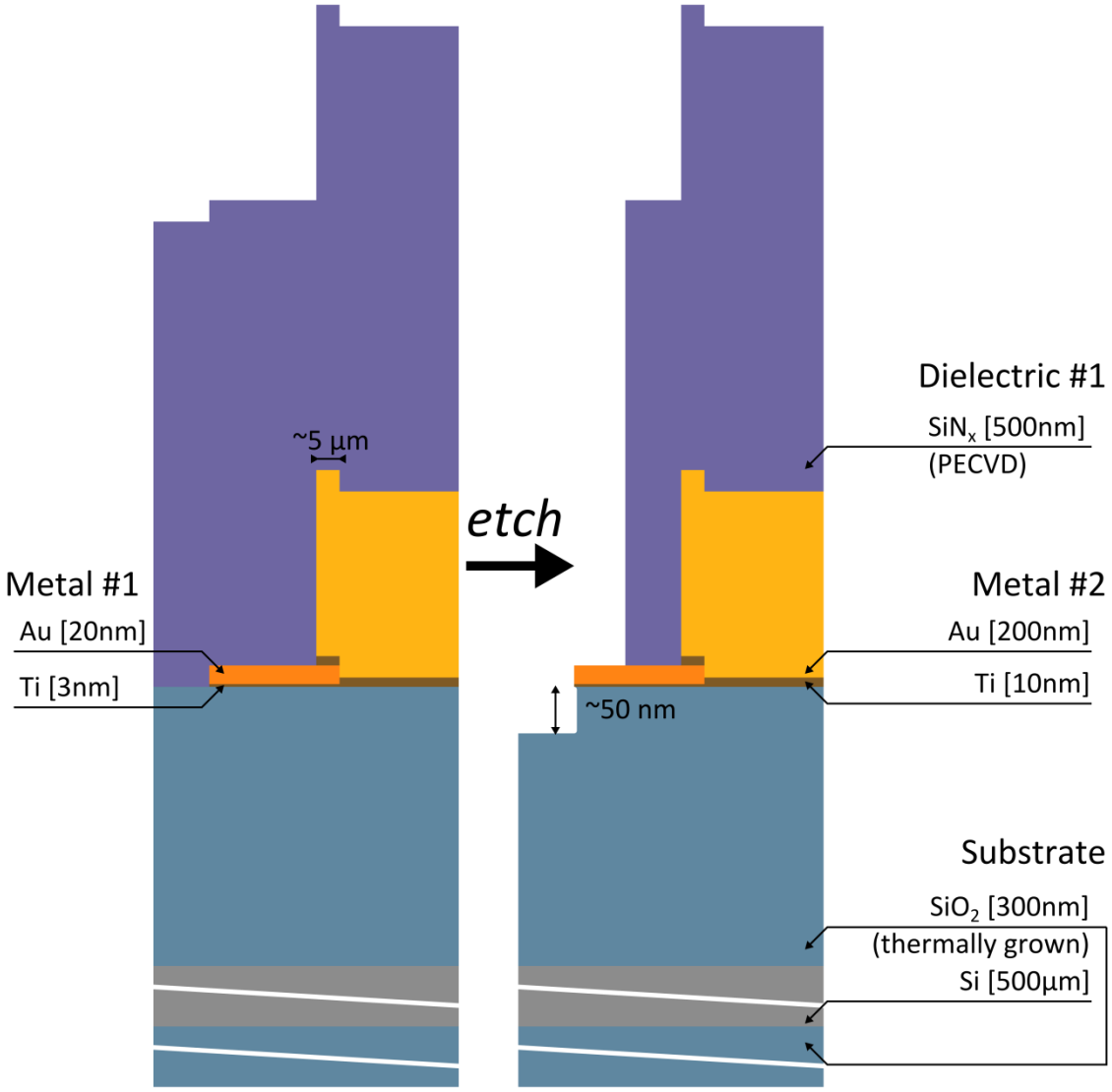

Figure 4.3. Cross-section schematic of the expected device layers: although focused on the stacking of layers it shows the planar nature of the technology. Moreover, one must point out the recipe of Reactive Ion Etching (RIE) for SiN_x also etches the thermally grown silicon oxide of the supporting substrate forming possible undercut beneath e-beam defined electrodes.

Four different designs were developed to determine the best compromise in terms of measurement reliability: minimising the magnitude of the electrolytic leakage current by reducing the surface area of the exposed electrodes under the constraints on multi-level lithography alignment capabilities, see Figure 4.4.

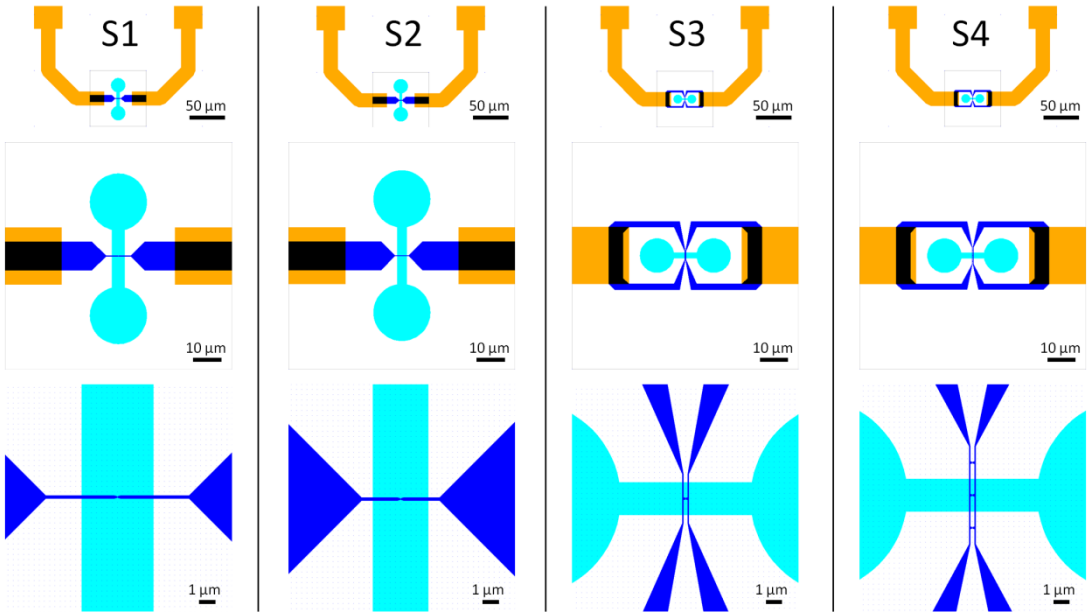

Figure 4.4. Four different layout designs were tested for the passivated electrodes investigating the lower electrode surface exposure: the shape in orange colour represents optically patterned electrodes, dark blue shapes are the e-beam defined electrodes, cyan shapes are the passivation openings. All nanometre-scale gaps were designed to be 40 nm wide: S1 and S2 are the simplest designs and feature two facing fingers but the size of the passivation opening is bigger for S1. S3 and S4 are designed to reduce the exposed surface area to a minimum. They comprise two thin rails with 1 pair of protrusions in the middle for S3 and 3 pairs of protrusions in S4 (this accounts for possible lithography misalignments), the width of the passivation opening is the same for both designs.

We detail the characteristic dimensions of the four layout designs, see Table 4.1.

	Symbol S1	**Symbol S2**	**Symbol S3**	**Symbol S4**
Exposed surface area (nominal)	~0.88 µm^2	~0.68 µm^2	~0.34 µm^2	~0.34 µm^2
Opening window width	4.4 µm	3.4 µm	2.0 µm	2.0 µm

Table 4.1. Characteristic dimensions of the four different layout designs.

Finally the overall design of the chip was 16×16 mm^2 die containing 24 bond pads arranged in staggered rows (3 pairs on each side), allowing 12 e-beam fields with one device per field to be contacted, see Figure 4.5.

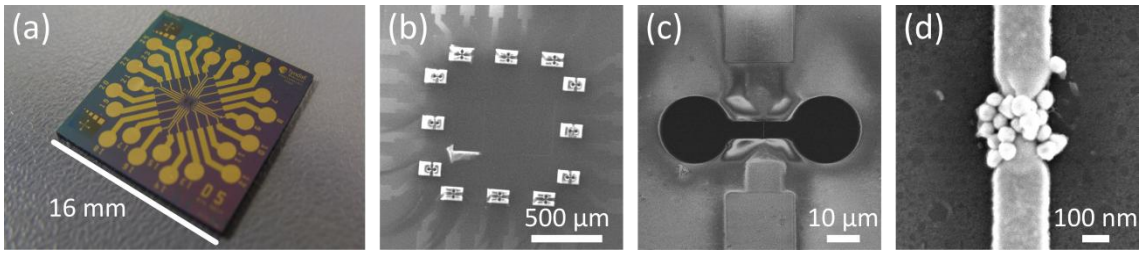

Figure 4.5. Zoom in on a device from chip-scale to nanometre scale. (a) A photograph of the chip shows the overall layout design. (b) Scanning Electron Micrograph at low magnification of the chip centre showing 12 distinct e-beam fields (white rectangles due to temporary charging markings of the SiN_x layer resulting from imaging each device beforehand). (c) Focus on one of the e-beam field containing a device: the dark shape is the opening in the passivation layer, the source and drain electrodes can be distinguished (vertical bars). (d) The e-beam electrodes and the assembly of nanocrystals bridging the gap (device: X-4835_W1_D5,S1_2122).

4.2.1.2 Custom sample holder

The sample holder design was developed in parallel with the layout design of the electrode structure. With the constraints of the size of the dedicated samples and the positioning of the bond pads, the key specifications were the design of the holder must ensure solvent tightness and robustness plus it had to be compact and present flexibility.

For the making of the cell, the best material resistant to possible corrosion processes resulting from contact with chemicals but allowing machining to be conducted on it is Teflon (Perspex may present a good alternative where transparency is a prerequisite). In our application, Teflon was thus chosen for making the plate comprising the cell. The O-ring ensuring solvent tightness is made of polytetrafluoroethylene (PTFE) as it is "an extremely inert material, unaffected by virtually every known chemical including most acids, alkalis and solvents" according to James Walker O-ring manufacturer. Aluminium was chosen for its mechanical properties for the making of the socket where the sample sits so as to allow to screws clamping the plate to be secured tightly without wearing out the threads of the screw holes. A minimum of 3 screws were used for this purpose positioned in an equilateral triangle fashion ensuring self levelling of the plate on top of the sample, see Figure 4.6a. The electrochemical cell holds ~110 µL of liquid.

The holder itself has a footprint of 40×40×28 mm^3 (respectively length, width, height) so it can fit under the objective of a conventional microscope with little adjustment on the stage. A hole is also drilled in the centre of the socket for back-lighting optics application. Slightly modified versions of the holder are currently used in the Nanotechnology Group for applications in nanowire-based electrochemistry sensing and electro-chemi-luminescence setups.

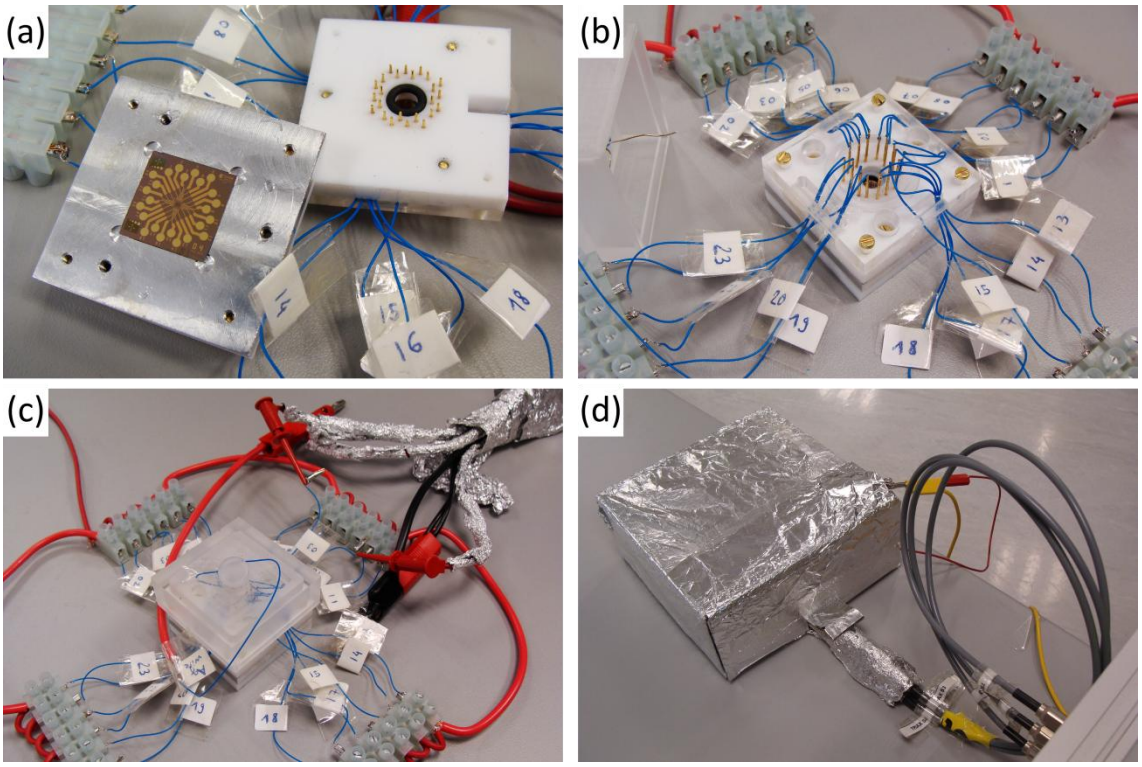

Figure 4.6. Detailed views of the sample holder. (a) A recessed aluminium socket serves as a holder for one 16×16 mm^2 sample. On the right hand side, the Teflon top plate (up-side-down in the picture) shows the spring-loaded probe tips and the O-ring in the middle. (b) The wires connecting the spring-loaded probes have been shortened down to ~ 10 cm and are grounded via the terminal blocks (screw-secured). The opening in the middle of the plate is the cell that can contain ~ 110 µL of liquid, on the left hand side the reference/counter electrodes integrated into the Perspex cap can also be seen. (c) The spring-loaded hooks are shown (their leads are shielded with aluminium foil). The cap that offers connections for nitrogen gas flow (blocked here) now covers the plate. (d) The grounded Faraday cage (shielding the custom chemical cell and connections against ambient background electrical noise) and the three triaxial cables connected to the parameter analyser are shown.

4.2.1.3 Contacting the devices

Chapter 3 demonstrated measurable source-drain currents through nanocrystal assemblies can be as low a few tens of pA. The custom contacting strategy has to comply with this demanding specification.

The reliability of contacts between the sample bond pads and the instrument is ensured via spring-loaded probes having a typical resistance <30 mΩ. The tips have a rounded radius and are plated with gold on top of an alloy of copper beryllium (Series S Duraseal: S-00-J-1.3-G-DS-36-1), see Figure 4.6a. While the opening on bond pads is 1.4 mm in diameter, each probe tip is 0.51 mm in diameter: this ensures good latitude in the approach positioning of the holder cap on top of the sample before securing the screws to clamp it in place.

Since we need to be able to measure such low currents (pA range or lower) we need to minimise the inevitable background electrical noise pick-up. A second issue that arises is ensuring the devices on samples are protected against Electrostatic Discharge (ESD).

Shielded spring-loaded probes have a foot print about three times larger than non shielded spring-loaded probes. As a compromise with the sample dimensions and layout design (i.e.: number of devices), unshielded spring-loaded probes were chosen.

Ideally, to establish connections between pairs of spring-loaded probes and the actual terminals of the measurement unit, an automated low noise multiplexer could be used to route the signals to the electrodes of interest. However, for simplicity we rely on manual switching.

The 1 m long non-shielded wire initially attached to the spring-loaded probes were shortened to 10 cm. When not connected to the parameter analyser for measurements, all probes were routed and secured with screws to grounded terminal blocks, see Figure 4.6b. This scenario is preferred to leaving the probes floating (but all shorted) to prevent any charge build-up and unwanted current flow when toggling wires (sequentially) to the measurement unit. From an electrochemical point of view, this approach was also proved correct.

The measurement unit terminals for the two working electrodes (WE1 and WE2) are connected to little spring-loaded hooks, see Figure 4.6c. These hooks are employed to clamp wires attached to probes contacting the electrodes of interest. We always followed the same protocol for a measurement: hooks were attached to the wires, while the wires are still secured with screws to the grounded terminal blocks. Then, the wires were released from the terminal blocks and the measurement was performed. Finally, the pair of probe wires were secured back with screws into the terminal blocks before the little hooks were detached.

Although neither the spring-loaded probes nor the wires were shielded, the spring-loaded hooks were shielded (by wrapping insulated leads with grounded aluminium foil as an electrical shield) to triaxial cables connected to the measurement unit. A custom grounded Faraday cage (currently a modified cardboard box covered with aluminium foil, see Figure 4.6d) was also used to limit the ambient background electrical noise to the minimum: noise pick-up <100 fA was demonstrated, see Figure 4.7.

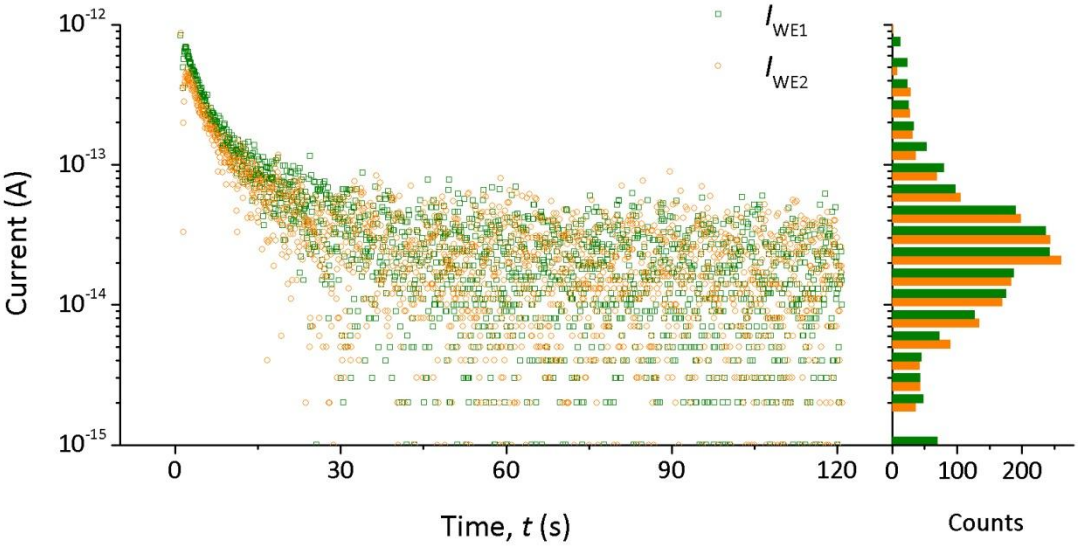

Figure 4.7. Minimising the ambient background electrical currents, ~30 fA is currently demonstrated in best conditions (in this test both spring-loaded probes contacting an empty nanoscale electrode gap were jointly biased under 0.5 V, current range reading was set to 100 pA with a resolution of 1 fA, 1 sample taken per measurement point: 1 measurement every ~20 ms).

4.2.2 DC measurements platform

4.2.2.1 3-terminal measurements

In standard electrochemistry, a working electrode is used to perform tests investigating oxidation-reduction processes of species dissolved in solution and/or adsorbed on the electrode surface; deposition of materials onto it or stripping of material from its surface, etc. The usual setup consists of three electrodes: the working electrode, WE, the (quasi) reference electrode, RE, and the counter electrode, CE. A potentiostat is used to apply a bias potential on the working electrode against the reference electrode which is supposed not to draw or supply any current. Current flowing at the reference electrode is normally balanced at the counter electrode. Employing two separate electrodes allows constant potentials to be maintained in the cell. However, for low currents (nA range) resulting from a small exposed working electrode surface, a counter electrode is no longer essential so that the reference electrode and counter electrode can be merged again.[30]

For certain applications such as ours, two working electrodes are needed and a different instrument called a bipotentiostat must be used.

Initial tests conducted with a commercial bipotentiostat CHI760C (specifically bought) showed limitations of the instrumentation in standard conditions. The channel for the second working electrode WE2 suffered from a higher background electrical noise pick-up than the channel corresponding to the working electrode WE1. Moreover, when testing the instrument on a

network resistor used to mimic devices under test (as explained in following paragraph 4.2.2.2), the instrument did not operate correctly.

As an alternative, a high resolution parameter analyser Agilent E5270B was thus used as a measuring unit for the main body of this work. Initial tests proving the relevance of the approach were conducted with another older parameter analyser, Agilent HP4156A (benchmarking tests: cyclic voltammetry of gold electrodes in 0.1 M sulphuric acid in water). With this configuration, low currents (sub pA resolution) could be measured and two working electrodes could be operated simultaneously, and separately in the same cell. We must point out this setup employs only three electrodes: the reference and counter electrodes being merged. From now on, we will define working electrode WE1 as the drain, working electrode WE2 as the source and the reference electrode as the gate, see Figure 4.8.

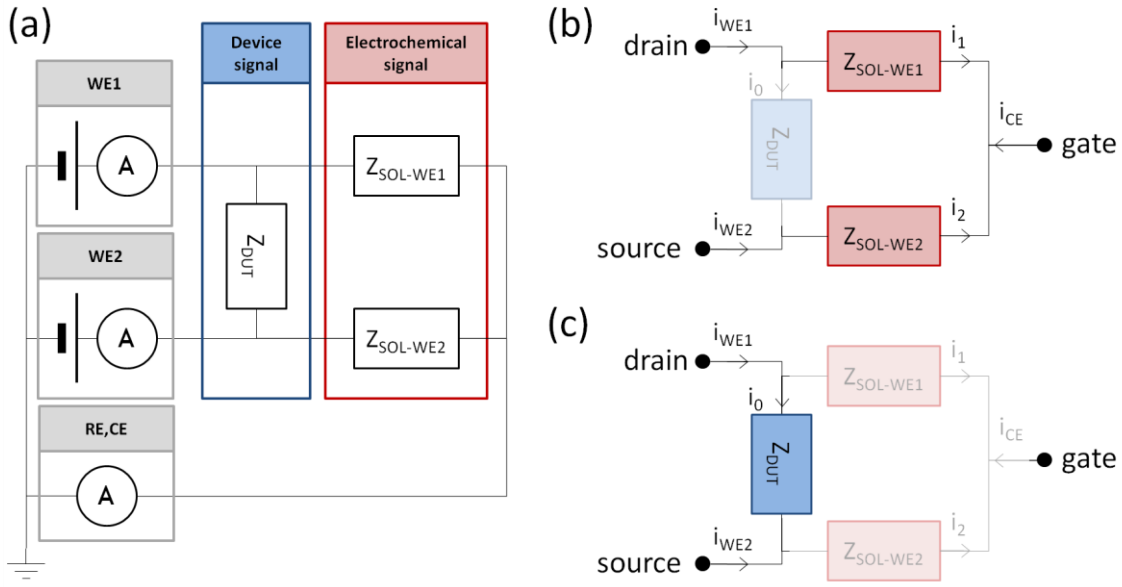

Figure 4.8. A parameter analyser is used to emulate a bipotentiostat. (a) Simplistic schematic of the instrumentation used connected to the device immersed into a liquid medium. (b) Electrochemical mode of functioning where there is no source-drain current. (c) Electrolytic gating mode of functioning where the reference electrode has virtually no current flow through it.

4.2.2.2 Functioning modes and limiting cases

We derive equations on our system of three electrodes.[28, 31] First of all, the continuity of currents dictates that the sum of currents passing through each electrode is null, see Equation 4.1.

$$\underbrace{i_{WE1}}_{+i_0+i_1} + \underbrace{i_{WE2}}_{-i_0+i_2} + i_{RE,CE} = 0$$

Equation 4.1. Continuity equation on currents.

In practice, currents measured may not strictly follow this equation if an entity is trapping charges or more likely if different current resolution ranges are employed for the three source measurement units, thus the values read by the instrument may partially invalidate Equation 4.1.

The system of two working electrodes associated to a reference electrode (and a counter electrode) is conceptually equivalent to a Field Effect Transistor driven by one gate. In terms of potentials applied, the expressions of the potential across the source and drain as well as the potential between source and gate can be found, see Equation 4.2.

$$\begin{cases} V_{DS} = V_{WE1} - V_{WE2} \\ V_{GS} = V_{RECE} - V_{WE2} \end{cases}$$

Equation 4.2. Equivalence between solid-state and electrochemistry names.

Two limiting cases can be highlighted: a pure electrochemical current mode (Figure 4.8b) and a source-drain current mode (Figure 4.8c). Let us assume the two working electrodes are totally independent from each other: no current flows from one to another. In this mode, the current flowing into/out of the working electrodes is compensated by the current flowing out of/into the counter electrode. The expression of the overall electrochemical current can thus be found, see Equation 4.3.

$$\begin{cases} i_0 = 0 \\ i_1 = i_{WE1} \Rightarrow I_{chem} = i_{WE1} + i_{WE2} \\ i_2 = i_{WE2} \end{cases}$$

Equation 4.3. Expression of the overall electrochemical current as the sum of the currents read on both working electrodes: WE1 and WE2.

In the source-drain current mode, it is assumed that the reference electrode does not pass any current: it just contributes to the system by pulling potentials on working electrodes. The current flowing via the reference electrode is thus assumed negligible and current flowing in/out the working electrode WE1, flows out/in the working electrode WE2. The expression of the source-drain current can thus be derived, see Equation 4.4.

$$\begin{cases} i_0 \approx i_{WE1} \approx -i_{WE2} \\ i_1 \approx i_2 \approx i_{RE,CE} \ll i_0 \\ i_0 = \dfrac{i_{WE1} - i_{WE2}}{2} \end{cases} \Rightarrow I_{sd} = \frac{i_{WE1} - i_{WE2}}{2}$$

Equation 4.4. Expression of the source-drain current as the average of the currents flowing through both working electrodes: WE1 and WE2.

To illustrate the concept of the two modes, we probe a resistor network of 3 resistors in which the resistance between the two working electrodes is Z_{DUT}=1 GΩ, and the resistances between each working electrode and the reference electrode are $Z_{SOL\text{-}WE1}$=5 GΩ and $Z_{SOL\text{-}WE2}$=5 GΩ. In this simple electrical setup, the continuity equation on currents is verified, and the two modes introduced above can be identified, see Figure 4.9.

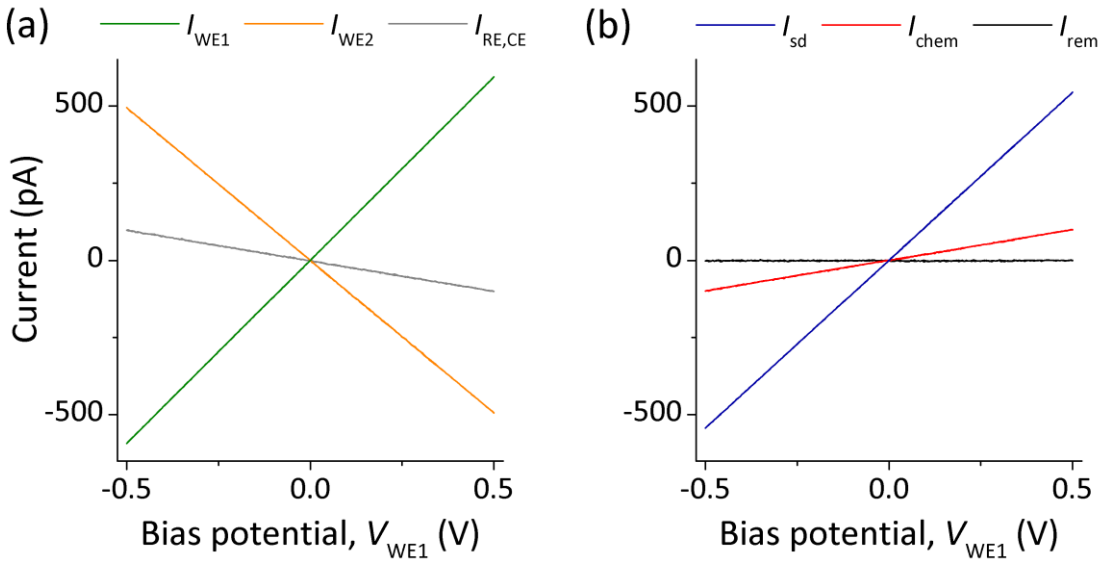

Figure 4.9. Example of measurements on a network of resistors: Z_{DUT}=1 GΩ, $Z_{SOL\text{-}WE1}$=5 GΩ, $Z_{SOL\text{-}WE2}$=5 GΩ. (a) The bias is swept on WE1, currents on all channels are read. (b) The transforms on currents show the source-drain current dominates with a residual through reference current but the sum of currents is virtually null. The transforms on currents are respectively: $I_{sd} = (-I_{WE1} + I_{WE2})/2$, $I_{chem} = I_{WE1} + I_{WE2}$ and $I_{rem} = I_{WE1} + I_{WE2} + I_{RE,CE}$.

4.2.2.3 Measurement methods

Having a third electrode to probe devices opens up a larger field of possibilities for characterising them. We developed an integrated instrument interfacing programme (in HP-VEE) to perform different types of measurements, exploring the contribution of bias potential between working electrodes WE1 and WE2, bias potential between working electrodes and the reference electrode and the time dependence of the response of the device under test.

Source-drain current-voltage type of measurements can still be performed, with the extra command on the reference electrode potential: the working electrode WE1 is biased against the reference electrode (WE2 is left at 0 V). One must make sure the potential difference between the two working electrodes is not too high in order to avoid electrochemical reactions between them. In practice, WE1 and WE2 can be jointly offset by a constant value against the reference whilst the potential is swept on WE1.

Conversely, one can jointly sweep the two working electrodes WE1 and WE2 by keeping a constant potential bias difference (ΔV) between them. In this way, possible electrochemical processes between the two working electrodes are kept to a minimum. This type of measurement, thereafter termed electrolytic gating, is analogous to FET device characterisation where the gate bias is swept whereas a constant low source-drain bias is applied. Using the same network resistor as tested above we perform an electrolytic gating test, see Figure 4.10.

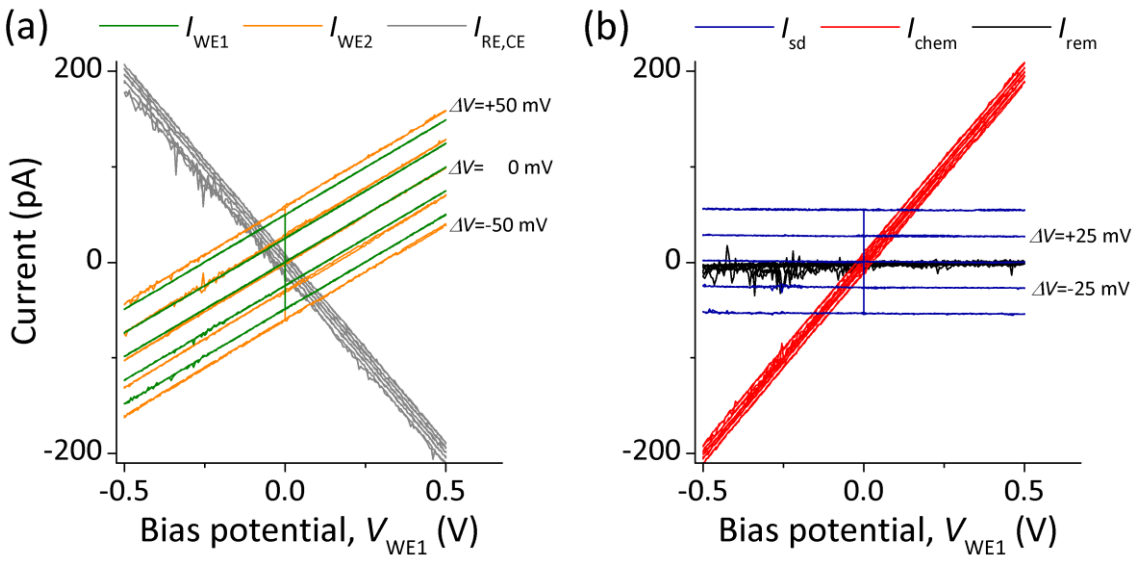

Figure 4.10. Example of artificial electrolytic gating on an assembly of a network of resistors: $Z_{\mathrm{DUT}} = 1\ \mathrm{G\Omega}$, $Z_{\mathrm{SOL\text{-}WE1}} = 5\ \mathrm{G\Omega}$, $Z_{\mathrm{SOL\text{-}WE2}} = 5\ \mathrm{G\Omega}$. (a) The bias is swept simultaneously on WE1 and WE2 with an offset potential between the two electrodes (ΔV) that is sequentially increased from -50 mV to +50 mV by steps of 25 mV. (b) The transforms on currents show the source-drain conductance is constant, $I_{sd} = (-I_{WE1} + I_{WE2})/2$ (simple resistor: $Z_{\mathrm{DUT}} = 1\ \mathrm{G\Omega}$), but the leakage current, $I_{\mathrm{chem}} = I_{WE1} + I_{WE2}$, is not negligible and even dominates above ±0.2 V. The remainder current is given by $I_{rem} = I_{WE1} + I_{WE2} + I_{RE,CE}$.

The impedance between source and drain is a simple resistor and as such is insensitive to any gating potential. This explains the constant current lines for I_{sd} on Figure 4.10b. For an effectively gated device, the response in current would not be constant and one would expect to notice an increase in current when the potential against the reference electrode is swept.

Measurements of currents over time are also made possible for different bias configurations of WE1 and WE2 against the reference electrode.

4.2.3 Fabrication-Characterisation process flow

For the making of nanocrystal assemblies between gold electrodes, we follow the same protocol as developed for chapter 3. A solution of 60 nm gold nanocrystals stabilised with citrate

1:10 diluted in de-ionised water is used as a source of nanocrystals for the directed assembly of a few of them (ideally one) using the dielectrophoretic force.

The candidate linker molecule used in the experiments was synthesised by Emma Harvey in the laboratory of Dr. Mary Pryce in DCU, Dublin. The compound is 1,2-Bis(5'-(3''-ethynylthiophene)-2'-methylthien-3'-yl)-cyclopentene and will be termed th-PCH-th. It is a symmetrical molecule thiophene-terminated on both ends with a moiety in the middle that can be irreversibly modified from an open-ring to a closed-ring form. Only the closed-ring isomer is oxidation-reduction active. The starting isomer is the open-ring form, it can be turned into the closed-ring isomer by UV irradiation or oxidative stress in solution (Appendix 6.7.1, p. 207).

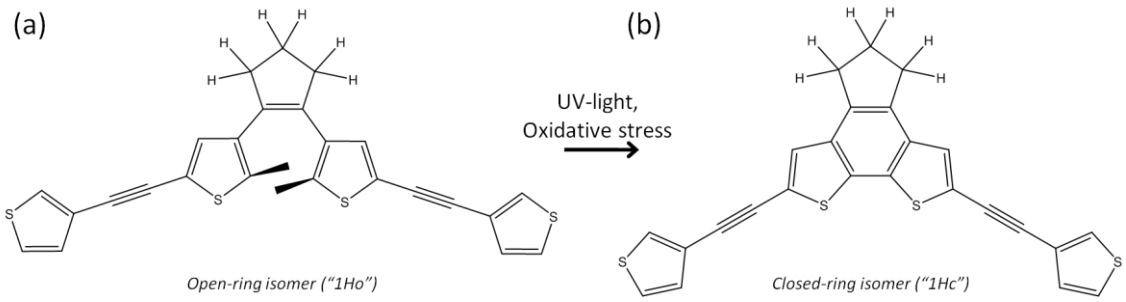

Figure 4.11. Chemical formula of the oxidation-reduction active linker molecule: 1,2-Bis(5'-(3''-ethynylthiophene)-2'-methylthien-3'-yl)-cyclopentene (th-PCH-th) has a calculated length of ~1.8 nm. (a) The open-ring isomer "1Ho" can be switched irreversibly to (b) the closed-ring "1Hc" (which is the only oxidation-reduction active isomer between the two) by UV-light irradiation or oxidative stress in a solution of dichloromethane for instance.

Electrode sets were directly immersed in a non-degassed solution of 2 mM th-PCH-th in dichloromethane to functionalise the nanocrystal assemblies. Measurements on as-trapped nanocrystal assemblies were not performed before the functionalisation step as the purpose of the development of the electrolytic gating technique is to show the modulation of the device conductance by controlling the gate bias. For qualitative measurements, the information of conductance before functionalisation is not essential, see Figure 4.12.

In practice, we measured 2 sets of electrodes as provided (without nanocrystals) to conduct electrochemistry studies; 5 sets of electrodes were measured to investigate the response of as-trapped nanocrystals in nano-gaps (4 in 10 mM tri-sodium citrate (TSC) in water, 1 in 10 mM tetrabutylammonium hexafluorophosphate (TBAHFP) in dichloromethane); finally on 4 electrode chips, 60 nm nanocrystals were trapped then functionalised and finally characterised in buffer analytes (3 in 10 mM tri-sodium citrate (TSC) in water, 1 in 10 mM tetrabutylammonium hexafluorophosphate (TBAHFP) in dichloromethane).

(a)

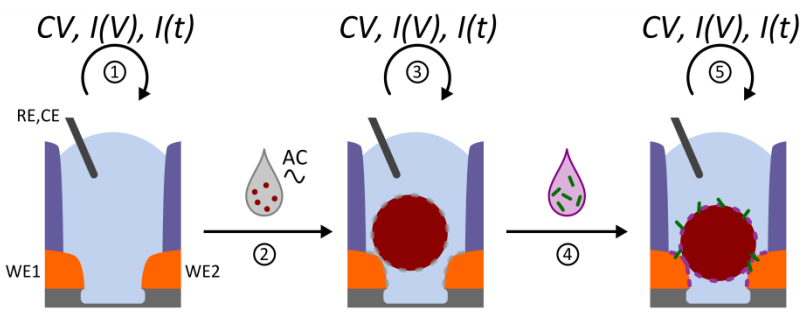

(b)

	CV	I(V) @Vg	I(t) @Vg	CV	I(V) @Vg	I(t) @Vg	CV	I(V) @Vg	I(t) @Vg
10 mM TBAHFP, DCM	✓	✓	✓	✓	✓	✓	✓	✓	✓
10 mM TSC, water	✓	✓	✓	✓	✓	✓	✓	✓	✓
0.1 M H_2SO_4, water	✓	✗	✗	✗	✗	✗	✗	✗	✗
1mM FcCOOH, 10 mM PBS, water	✓	✗	✗	✗	✗	✗	✗	✗	✗

Figure 4.12. Fabrication process flow and characterisation process flow. (a) After 60 nm gold nanocrystals are trapped the devices are immersed in a solution of 2 mM th-PCH-th in dichloromethane. (b) For each fabrication step, the measurement techniques and analytes employed are detailed, pairs of bare electrodes can be tested with cyclic voltammetry techniques (CV) or the source-drain current can be monitored during sweeping the gate potential (I(V) @Vg) or over time (I(t) @Vg). After nanocrystals were trapped by dielectrophoresis, devices were only tested in buffer analytes primarily with the electrolytic gating technique or the source-drain current was monitored over time. Cyclic voltammetry may also be tried in particular situations, for instance in case of no source-drain current detected or for large source-drain conductance devices.

4.3 Results

Results presented subsequently are primarily intended to demonstrate the abilities and flexibility of the setup. The aim of the measurements acquired was indeed to demonstrate the functioning of the setup in the first place and should be understood as providing qualitative results. Quantitative analysis of the data may also be considered in certain specific cases.

4.3.1 Electrochemistry mode

Electrodes for contacting assemblies of nanocrystals are made of gold material. A well known technique to characterise or clean electrodes is to perform cyclic voltammetry tests in 0.1 M sulphuric acid in water (pH~1). The potential on the electrodes is swept repeatedly (typically between 0 V and 1.4 V) with a constant scan rate so as to oxidise and then reduce the gold electrode surface under test.

We can test the fabricated nanometre-scale electrodes with this protocol, see Figure 4.13. Depending on the design of the electrodes (exposed surface area, geometry, roughness, etc.) and the voltage scan rate employed during the measurement the magnitude of the response in current differs. Typically, one can expect a current on the order of 50 pA at the reduction peak (similar to ref. [32], but 10 times higher current than reported on an etched nanoelectrodes[33]).

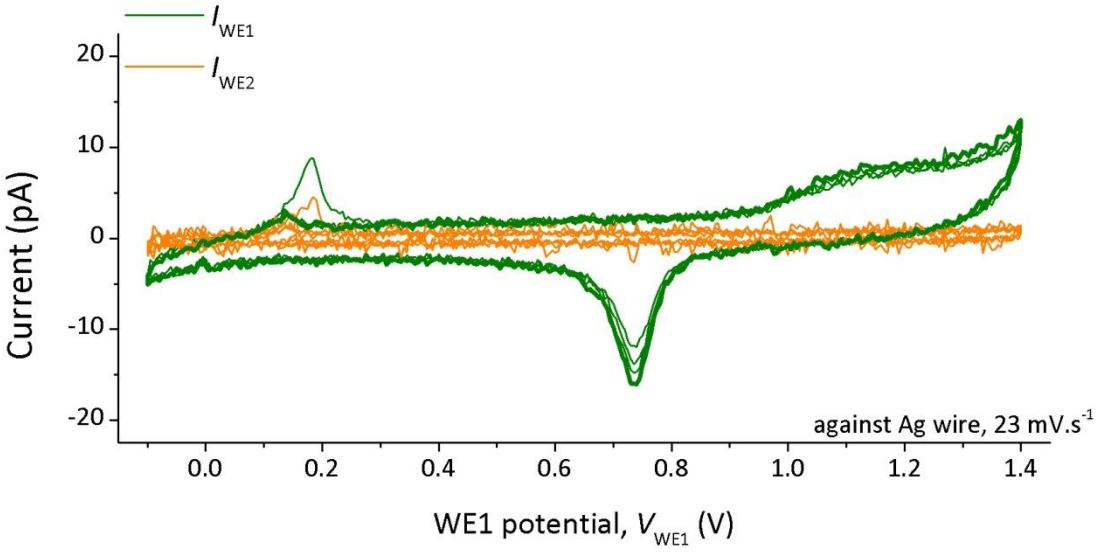

Figure 4.13. Cyclic voltammogram in 0.1 M sulphuric acid in water on the pair of electrodes from device X-4835_W1_B4,S3_0102: electrode "02" does not show any particular signal, whereas the electrode "01" show the characteristic oxidation plateau above the potential 1.1 V and the characteristic reduction peak ~0.73 V (for clarity, the trace of the last cycle is highlighted with a thicker line).

The oxide layer formed in the forward trace is supposed to grow on the outside of the electrode whereas the reduction (reverse trace) is supposed to get rid of all the oxygen thereafter. From such testing of gold electrodes in sulphuric acid one can extrapolate the surface roughness of the electrode. The area under the reduction peak is the charge exchanged during the reduction process and is estimated to be $386\ \mu C.cm^{-2}$ for Au (111) surface.[34-35] On granular films and three-dimensional geometry, like ours, the charge per unit of surface can be dramatically increased by a factor >5 if not ~30.[36]

Cyclic voltammetry of gold surfaces with a calibrated quasi-reference electrode such as Ag/AgCl results in a reduction peak centred at 0.8V. In a setup using a simple silver wire, the peak position is shifted towards lower values as in Figure 4.13 where it is approximately ~ 0.73V and can even drift to a minimum of ~ 0.55V. From an experimental point of view, we found the shift of potential for the reduction peak can be restored by running several cyclic voltammetry tests on a dummy planar gold electrode at strong negative potentials (<-1 V) with the Ag wire reference electrode resulting in the hydrolysis of water and formation of micro-bubbles. In all cases, the possible drift of the reference potential results in data being translated on the bias potential axis. Employing a wire as opposed to a calibrated quasi-reference electrode along with a platinum counter electrode will also result (in a first approximation) in a slight broadening of oxidation-reduction peaks but will not alter the peak separation.

In certain cases, one must acknowledge the presence of other peaks in the cyclic voltammetry traces such as toward ~ 0.15 V, see Figure 4.13. Over a few repeats of the sweep cycles, the peak fades away which suggests that the electrochemical contribution of an unidentified adsorbate is decaying.

To pursue the tests of functioning of our custom setup, we rely on testing the oxidation-reduction of ferrocene carboxylic acid. The compound dissolved in an aqueous electrolyte can be reversibly oxidised and reduced at the contact of gold electrodes. Because of the very small surface area of the electrodes exposed to the solution and the value of voltage scan rate, the current-voltage characteristic of the cyclic voltammetry tests is sigmoidal (in place of “duck shape” peaks with macro-scale electrodes), see Figure 4.14.

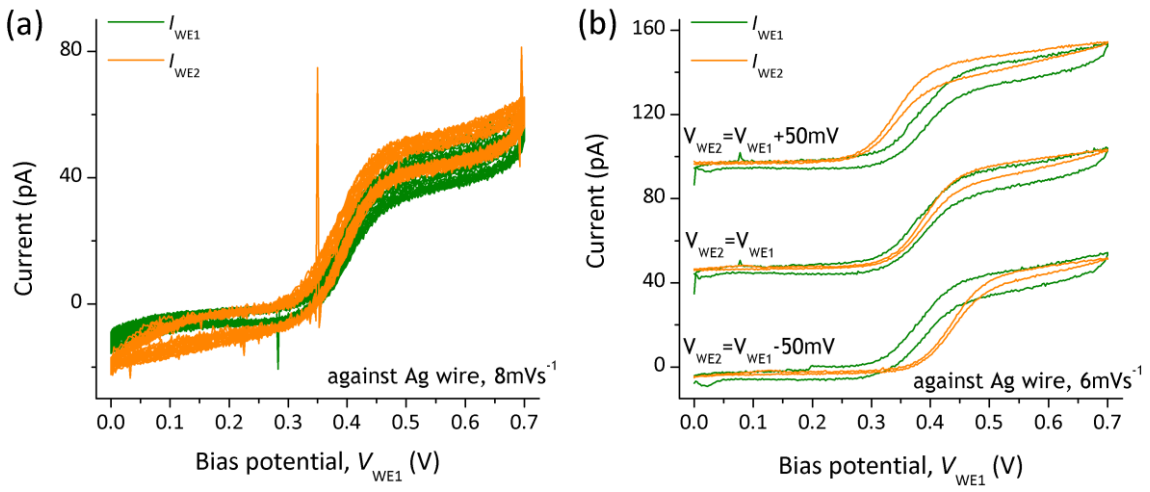

Figure 4.14. Cyclic voltammetry of 1 mM ferrocene carboxylic acid in water (10 mM PBS as a supporting electrolyte): (a) repeatability of the electrochemical response is tested on the pair of facing electrodes 1718 (test repeated 20 times); (b) functioning of the bipotentiostat mode is tested on two distant electrodes "17" and "15" (all measurements were acquired on device X-4835_W1_D1,S3).

Tests are conducted in a solution of 1 mM ferrocene carboxylic acid in a supporting electrolyte of 10 mM Phosphate-buffered saline (PBS) in water. They show parallel electrochemical reactions can occur repeatedly and consistently on distant electrodes (separated by ~320 µm) or facing electrodes (separated by ~40 nm), with independent control of the electrode potentials. This unambiguously proves our custom setup acts as a simplified bipotentiostat with high resolution for low currents (ranging between sub pico-amperes to sub micro-amperes).

In preparation of the test of assemblies of nanocrystals trapped in nano-gaps, we investigate the electrochemical response of the electrodes in two different buffer solutions: on one hand, a 10 mM trisodium citrate in water solution (a standard buffer for gold nanocrystals), see Figure 4.15a; on the other hand, a 10 mM tetrabutylammonium hexafluorophosphate that dissolves the th-PCH-th molecules well, see Figure 4.15b.

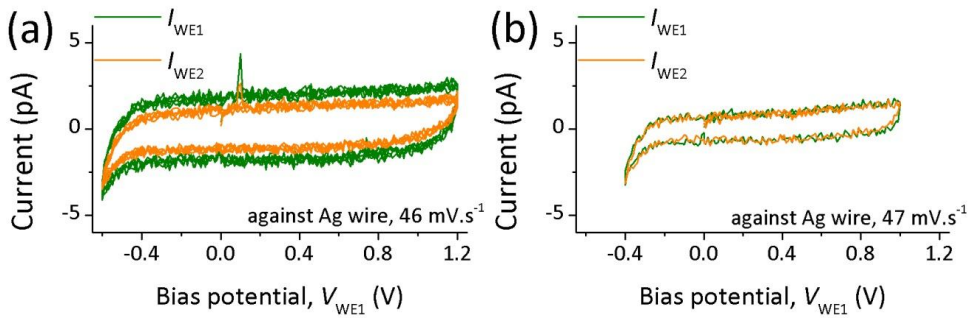

Figure 4.15. Background cyclic voltammetry for the quantification of the electrolytic leakage current thus defining the electrochemical potential bias window of action: a, tests on the pair of facing electrodes from device X-4835_W1_C3,S3_0102 in 10 mM trisodium citrate in water; b, tests on the pair of facing electrodes from device X-4835_W1_D3,S4_0304 in 10 mM tetrabutylammonium hexafluorophosphate in dichloromethane.

Both background cyclic voltammetry tests show a nearly flat response over a range bigger than 1 V: between -0.5 V and 1.2 V in water, between -0.3 V and 1.0 V in dichloromethane. The magnitude of the blank electrochemical current is limited to <10 pA at a voltage scan rate approaching ~ 50 mV/s. From a solvent point of view, this demonstrates the possible latitude of reference potential range. Also, it could be inferred that one can choose the solvent according to the experimental needs.

4.3.2 Dielectrophoretic trapping

Compared to chapter 3, the best conditions for trapping nanocrystals using the dielectrophoretic force in the electrode gap are altered as the substrate is different: low p-doped silicon wafer, thicker thermally grown silicon oxide (300 nm thick as opposed to <100 nm for chapter 3), capping PECVD silicon nitride, not to mention the change in topography of the landscape near the gap due to the passivation layer and the different electrode layout designs.

Scanning Electron Microscope images tend to show an over etch of the silicon dioxide occurred during the opening of the silicon nitride passivation layer around the electrodes, possibly leading to under-cut of a few nanometres. The over-etching results in a three-dimensional configuration around the electrodes.

We seem to face a strong dependency of the trapping parameters regarding the electrode design. The best trapping potential for symbols S1 and S2 seems to be ~3.6 V_{pp} whereas it seems it is ~3.8 V_{pp} for symbols S3 and S4. However, even for larger peak-to-peak voltage applied (~4.2 V_{pp}) the presence of few nanocrystals (typically less than 10) between and/or covering the nanometre-scale gaps can still lead to currents below the measurement limit (open-circuits) or low conductance ranging from 10^{-9} G_0 to 1 G_0 (sub 1 G_0) or higher (>1 G_0) device conductance, see Figure 4.16.

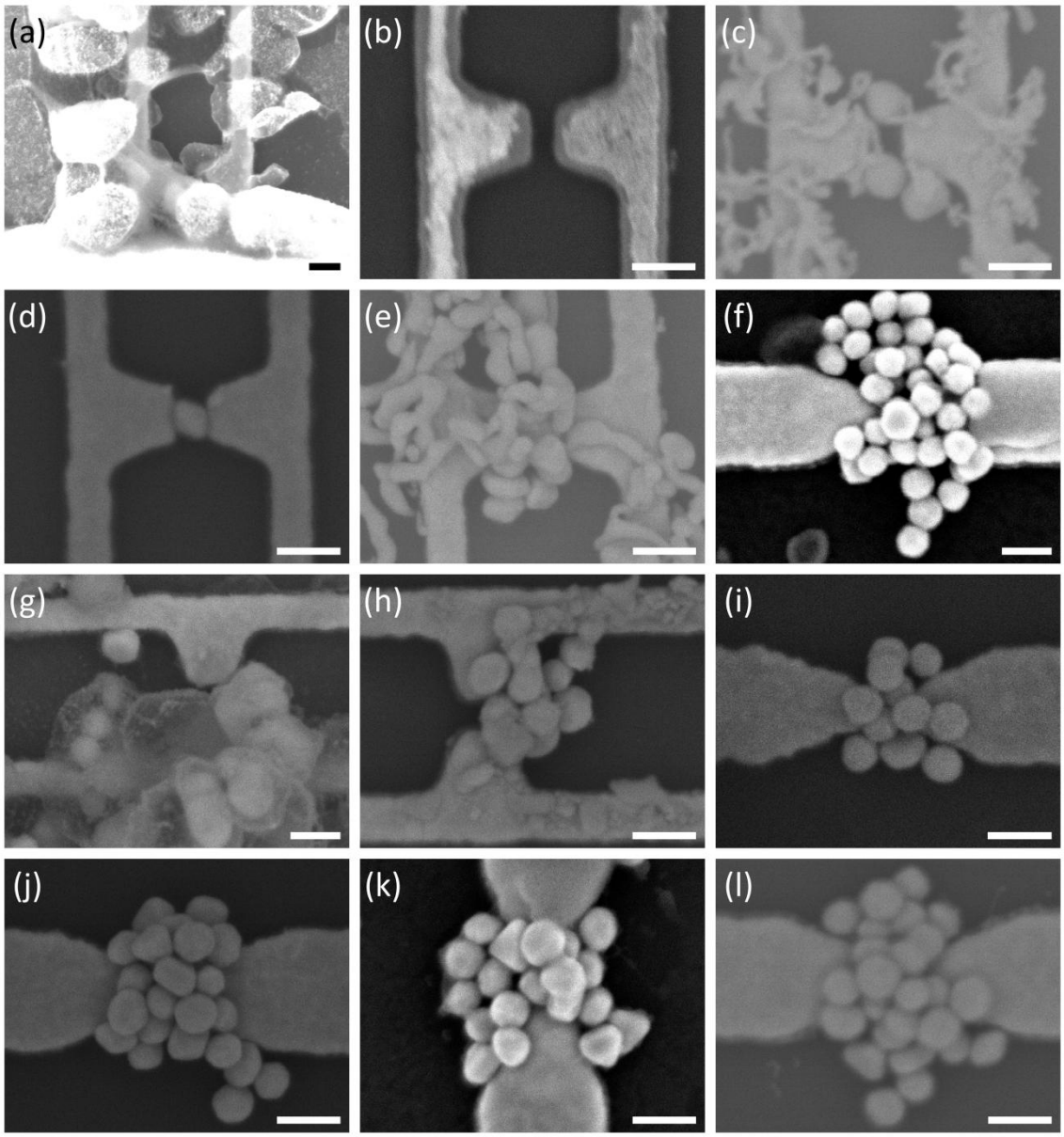

Figure 4.16. Overview of Scanning Electron Microscope images of devices discussed in the text, most devices present trapped nanocrystals in the nano-gap (all scale bars are 100 nm long): a, X-4835_W1_B4,S3_0102; b, X-4835_W1_D1,S3_1718; c, X-4835_W1_C3,S3_0102; d, X-4835_W1_D3,S4_0304; e, X-4835_W1_C3,S3_1314; f, X-4835_W1_D5,S1_1516; g, X-4835_W1_B4,S3_1112; h, X-4835_W1_B4,S3_1920; i, X-4835_W1_C2,S2_0506; j, X-4835_W1_C2,S2_1516; k, X-4835_W1_D5,S1_2122; l, X-4835_W1_D4,S1_0506. Images were taken using the JEOL JSM 7001-F instrument, using the Gentle-Beam mode (GB-L) with a beam voltage of 3 kV and a substrate bias of 0.2 kV, back-scattered electron filtering (EV, 11) may have been employed for certain pictures but eventually appears not strictly necessary. Electrodes chips may have been rinsed in dichloromethane and/or sulphuric acid and/or isopropyl alcohol to remove adsorbed solution residues (salts).

One needs to understand and refine the parameters currently used for trapping: as no log-normal distribution is observed unlike chapter 3 for the conductance of nanocrystals trapped. It seems the over-etching must have an effect as particles are seen to fit in. Unifying the electrode design employed will probably also help in reaching more consistent results.

4.3.3 Electrical instability of the nanocrystal assemblies

We investigated a substantially smaller number of devices compared to chapter 3. However, the setup provides the ability to carry out measurements of devices in vacuum conditions, water based and dichloromethane-based media.

It appears the nanocrystal assemblies are much more fragile in the present electrode configurations than in chapter 3, see Figure 4.17. Devices were initially tested in a bias voltage window of ±0.5 V, but the onset of instabilities at lower bias potential V_{ds} lead to reduce the investigation potential to merely ±0.1 V, even though it may not prevent gradual and/or sudden conductance changes for all devices.

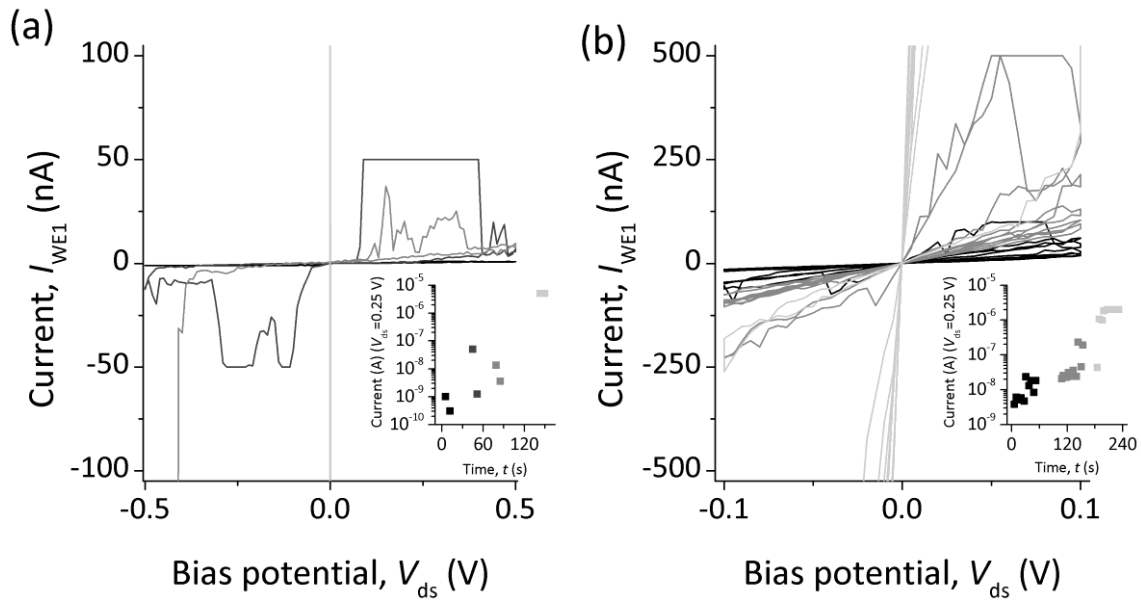

Figure 4.17. Lack of repeatability of I(V) measurements (WE1 is biased whereas WE2 is left at 0 V): a, device X-4835_C3,S3_1314 is measured four times with sweeps between ±0.5 V with an ever increasing conductance before breaking of the device; b, device X-4835_W1_D5,S1_1516 is measured repeatedly in a smaller bias window ±0.1 V but also presents instabilities (without breaking). Measurements were both carried out in an aqueous buffer solution of 10 mM trisodium citrate, flat portion of traces are the result of the reach of the current compliance.

It turns out that a substantially larger number of devices present either an open-circuit characteristic: the source-drain current is null but a residual electrochemical current is noticeable on both electrodes when taken separately (although nanocrystals are assembled in the nano-

scale gap) or present a conductance $G_{dev} > 1\ G_0$. For large conductance devices, it looks the assembly suffers degradation when only one of the electrodes is biased (WE1 is driven, WE2 is off, i.e.: single potentiostat mode) and the voltage is swept >0.2V in a solution of 0.1 M sulphuric acid (pH~1) or >0.35 V in the solution of tri-sodium citrate (pH~6), see Figure 4.18.

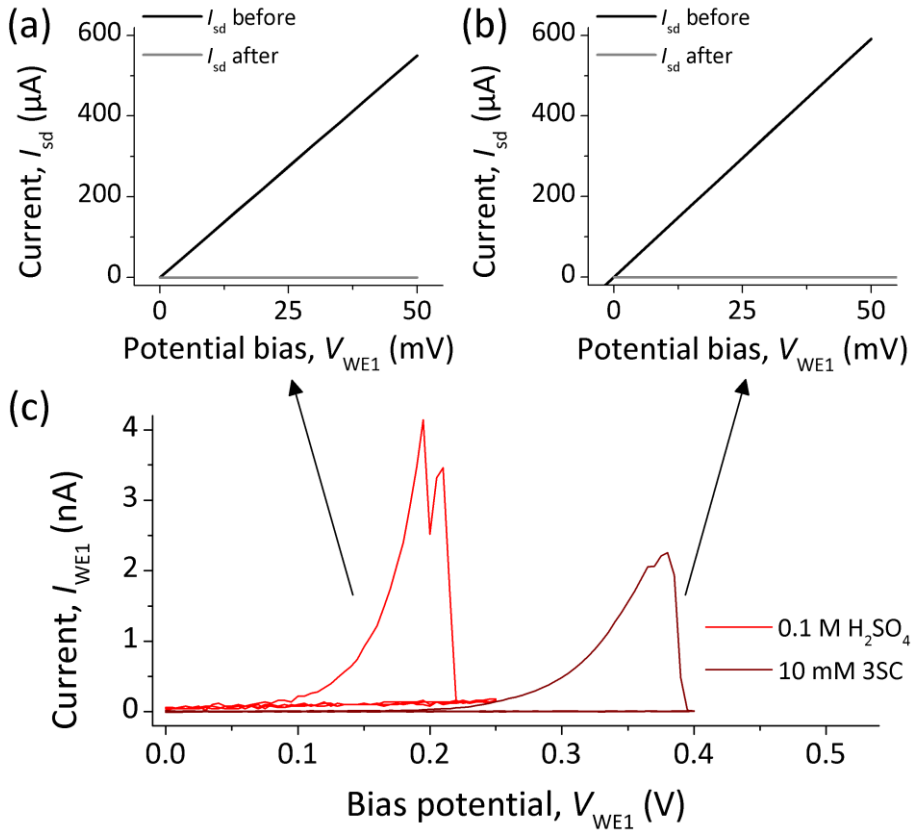

Figure 4.18. For large conductance devices, cyclic voltammetry sweeps performed on one of the electrodes (the other being left floating) show an irreversible surface reaction must occur and eventually leads to the dramatic degradation of the source-drain conductance. (a) Source-drain current traces for the device X-4835_W1_B4,S3_1112 are shown before and after the CV scans. (b) Source-drain current traces for the device X-4835_W1_B4,S3_1920 are shown before and after the CV scans. (c) The potential at which this electrochemical stress takes place is sensitive to the pH of the buffer solution: the device X-4835_W1_B4,S3_1112 is tested in 0.1 M sulphuric acid in water; the device X-4835_W1_B4,S3_1920 is stressed in a buffer of 10 mM tri-sodium citrate.

In all cases investigated (4 devices in sulphuric acid, 1 device in tri-sodium citrate), the high conductance of the device is kept as long as the potential sweep does not pass the critical value. However, once the asymmetric bell-shape curve is observed (any other retraces are flat), probing the device to measure a source-drain current shows the there is no longer any measurable conduction through the nanocrystal assembly. Conversely if the sweep approaches the threshold potential close enough, the source-drain conductance is significantly altered. In practice, we

suggest this irreversible phenomenon could be used to modify a high-conduce device ($G > G_0$) so as to adjust its conductance to the tunnelling regime ($G < G_0$).

4.3.4 Time dependent measurements

For some of the devices measured and presenting unstable source-drain characteristics, time dependent measurements were carried out.[37] Traces of currents on both working electrodes WE1 and WE2 are recorded using the most suitable current reading range (to obtain the best trace resolution) so as to investigate possible stochastic modulation of device conductance at constant bias potential excitation as opposed to a situation where a potential bias sweep is applied.

Amongst the few devices tested with this time dependent technique, only one device clearly shows two-state level conductance for the first few minutes of the test, see Figure 4.19. Further tests tend to show more but not as well defined conductance levels.

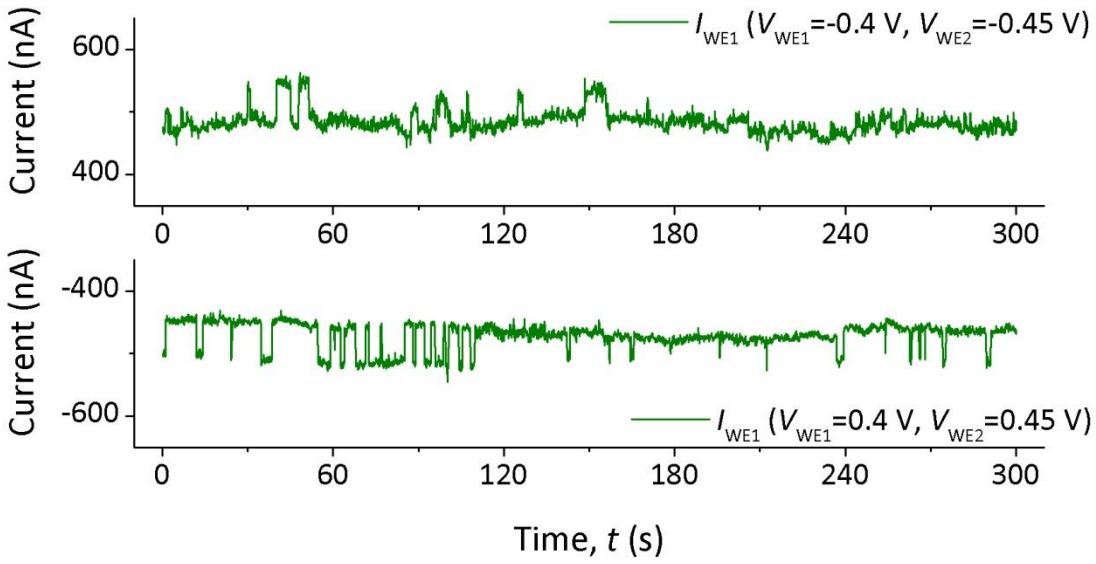

Figure 4.19. Stochastic switching of a device conductance on an assembly of as trapped nanocrystals (device: X-4835_W1_C2,S2_0506, medium: buffer of 10 mM tri-sodium citrate in water). This type of traces was observed for only one device amongst the few devices (~ 10) tested with this method.

Several scenarios have been proposed to explain these current traces in the molecular electronics community: changes in conformation of molecules, electron localisation or breaking of molecule-surface bonds.[38] In the present device however, the assembly of nanocrystals was not functionalised so that the fluctuations do not originate from th-PCH-th linker molecules.

4.3.5 Testing the electrolytic gating

The main advantage of a three terminal probing system is to give the ability to pull the energy levels of the device under test in the system compared to the third electrode acting as the reference potential. Based on the potential ranges determined in the preliminary electrochemistry studies (paragraph 4.3.1), we investigate the influence of the "gate voltage" of the nanocrystal assemblies trapped between the source and drain electrodes.

To qualify the method, we start by testing the nanocrystal assemblies as trapped in the nanometre-scale gap. A solution of 10 mM tri-sodium citrate in water is used as a buffer electrolyte for the measurements. Typically, a small source-drain bias (up to ±50 mV) is applied between the two working electrodes WE1 and WE2 on top of the driving sweeping bias (for both working electrodes) against the reference electrode ($V_{RE,CE} = 0$ V). In the best-case scenario, a set of constant current curves can be observed across the sweeping bias range indicating that the as-trapped nanocrystal device is insensitive to the electrolytic gating, see Figure 4.20.

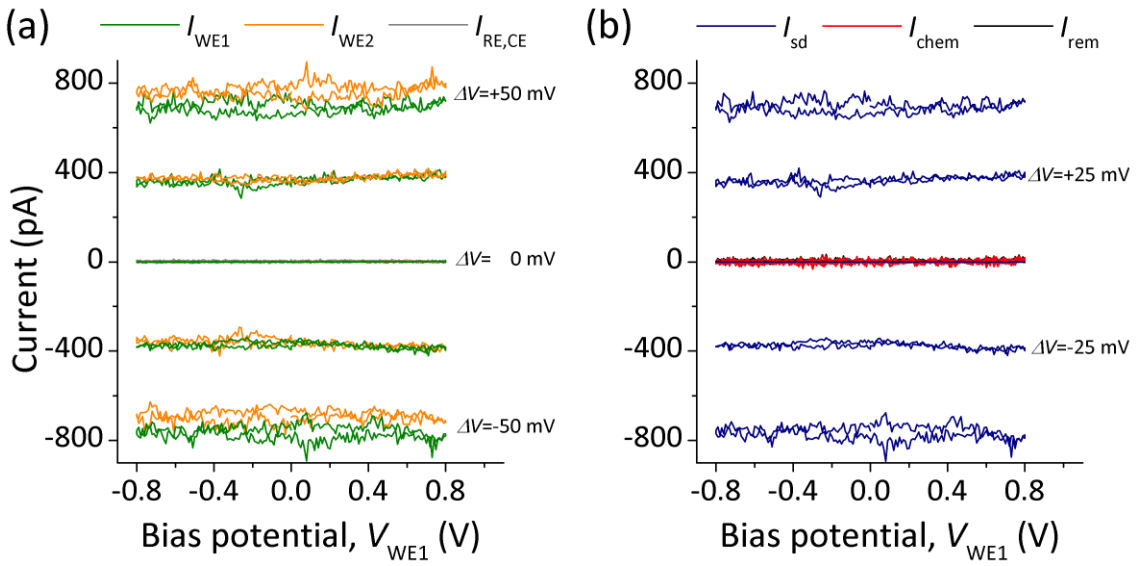

Figure 4.20. Background electrolytic gating tests on as trapped nanocrystal assemblies: the device under test does not show any dependence on the electrolytic gating potential swept (device: X-4835_W1_C2,S2_1516, medium: buffer of 10 mM tri-sodium citrate in water). The transforms on currents are respectively: $I_{sd} = (-I_{WE1} + I_{WE2})/2$, $I_{chem} = I_{WE1} + I_{WE2}$ and $I_{rem} = I_{WE1} + I_{WE2} + I_{RE,CE}$.

The purpose of the development of the electrolytic gating technique is to control the conductance of the electrode-molecule-nanocrystal junctions. As opposed to chapter 3 where source-drain bias measurements were carried out before and after functionalisation, four chips (containing 12 electrode pairs each) were prepared by immersion in 2 mM solution of th-PCH-th

molecules in dichloromethane directly after the application of an AC field in a nanocrystal solution targeting trapping of nanocrystals.

From the measurement series in both aqueous and non-aqueous solvents, 8 devices presenting low conductance (<1 G_0) were effectively tested with the electrolytic technique. Similarly to the non functionalised nanocrystal assemblies, the degradation of the conductance was also observed for most devices for "gate bias" potential substantially smaller than the potentials at which oxidation-reduction of the th-PCH-th molecule normally occur: V_{T1}~0.4 V and V_{T2}~0.6 V (see Appendix 6.7.1, p. 207 for cyclic voltammetry characterisation of the molecule). The degradation eventually leads to open-circuits if test cycles are too numerous, see Figure 4.21.

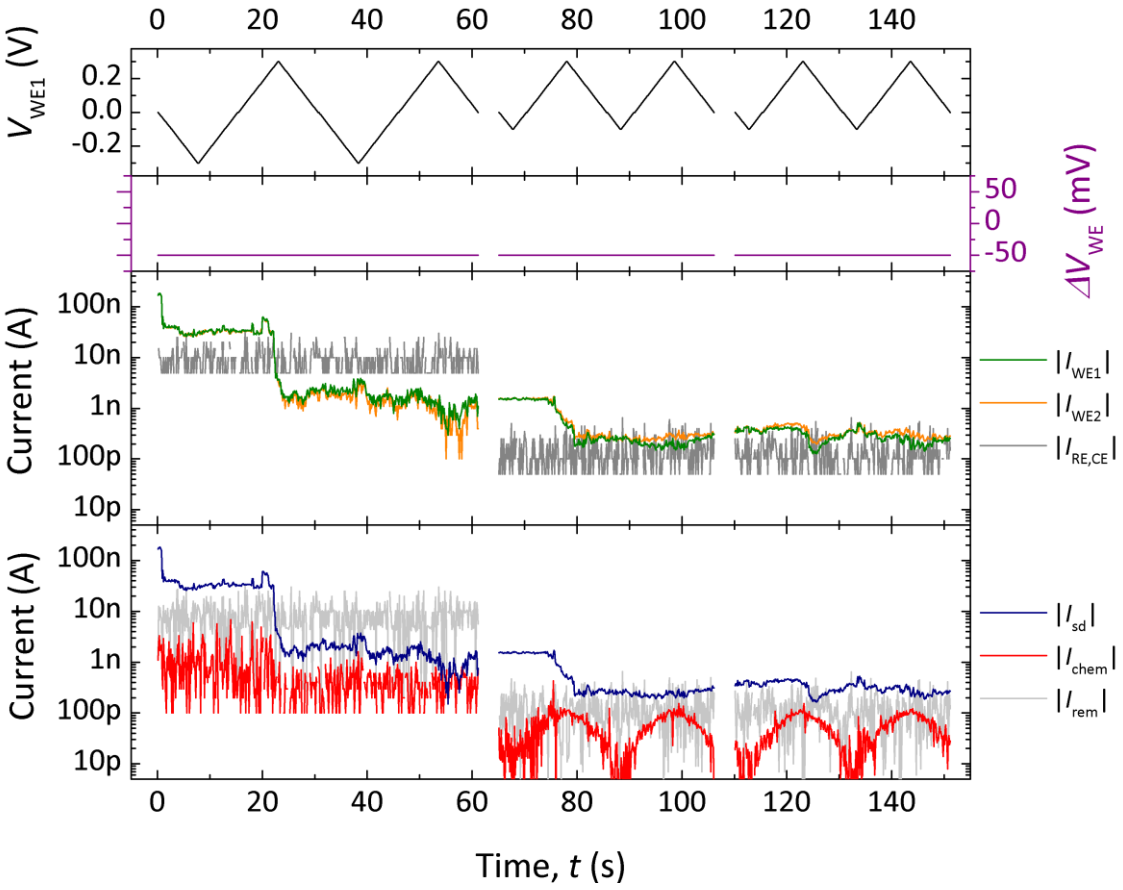

Figure 4.21. Electrolytic gating is likely to cause destabilisation to the device under test (device: X-4835_W1_D5,S1_2122, medium: buffer of 10 mM tri-sodium citrate in water, $\Delta V = -50$ mV), 3 tests (repeated twice each time) of "gate bias" sweeping makes the current irreversibly decay; the change in current magnitude for the reference electrode originates from the change in current sensitivity between tests 1 and 2. The transforms on currents are respectively: $I_{sd} = (-I_{WE1} + I_{WE2})/2$, $I_{chem} = I_{WE1} + I_{WE2}$ and $I_{rem} = I_{WE1} + I_{WE2} + I_{RE,CE}$.

Amongst these 8 devices, only 1 device showed behaviour consistent with the electrolytic gating test for accessing an energy level near the Fermi level or at least lowering its energy barrier compared to the Fermi level of the metal electrodes, see Figure 4.22.

First of all, the conductance was found to be independent on the "gate bias" in the ±0.4 V range (source-drain bias limited to ±20 mV). The series of approximately constant currents for different source-drain bias values can be observed in the first sequence (steps of 10 mV), see Figure 4.22. In particular, the source-drain current is very limited for a 0 V source-drain bias: the current read is the Faradic current with the solution (plus a residual contribution due to imperfect instrumentation control, cf. 4.4.1.1).

At the beginning of the second test, the source-drain current was comparable to the final value of the current measured at the end of the first test. For larger "gate bias" potentials applied, the conductance was found correlated to the gate excitation to a certain degree. Two bumps in the current trace can repeatedly be observed when the gate potential exceeds 0.4 V. The positions of the bump in the current traces are delayed compared to the excitation of the gate bias. This modulation of the current seems to be in agreement with the threshold values of oxidation-reduction ($V_{T1} \sim 0.4$ V and $V_{T2} \sim 0.6$ V) for the th-PCH-th molecule.

During the third electrolytic gating test, the current trace starting at the same level as it was during the last scan increased consistently with the gate bias potential excitation. However, at a gate bias potential ~ 1 V, the device failed as indicated by the sudden drop in current to the noise level for this current range. The remainder of the cycle of gate excitation showed the device was destroyed as it did not pass any source-drain current anymore.

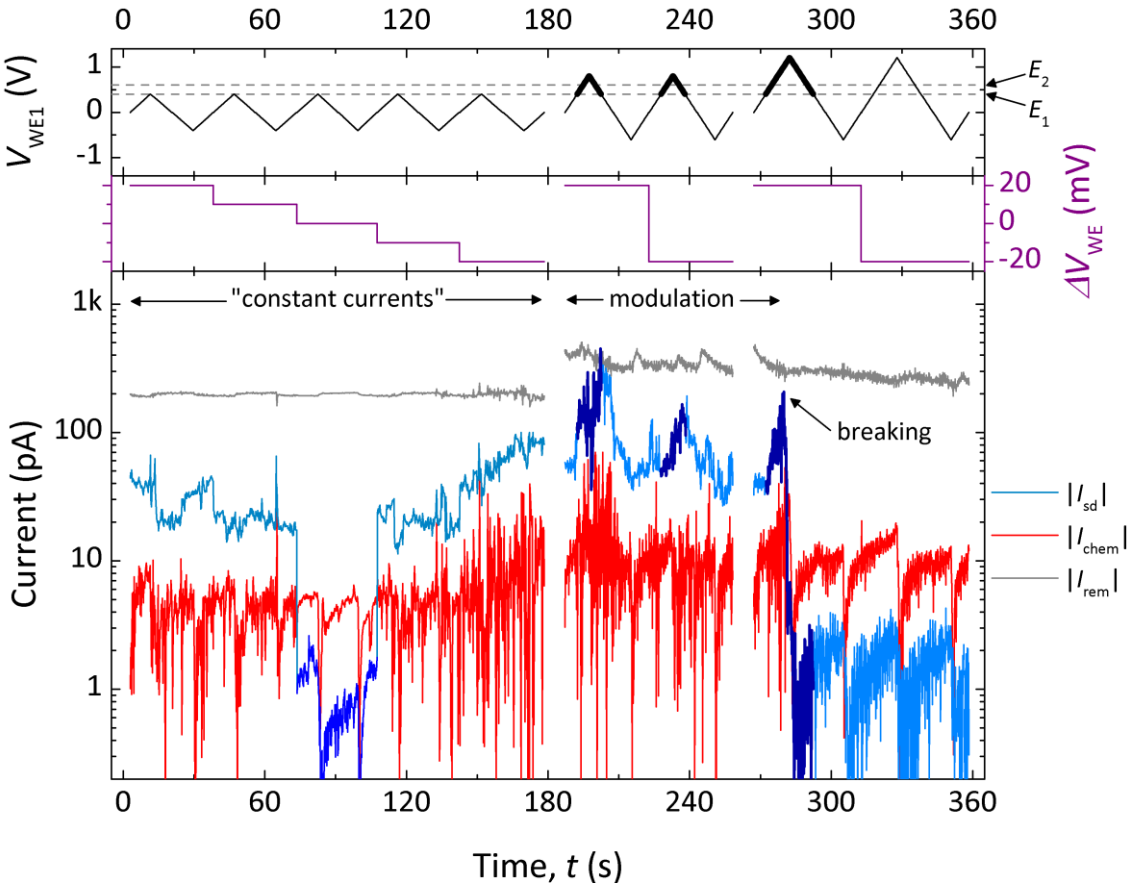

Figure 4.22. Demonstration of source-drain current modulation by electrolytic gating (device: X-4835_W1_D4,S1_0506, medium: buffer of 10 mM tri-sodium citrate in water, $\Delta V = \pm 20$ mV). During the first test, the source-drain bias is changed in steps of 10 mV and the gate bias potential is kept lower than the first oxidation-reduction threshold potential: the source-drain current is approximately constant (when the source-drain bias is zero, the test is equivalent to a cyclic voltammetry test on both electrodes). If the gate bias is swept above the oxidation-reduction potential threshold, the current tends to increase reversibly. For the last test, the device fails after the gate bias potential exceeds ~1 V. The transforms on currents are respectively: $I_{sd} = (-I_{WE1} + I_{WE2})/2$, $I_{chem} = I_{WE1} + I_{WE2}$ and $I_{rem} = I_{WE1} + I_{WE2} + I_{RE,CE}$. The different shades of blue on the current I_{sd} are guides to the eye.

Nevertheless, we must report that for this device and likewise for others devices or electrodes immersed in the solution of 2 mM th-PCH-th molecules as the functionalisation step, cyclic voltammetry tests performed in the appropriate potential window between ~0.0 V and 1.0 V (in blank electrolyte of either 10 mM tri-sodium citrate in water or 10 mM tetrabutylammonium hexafluorophosphate in dichloromethane) did not show any signature of surface oxidation-reduction activity contrary to what could be expected if th-PCH-th molecules were bound to the surface and still electrochemically active.

In Figure 4.22 the current flowing on the reference electrode is not negligible and uncorrelated to the current flowing into/out of the working electrodes. This situation arose in multiple tests and is retrospectively believed to be a marker of the need for the reference electrode to be cleaned and/or the buffer solution to be refreshed as parasitical electrochemical processes must be taking place at the vicinity of the reference electrode surface (set at 0 V).

Electrolytic gating tests were also carried out on devices presenting high conductance (>1 G_0). A gradual degradation of the conductance is observed for nearly all nanocrystal assemblies in this configuration as soon as the gate bias is brought above ~0.3 V.

4.4 Discussion

4.4.1 Improvements in the experimental setup

The development of this entirely new chemical cell over sample probing platform has been demanding and shown several aspects can be improved to achieved higher measurement performance and reliable quantitative results.

4.4.1.1 Instrumentation

On the instrumentation side, the programme currently performs measurements in the "spot mode" so that data points are queried by and retrieved to the controlling PC one at a time. Although valid this approach implies data to be transmitted with a minimum delay of ~ 20 ms limiting the voltage step resolution for high voltage scan-rates measurements. At this early stage of nanocrystal assembly characterisation, it is not a critical shortcoming. However we can foresee the ability to perform quicker measurements could bring new information in the case contacted nanocrystal assemblies are viewed as sensor devices. Thankfully, the E5270B parameter analyser offers the possibility of buffering data packets and should thus eliminate this limitation.

Presently, in the case of devices with a non open-circuit between the two working electrodes, it is not possible to simultaneously sweep the bias voltage on the two working electrodes in a perfect manner. Being able to do so, would provide information on the possible chemical reaction at the working electrodes independently. Currently, because the sweeping requests are sequential, a temporary offset bias between the two working electrodes appears. The expected outcome of this measurement technique can completely be overshadowed because the resulting source-drain current can be larger than electrochemical current. Tests reported on the instability of the high conductance junctions (>1 G_0, paragraph 4.3.3) were performed with only one electrode biased (the other was left floating), but the issue can be resolved by leveraging the ability of the E5270B parameter analyser to simultaneously copy the biasing request from one channel to another.

Currently the compliance on currents flowing through the working electrodes can be used to determine the current range reading for each of them. The reference electrode compliance is set to the sum of the compliance on working electrodes (based on Equation 4.1) and so the current range reading can be chosen accordingly. We have seen this can result in limiting the current on the reference electrode in certain cases, see Figure 4.22. In case of a symmetrical current range reading for both working electrodes, a method forcing an overall common current range reading for all electrodes (WE1, WE2 and RE) could also be implemented so as to provide more consistency in the measurement of currents.

Along the same lines, as we have seen, the sum of currents flowing into/from the system may not be null contrary to the assumption of Equation 4.1. Therefore, all currents should be presented to the scientist during the course of the experiment so as to provide a complete overview and allow early detection of possible parasitic reactions at the reference electrode.

4.4.1.2 Sample holder

Efforts on minimising the ambient background electrical noise resulted in an electrical noise pick-up less than 100 fA (for a current reading range of 0.1 nA, paragraph 4.2.1.3). Coaxial connections could be implemented down to the spring-loaded probes to lower even more efficiently. We foresee that reduction of the ambient electrical noise pick-up by 1 decade is manageable, although one must keep in mind the range for current reading on the instrument may also limit the resolution of the measurement.

On the connectivity of the different electrodes, three-state toggle switches could be implemented for each of them: the default state would be grounded, and the two other states of the switch would be working electrodes WE1 and WE2 respectively. In this manner, electrodes could all be tested in parallel (i.e.: all toggled on WE1) for sulphuric acid scan cleaning for instance.

Working with aqueous solutions is practical as the simple Perspex cap limits evaporation properly. However, in presence of more volatile solution, the solvent tend to evaporate very quickly leading to potentially dramatic change in salt concentration of the supporting electrolyte as noticed experimentally for the buffer solution of 10 mM tetrabutylammonium hexafluorophosphate in dichloromethane. Moreover, contamination of the solution may take place over the course of the measurements (several hours are needed to probe the 12 devices on one sample). Renewal of the buffer electrolyte solution can be achieved with an automatic syringe or a microfluidic setup mounted on top of the samples: this was respectively demonstrated and is being developed by Dr. Pierre Lovera for the electro-chemi-luminescence setup based on this platform.

In place of macroscopic silver wire as a reference electrode, quasi-reference electrode and counter electrode can also be directly processed on the chip as demonstrated by Karen Dawson for her work on electrochemistry also based on this platform.

4.4.1.3 Device design

The range current flowing between source-drain through the nanocrystal assembly spans across several decades starting from ~ 100 pA and up to thousands of nA or even mA. We demonstrated the electrochemical (leakage) current is limited to ~ 10 pA. For more practicality,

we propose the device design could be altered in two main ways to release the constraints on tolerance for the fabrication of samples.

A background electrochemical current 10 times higher is probably bearable. Even without reaching this limit, larger opening windows in the passivation layer could be designed minimising the risk of dramatic misalignment during the fabrication process (in total 6 samples out of 18 were partially or totally compromised during the process).

Along the same lines, the geometry of electrodes could be unified and the simplest layout design symbol of "facing fingers" (Figure 4.4, symbol 1) could be retained. The benefit of employing only one symbol would be to have only one set of dielectrophoresis trapping conditions.

Furthermore, as a parallel fabrication process characterisation, test or calibration structures could be written so as to limit the over-etching of the passivation layer grinding the supporting the silicon dioxide and thus limiting the under-cut of it (unavoidable at the nano-scale). Metal electrode integrity could also be investigated as well as functionalisation surface tests.

Along the same lines, to fully qualify the electrode chips, one can ensure the layer of 300 nm of thermal oxide is insulating the electrodes from the p-doped silicon substrate. The oxide layer at the back of the chip can be scratched so as to allow the formation of a contact and testing of possible leakage currents through the substrate can be tested.

4.4.2 Nanocrystal assembly reliability

Tests conducted on highly-conductive source-drain devices ($G > G_0$) showed the bias of only one electrode (the other being left floating) induces a dramatic reduction of the conductance and potentially complete destruction of it if the potential of ~ 0.4 V is exceeded. This phenomenon could possibly be used to engineer the source-drain conductance of nanocrystal assemblies to sub 1 G_0 conductance devices.

However, from the restrained set of 8 sub 1 G_0 and 4 above 1 G_0 conductance devices that were tested using the electrolytic gating technique, it seems the nanocrystal assemblies could be too fragile for the gate bias application.

We propose the application of the gate bias, modifying the depth of the electrical double-layer at the interface electrode liquid, plays a key role in the deleterious perturbation of the measured source-drain conductance. Since the oxidation of the gold electrode surface is unlikely: working electrodes are not brought above 0.4 V (against Ag wire) when the decay of the conductance starts to occur, we propose the gate bias disrupt the balance of forces stabilising the

nanocrystal(s) trapped in between the electrodes. The disruption of forces may result in the physical reorganisation of the nanocrystal assembly leading to sufficient displacement of nanocrystals to impede further tunnelling current. Tunnelling current is strongly dependent on the distance between metal nodes, as shown in chapter 3, and a few extra angstroms are enough to render the tunnelling current practically immeasurable.

The review of devices by Scanning Electron Microscopy cannot reveal the postulated gap afterwards as the imaging resolution is not sufficient. The demand reaches the limit of the instrument whilst the sample is highly charging because of the thick layers of dielectrics sandwiching the electrodes (~300 nm of thermally grown silicon dioxide and ~500 nm of PECVD silicon nitride).

Although the window of potential for which the electrochemical current is ~10 pA seems rather large (Figure 4.15), trapped nanocrystal assemblies may not practically be the route to test the electrochemically gating of molecules. Nevertheless, the development of electromigration break-junction on platinum wires for ~1 nm nano-gaps by John MacHale in the Nanotechnology Group at room temperature in vacuum that shows good stability (no relaxation of the conductance is observed for platinum wires as opposed to electromigration on gold wires) could present an opportunity to directly test the electrochemically gating technique on molecules bridging electrode gaps directly.

4.4.3 Electrolytic gating & molecular functionalisation

As discussed in section 1.2.1.3 of chapter 1 (p. 10), the electrolytic gating is supposed to pull up/down the molecular levels in the contacting molecules. In first approximation, pulling the gate bias must result in a modification of the tunnelling profile by lowering of the barrier. Within this naïve and qualitative description, the conductance must progressively increase as $\propto \sqrt{V_{gate}}$ (according to the Simmons model).[39] However, as soon as the energy level channel on the molecule is reached, a drastic change in conductance is expected.

We did not observe any sort of electrolytic gating for plain as-trapped citrate stabilised nanocrystals. In most cases of the devices functionalised devices in 2 mM th-PCH-th molecules in dichloromethane for ~24 h (or more ~48 h) there is no notable, repeatable, consistent increase of the source-drain current with the excitation gate potential bias (sweeping both working electrodes WE1 and WE2 together with a constant bias voltage difference of ±20 mV or ±50 mV). However for one single device we report the modulation of the device conductance with the sweeping of the gate bias (Figure 4.22).

In most cases, the results presented on electrolytic gating do not show unambiguous modulation of the conductance in relation with the expected oxidation reduction activity. Moreover, cyclic voltammetry of electrodes that had been immersed in the linker solution does not show any surface oxidation-reduction activity: we did not identify oxidation bump(s) and converse reduction dip(s) in the traces however repeated twice or more to allow conversion from the open-ring isomer to the oxidation-reduction active closed-ring isomer (Appendix 6.7.1, p. 207).

We can suggest several possibilities. First of all, in the worst case scenario: there is either no molecule or too little coverage of the gold surfaces and thus the electrode-nanocrystal interfaces. Since the exposed electrode surface was made small ($< 1\ \mu m^2$), a limited molecular coverage would result in the electrochemical current to be overshadowed by the Faradic current.

On the other hand, the sets of electrodes have been tested in both aqueous and non-aqueous electrolytes: aqueous electrolytes are supposedly preventing organo-metallic molecules (such as th-PCH-th) desorbing although one ignore the composition of the solvation shell around these compounds attached to the gold surfaces[40] and so the efficiency of the electrolytic gating or electrochemistry; the dichloromethane electrolyte does not bring any better molecular signature even though it should better solvate candidate molecules.

A third argument is that molecules bonded on gold surfaces of the sets of electrodes tested may also not be oxidation-reduction active anymore: in principle, they can bind on any of the four thiophene rings. The coupling with gold surfaces could be such that the molecular orbitals are so much changed that the oxidation-reduction characteristics are lost. Or the conversion from open-ring to closed-ring cannot happen when molecules are attached on a surface.

To rule out this later possibility, one can propose a trial experiment needing two types of similar molecules to be synthesised. For this test molecules would have one thiophene anchor group, and an oxidation-reduction unit spaced in one case by an alkyl chain for molecule A and a conjugated chain for molecule B. In this way, the electronic coupling (or charge transfer) with the active unit is limited for molecule A but not for molecule B and surface oxidation-reduction testing the surface functionalisation would give insights on the necessity or not of limiting the electronic coupling of active units with metallic electrodes.

Another effect that remains to be investigated is the overall pH of the buffer electrolyte solution as modulation of the conductance of single molecules contacted by STM[41] or polymer films were found dependent on the pH.

Currently electrode gold surfaces are cleaned following the resist strip protocol and stored in isopropryl alcohol before dielectrophoretic trapping. Further exhaustive tests of surface functionalisation must be completed to establish if electrolytic gating of molecule conductance can be achieved for molecular electronics purpose.

4.5 Conclusion

We report on an entirely new platform developed by the author for conducting without sample damage electrochemical and/or electrolytic gating measurements. The new sample layout design, dedicated custom sample holder along with electrical contacting strategies and the extended instrumentation tool mimicking a bipotentiostat are presented.

The relevance of the approach for electrochemistry on-chip and at the nanometre-scale is demonstrated. Nanocrystals can be trapped by dielectrophoresis in the nano-gaps, but more repeats are needed to qualify the trapping parameters needed to obtain larger statistics on devices initially presenting a low conductance (< 1 G_0). From the limited set of devices obtained, it appears the nanocrystal assemblies are less stable in liquid medium than when tested in vacuum.

The development of the electrolytic gating corroborates this observation. Based on the experimental work presented, the electrolytic gating technique still remains a promising possibility for gating molecules as effects, even though deleterious and/or unreliable, could be seen on the conductance of certain devices. In the case of one device amongst the 8 functionalised devices that could be tested with the electrolytic gating technique, the conductance could be modulated with the gate bias. In most cases however, no signature of the presence of oxidation-reduction active molecules could be ascertained with this technique and more interestingly no oxidation-reduction signal could be observed on functionalised electrodes using the conventional cyclic voltammetry technique. Lack of molecule attachment apart, we propose the oxidation-reduction active centres may not have been reached because of solvation issue or merely deactivated by coupling to the gold surfaces.

In parallel with qualification tests of surface functionalisation by molecules, we propose to test stable sub 1 nm nano-gaps made by electromigrated break-junction on platinum electrodes at room temperature with the electrolytic gating, as these nano-gaps promise to be readily functionalised by bridging oxidation-reduction molecules.

4.6 References

1. Damle, P.; Rakshit, T.; Paulsson, M.; Datta, S., Current-voltage characteristics of molecular conductors: two versus three terminal. *Nanotechnology, IEEE Transactions on* **2002,** *1* (3), 145-153.
2. Kubatkin, S.; Danilov, A.; Hjort, M.; Cornil, J.; Bredas, J.-L.; Stuhr-Hansen, N.; Hedegard, P.; Bjornholm, T., Single-electron transistor of a single organic molecule with access to several redox states. *Nature* **2003,** *425* (6959), 698-701.
3. Song, H.; Kim, Y.; Jang, Y. H.; Jeong, H.; Reed, M. A.; Lee, T., Observation of molecular orbital gating. *Nature* **2009,** *462* (7276), 1039-1043.
4. Battacharyya, S.; Kibel, A.; Kodis, G.; Liddell, P. A.; Gervaldo, M.; Gust, D.; Lindsay, S., Optical Modulation of Molecular Conductance. *Nano Letters* **2011,** *11* (7), 2709-2714.
5. Smaali, K.; Lenfant, S. p.; Karpe, S.; Oçafrain, M. t. n.; Blanchard, P.; Deresmes, D.; Godey, S.; Rochefort, A.; Roncali, J.; Vuillaume, D., High On−Off Conductance Switching Ratio in Optically-Driven Self-Assembled Conjugated Molecular Systems. *ACS Nano* **2010,** *4* (4), 2411-2421.
6. Banerjee, P.; Conklin, D.; Nanayakkara, S.; Park, T.-H.; Therien, M. J.; Bonnell, D. A., Plasmon-Induced Electrical Conduction in Molecular Devices. *ACS Nano* **2010,** *4* (2), 1019-1025.
7. Yamaguchi, H.; Terui, T.; Noguchi, Y.; Ueda, R.; Nasu, K.; Otomo, A.; Matsuda, K., A photoresponsive single electron transistor prepared from oligothiophene molecules and gold nanoparticles in a nanogap electrode. *Applied Physics Letters* **2010,** *96* (10), 103117-103119.
8. Quek, S. Y.; Kamenetska, M.; Steigerwald, M. L.; Choi, H. J.; Louie, S. G.; Hybertsen, M. S.; Neaton, J. B.; Venkataraman Latha, Mechanically controlled binary conductance switching of a single-molecule junction. *Nat Nano* **2009,** *4* (4), 230-234.
9. Zhou, J.; Chen, G.; Xu, B., Probing the Molecule−Electrode Interface of Single-Molecule Junctions by Controllable Mechanical Modulations. *The Journal of Physical Chemistry C* **2010,** *114* (18), 8587-8592.
10. Franco, I.; George, C. B.; Solomon, G. C.; Schatz, G. C.; Ratner, M. A., Mechanically Activated Molecular Switch through Single-Molecule Pulling. *Journal of the American Chemical Society* **2011,** *133* (7), 2242-2249.
11. Cardamone, D. M.; Kirczenow, G., Electrochemically Gated Oligopeptide Nanowires Bridging Gold Electrodes: Novel Bio-Nanoelectronic Switches Operating in Aqueous Electrolytic Environments. *Nano Letters* **2010,** *10* (4), 1158-1162.
12. Xiao, X.; Brune, D.; He, J.; Lindsay, S.; Gorman, C. B.; Tao, N., Redox-gated electron transport in electrically wired ferrocene molecules. *Chemical Physics* **2006,** *326* (1), 138-143.
13. He, J.; Fu, Q.; Lindsay, S.; Ciszek, J. W.; Tour, J. M., Electrochemical Origin of Voltage-Controlled Molecular Conductance Switching. *Journal of the American Chemical Society* **2006,** *128* (46), 14828-14835.
14. Chen, F.; Nuckolls, C.; Lindsay, S., In situ measurements of oligoaniline conductance: Linking electrochemistry and molecular electronics. *Chemical Physics* **2006,** *324* (1), 236-243.
15. Xu; Xiao; Yang, X.; Zang, L.; Tao, Large Gate Modulation in the Current of a Room Temperature Single Molecule Transistor. *Journal of the American Chemical Society* **2005,** *127* (8), 2386-2387.
16. Tao, N., Measurement and control of single molecule conductance. *J. Mater. Chem.* **2005,** *15*, 3260 - 3263.
17. Chen, F.; He, J.; Nuckolls, C.; Roberts, T.; Klare, J. E.; Lindsay, S., A Molecular Switch Based on Potential-Induced Changes of Oxidation State. *Nano Letters* **2005,** *5* (3), 503-506.
18. Xiulan Li; Bingqian Xu; Xiaoyin Xiao; Xiaomei Yang; Ling Zang; Tao, N., Controlling charge transport in single molecules using electrochemical gate. *Faraday Discuss.* **2006,** *131*, 111 - 120.
19. David I. Gittins; Donald Bethell; David J. Schiffrin; Nichols, R. J., A nanometre-scale electronic switch consisting of a metal cluster and redox-addressable groups. *Letters to nature* **2000**.

20. Haiss, W.; vanZalinge, H.; Higgins, S. J.; Bethell, D.; Hobenreich, H.; Schiffrin, D. J.; Nichols, R. J., Redox State Dependence of Single Molecule Conductivity. *J. Am. Chem. Soc.* **2003,** *125* (50), 15294-15295.
21. Tran, E.; Duati, M.; Ferri, V.; Müllen, K.; Zharnikov, M.; Whitesides, G. M.; Rampi, M. A., Experimental Approaches for Controlling Current Flowing through Metal-Molecule-Metal Junctions. *Advanced Materials* **2006,** *18* (10), 1323-1328.
22. Tran, E.; Duati, M.; Whitesides, G. M.; Rampi, M. A., Gating current flowing through molecules in metal–molecules–metal junctions. *Faraday Discuss.* **2006,** *131*, 197-203.
23. He, H. X.; Li, X. L.; Tao, N. J.; Nagahara, L. A.; Amlani, I.; Tsui, R., Discrete conductance switching in conducting polymer wires. *Physical Review B* **2003,** *68* (4), 045302.
24. Forzani, E. S.; Li, X.; Tao, N., Hybrid Amperometric and Conductometric Chemical Sensor Based on Conducting Polymer Nanojunctions. *Anal. Chem.* **2007,** *79* (14), 5217-5224.
25. Huixin He; Jisheng Zhu; Nongjian J. Tao; Larry A. Nagahara; Islamshah Amlani; Tsui, R., A Conducting Polymer Nanojunction Switch. *J. Am. Chem. Soc.* **2001,** *123* (31), 7730-7731.
26. Shimotani, H.; Diguet, G.; Iwasa, Y., Direct comparison of field-effect and electrochemical doping in regioregular poly(3-hexylthiophene). *Applied Physics Letters* **2005,** *86* (2), 022104-022104-3.
27. Schultze, J. W.; Bressel, A., Principles of electrochemical micro- and nano-system technologies. *Electrochimica Acta* **2001,** *47* (1-2), 3-21.
28. Mészáros, G.; Kronholz, S.; Karthäuser, S.; Mayer, D.; Wandlowski, T., Electrochemical fabrication and characterization of nanocontacts and nm-sized gaps. *Applied Physics A: Materials Science & Processing* **2007,** *87* (3), 569-575.
29. Berduque, A. Characterisation of packaged microelectrode devices for sensor applications. UCC, Cork, 2003.
30. Bard, A. J.; Faulkner, L. R., *Electrochemical Methods (Second Edition)*. John Wiley & Sons, Inc.: 2001; Vol. 1.
31. Hugelmann, M.; Hugelmann, P.; Lorenz, W. J.; Schindler, W., Nanoelectrochemistry and nanophysics at electrochemical interfaces. *Surface Science* **2005,** *597* (1-3), 156-172.
32. Kronholz, S.; Karthäuser, S.; Mészáros, G.; Wandlowski, T.; van der Hart, A.; Waser, R., Protected nanoelectrodes of two different metals with 30 nm gapwidth and access window. *Microelectronic Engineering* **2006,** *83* (4-9), 1702-1705.
33. Mészáros, G.; Li, C.; Pobelov, I.; Wandlowski, T., Current measurements in a wide dynamic range-applications in electrochemical nanotechnology. *Nanotechnology* **2007,** *18* (42), 424004.
34. Trasatti, S.; Petrii, O. A., Real surface area measurements in electrochemistry. *Journal of Electroanalytical Chemistry* **1992,** *327* (1-2), 353-376.
35. Burke, L.; Nugent, P., The electrochemistry of gold: I the redox behaviour of the metal in aqueous media. *Gold Bulletin* **1997,** *30* (2), 43-53.
36. Dawson, K.; Strutwolf, J. r.; Rodgers, K. P.; Herzog, G. g.; Arrigan, D. W. M.; Quinn, A. J.; O'Riordan, A., Single Nanoskived Nanowires for Electrochemical Applications. *Analytical Chemistry* **2011,** *83* (14), 5535-5540.
37. Diez-Perez, I.; Hihath, J.; Hines, T.; Wang, Z.-S.; Zhou, G.; Mullen, K.; Tao, N., Controlling single-molecule conductance through lateral coupling of [pi] orbitals. *Nat Nano* **2011,** *6* (4), 226-231.
38. Ramachandran, G. K.; Hopson, T. J.; Rawlett, A. M.; Nagahara, L. A.; Primak, A.; Lindsay, S. M., A Bond-Fluctuation Mechanism for Stochastic Switching in Wired Molecules. *Science* **2003,** *300* (5624), 1413-1416.
39. Simmons, J. G., Generalized Formula for the Electric Tunnel Effect between Similar Electrodes Separated by a Thin Insulating Film. *Journal of Applied Physics* **1963,** *34* (6), 1793-1803.
40. Hopkins, A. J.; McFearin, C. L.; Richmond, G. L., SAMs under Water: The Impact of Ions on the Behavior of Water at Soft Hydrophobic Surfaces. *The Journal of Physical Chemistry C* **2011,** *115* (22), 11192-11203.

41. Scullion, L.; Doneux, T.; Bouffier, L.; Fernig, D. G.; Higgins, S. J.; Bethell, D.; Nichols, R. J., Large Conductance Changes in Peptide Single Molecule Junctions Controlled by pH. *The Journal of Physical Chemistry C* **2011,** *115* (16), 8361-8368.

Chapter 5 – Conclusion

5.1 Summary

The objective of this thesis work was to develop methods for forming and interfacing nanocrystal-molecule nanostructures in order to explore their electrical transport properties in various controlled environments.

Chapter 2 was based on earlier Dr. Claire Barrett's experimental work on the formation of hybrid nanostructures, called *n*-mers, comprising nanocrystals linked by molecules. We developed a method to model the formation of these *n*-mer nanostructures on the basis of a system of rate-equations characterising the various populations of this many-body system. This phenomenological model can accommodate different cases scenario of cluster growth and essentially fit the distributions of populations found experimentally. We reviewed the mass transport properties of the entities involved (molecules and the different *n*-mers being formed) using random-walk simulations. This yielded to estimates for the enthalpies of reaction for molecular decoration of nanocrystal surfaces and *n*-mer association on the basis of the values of the optimised fit parameters. We found activation energies for the forward and reverse reactions to be on the order of ~ 100 meV and ~ 380 meV (commensurate with the thermal energy), respectively. Complementary experimental data and theoretical considerations can be included in the model to refine its results. Presently, the model framework is capable of describing and predicting the formation of *n*-mers in strict experimental conditions (i.e. temperature control, etc.).

Chapter 3 demonstrated a versatile method for laterally contacting molecules combining conventional top-down e-beam lithography with bottom-up dielectrophoretic trapping of small number (<5) citrate-stabilised gold nanocrystals (~60 nm in diameter) for the deployment of metallic nodes as a contacting strategy for molecular electronics. We showed that the distribution of conductance for as-trapped nanocrystal(s) in nanometre-gaps follows a log-normal law because of the inevitable angstrom variability of the nanocrystal—electrode interface (the implementation of an *in situ* and well tailored feedback technique could only narrow but not suppress this effect). Evidences of sub-nanometre reorganisation of the nanocrystal—electrode interfaces were also shown as a result to the exposure to non-aqueous solvents mediating the adsorption of molecules. The platform of nanocrystal assemblies bridging nanometre-scale gaps has been bringing into light the influence of immiscible mediums on (sub-)nanometre curved interfaces opening interesting possibility for the characterisation of emulsions near surfaces in extremely confined/close vicinity. Moreover, across the acquired dataset we showed molecular functionalisation of nanocrystal assemblies with the "rigid-rod" linker 1,4 di(3-thiophene) ethynylbenzene (synthesised by Emma Harvey in Dr. Mary Price's laboratory,

Dublin) was successful in more than ~ 10% of the devices manufactured. We believe the single conductance of this molecular wire is ~ 7.8×10^{-5} G_0, while the conductance of partial bonding configurations (one end only) is ~ 6.6×10^{-7} G_0.

Chapter 4 reported on the development of an entirely new platform developed for conducting electrochemical and/or electrolytic gating measurements on an electrode chip. Thanks to this setup, on-chip electrochemistry was demonstrated at the nanometre-scale, conversely nanocrystals could be directed in nano-gaps via the dielectrophoretic force allowing the investigation of the electrolytic gating technique on nanocrystal assemblies functionalised with the switching molecule 1,2-Bis(5'-(3''-ethynylthiophene)-2'-methylthien-3'-yl)-cyclopentene (synthesised by Emma Harvey in Dr. Mary Price's laboratory, Dublin). Although the assemblies of nanocrystals presented more instability in liquid medium compared to under vacuum conditions, and despite the limited number of effective devices operating in the tunnelling regime, we showed in the case of 1 device (out of 8 devices that could be tested with the electrolytic gating technique) that the conductance seemed to be controlled by the gate bias. However, the enhancement in conductance was limited to a ~ 10 fold increase and tended to indicate no extra conductance channel was triggered. Moreover, no signature of oxidation-reduction activity from surface attached molecules could be ascertained. We proposed solvation effects in the heterogeneous nanocrystal-electrode interface and/or molecular coupling with the electrodes (charge transfer) impeded oxidation-reduction processes either because of immiscibility issues or because of the deactivation of the active centres on switching molecules.

Overall, the work presented in this thesis project has brought into light physical and chemical processes taking place at the extremely narrow and curved interface between two nanocrystals or one nanocrystal and a metallic grain of the electrode. The formation of *n*-mers and the molecular functionalisation of assemblies of nanocrystals bridging electrodes are two similar problems. The formation of molecular bridges at this kind of interfaces necessitates molecules to diffuse from a large liquid reservoir into the region in the first place. Molecular bonding must occur to the surface for both molecular ends: this is an unlikely statistical process in itself as it depends on orientation of surfaces, on steric hindrance at the surface and on binding energies. Finally, based on geometrical arguments and the range of binding energies involved for molecules on metal surfaces, the relaxation time of desorption for a molecule ($\tau_{1\ \mathrm{eV}}\sim 3\ \mathrm{h}$, $\tau_{1.1\ \mathrm{eV}}\sim 6\ \mathrm{days}$) tends to indicates the sustainability of a hybrid interface of two metallic nodes decorated with molecules can only hold if few molecules are bridging the interface. The time scale of DC electrical measurements cannot resolve these toggling events occurring on the picosecond regime.

A second broad aspect the work touched is the emulsion problem at the interface between metallic nodes. The formation of *n*-mers and the functionalisation of nanocrystal assemblies must be mediated with non aqueous solvents dissolving molecules. On the other hand these non-aqueous solvents (such as acetone or dichloromethane) are incompatible with nanocrystals colloids as they destabilise the dispersal (e.g. in case of addition of large quantity of acetone) or they affect the electrical tunnelling conductance of nanocrystal assemblies in nanometre gaps. Molecular dynamics simulations performed by Victor Akujobi Dr. Michael Nolan and Dr. Damien Thompson, Tyndall , show the length scale of the emulsion front between immiscible liquids is of the same order of the distance between metallic nodes. A complete understanding of the effect of emulsion in (sub-)nanometre region will necessitate further work.

5.2 Future works

Phenomena that may play a minor role in the macroscopic world can be dominant at the nanometre-scale. This must be an indication that one has to be careful with assumptions and the scaling down of well established phenomenon at the macro-scale or even the micro-scale. In other words, thinking outside the box is a prerequisite.

We propose a few ideas mainly taken from the literature that are regarded as promising.

5.2.1 Memristor

In the early 1970s, L. Chua proposed the idea of the fourth elementary passive components in electronics, termed the memristor.[1] Until recently, no clear experimental demonstration had been given for the fabrication process of such a device.[2] The idea of memristor was rather marginal at start however it is nowadays gaining interest. A memristor has three main intricate properties:[1]

i. its current-voltage $I(V)$ characteristic is always pinched at 0 V,
ii. increasing the voltage bias scan-rate of the current-voltage makes the hysteresis vanish,
iii. it does not store energy.

The definition of what a memristor is covered by the formula: $V = R(X) \times I$, where X can be any state variable (or set of them) controlling the system.[3-4] It could be interesting to demonstrate if assemblies of nanocrystals fall in this class of devices[5] as it was shown memristors can simplify the building of logic circuits with the replacement of transistors.

5.2.2 Contact

On the other hand, some ideas could be included in the making of assemblies of nanocrystals in nano-gaps functionalised with molecules. As we have seen contacting molecules present plenty of difficulties. The phenomenon of Fermi level pinning that is usually seen as an issue in the CMOS industry for gate oxide materials. However, as it appears the work-function at the surface of electrodes can be engineered by a layer of dedicated molecules,[6] it opens the possibility of a more controlled alignment molecular orbitals with the Fermi level of the electrodes. The picture suggested is in fact quite similar to the way alkane-thiol molecules are employed in micro-scale array to cap and stabilise nanocrystals[7] for different reasons however.

Works on controlled electromigration break-junction on gold electrodes or platinum electrodes[8] have shown metal atoms can move in constrictions inducing “self-breaking” of wires or enlargement of forced nanometre-gaps (from ~1 nm to up to ~3 nm). Phenomenon occurring

in electromigrated gaps is believed to be ubiquitous, and so diffusion of atoms of electrode materials is likely to happen to accommodate thermodynamic equilibrium provided enough energy is provided to the surface material. The development of "healing" molecules capping surfaces could be employed to raise the diffusion barrier enhancing the stability at the nanometre scale: freezing electrode geometry and revealing only peculiar atomic configuration at the surface.

A lot of research works are based on molecules terminated with a sulphur atom for binding on gold atoms. Although mechanically strong, the bonds are believed to develop an s-orbital that is less favourable for charge transport carrier than p-orbital configuration. The use of nitrogen in anchoring groups originates from this observation. However the mechanical strength is much weaker in this case. Some research is currently on going employing multi-pod molecules[9] to increase the chance of charge flow via the multiple bound atoms or potentially via the delocalised orbitals of the "tentacles" as suggested by modulation of single molecular conductance recently uncovered using the STM technique.[10-11]

5.2.3 Architectures

The foundation of CMOS technology lays intricately on a two-dimensional technology. Depth exists in the device but connectivity from one device to another relies on stacking levels of metallic wires. Although straightforward, this paradigm has no optimal basis. Brains of living creatures are three-dimensional in nature. Careful tailoring of three-dimensional assemblies[12] by the means of polymerisation[13] for instance could bring advances in molecular electronics.

In a similar sense of meaning, ternary or higher state of logic could be engineered in place of binary logic, as nanotechnology systems can implement more than simply two states.[14]

An impressive body of work has been done on the development of defect-tolerant systems from both hardware and software point of view for critical unmanned missions in space for instance. Because it is so difficult or impossible to make perfect components,[15] redundancy of elementary part in a single device is believed to be one of the fundamental key of its functioning. The experiment "TERAMAC" of building a computer with defective parts[15-18] but with high performance brought insights in the development of defect-tolerant systems for nanotechnology. Instead of working towards zero defects, a calibration mechanism is carried out externally so that "process precision [is replaced] by software precision"[15] as demonstrated with a 160 kb memory device built on rotaxane molecules[19] and in design of circuits.[20-21]

Finally, "self-healing" may also be built in systems. A recent publication demonstrated lasing in living cells.[22] Even if proteins are destroyed in the cell because of light emission by the

engineered cell, more proteins are produced to compensate their loss. In the long run, similar mechanisms could be implemented to repair potentially defective device parts.

5.2.4 Closing word

Living matters is certainly a good demonstration of nanotechnology, proving that this framework can work. And as such, as nanotechnology advances, processes implemented by living creatures are more and more studied. Although there is no need to replicate these processes one should contemplate what proves to be working (and not working) as a mine of experiments running since billions of years on our planet[23] to design more efficient architectures with an integrated point of view for molecular electronics as for energy harvesting.

5.3 References

1. Chua, L., Memristor-The missing circuit element. *Circuit Theory, IEEE Transactions on* **1971,** *18* (5), 507-519.
2. Strukov, D. B.; Snider, G. S.; Stewart, D. R.; Williams, R. S., The missing memristor found. *Nature* **2008,** *453* (7191), 80-83.
3. Chua, L. O.; Sung Mo, K., Memristive devices and systems. *Proceedings of the IEEE* **1976,** *64* (2), 209-223.
4. Di Ventra, M.; Pershin, Y. V.; Chua, L. O., Circuit Elements With Memory: Memristors, Memcapacitors, and Meminductors. *Proceedings of the IEEE* **2009,** *97* (10), 1717-1724.
5. Kim, T. H.; Jang, E. Y.; Lee, N. J.; Choi, D. J.; Lee, K.-J.; Jang, J.-t.; Choi, J.-s.; Moon, S. H.; Cheon, J., Nanoparticle Assemblies as Memristors. *Nano Letters* **2009,** *9* (6), 2229-2233.
6. Hofmann, O. T.; Egger, D. A.; Zojer, E., Work-Function Modification beyond Pinning: When Do Molecular Dipoles Count? *Nano Letters* **2010,** *10* (11), 4369-4374.
7. Liao, J.; Agustsson, J. S.; Wu, S.; Schönenberger, C.; Calame, M.; Leroux, Y.; Mayor, M.; Jeannin, O.; Ran, Y.-F.; Liu, S.-X.; Decurtins, S., Cyclic Conductance Switching in Networks of Redox-Active Molecular Junctions. *Nano Letters* **2010,** *10* (3), 759-764.
8. Prins, F.; Hayashi, T.; Steenwijk, B. J. A. d. V. v.; Gao, B.; Osorio, E. A.; Muraki, K.; Zant, H. S. J. v. d., Room-temperature stability of Pt nanogaps formed by self-breaking. *Applied Physics Letters* **2009,** *94* (12), 123108.
9. Ie, Y.; Hirose, T.; Nakamura, H.; Kiguchi, M.; Takagi, N.; Kawai, M.; Aso, Y., Nature of Electron Transport by Pyridine-Based Tripodal Anchors: Potential for Robust and Conductive Single-Molecule Junctions with Gold Electrodes. *Journal of the American Chemical Society* **2011,** *133* (9), 3014-3022.
10. Diez-Perez, I.; Hihath, J.; Hines, T.; Wang, Z.-S.; Zhou, G.; Mullen, K.; Tao, N., Controlling single-molecule conductance through lateral coupling of [pi] orbitals. *Nat Nano* **2011,** *6* (4), 226-231.
11. Meisner, J. S.; Kamenetska, M.; Krikorian, M.; Steigerwald, M. L.; Venkataraman, L.; Nuckolls, C., A Single-Molecule Potentiometer. *Nano Letters* **2011,** *11* (4), 1575-1579.
12. Maye, M. M.; Kumara, M. T.; Nykypanchuk, D.; Sherman, W. B.; Gang, O., Switching binary states of nanoparticle superlattices and dimer clusters by DNA strands. *Nat Nano* **2009,** *advance online publication*.
13. Okawa, Y.; Mandal, S. K.; Hu, C.; Tateyama, Y.; Goedecker, S.; Tsukamoto, S.; Hasegawa, T.; Gimzewski, J. K.; Aono, M., Chemical Wiring and Soldering toward All-Molecule Electronic Circuitry. *Journal of the American Chemical Society* **2011,** *133* (21), 8227-8233.
14. Porath, D.; Millo, O., Single electron tunneling and level spectroscopy of isolated C[sub 60] molecules. *Journal of Applied Physics* **1997,** *81* (5), 2241-2244.
15. Joachim, C.; Gimzewski, J. K.; Aviram, A., Electronics using hybrid-molecular and mono-molecular devices. *Nature* **2000,** *408* (6812), 541-548.
16. Heath, J. R.; Kuekes, P. J.; Snider, G. S.; Williams, R. S., A Defect-Tolerant Computer Architecture: Opportunities for Nanotechnology. *Science* **1998,** *280* (5370), 1716-1721.
17. DeHon, A.; Naeimi, H., Seven strategies for tolerating highly defective fabrication. *Design & Test of Computers, IEEE* **2005,** *22* (4), 306-315.
18. Stan, M. R.; Franzon, P. D.; Goldstein, S. C.; Lach, J. C.; Ziegler, M. M., Molecular electronics: from devices and interconnect to circuits and architecture. *Proceedings of the IEEE* **2003,** *91* (11), 1940-1957.
19. Green, J. E.; Wook Choi, J.; Boukai, A.; Bunimovich, Y.; Johnston-Halperin, E.; DeIonno, E.; Luo, Y.; Sheriff, B. A.; Xu, K.; Shik Shin, Y.; Tseng, H.-R.; Stoddart, J. F.; Heath, J. R., A 160-kilobit molecular electronic memory patterned at 10^{11} bits per square centimetre. *Nature* **2007,** *445* (7126), 414-417.
20. Collier, C. P.; Wong, E. W.; Belohradský, M.; Raymo, F. M.; Stoddart, J. F.; Kuekes, P. J.; Williams, R. S.; Heath, J. R., Electronically Configurable Molecular-Based Logic Gates. *Science* **1999,** *285* (5426), 391-394.

21. Snider, G.; Kuekes, P.; Hogg, T.; Williams, R. S., Nanoelectronic architectures. *Applied Physics A: Materials Science & Processing* **2005,** *80* (6), 1183-1195.
22. Gather, M. C.; Yun, S. H., Single-cell biological lasers. *Nat Photon* **2011,** *advance online publication*.
23. Fioravanti, G.; Haraszkiewicz, N.; Kay, E. R.; Mendoza, S. M.; Bruno, C.; Marcaccio, M.; Wiering, P. G.; Paolucci, F.; Rudolf, P.; Brouwer, A. M.; Leigh, D. A., Three State Redox-Active Molecular Shuttle That Switches in Solution and on a Surface. *Journal of the American Chemical Society* **2008,** *130* (8), 2593-2601.

Chapter 6 – Appendices

6.1 Generalised Multiparticle Mie theory

This section is taken from ref. [1].

Simulations were developed by Dr Gaëtan Lévêque of the Photonics Theory Group at Tyndall using the Generalised Multiparticle Mie (GMM) method to investigate the optical response (extinction cross-section) of clusters of spherical nanocrystals.[2] For nanocrystals with diameters of a few tens of nanometres, the permittivity of bulk gold must be corrected to take into account the fact that the mean free path of the electrons in the nanocrystals is less than the corresponding value for bulk gold (~ 40 nm). This procedure has been described by Hövel *et al.*[3] The extinction is calculated for two orthogonal electric field polarisations, parallel ($E_{//}$) and perpendicular ($E_{\perp}$) to the 2-mer axis, respectively.

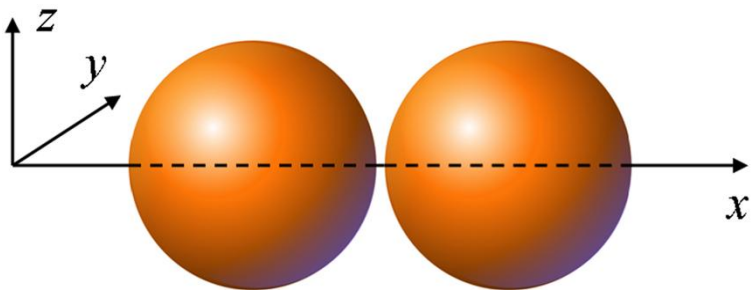

Figure 6.1. Illustration of a nanocrystal 2-mer in the co-ordinate system used for GMM simulations. The orthogonal field polarisations are $E_{//}$ along the major axis of the 2-mer (x-axis) and $E_{\perp}$ along the axes perpendicular to the major axis (y-axis and z-axis).

Inset of Figure 2.8a shows results from Dr Lévêque's modelled extinction spectra for both $E_{//}$ and $E_{\perp}$ field polarisations for a 2-mer formed from d = 20 nm nanocrystals, where the edge-edge separation of the nanocrystals was fixed at 1.2 nm (corresponding to the expected length of the Re linker). For such small nanocrystals, the absorbance is orders of magnitude larger than the scattering at all wavelengths. It is important to note that these spectra have not been normalised to calculate an absolute extinction coefficient, but have been scaled to illustrate the dominant features in the simulation results. Several key features are immediately evident: Both field polarisations show two clear peaks, a shorter wavelength feature (~ 525 nm), close to the plasmon resonance for the isolated nanocrystal monomers and another resonance close to 600 nm. For the $E_{//}$ spectrum, the strongest resonance is observed close to 600 nm, which has been attributed to a longitudinal plasmon mode in the dimer. The dominant absorbance peak in the simulated data for $E_{\perp}$ is closer to the resonance for the unmodified nanocrystal monomers, where this feature has previously been ascribed to transverse modes in weakly-coupled nanocrystals.[4-7] In the 2-mer simulations, the permittivity of the surrounding medium (ε = 1.88) was chosen based on GMM simulations of isolated d = 20 nm gold nanocrystals in dielectric

media, in order to provide a red-shift of the single nanocrystal plasmon resonance ($\Delta\lambda \sim 3\ \mathrm{nm}$), relative to simulations for the same nanocrystals in water. This assumption was based on the observation of a rapid red-shift of the measured UV-visible response for the d = 20 nm nanocrystals upon addition of the Re linkers, which is likely due to formation of a (partial) monolayer of the Re linkers at the surface of the gold nanocrystal.[8-9]

6.2 Curve fitting

Tool boxes or integrated solutions for fitting experimental data are available in commercial software packages, such as Matlab or Origin. Practically, they come as easy step-by-step methods for linear and non-linear data sets. A broad catalogue of widely-used functions is notably available in the Origin software which makes curve fitting easy in common cases. However, one needs to develop custom scripts when data fitting involves solving a set of equations consistently. For practical reasons, the scripting language chosen for developing custom curve fitting was Matlab. Information provided thereafter is summarised from ref. [10]

The principle of curve fitting is based on comparing the locus of a suggested curve to the curve of the raw data. The difference between suggested points $\left(\hat{Y}_i\right)$ and measured points (Y_i) needs to be minimised. Typically, one uses the residual sum of squares estimator, $RSS = \sum_{i=1}^{n}\left(Y_i - \hat{Y}_i\right)^2$, to obtain the best fit possible by trying to bring all the n values $\left(\hat{Y}_i\right)$ as close as possible to the n values (Y_i) and indeed bringing the value $RSS \longrightarrow 0$.

One can introduce a weighting coefficient (w_i) for each measured point comprising information on the quality of the measure at this one point or the relevance of this point within the data set. Different weighting mechanisms can be derived, for instance (w_i) can be defined as the inverse of the standard deviation (σ_i) of the measurement points ($w_i = 1$ in the case $\sigma_i = 1$). In place of the residual sum of squares estimator, RSS, the weighted sum of squares estimator, $\chi^2 = \sum_{i=1}^{n} w_i \cdot \left(Y_i - \hat{Y}_i\right)^2$, is used in this case. Provided that all $(w_i = 1)$, the two estimators are thereby equivalent.

One has to introduce other estimators in order to compare fitting of data sets with a different number of points, etc. First of all, one can normalise the RSS (respectively χ^2) by the number of measured points, n, to which is subtracted the number of free (and optimised) parameters, p, used to calculate the suggested curve. This defines the least mean square estimator, $s^2 = \frac{RSS}{n-p}$. The total sum of squares, $TSS = \sum_{i=1}^{n}(Y_i - \langle Y_i \rangle)^2$, where $\langle Y_i \rangle$ is the mean value of the measured points (Y_i), is used to evaluate the R^2 estimator one must be familiar with from linear curve fitting: $R^2 = 1 - \frac{RSS}{TSS}$. The values of these estimators reflect the goodness of the fit: ideally, $s^2 \longrightarrow 0$ whereas $R^2 \longrightarrow 1$.

As for measurements, one can investigate the accuracy or uncertainty of a fit by performing other calculations once the best fit conditions are found. Let us call, f, the function (or set of functions) driving the suggested curve, (X_i) the controlled values of the experiment, $\left(P_j\right)$ the parameters of the function f. Based on mathematical considerations we will not expose, two

estimators qualifying the parameters of the suggested curve can be derived. First of all, $d_{P_j} = 1 - \frac{1}{C_{jj}(C^{-1})_{jj}}$ corresponds to the dependency of the parameter: $0 \leq d_{P_j} \leq 1$, $d_{P_j} \longrightarrow 1$ indicates a strong dependency. Conversely, $s_{P_j} = \sqrt{C_{jj}}$ is the standard error on the parameter: $0 \leq s_{P_j} \leq 1$, $s_{P_j} \longrightarrow 0$ in the best case scenario. One needs to calculate the square $(p \times p)$ matrix, C, defined by $C = (F'F)^{-1}s^2$ where F is a $(n \times p)$ matrix which values are partial derivatives of the function, $F_{i,j} = \frac{1}{\sigma^2}\frac{\partial f(X_i,P_j)}{\partial P_j}$. In practice, the values of the function f at each X_i and about each P_j (typically, $\pm$ 10 %) are calculated. Then a 3rd to 5th order polynomial is fitted to the set of values found at each X_i and about each P_j. The value of the first derivative of these polynomials at (X_i, P_j) gives $\frac{\partial f(X_i,P_j)}{\partial P_j}$.

6.3 Analytical results of simple rate-equation system

6.3.1 Two-species limited rate-equation system

Assuming a two-species limited system along with a non dependence of molecular coverage, one can derive an analytical solution for monomer and dimer populations. We first recall the simple coupled differential system.

$$\begin{cases} \dfrac{\partial N_1}{\partial t} = -2\times k_a \cdot N_1^2 + 2\times k_d \cdot N_2 \\ \dfrac{\partial N_2}{\partial t} = +k_a \cdot N_1^2 - k_d \cdot N_2 \end{cases}$$
$$N_1 + 2\times N_2 = N_0$$

Using the continuity equation, this can be simplified into a single equation on the numbers of monomers for instance.

$N_2 = (N_0 - N_1)/2$ thus giving $\dfrac{\partial N_1}{\partial t} = -2\times k_a \cdot N_1^2 + k_d \cdot (N_0 - N_1)$

The differential equation is rewritten to exhibit the characteristic polynomial in N_1:

$$\frac{\partial N_1}{\partial t} = N_1^2 \times \underbrace{(-2\times k_a)}_{a} + N_1 \times \underbrace{(-k_d)}_{b} + \underbrace{k_d \times N_0}_{c} \text{ or } P(X) = a\cdot X^2 + b\cdot X + c$$

Find roots

$\Delta = b^2 - 4\times a\cdot c$, and so $\lambda, \mu = \dfrac{-b \pm \sqrt{\Delta}}{2\times a}$

Differential equation is rewritten again

$$\frac{\partial N_1}{(N_1 - \lambda)\times(N_1 - \mu)} = a\cdot \partial t$$

Two cases depending on a double root or two different roots of the polynomial

6.3.1.1 Two different polynomial roots

Differential equation is rewritten again using partial fraction expansion

$$\frac{\partial N_1}{(N_1 - \lambda)} - \frac{\partial N_1}{(N_1 - \mu)} = a\cdot(\lambda - \mu)\cdot \partial t$$

Resolution is now made easy

$$\left[\ln\left(N_1-\lambda\right)-\ln\left(N_1-\mu\right)\right]=a\cdot\left(\lambda-\mu\right)\cdot\partial t \text{ rewritten as } \left[\ln\left(\frac{\left(N_1-\lambda\right)}{\left(N_1-\mu\right)}\right)\right]=a\cdot\left(\lambda-\mu\right)\cdot\partial t$$

Now one cans integral the solution

$$\ln\left(\frac{\left(N_1-\lambda\right)}{\left(N_1-\mu\right)}\right)-\ln\left(\underbrace{\frac{\left(N_1\left(t_0\right)-\lambda\right)}{\left(N_1\left(t_0\right)-\mu\right)}}_{\kappa}\right)=\underbrace{a\cdot\left(\lambda-\mu\right)}_{-1/\tau}\cdot\left(t-t_0\right)$$

That can be rewritten under the form

$$\ln\left(\frac{\frac{\left(N_1-\lambda\right)}{\left(N_1-\mu\right)}}{\kappa}\right)=-\frac{t-t_0}{\tau} \text{ rewritten as } \frac{\left(N_1-\lambda\right)}{\left(N_1-\mu\right)}=\kappa\cdot\exp\left(\underbrace{-\frac{t-t_0}{\tau}}_{u}\right)$$

That is rewritten to exhibit the coverage function

$N_1\times\left(1-\kappa\cdot\exp\left(u\right)\right)=\lambda-\mu\cdot\kappa\cdot\exp\left(u\right)$ which is in the end

$$\boxed{N_1=\frac{\lambda-\mu\cdot\kappa\cdot\exp\left(u\right)}{1-\kappa\cdot\exp\left(u\right)}}$$

We rewrite the equation so as to get a symmetrical expression

$\kappa=\exp\left(d\right)$ and $v=u+d$ so in the end we end up with

$$N_1=\frac{-\lambda\cdot\exp\left(-x\right)+\mu\cdot\exp\left(x\right)}{2\cdot sh\left(x\right)}$$

Although symmetrical, it seems the solution diverges when x tends toward 0, however it only happens when kappa =1, which is not allowed, otherwise it is a double polynomial root.

6.3.1.2 Double polynomial root

Differential equation is rewritten again

$$\frac{\partial N_1}{\left(N_1-\lambda\right)^2}=a\cdot\partial t$$

Resolution is now made easy

$$\frac{1}{2}\times\left[-\frac{1}{(N_1-\lambda)}\right]' = a\cdot\partial t$$

Now one cans integral the solution

$$\underbrace{\frac{1}{(N_1(t_0)-\lambda)}}_{\kappa} - \frac{1}{(N_1-\lambda)} = \underbrace{2\times a}_{-1/\tau}\cdot(t-t_0)$$

That can be rewritten under the form

$$\frac{1}{(N_1-\lambda)} = \frac{1}{\kappa} + \underbrace{\frac{(t-t_0)}{\tau}}_{u}$$

That is rewritten to exhibit the coverage function

$N_1 = \lambda + \dfrac{\kappa\cdot\tau}{\tau+\kappa\cdot(t-t_0)}$ which is similar to $\boxed{N_1 = \lambda + \dfrac{\kappa}{1+\kappa\cdot u}}$

6.3.1.3 Population evolution

Whatever the analytical solution looks like for $N_1(t)$, we know one has to satisfy the continuity equation and indeed, it gives the value of $N_2(t)$. We plot the proportion of *n*-mers as if they were counted on the SEM.

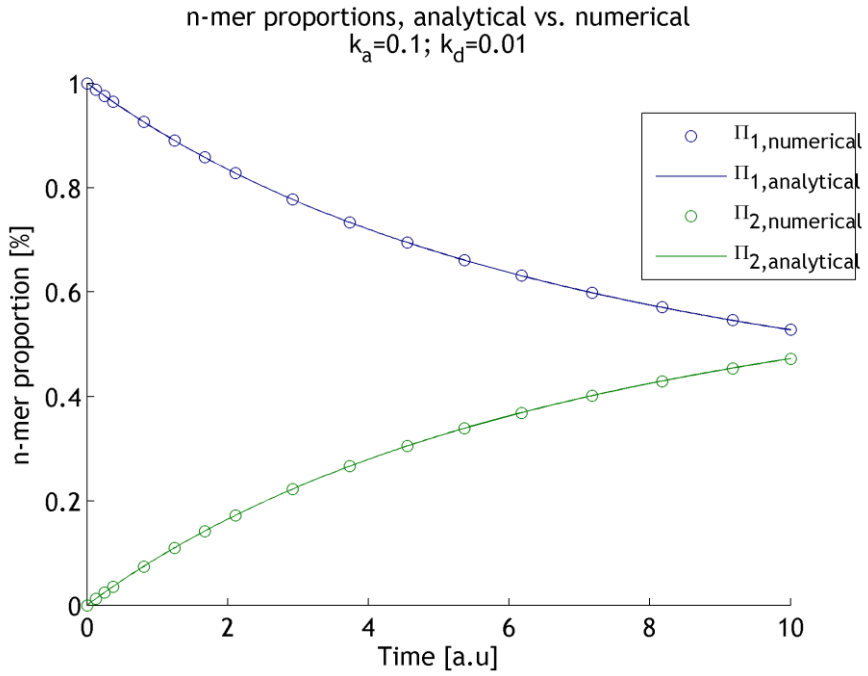

Figure 6.2. Benchmark between analytically and numerically calculation of *n*-mers proportions for a 2-species limited system.

6.3.2 Molecular coverage

Unlike the previous case, the analytical solution of the molecular coverage is found without any additional assumption. However, deriving its expression is actually very similar to what is done for the two-species limited system. We recall the modified Langmuir isotherm equation:

$$\frac{\partial\theta}{\partial t} = (1-\theta)\cdot(r-\theta\times m_{\max})\cdot h_a - \theta\cdot h_d$$

Differential equation is rewritten to exhibit characteristic polynomial

$$\frac{\partial\theta}{\partial t} = \theta^2\times\underbrace{(m_{\max}\cdot h_a)}_{a} + \theta\times\underbrace{(-h_d - h_a(r+m_{\max}))}_{b} + \underbrace{r\cdot h_a}_{c} \text{ or } P(X) = a\cdot X^2 + b\cdot X + c$$

Find roots

$\Delta = b^2 - 4\times a\cdot c$, and so $\omega_{1,2} = \dfrac{-b\pm\sqrt{\Delta}}{2\times a}$

Differential equation is rewritten again

$$\frac{\partial\theta}{(\theta-\omega_1)\times(\theta-\omega_2)} = a\cdot\partial t$$

Two cases depending on a double root or two different roots of the polynomial

6.3.2.1 Two different polynomial roots

Differential equation is rewritten again using partial fraction expansion

$$\frac{\partial\theta}{(\theta-\omega_1)} - \frac{\partial\theta}{(\theta-\omega_2)} = a\cdot(\omega_1-\omega_2)\cdot\partial t$$

Resolution is now made easy

$$\left[\ln(\theta-\omega_1) - \ln(\theta-\omega_2)\right]' = a\cdot(\omega_1-\omega_2)\cdot\partial t \text{ rewritten as } \left[\ln\left(\frac{(\theta-\omega_1)}{(\theta-\omega_2)}\right)\right]' = a\cdot(\omega_1-\omega_2)\cdot\partial t$$

Now one cans integral the solution

$$\ln\left(\frac{(\theta-\omega_1)}{(\theta-\omega_2)}\right) - \ln\left(\underbrace{\frac{(\theta_0-\omega_1)}{(\theta_0-\omega_2)}}_{\kappa}\right) = \underbrace{a\cdot(\omega_1-\omega_2)}_{-1/\tau}\cdot(t-t_0)$$

That can be rewritten under the form

$$\ln\left(\frac{\frac{(\theta-\omega_1)}{(\theta-\omega_2)}}{\kappa}\right)=-\frac{t-t_0}{\tau} \text{ rewritten as } \frac{(\theta-\omega_1)}{(\theta-\omega_2)}=\kappa\cdot\exp\left(\underbrace{-\frac{t-t_0}{\tau}}_{u}\right)$$

That is rewritten to exhibit the coverage function

$\theta\times(1-\kappa\cdot\exp(u))=\omega_1-\omega_2\cdot\kappa\cdot\exp(u)$ which is in the end

$$\theta=\frac{\omega_1-\omega_2\cdot\kappa\cdot\exp(u)}{1-\kappa\cdot\exp(u)}$$

Again it can be made as a symmetrical expression by making

$\kappa=\exp(d)$ and $v=u+d$ so in the end we end up with

$$\theta=\frac{-\omega_1\cdot\exp(-x)+\omega_2\cdot\exp(x)}{2\cdot sh(x)}$$

Although symmetrical, it seems the solution diverges when x tends toward 0, however it only happens when kappa =1, which is not allowed, otherwise it is a double polynomial root.

6.3.2.2 Double polynomial root

Differential equation is rewritten again

$$\frac{\partial\theta}{(\theta-\omega_0)^2}=a\cdot\partial t$$

Resolution is now made easy

$$\frac{1}{2}\times\left[-\frac{1}{(\theta-\omega_0)}\right]'=a\cdot\partial t$$

Now one cans integral the solution

$$\underbrace{\frac{1}{(\theta_0-\omega_0)}}_{\kappa}-\frac{1}{(\theta-\omega_0)}=\underbrace{2\times a}_{-1/\tau}\cdot(t-t_0)$$

That can be rewritten under the form

$$\frac{1}{(\theta-\omega_0)}=\frac{1}{\kappa}+\underbrace{\frac{(t-t_0)}{\tau}}_{u}$$

That is rewritten to exhibit the coverage function

$$\theta=\omega_0+\frac{\kappa\cdot\tau}{\tau+\kappa\cdot(t-t_0)}$$ which is similar to $$\boxed{\theta=\omega_0+\frac{\kappa}{1+\kappa\cdot u}}$$

6.3.2.3 *Coverage evolution*

We present a plot of analytical and numerical solution of the coverage.

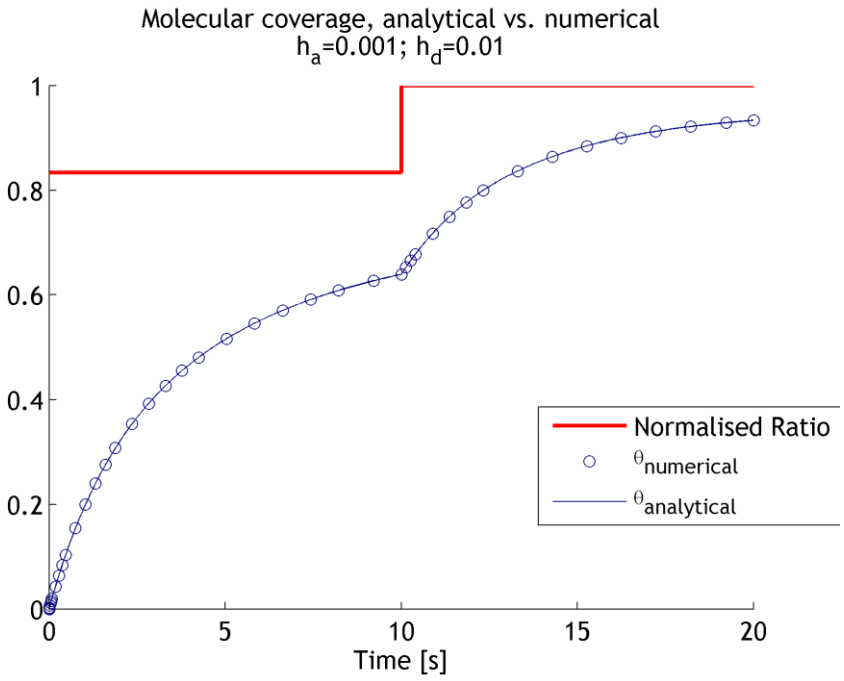

Figure 6.3. Benchmark of analytically and numerically calculated solutions of molecular coverage, for two different ratio set-points (250, then 500) with a maximum of 300 molecules per nanocrystal surface area.

6.4 Random-walk

6.4.1 Mean reservoir approximation

Practically, molecules are added little by little using very small aliquots while mixing thoroughly such that we suggest that the two descriptions can be superimposed (Figure 6.4a) to depict the distribution of both particles in solution. Although this might be a stretch of the reality the combination of reduced amounts of molecules and mixing prevents the almost instantaneous formation of large nanostructures observed at the pipette vicinity when none of these cares are taken. As a matter of fact the assumed mean-field distribution greatly simplifies the modelling.

Moreover it was observed experimentally that in order to get nanostructures of interest such as 2-mers or 3-mers, molecules must be in large excess compared to nanocrystals. As the more obvious feature of an *n*-mer is its number of constitutive nanocrystals, we simplify the description by spatially broadening the distribution of molecules. Given the fact that the ratio molecule:nanocrystal is large, we indeed consider a reservoir of molecules in which nanocrystals are immersed. The typical length in this context is thus L the mean distance between two nanocrystals (Figure 6.4b).

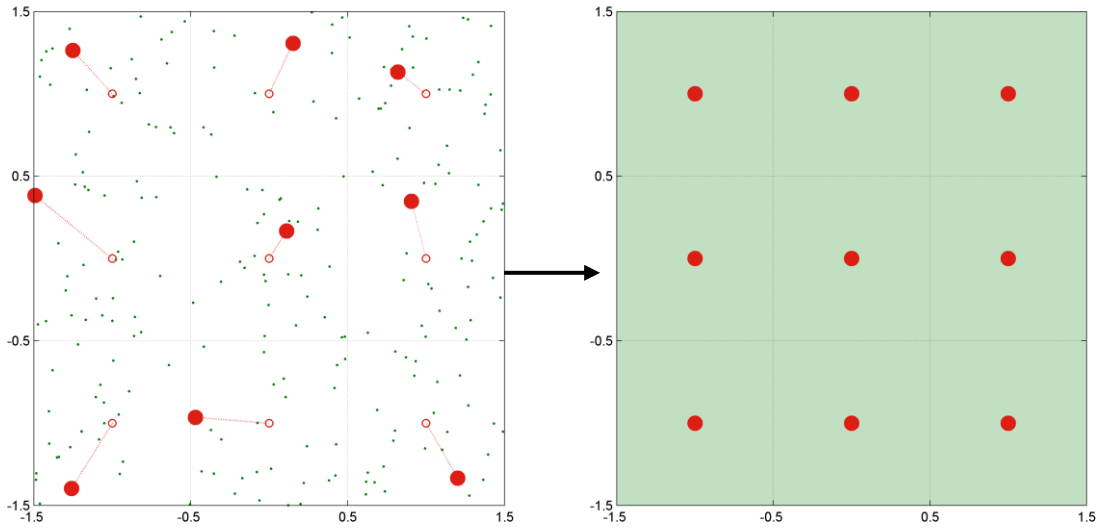

Figure 6.4. a, Two dimensional representation of the suggested superposition of the two distributions of different particles: the green dots are molecule positions, the red discs are the nanocrystal position randomly offset from the ideal position (open circles), molecule:nanocrystal ratio is 25 in the schematic. b, Mean-field representation of the reservoir of molecules available in which nanocrystals are immersed following a strict cubic lattice.

The time step used is therefore: $\tau = 6D/L^2$.

6.4.2 Modelling of clusters formation

In order to model cluster growth, there are at this point two case scenarios: we can either track individually all free particles involved or rather track individual clusters. We choose to focus only on individual clusters and leave molecules as a large continuum bath for two main reasons: (i) experimentally clusters can only be characterised by the number of nanocrystals (n) hence the terminology *n*-mers, (ii) the amount of processed information for the computations is dramatically decreased.

We must point out a golden rule for the formation of any cluster. As molecules are acting as linkers between nanocrystals, at minimum, $N_{ml} \geq N_{nc} - 1$, where N_{ml} is the number of molecules in the cluster and N_{nc} the number of nanocrystals. This relationship holds true for any cluster, no matter which three-dimensional structure is at stake. Nevertheless, the contact area between two nanocrystal does not limit the number of linker molecules to unity at all.

Assuming this rule is followed, we propose that the interactions between clusters can be described in a similar fashion to the Langmuir isotherm equation. Nevertheless, as the description of cluster formation is done on the nanocrystal content level, there are some differences in the physical meaning of rate constants employed, more precisely on the steric gene factor.

Conversely, dissociation of a cluster into sub-clusters may only occur if $N_{nc} > 1$.

6.4.3 Adsorption, Desorption, Aggregation, Dissociation events

We concentrate on the interactions at the surface level when molecules and nanocrystal surfaces are in contact.

6.4.3.1 Adsorption of a molecule on a nanocrystal surface

To implement the adsorption of molecules on nanocrystal surfaces, we consider that at all time a nanocrystal surface may accept a certain number of molecules. The amount of molecules that may adsorb is given by the ratio of all the free molecules normalised by the number of nanocrystals involved. This description assumes that at any given time during the course of a simulation, (at least) one nanocrystal surface is on the way of all these molecules.

Moreover as the relative coverage may screen the binding of approaching molecules, the factor of steric hindrance $(1-\theta)$ is taken into account. The binding of a molecule is considered proportional to the number of nanocrystals in a cluster to reflect the dependence of the surface

area with the cluster complexity. Finally the factor $\exp(-\beta \cdot E_a)$ embedding the activation energy is supposed to drive the process (with $\beta^{-1} = k_B T$).

6.4.3.2 Desorption of a molecule from a nanocrystal surface

Desorption of molecules from a nanocrystal surface is implemented so that every molecules attached to the surface can equally leave it. The bath is assumed to be able to host them again without any limitation so that in the end desorption is only driven by the constant $\int_0^\tau \upsilon_d \times \exp(-\beta \cdot E_d) \cdot dt = \upsilon_d \times \exp(-\beta \cdot E_d) \times \tau$.

6.4.3.3 Association of two clusters

Aggregation between two clusters is said to be mediated by at least one molecule ($N_{ml} \geq N_{nc}$). That condition being fulfilled, we also assume the aggregation only involves two nanocrystal surfaces. In this case, the steric gene is only a two body problem. The coverage of the two nanocrystals will dictate if aggregation is possible via the equation $f(\theta_a, \theta_b) = \theta_a(1-\theta_b) + \theta_b(1-\theta_a)$ and as shown on Figure 2.6.

This two-nanocrystal-only rule is a bit of a weakness in the model as it cannot account for the formation of circular trimer for instance. Nevertheless it will not impede on the accuracy of the results as we do not model *n*-mers conformation but merely their structure. Finally aggregation between two clusters is proportional to the factor $\exp(-\beta \cdot E_a)$ to take the activation energy into account.

6.4.3.4 Dissociation into sub-clusters

We also deal with the possibility of a cluster dissociating into sub-clusters. In order to implement dissociations, we consider a cluster as a linear chain of nanocrystals and each junction between two nanocrystals may be broken. This mechanism is driven by the factor $\int_0^\tau \upsilon_d \times \exp(-\beta \cdot E_d) \cdot dt = \upsilon_d \times \exp(-\beta \cdot E_d) \times \tau$. As the steric hindrance factor accounts for the overall coverage contribution and not a single nanocrystal-molecule junction, its value is fixed to $S = 1$ in this situation.

6.4.4 Implementation

We shall start with the random-walk model. First of all it is necessary to define the extension of the mesh in the three directions of space. As a matter of fact this also defines the number of nanocrystals present in the pool since we assume that, at start, nanocrystals are distributed in a

cubic lattice (1 particle per node). Typically we work with a handful of $(2\times 2+1)^3 = 125$ nanocrystals. The constant time-step value was derived accordingly and so we have to specify the number of iterations corresponding to the duration of an experiment. The benchmark data-set is based on a two hour experiment (different from the main text) leading to about $530{,}000$ iterations to complete a test. Finally as random-walk simulations are based on stochastic events, we need to repeat the simulation tests a certain number of times to smooth the distribution of populations. Practically a sequence of 20 simulation tests is performed to ascertain a stable response.

The rate equation model does not need any of those settings because *n*-mers populations are modelled on average, taking *n*-mers numbers as continuous values. In place of a maximum number of iterations, the physical values of the experimental time range is merely fed in.

To quantify the fidelity of the simulation results in regard to the experimental data points, we rely on the least mean square method. As one can expect we aim at modelled populations being very close to the distributions of *n*-mers counted. Consequently input parameters are varied so as to decrease the least mean square estimator defined by $\chi = \sqrt{S/(n\cdot p)}$ with $S = \sum_{j=1}^{p}\sum_{i=1}^{n}\left(\Pi_i^{\text{simu}}(t_j) - \Pi_i^{\text{exp}}(t_j)\right)^2$, where p is the number of measurement points scattered on the time axis, n the number of species, $\left(\Pi_i^{\text{simu}}, \Pi_i^{\text{exp}}\right)$ are respectively the relative proportion of clusters (as counted) of simulated and experimental i-mers at the time of measurement t_j.

We will always present simulation results along with χ being the average mismatch between simulations and experiments against the scale of concentration.

An interesting set of parameters is found when a reasonably low value of the least mean square estimator is obtained $(\chi \to 0)$. Optimisation techniques based on the steepest descent algorithm exist and can be used to extract parameters leading to a best fit. This method is indeed implemented for the rate-equation model. The search for the best parameter values is thus automatic.

In spite of this very efficient methodology, the parameter search was kept manual for random-walk simulations. It all comes from the fact that about 40 hours are required to complete a set of 20 simulation tests. Despite several attempts of code optimisation this computation time has not been reduced significantly. In comparison, numerical solving of the rate equations on the same desktop PC using the same MATLAB platform only takes a few tens of seconds even for an experimental time scale of several days.

At this point we can explain why we chose to work with merely 125 nanocrystals. It seems to be a good trade-off between inherent simulation stochastic fluctuations and computation time. When testing a new set of parameters, one can have a look at the early stage to check that the monomer population is neither collapsing too quickly nor staying pinned at its initial value. Consequently the manual method for searching interesting parameters will not provide as good results in terms of optimising χ . The χ value is likely to be slightly overestimated in this case but this does tarnish the physical relevance of this modelling approach.

6.4.5 Results

For a start we must point out that the two different modelling approaches – the rate-equation and the random walk models – lead to very similar outcomes. This tends to indicate that the two methods for depicting the process of *n*-mers structures are consistent.

As discussed earlier, we know the population of *n*-mers evolve in a linked fashion so as to keep the number of nanocrystals constant. The results of both type of simulations show that two extreme trends can take place for a given molecule:nanocrystal ratio historical (i.e: integral) set-point, see Figure 6.5.

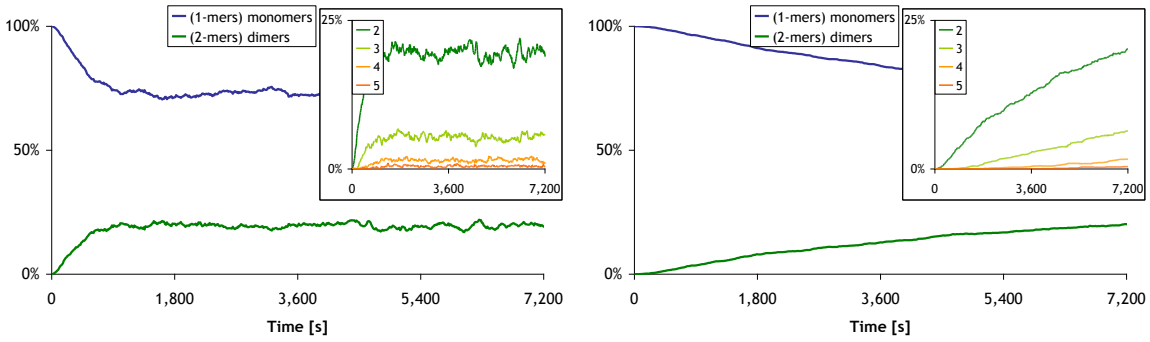

Figure 6.5. Two types of population evolution is observed (Random-walk results are presented). (a) the system can evolves quickly and reach plateaus. One can observe fluctuations in the populations due to the dynamic equilibrium nature of the *n*-mer formation process. The curves are constructed the average upon 20 simulations (similar to scenario B in the main text). (b) One the other hand *n*-mers populations can be evolving more slowly and continuously (similar to scenario A in the main text).

On one hand the populations of *n*-mers can reach different plateaus shortly after the molecular aliquot addition. In this case, the system of *n*-mers responds quickly to the addition of molecules: seamlessly reaching a steady-state regime. This means a new global equilibrium is defined. Although overall each population size remains constant, a dynamic equilibrium takes place as can be seen on the plot from the random-walk model, see Figure 6.5b.

Such a rapid response would not imply a process that is either diffusion-limited (high number of encounters) nor is kinetically constrained (the association activation energy is overcome easily). This behaviour is observed for $E_a \leq 10 \times k_B T$. The population curves soon reach plateaus as we can expect since the barrier is low.

Conversely the other case scenario consists of *n*-mers populations evolving smoothly. In this situation, all populations keep changing over time since the *n*-mers system tends to look for a distant equilibrium. This happens for $E_a \geq 12 \times k_B T$. Hence experimentally the distribution of *n*-mers should look unstable. Unlike the first case, the process can be limited by sparse collisions of species and/or slow reaction kinetics at encounters (the association activation energy is then high compared to $k_B T$). Interestingly we must also underline the fact that the process can appear to be frozen and possibly mistakenly interpreted at equilibrium but in lieu is actually extremely slow.

6.5 Pace of change of UV-vis absorption spectra

To further investigate the mechanisms at stake, we introduce the weighted mean estimator characterising the pace of change in the overall UV-visible absorption spectra, see Equation 6.1.

$$\lambda_c = \frac{\sum_\lambda (A(\lambda) \times \lambda)}{\sum_\lambda A(\lambda)}$$

Equation 6.1. UV-visible absorption spectra weighted mean factor.

Although there is no trivial relationship between λ_c and the *n*-mers population that could lead to quantitative information, we can still get qualitative insights of the process. As it is not possible experimentally to add too many molecules at a time without ending with large aggregates, we look at the optical response of the system to a near constant slope ramp followed by no further additions, see Figure 6.6. We can notice a behaviour that is fairly (sub) linear and goes ahead even when the ratio is kept constant. From this picture, we know the formation of *n*-mers is slow compared to molecular addition (at least in this case).

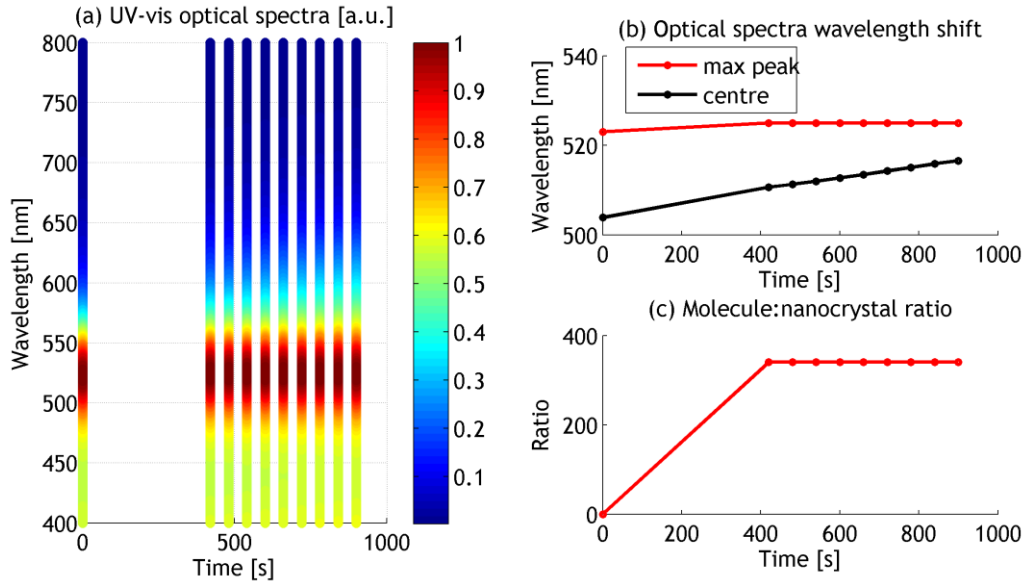

Figure 6.6. Pace of change of the UV-visible spectra as exhibited by the weighted mean factor. Whereas the no more aliquots of molecules are added, the optical is still changing almost linearly over time: indicating the slow nature of the process (experimental data taken from another subsequent experiment).

Along the same line, it has been reported that experimentally, fast additions lead to fast formation whereas slow additions results in sluggish formation and more molecules seem needed. In other words, the formation seems to be dependent on the pace of addition and to a lesser extent to the overall quantity of added molecules, $R_{mol:nc}$.

6.6 Comprehensive fabrication process

The fabrication process of nanocrystal assemblies, the testing in dichloromethane and the subsequent molecular functionalisation is detailed thereafter, see Figure 6.7.

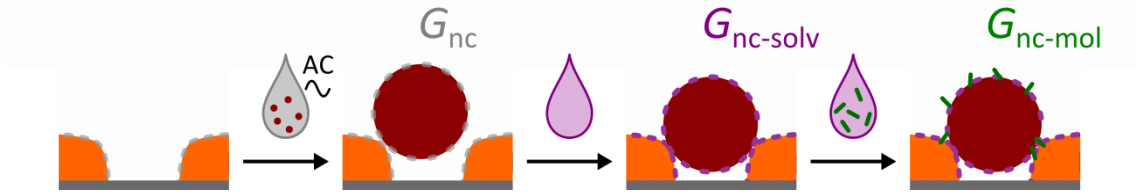

Figure 6.7. Schematic of the comprehensive fabrication process flow steps.

Once the patterning of nanometre scale electrodes is finished, the fabrication process steps are done in non clean-room environments for practical reasons. In order to minimise possible contaminations of the devices, samples are stored in isopropyl alcohol up until the dielectrophoretic trapping routine starts.

A drop (4 µL) of commercially available colloidal solution of citrate stabilised Au nanocrystals in water (1:10 diluted in de-ionised water) is placed on the central region of the sample. An AC voltage with frequency (f=1 MHz) and peak-to-peak amplitude ($V_{p\text{-}p}$) in the range $2.0 \leq V_{p\text{-}p} \leq 2.3$ V is applied for 60 seconds to trap the nanostructures. For each set of values for the trapping parameters (f, $V_{p\text{-}p}$), the process is repeated across 4 sets of 6 nanogaps each on the same chip. When the process is completed for all electrodes, the sample is briefly rinsed in isopropyl alcohol (<5 min) and blown dry in a gentle stream of nitrogen.

Consecutively after dielectrophoretic trapping, the sample is loaded in a controlled atmosphere/vacuum probe station (Lakeshore TTPX Cryogenic Probe Station) interfaced to a parameter analyzer (Agilent HP4156A). The chamber is pumped down to vacuum conditions, typically on the order of 2.5×10^{-4} Pa, before room temperature current-voltage, $I(V)$, characteristics for each device is measured. This first series of electrical measurement is performed so as to detect which devices present a measurable conductance, G_{nc}.

When the first electrical characterisation flow is completed, the sample is unloaded from the chamber and directly immersed in a vial of dichloromethane (chemical grade: “reagent”) for ~24 hours at room temperature and kept in the dark. Afterwards, the sample may be briefly rinsed in isopropyl alcohol (<5 min) and blown dry in a gentle stream of nitrogen.

The sample is loaded again in the probe station under vacuum for the second time. Current-voltage measurements are performed on the same devices so as to monitor the possible change in electrical response after solvent immersion and estimate the new conductance, $G_{nc\text{-}solv}$.

The second campaign of electrical measurement completed, the sample is removed from the chamber and immersed in the 2mM DTEB in dichloromethane molecular candidate solution for ~24 hours at room temperature in the dark. The sample is then rinsed briefly in isopropyl alcohol (<5 min) and blown dry in a gentle stream of nitrogen.

For the last time, the sample is loaded in the probe station chamber pumped down to the base vacuum pressure. Each device is electrically characterised a third time to estimate the new current-voltage response giving an estimate of the conductance after molecular fictionalization, $G_{nc\text{-}mol}$.

At the end of the joint process-characterisation flow, the sample is imaged using a Scanning Electron Microscope (JEOL JSM-7500-F) to visually characterise the nanocrystal assembly bridging the nanometre-scale gap.

6.7 Electrochemistry

6.7.1 Cyclic voltammetry of the functional molecule

The functional molecule used in the experiments was synthesized by Emma Harvey in Mary Pryce Group in Dublin College University. The compound is 1,2-Bis(5'-(3''-ethynylthiophene)-2'-methylthien-3'-yl)-cyclopentene, abbreviated th-PCH-th for simplicity (th stand for the thiophene anchor groups at both ends, PCH for the cyclopentene loaded with hydrogen as opposed to other possible atoms like fluoride or even radicals). The molecule has two isomer forms. The open-ring isomer can be irreversibly altered into the closed-ring isomer using UV light or electrochemistry.

The compound is characterised by cyclic voltammetry, see Figure 6.8. A solution of 1 mM th-PCH-th (open-form) dissolved in dichloromethane (using tetrabutylammonium hexafluorophosphate as the supporting electrolyte) is prepared. A glassy carbon working electrode, with a silver wire reference, and platinum wire counter electrode were used. A total of six sweeps were run making three complete cycles between 0 V and 1.4 V. In the first oxidation sweep, there are no oxidation waves until approximately 1.2 V. This first sweep irreversibly modifies the compound from the open-ring to the closed-ring isomer.

Following this, on the first reverse sweep (from 1.4 V to 0 V), two reduction waves were observed at approximately 0.6 and 0.35V. The subsequent oxidation process showed two new oxidation waves at approximately 0.4 and 0.65V: the separation between pair of oxidation-reduction peaks is ~59 mV which indicates a single electron transfer process.

The two last cycle confirms the two oxidation-reduction processes as two new oxidation-reduction waves below 1.0 V are due to the ring-closed compound and represent transitions for $1Hc^{2+}$ (oxidation: 0.65 V and reduction: 0.6 V) and for $1Hc^{1+}$ (oxidation: 0.4 V and reduction: 0.35 V).

In summary, the irreversible oxidative ring-closing is taking in the first place from the open-ring isomer to the closed-ring isomer (potential swept from 0.0 V to >1.2 V) then the compound closed ring isomer of th-PCH-th shows oxidation-reduction processes.

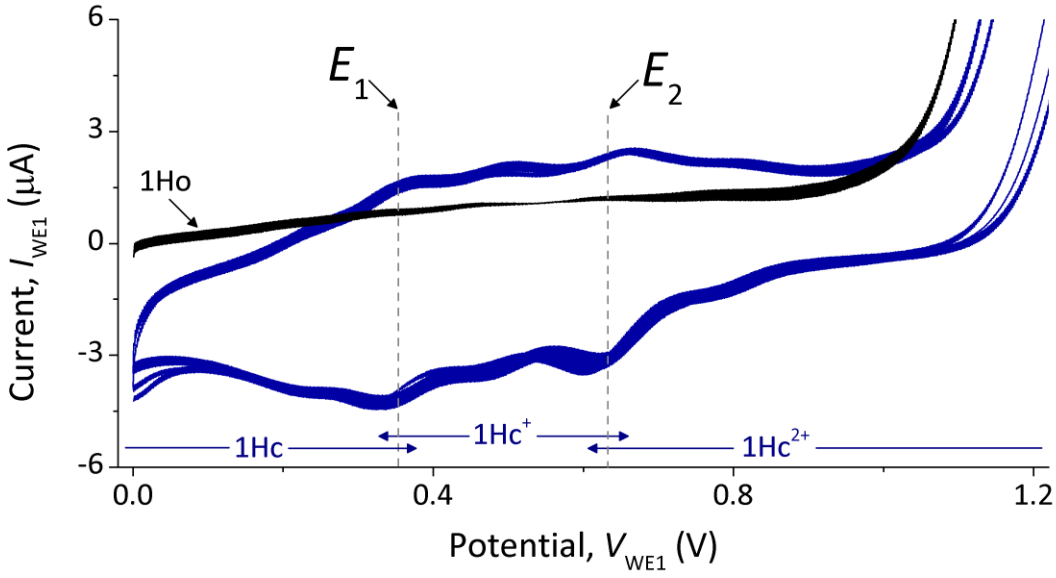

Figure 6.8. Cyclic voltammetry of the th-PCH-th compound in tetrabutylammonium hexafluorophosphate in dichloromethane.

6.7.2 Preparation of the quasi-reference electrode: Ag wire

The widely used technique to prepare a quasi reference electrode of consisting of a silver wire (Ag) is to run a Cyclic-voltammetry scan in a buffer solution of 1 M KCl with a calibrated Ag/AgCl reference electrode, a platinum counter electrode and the silver wire as a working electrode in a bias range of [0,1] V.

Afterwards, an open circuit potential test is performed for 60 minutes in which the reference and counter electrode is the usual Ag/AgCl electrode while the working electrode is the prepared silver wire. CVs are ran in the electrolyte of choice in a bias range of [-1,+1]V. One should only observe a flat signal.

Because we implemented a simplified version of (bi-)potentiostat merging reference and counter electrodes, we do not precondition the Ag wire.

6.8 References

1. Barrett, C. Charge Transport in Nanoscale Structures and Devices. University College Cork, Cork, 2009.
2. Xu, Y.-l., Electromagnetic scattering by an aggregate of spheres. *Appl. Opt.* **1995,** *34* (21), 4573-4588.
3. Hoevel, H.; Fritz, S.; Hilger, A.; Kreibig, U.; Vollmer, M., Width of cluster plasmon resonances: Bulk dielectric functions and chemical interface damping. *Physical Review B* **1993,** *48* (24), 18178.
4. Schmitt, J.; Mächtle, P.; Eck, D.; Möhwald, H.; Helm, C. A., Preparation and Optical Properties of Colloidal Gold Monolayers. *Langmuir* **1999,** *15* (9), 3256-3266.
5. Jensen, T.; Kelly, L.; Lazarides, A.; Schatz, G. C., Electrodynamics of Noble Metal Nanoparticles and Nanoparticle Clusters. *Journal of Cluster Science* **1999,** *10* (2), 295-317.
6. Zhong, Z.; Patskovskyy, S.; Bouvrette, P.; Luong, J. H. T.; Gedanken, A., The Surface Chemistry of Au Colloids and Their Interactions with Functional Amino Acids. *The Journal of Physical Chemistry B* **2004,** *108* (13), 4046-4052.
7. Billaud, P.; Marhaba, S.; Cottancin, E.; Arnaud, L.; Bachelier, G.; Bonnet, C.; Del Fatti, N.; Lerme, J.; Vallee, F.; Vialle, J. L.; Broyer, M.; Pellarin, M., Correlation between the Extinction Spectrum of a Single Metal Nanoparticle and Its Electron Microscopy Image. *The Journal of Physical Chemistry C* **2008,** *112* (4), 978-982.
8. Haiss, W.; Thanh, N. T. K.; Aveyard, J.; Fernig, D. G., Determination of Size and Concentration of Gold Nanoparticles from UV−Vis Spectra. *Analytical Chemistry* **2007,** *79* (11), 4215-4221.
9. Grady, N. K.; Halas, N. J.; Nordlander, P., Influence of dielectric function properties on the optical response of plasmon resonant metallic nanoparticles. *Chemical Physics Letters* **2004,** *399* (1-3), 167-171.
10. OriginLabs, *OriginPro Documentation*.

Publication list

Journal articles

Barrett, C.; Sassiat, N.; Leveque, G.; Thompson, D.; Nolan, M.; Doyle, H.; Iacopino, D. & Quinn A. J. Formation and optical properties of plasmonic nanocrystal-molecule nanostructures. In preparation.

Sassiat, N.; MacHale, J.; Barrett, C.; Pryce, M. T.; Harvey, E. C.; Cafolla, A. A.; Thompson D. & Quinn A. J. Interfacing molecules with nanocrystals: laterally-contacted “few-molecule” devices. In preparation.

Electrochemical interfacing of nanocrystal-molecule nanostructures. In preparation.

Conference poster presentations

Sassiat, N.; MacHale, J.; Barrett, C.; Pryce, M.T.; Harvey, E.C.; Cafolla, A.A.; Thompson, D. ; & Quinn, A.J. Conductance analysis and electrochemical switching in "few-molecule" nanocrystal devices. Tyndall Poster Competition 2011, Tyndall, Cork, 22nd July 2011.

Sassiat, N.; Barrett, C.; Pryce, M.; Harvey, E.; Cafolla, A.A. & Quinn, A.J. Interfacing molecules with nanocrystals: Laterally-contacted “few-molecule” devices. ElecMol10 International Conference, Grenoble, France, 6-10 December 2010.

Sassiat, N.; Barrett, C. & Quinn, A.J. Process Modelling of the Formation of Nanocrystal-Molecule Nanostructures. International Conference on Molecular Electronics, Emmetten, Switzerland 5-9 January 2010.

Sassiat, N.; Barrett, C. & Quinn, A.J. Process Modelling of the Formation of Nanocrystal-Molecule Nanostructures. Trends in Nanotechnology (TNT) 2009, Barcelona, Spain, 7-11 September 2009.

Sassiat, N.; Barrett, C. & Quinn, A.J. Formation and Modelling of Nanocrystal-Molecule Nanostructures. CUSO - REGIO - Summer School: Quo vadis electron - from radicals to ET, Villars-sur-Ollon, Switzerland, 31 August 4 September 2008.